Development of blood-brain barrier spheroid models based on human induced pluripotent stem cells (hiPSCs) and investigation of shear stress on hiPSC-derived brain capillary endothelial-like cells

Entwicklung von Sphäroid-Modellen der Blut-Hirn-Schranke basierend auf menschlichen induzierten pluripotenten Stammzellen (hiPSCs) und Untersuchung der Scherbeanspruchung von hiPSC-abgeleiteten Hirnkapillarendothel-ähnlichen Zellen

Doctoral thesis for a doctoral degree
at the Graduate School of Life Sciences,
Julius-Maximilians-Universität Würzburg,
Section: Biomedicine
submitted by

Sanjana Mathew-Schmitt
from

Bangalore

Würzburg 2022

Submitted on:

……

Office stamp

Members of the committee
Chairperson: Prof. Dr. Thomas Dandekar

……
Primary supervisor: PD Dr. Marco Metzger

……

Supervisor (second): Prof. Dr. Heike Walles

……

Supervisor (third): Prof. Dr. Paul Dalton

……

Supervisor (fourth): Dr. Antje Appelt-Menzel

……

Date of public defense:

Date of receipt of certificates:

Dedicated to my parents

Prof. P. M. Mathew & Mrs. Ancy Mathew

എന്റെ മാതാപിതാക്കൾക്ക് സമർപ്പിക്കുന്നു

Meinen Eltern gewidmet

"Whether you're a brother or whether you're a mother
You're stayin' alive, stayin' alive"
– Bee Gees

1. ABSTRACT

A highly regulated microenvironment is essential in maintaining normal functioning of the central nervous system (CNS). The existence of a biological barrier, termed as the blood-brain barrier (BBB), at the blood to brain interface effectively allows for selective passage of substances and pathogens into the brain (Kadry, Noorani et al. 2020). The BBB chiefly serves in protecting the brain from extrinsic toxin entry and pathogen invasions. The BBB is formed mainly by brain capillary endothelial cells (BCECs) which are responsible for excluding ~ 100% of large-molecule neurotherapeutics and more than 98% of all small-molecule drugs from entry into the brain. Minimal BBB transport of major potential CNS drugs allows for attenuated effective treatments for majority of CNS disorders (Appelt-Menzel, Oerter et al. 2020). Animals are generally used as model systems to study neurotherapeutic delivery into the brain, however due to species based disparity, experimental animal models lead to several false positive or false negative drug efficacy predictions thereby being unable to fully predict effects in humans (Ruck, Bittner et al. 2015). An example being that over the last two decades, much of the studies involving animals lead to high failure rates in drug development with ~ 97% failure in cancers and ~ 99% failure for Alzheimer´s disease (Pound 2020). Widespead failures in clinical trials associated with neurological disorders have resulted in questions on whether existing preclinical animal models are genuinely reflective of the human condition (Bhalerao, Sivandzade et al. 2020). Apart from high failure rates in humans, the costs for animal testings is extremely high. According to the Organisation for Economic Co-operation and Development (OECD), responsible for determining animal testing guidelines and methodology for government, industry, and independent laboratories the average cost of a single two-generation reproductive animal toxicity study worldwide is 318,295 € and for Europe alone is ~ 285,842 € (Van Norman 2019). Due to these reasons two separate movements exist within the scientific world, one being to improve animal research and the other to promote new approach methodologies with the European government setting 2025 - 2035 as a deadline for gradually disposing the use of animals in pharmaceutical testing (Pound 2020).

The discovery of human induced pluripotent stem cell (hiPSC) technology in 2006 (Takahashi and Yamanaka 2006, Takahashi, Tanabe et al. 2007) revolutionized the field of drug discovery *in-vitro*. HiPSCs can be differentiated into various tissue types that mimic disease phenotypes, thereby offering the possibility to deliver humanized *in-vitro* test systems. With respect to the BBB, several strategies to differentiate hiPSCs to BCECs (iBCECs) are reported over the years (Appelt-Menzel, Oerter et al. 2020). However, iBCECs are said to possess an epithelial or undifferentiated phenotype causing incongruity in BBB lineage specifications (Lippmann,

Azarin et al. 2020). Therefore, in order to identify a reliable differentiation strategy in deriving iBCECs possessing hallmark BBB characteristics, which can be used for downstream applications, the work in this thesis compared two methods, namely the co-differentiation (CD) and the directed differentiation (DD). Briefly, CD mimics a brain like niche environment for iBCEC specification (Lippmann, Al-Ahmad et al. 2014), while DD focuses on induction of the mesoderm followed by iBCEC specification (Qian, Maguire et al. 2017). The results obtained verified that while iBCECs derived via CD, in comparison to human BCEC cell line hCMEC/D3 showed the presence of epithelial transcripts such as E-Cadherin (CDH1), and gene level downregulation of endothelial specific platelet endothelial cell adhesion molecule-1 (PECAM-1) and VE-cadherin (CDH5) but demonstrated higher barrier integrity. The CD strategy essentially presented iBCECs with a mean trans-endothelial electrical resistance (TEER) of ~ 2000 – 2500 Ω*cm^2 and low permeability coefficients (PC) of < 0.50 µm/min for small molecule transport of sodium fluorescein (NaF) and characteristic BCEC tight junction (TJ) protein expression of claudin-5 and occludin. Additionally, iBCECs derived via CD did not form tubes in response to angiogenic stimuli. DD on the other hand resulted in iBCECs with similar down regulations in *PECAM-1* and *CDH5* gene expression. They were additionally characterized by lower barrier integrity, measured by mean TEER of only ~ 250 – 450 Ω*cm^2 and high PC of > 5 µm/min in small molecule transport of NaF. Although iBCECs derived via DD formed tubes in response to angiogenic stimuli, they did not show positive protein expression of characteristic BCEC TJs such as claudin-5 and occludin. These results led to the hypothesis that maturity and lineage specification of iBCECs could be improved by incorporating *in-vivo* like characteristics *in-vitro*, such as direct co-culture with neurovascular unit (NVU) cell types via spheroid formation and by induction of shear stress and fluid flow. In comparison to standard iBCEC transwell mono-cultures, BBB spheroids showed enhanced transcript expression of *PECAM-1* and reduced expression of epithelial markers such as *CDH1* and claudin-6 (*CLDN6*). BBB spheroids showed classical BCEC-like ultrastructure that was identified by TJ particles on the protoplasmic face (P-face) and exoplasmic face (E-face) of the plasma membrane. TJ strands were organized as particles and particle-free grooves on the E-face, while on the P-face, partly beaded particles and partly continuous strands were identified. BBB spheroids also showed positive protein expression of claudin-5, VE-cadherin, PECAM-1, glucose transporter-1 (GLUT-1), P-glycoprotein (P-gp) and transferrin receptor-1 (Tfr-1). BBB spheroids demonstrated higher relative impedance percentages in comparison to spheroids without an iBCEC barrier. Barrier integrity assessments additionally corresponded with lower permeability to small molecule tracer NaF, with spheroids containing iBCECs showing higher relative fluorescence unit percentages (RFU%) of ~ 90% in apical compartments, compared to ~ 80% in spheroids without iBCECs. In summary, direct cellular contacts in the complex spheroid model resulted in enhanced maturation of iBCECs.

A bioreactor system was used to further assess the effect of shear stress. This system enabled inclusion of fluidic flow and shear stress conditions in addition to non-invasive barrier integrity measurements (Choi, Mathew et al. 2022). iBCECs were cultured for a total of seven days post differentiation (d17) within the bioreactor and barrier integrity was non-invasively monitored. Until d17 of long-term culture, TEER values of iBCECs steadily dropped from ~ 1800 Ω*cm^2 ~ 400 Ω*cm^2 under static conditions and from ~ 2500 Ω*cm^2 to ~ 250 Ω*cm^2 under dynamic conditions. Transcriptomic analyses, morphometric analyses and protein marker expression showed enhanced maturation of iBECs under long-term culture and dynamic flow. Importantly, on d10 claudin-5 was expressed mostly in the cytoplasm with only ~ 5% iBCECs showing continuous staining at the cell borders. With increase in culture duration, iBCECs at d17 of static culture showed ~ 18% of cells having continuous cell border expression, while dynamic conditions showed upto ~ 30% of cells with continuous cell-cell border expression patterns. Similarly, ~ 33% of cells showed cell-cell border expression of occludin on d10 with increases to ~ 55% under d17 static and up to ~ 65% under d17 dynamic conditions, thereby indicating iBCEC maturation.

In conclusion, the data presented within this thesis demonstrates the maturation of iBCECs in BBB spheroids, obtained via direct cellular contacts and by the application of flow and shear stress. Both established novel models need to be further validated for pharmaceutical drug applications together with *in-vitro-in-vivo* correlations in order to exploit their full potential.

2. ZUSAMMENFASSUNG

Eine hochregulierte Mikroumgebung ist für die Aufrechterhaltung der normalen Funktion des Zentralen Nervensystems (ZNS) unerlässlich. Das Vorhandensein einer biologischen Barriere, der so genannten Blut-Hirn-Schranke (BHS), als Schnittstelle zwischen Blutkreislauf und Gehirn ermöglicht den selektiven Durchgang von Substanzen und Pathogenen in das Gehirn (Kadry, Noorani et al. 2020). Die BHS dient hauptsächlich dazu, das Gehirn vor dem Eindringen von Toxinen von außen und dem Eindringen von Krankheitserregern zu schützen. Die BHS wird hauptsächlich von Hirnkapillarendothelzellen (engl. *brain capillary endothelial cells*, BCECs) gebildet, die dafür verantwortlich sind, dass ~ 100% der großmolekularen Neurotherapeutika und mehr als 98% aller kleinmolekularen Medikamente nicht in das Gehirn gelangen können. Ein eingeschränkter BHS-Transport wichtiger potenzieller Wirkstoffe führt zu einer abgeschwächten Wirksamkeit der Behandlung der meisten ZNS-Erkrankungen (Pardridge 2005). Mäuse, Ratten, Schweine und Rinder werden in der Regel als Modellsysteme verwendet, um die Verabreichung von Neurotherapeutika in das Gehirn zu untersuchen. Aufgrund der Unterschiede zwischen den Spezies führen experimentelle Tiermodelle jedoch vermehrt zu falsch positiven oder falsch negativen Vorhersagen über die Wirksamkeit von Medikamenten, so dass sie nicht in der Lage sind, die Wirkungen beim Menschen vollständig vorherzusagen (Ruck, Bittner et al. 2015). Ein Beispiel dafür ist, dass in den letzten zwei Jahrzehnten ein Großteil der Studien an Tieren zu Misserfolgsraten in der Wirkstoffzulassung geführt hat. Bei einer Fehlerrate von 97% im Zusammenhang mit Krebs und ~99% bei Alzheimer führt dies zum Therapieversagen (Pound 2020). Die weit verbreiteten Misserfolge bei klinischen Versuchen im Zusammenhang mit neurologischen Erkrankungen haben zu der Frage geführt, ob die bestehenden präklinischen Tiermodelle wirklich die Physiologie des Menschen widerspiegeln (Bhalerao, Sivandzade et al. 2020). Abgesehen von den hohen Ausfallraten sind die Kosten für Tierversuche extrem hoch. Nach Angaben der Organisation für wirtschaftliche Zusammenarbeit und Entwicklung (engl. *Organisation for Economic Co-operation and Development*, OECD), welche für die Festlegung von Tierversuchsrichtlinien und -methoden für die Regierung, die Industrie und unabhängige Labore zuständig ist, belaufen sich die durchschnittlichen Kosten für eine einzige Zwei-Generationen-Studie zur Reproduktionstoxizität an Tieren weltweit auf 318.295 € und allein für Europa auf ~ 285.842 € (Van Norman 2019). Aus diesen Gründen gibt es zwei unterschiedliche Bemühungen unter den Wissenschaftlern. Zum einen zur Verbesserung der Tierforschung und zum anderen zur Förderung neuer Methoden gemäß den 3R (eng. *replace, reduce, refine*), wobei die europäische Regierung die Jahre 2025 bis 2035 als Frist für den schrittweisen Verzicht auf Tierversuche in der Forschung festgelegt hat (Pound 2020). Die

Entdeckung der humanen induziert pluripotenten Stammzell (hiPSC)-Technologie im Jahr 2006 (Takahashi und Yamanaka 2006, Takahashi, Tanabe et al. 2007) hat den Bereich der Arzneimittelforschung revolutioniert, da hiPSCs in verschiedene Gewebetypen differenziert werden können und damit die Möglichkeit bieten, humanisierte *in-vitro*-Testsysteme bereitzustellen, die zur Untersuchung verschiedener Krankheiten verwendet werden können.

In Bezug auf die BHS wurde im Laufe der Jahre mehrere Strategien zur Differenzierung von hiPSCs zu BCECs (iBCECs) etabliert (Appelt-Menzel, Oerter et al. 2020), allerdings wird ihnen ein epithelialer Phänotyp nachgesagt, was zu Fragen in der Spezifikation der BBB führt (Lippmann, Azarin et al. 2020). Um eine verlässliche Differenzierungsstrategie für die Gewinnung von iBCECs mit charakteristischen BHS-Merkmalen zu finden, welche für Downstream-Anwendungengenutztwerden können, wurden in dieser Arbeit zwei Methoden verglichen. Die Ko-Differenzierung (engl. *co-differentiation*, CD) und die gerichtete Differenzierung (engl. *directed differentiation*, DD). Zusammengefasst simuliert die CD eine ZNS-ähnliche Mikroumgebung für die Spezifikation der iBCECs nach (Lippmann, Al-Ahmad et al. 2014), während sich die DD auf die Induktion des Mesoderms und die anschließende iBCEC-Spezifikation konzentriert (Qian, Maguire et al. 2017). Die erzielten Ergebnisse bestätigten, dass iBCECs, welche mittels CD abgeleitet wurden, im Vergleich zur humanen BCEC-Zelllinie (hCMEC/D3) zwar epitheliale Transkripte wie E-Cadherin (CDH1) besitzen, aber eine Herabregulierung von Thrombozyten-Endothelzell-Adhäsionsmolekül-1 (PECAM-1) und VE-Cadherin (CDH5) aufweisen. Die von CD abgeleiteten iBCECs hatten zudem eine höhere Barriere-Integrität und Funktionalität gezeigt. Im Wesentlichen führte die CD-Strategie zu iBCECs mit einem hohen transendothelialen elektrischen Widerstand (engl. *Transendothe lialelectrical resistance*, TEER) von 2000 - 2500Ω*cm^2, einem niedrigen Permeabilitätskoeffiz ienten (eng. *Permeability co-efficient*, PC) von < 0,50 µm/min für den Transport kleiner Moleküle wie Natriumfluorescein (NaF) und einer charakteristischen Expression von BCEC-spezifischen Tight Junction (TJ)-Proteinen wie Claudin-5 und Occludin. Außerdem bildeten iBCECs, welche über CD gewonnen wurden, keine Gefäßstrukturen als Reaktion auf angiogene Stimuli. DD hingegen führte zu iBCECs mit einer ähnlichen Herabregulierung der *PECAM-1*- und *CDH5*-Genexpression, die zusätzlich durch eine geringere Barriereintegrität, gemessen an einem niedrigen TEER von nur ~ 250 - 450 Ω*cm^2 und einem hohen PC von > 5 µm/min, bei dem Transport von NaF gekennzeichnet war. Obwohl die über DD gewonnenen iBCECs in der Lage waren Gefäßnetze auszubilden, zeigten sie keine Expression der charakteristischen BCEC-TJs wie Claudin-5 und Occludin.

Diese Ergebnisse führten zu der Hypothese, die *in-vitro* Differenzierung und Reifung von iBCECs zu verbessern, indem *in-vivo*-ähnliche Stimuli *in-vitro* angewandt werden, wie z. B. die direkte Kokultur mit Zelltypen der neurovaskulären Einheit (NVE) durch Sphäroidbildung und die Induktion von Scherstress in einem dynamischen Flussmodell. Im Vergleich zu iBCEC-

basierten Transwellmodellen, die zumeist in Monokulturen aufgebaut werden, zeigten die BHS-Sphäroide eine erhöhte Expression von *PECAM-1* und eine reduzierte Expression von Epithelmarkern wie E-Cadherin *(CDH1)* und Claudin-6 (*CLDN6*). BHS-Sphäroide zeigten eine klassische BCEC-ähnliche Ultrastruktur, die durch TJ-Partikel auf der protoplasmatischen Phase (P-Phase) und der exoplasmatischen Phase (E-Phase) der Plasmamembran gekennzeichnet war. Die TJ-Stränge waren als Partikel und partikelfreie Rillen auf der E-Phase organisiert, während auf der P-Phase teils Partikel und teils kontinuierliche Stränge zu erkennen waren. BHS-Sphäroide zeigten auch eine positive Proteinexpression von Claudin-5, VE-Cadherin, PECAM-1, Glukose-Transporter-1 (GLUT-1), P-Glykoprotein (P-gp) und Transferrin-Rezeptor-1 (Tfr-1). Die BHS-Sphäroide wiesen ebenfalls höhere relative Impedanzwerte im Vergleich zu Sphäroiden ohne iBCEC-Barriere auf. Die Bewertung der Integrität der Barriere korrespondierte zudem mit einer geringeren Permeabilität für den niedermolekularen Tracer NaF, wobei Sphäroide mit iBCECs einen höheren Prozentsatz an relativen Fluoreszenzeinheiten (RFU%) von etwa 90% in den apikalen Kompartimenten aufwiesen, verglichen mit etwa 80% in Sphäroiden ohne iBCECs. Zusammenfassend lässt sich sagen, dass direkte zelluläre Kontakte im komplexen Sphäroidmodell zu einer verstärkten Reifung von iBCECs führten.

In-vivo ist die BHS Scherbelastungen ausgesetzt, die einen wichtigen und oft vernachlässigten physiologischen Stimulus darstellen (Cucullo, Hossain et al. 2011). Um die Auswirkung von Scherstress auf die Eigenschaften und die Reifung von iBCECs zu messen, wurden diese in einem Bioreaktorsystem kultiviert.(Choi, Mathew et al. 2022). Hier war es möglich, iBCECs für insgesamt sieben Tage nach der Differenzierung (d17) erfolgreich in diesem System zu kultivieren und zusätzlich die Barriereintegrität nicht-invasiv zu überwachen. Bis d17 der Langzeitkultur fielen die TEER-Werte von iBCECs stetig von ~ 1800 Ω*cm2 ~ 400 Ω*cm2 unter statischen Bedingungen bzw. von ~ 2500 Ω*cm2 auf ~ 250 Ω*cm2 unter dynamischen Bedingungen. Zusätzliche Untersuchungen und Vergleiche von iBCECs unter diesen Kulturbedingungen mittels transkriptioneller und morphometrischer Analysen, sowie Expression von Proteinmarkern zeigten, dass iBCECs aufgrund der Langzeitkultur und des dynamischen Flusses eine verstärkte Reifung vorweisen. Wichtig ist, dass Claudin-5 bei d10 hauptsächlich im Zytoplasma exprimiert wurde und nur etwa 5% der iBCECs eine kontinuierliche Färbung an den Zellgrenzen aufwiesen. Mit zunehmender Kulturdauer zeigten iBCECs bei d17 in statischer Kultur ~ 18% der Zellen mit kontinuierlicher Zellrandexpression, während unter dynamischen Bedingungen bis zu ~ 30% der Zellen kontinuierliche Zellrandexpressionsmuster aufwiesen. In ähnlicher Weise zeigten ~ 33% der Zellen eine Zell-Zell-Grenzexpression von Occludin an d10 mit einem Anstieg auf ~ 55% unter d17 statischen und bis zu ~ 65% unter d17 dynamischen Bedingungen, was auf eine iBCEC-Reifung hinweist. Zusammenfassend zeigen die in dieser Arbeit vorgestellten Daten die Reifung von iBCECs in

BHS Sphäroiden, die durch direkte Zell - Zell Kontakte und in dynamischen Strömungsmodellen durch die Anwendung von Scherspannungen erreicht wird. Beide etablierten neuen Modelle müssen für pharmazeutische Anwendungen zusammen mit *In-vitro-in-vivo*-Korrelationen weiter validiert werden, um ihr volles Potential zu beweisen.

3. LIST OF FIGURES

4. LIST OF TABLES

5. LIST OF ABBREVIATIONS

Abbreviation/Symbol	Full form
ABC	ATP-binding cassette
ACs	Astrocytes
AD	Alzheimer´s disease
AJ	Adherens junction
AMT	Adsorptive mediated transcytosis
Ang-1	Angeopoetin 1
ATP	Adenosine triphosphate
AQP-4	Aquaporin-4
BBB	Blood-brain barrier
BM	Basement membrane
BCEC	Brain capillary endothelial cell
BCRP	Breast Cancer Resistance Protein
BCSFB	Blood cerebrospinal fluid barrier
Ca	Calcium
c-Myc	Cellular myelocytomatosis oncogene
cDNA-RT	cDNA reverse transcriptase
CD 13	Cluster of differentiation 13
CD	Co-differentiation
CD 1	Co-differentiation using the IMR90-4 hiPSC line
CD 2	Co-differentiation using the SBAD-02-01 hiPSC line
CD $1/2_{(2D)}$	Co-differentiated iBCECs mono-cultured on transwells
CD $1/2_{(3D)}$	Co-differentiated iBCECs in spheroids
Cl^-	Chloride
CNS	Central nervous system
C_{cell}	Cellular electrical capcitance
$C_{electrode}$	Electrode electrical capcitance
CLSM	Confocal laser scanning microscopy
CSF	Cerebrospinal fluid
CO_2	Carbon dioxide
DAPI	4′,6-diamidino-2-phenylindole
DD	Directed-differentiation
DD1	Directed-differentiation using the IMR90-4 hiPSC line
DD 2	Directed-differentiation using the SBAD-02-01 hiPSC line

Abbreviation/Symbol	Full form
DD $1/2_{(2D)}$	Directed-differentiated iBCECs mono-cultured on transwells
DD $1/2_{(3D)}$	Directed-differentiated iBCECs in spheroids
d	days
Da	Dalton
E-cadherin	Epithelial cadherin
E-face	Ectoplasmic leaflet
ECM	Extracellular matrix
EIS	Electrical impedance spectroscopy
ER	Efflux ratio
ESC	Embryonic stem cell
EVOM	Enterprise Vault Operations Manager
FFEM	Freeze fracture electron microscopy
Foxf2	Forkhead Box F2
Foxq1	Forkhead Box Q1
GDNF	Glial cell line-derived neurotrophic factor
GF	Growth factor
GFAP	Glial fibrillary acidic protein
GLUT1	Glucose transporter 1
GLUT2	Glucose transporter 2
GLUT3	Glucose transporter 3
h	Hours
hbFGF	Human basic fibroblast growth factor
hCMEC/D3	Human brain microvascular endothelial cell line
hiPSC	Human induced pluripotent stem cell
hTERT	Human telomerase reverse transcriptase
HUVEC	Human umbilical vein endothelial cell
Ig	Immunoglobulin
iBCEC	hiPSC derived BCECs
iNPCs	hiPSC derived NPCs
INSR	Insulin receptor
ISF	Interstitial fluid
JAM	Junctional adhesion molecule
K	Potassium
KDa	Kilo Dalton
$K_{p,uu}$	Unbound partition co-efficient
$K_{p,\ brain}$	Ratio of total concentration of drug in brain versus blood

Abbreviation/Symbol	Full form
KLF 4	Kruppel like factor 4
LDL	Low-density lipoprotein
MAGUK	Membrane-associated guanylate kinases
Mg	Magnesiuk
MCT	Monocarboxylate transporter
MCT1	Monocarboxylate transporter 1
MCT8	Monocarboxylate transporter 8
min	Minutes
MRP	Multidrug resistance protein
MW	Molecular weight
Na	Sodium
NaF	Sodium fluorescein salt
N-Cadherin	Neural Cadherin
NG2	Neural-glial antigen 2
NPC	Neural progenitor cell
NVU	Neurovascular unit
OCT-4	Octamer-binding transcription factor-3/4
Papp	Apparent Permeability coefficient
pH	Potential of Hydrogen
PECAM-1	Platelet endothelial cell adhesion molecule 1
P-gp	P-glycoprotein
PC	Permeability coefficient
PCs	Pericytes
P-Face	Protoplasmic leaflet
PLL	Poly-L-Lysine
PDGFR-β	Platelet derived growth factor receptor beta
PNVP	Perineural vascular plexues
qRT-PCR	Quantitative real-time polymerase chain reaction
$R_{membrane}$	Ohmic resistance of membrane
R_{medium}	Ohmic resistance of medium
RA	Retinoic acid
RGS5	Regulator of G protein signaling 5
ROCK	Rho-associated coiled-coil containing kinase
RMT	Receptor mediated transcytosis
S100-β	Calcium-binding protein B
SLC	Solute carrier

Abbreviation/Symbol	Full form
SOX 1	SRY-related HMG-box 1
SOX 2	SRY-related HMG-box 2
SV40	Species of virus 40
TEER	Transendothelial electrical resistance
TF	Transcription factor
TfR	Transferrin receptor
TGF-β	Transforming growth factor beta
TJ	Tight junction
VE-cadherin	Vascular endothelial cadherin
VEGF	Vascular endothelial growth factor
VWF	Von Willebrand factor
Wnt	Wingless integrated
Z	Impedance
Zic3	Zic Family Member 3
ZO-1	Zonula occludens 1
ZO-2	Zonula occludens 2
α-SMA	Alpha smooth muscle actin

6. LIST OF SYMBOLS

Symbol	Full form
%	Percentage
cm	Centimeter
cm/s	Centimeter per second
cm^3	Cubic centimeter
Hz	Hertz
m^2	Square meter
mm^3	Cubic millimeter
$nl/gmin^{-1}$	Nano-liter per grams per minute
kg	Kilogram
fmol/µg	Femtomole per microgram
$\Omega*cm^2$	Ohms per centimeter squared
µg	Micrograms
µM	Micromolar
µm	Micrometer
µm/s	Micrometer per second

7. INTRODUCTION

7.1 Barriers at the central nervous system (CNS), brief history

The brain is the most energy expensive organ in the human body. An average human brain is ~1.5 kilograms (kg) and occupies an area of 1,200 centimeter cube (cm^3) with ~ 100 billion neurons (Hartmann, Ramseier et al. 1994). Although it comprises only 2 percent (%) of the total human body weight, the brain consumes 20% of the body´s metabolic energy, thereby consuming ~ 15 - 20 Watts of power (Raichle and Gusnard 2002). Highly regulated microenvironments and biochemical exchanges are therefore required in promoting its everyday functioning. The biological barriers responsible for this high regulation is established by different cellular components at three key interfaces of the central nervous system (CNS). These interfaces consists of the blood cerebrospinal fluid barrier (BCSFB), formed by epithelial cells of the choroid plexus, the avascular arachnoid epithelium, known as the arachnoid barrier, underlying the dura mater and the blood-brain barrier (BBB) formed by endothelial cells of the cerebral capillaries (Kadry, Noorani et al. 2020) *(Figure 1)*. In the year 1695, a London physician named Humphrey Ridley first commented on the “tightness” of cerebral blood vessels in his book titled “The anatomy of the brain”, 150 years before the experiments of the German scientists Ehrlich, Goldmann and Lewandowsky (Liddelow 2011, Thakur, Sonig et al. 2012, Veith, Watanabe et al. 2015). In 1885, German scientist and Nobel laureate, Paul Ehrlich injected a variety of vital dyes intravenously into the peritoneum of animals, where he observed that all organs of the animals were stained except for the brain and spinal cord (Ehrlich 1885). He interpreted that these results were observed due to the low binding affinities of Trypan blue, a dye with a molecular weight (MW) of 960 Daltons (Da). Further experiments by Goldmann and Lewandowsky disproved Ehrlich´s theory in the 1900´s, when they noted that Trypan blue showed the lowest toxicity and quickest spread specifically into the CNS. Goldmann reported that all organs of the animals including the choroid plexus were rapidly stained blue, excluding the brain and spinal cord (Goldmann 1913). Lewandowsky reported that in order for substances to shuttle into and out of the CNS, the brain vessel wall displayed a specific affinity for selected substances only, thereby describing for the first time the phenomenon of selective substance passage in the CNS (Lewandowsky 1909). These early studies gave the first indications that there was strict compartmentalization between the brain and the rest of the circulatory system (Liddelow, Dziegielewska et al. 2014, Saunders, Dreifuss et al. 2014).

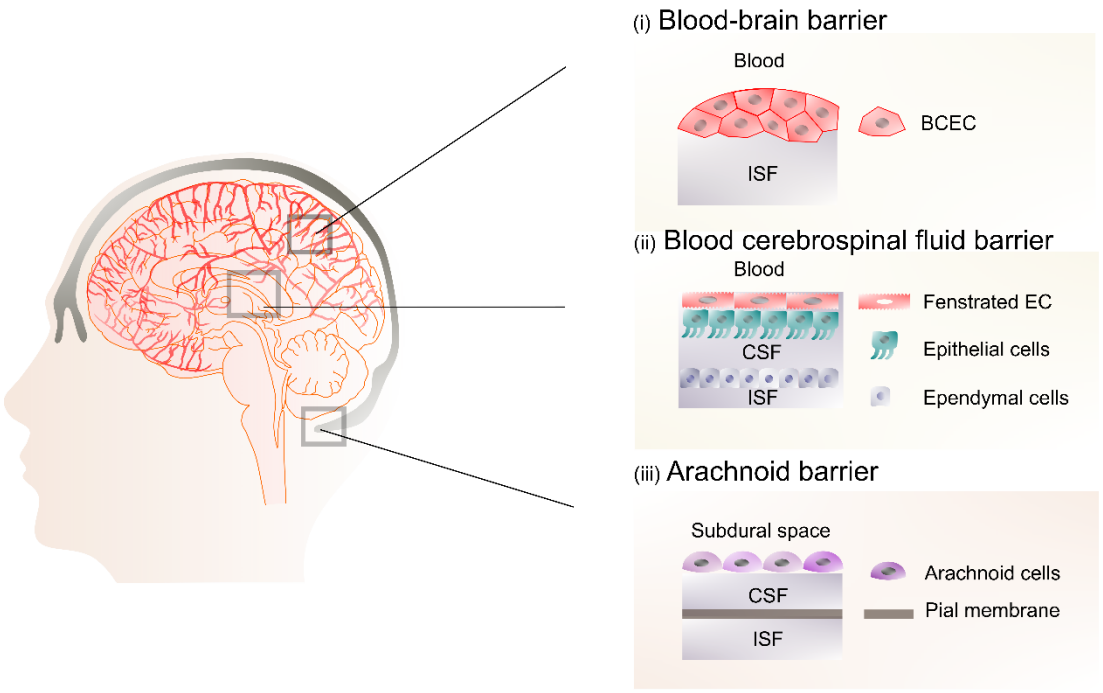

Figure 1: Schematic of biological barriers at the CNS

The blood-brain barrier (BBB) is the barrier between the lumen of cerebral blood vessles and brain parenchyma. Here, endothelial cells that line the lumen are non-fenestrated, and have specialized transport mechanisms that monitor the entry of substances into the brain (i). Blood cerebrospinal fluid barrier (BCSFB) is the barrier between the choroid plexus blood vessels and the cerebrospinal fluid. Here the endothelial cells are fenestrated and epithelial cells posses' apical tight junctions that restrict the entry of substances (ii). The avascular arachnoid epithelium lies under the dura. Here, epithelial-like arachnoid barrier cells regulate the movement of substances into the brain (iii). The interstitial fluid (ISF) surrounds the parenchymal cells of the brain and spinal cord while cerebrospinal fluid (CSF) fills the larger spaces within and around the CNS. Figure adapted and redrawn from (Kadry, Noorani et al. 2020).

7.2 Blood-brain barrier

Due to the high-energy consumption of the brain, maintenance of a proper vascular system is required for its optimal functioning and nutrient supply. This supply is centrally provided by the BBB. Although it does not appear in his paper, coining of the term "BBB" (german: Blut-Hirn-Schranke) is often attributed to Lewandowsky. The first person to use this term however was, Stern in the early 1920s (Stern and Rothlin 1918, Saunders, Dreifuss et al. 2014). The length of this extensive capillary network in the brain is said to be ~ 400 miles with a surface area of ~ 20 meter squared (m^2) (Begley, Brightman et al. 2003, Keller 2013, Wong, Ye et al. 2013, Wevers and de Vries 2016). These capillaries supply the brain with nutrients and blood with a maximum diffusion distance of 8 – 25 (µm) from the proximity to the neurons, thereby forming the largest interface for blood and CNS cross talk (Tajes, Ramos-Fernández et al. 2014). The BBB heavily regulates the entry of nutrients, removal of toxins and prevents the entry of

pathogens into the CNS ergo maintaining brain homeostasis. It strictly limits the passive diffusion of polar substances from the blood to brain, mediates influx of nutrients to the brain parenchyma as well as efflux of metabolites from the brain into the blood with additional regulation and migration of circulating immune cells, thereby serving as a selective diffusion barrier (Begley, Brightman et al. 2003, Abbott, Patabendige et al. 2010). It´s specifically characterized with the presence of tight cellular junctions and lack of fenestrations (Hawkins and Davis 2005, Abbott and Friedman 2012, Daneman 2012, Daneman and Prat 2015). The neurovascular unit (NVU) on the other hand is comprised of intimate contacts between BCECs, astrocytes (ACs), pericytes (PCs), microglia, neurons, and extracellular matrix (ECM) components that form the basement membrane (BM) (Lochhead, Yang et al. 2020). Understanding the function of the NVU in coalition with the BBB is key in deciphering brain function and physiology.

7.2.1 Blood-brain barrier *in-vivo* development

The development and differentiation of the BBB can be subdivided into three phases namely, angiogenesis, differentiation and maturation *(Figure 2, A-C)* (Haddad-Tóvolli, Dragano et al. 2017). Endothelial tubes develop from differentiating endothelial cell precursors, called angioblasts that are of mesodermal origin. The angioblasts further differentiate into BCECs that form interconnected vascular tubes, enabling the formation of a primitive network of brain vessels (ElAli, Theriault et al. 2014). Angiogenesis from angioblast precursors aids the establishment of the preineural vascular plexus (PNVP), once the PNVP is established, the distinct process involving BBB capillary formation and invasion of the rudimentary brain begins (Hogan, Ambler et al. 2004). The human cerebral cortex begins its neuronal development at the 6th week of gestation and intracerebral zonation begins at the 8th week (Saili, Zurlinden et al. 2017) with first intrinsic capillary connections to the gray matter developing at the 15th week of gestation (Marín-Padilla 2012). These growing capillaries are characterized by the presence of brain endothelial cell sprouts having filopodial protrusions that evaluate and search for cues in order to determine vessel direction (Paredes, Himmels et al. 2018). BCECs from the PNVP then penetrate the neuroectoderm depending on a concentration gradient of vascular endothelial growth factor (VEGF), thereby giving rise to immature brain vessels (Raab, Beck et al. 2004, Haddad-Tóvolli, Dragano et al. 2017). VEGF is secreted by neural progenitors (NPCs) and it serves as a major driving force for endothelial cell migration (Risau, Hallmann et al. 1986). Along with VEGF, neural Wingless/Integrated (Wnt) signaling is crucial for the development of the BBB. Various Wnt ligands such as Wnt7a, Wnt7b and Wnt3a are secreted by the neuroepithelium, thereby activating the Wnt/βCatenin signaling in newborn endothelial cells leading to induction of genes critical for vascular patterning and BBB formation (Bautch and James 2009, Daneman, Agalliu et al. 2009, Liebner and Plate 2010, Wang, Rattner et al.

2012). Developing BCECs additionally secrete a wide range of bioactive molecules that specifically trigger the attraction, mobilization, and recruitment of PCs and ACs at the abluminal side of the newly formed vascular network leading to a final maturation and barriergenesis (Winkler, Bell et al. 2011, ElAli, Theriault et al. 2014, Saili, Zurlinden et al. 2017). It remains a controversial discussion regarding the possibility of humans being already born with a fully functional BBB since the mechanisms involved in establishing neurovascular couping and microarchitecture of BCECs still remains undefined (Coelho-Santos and Shih 2020).

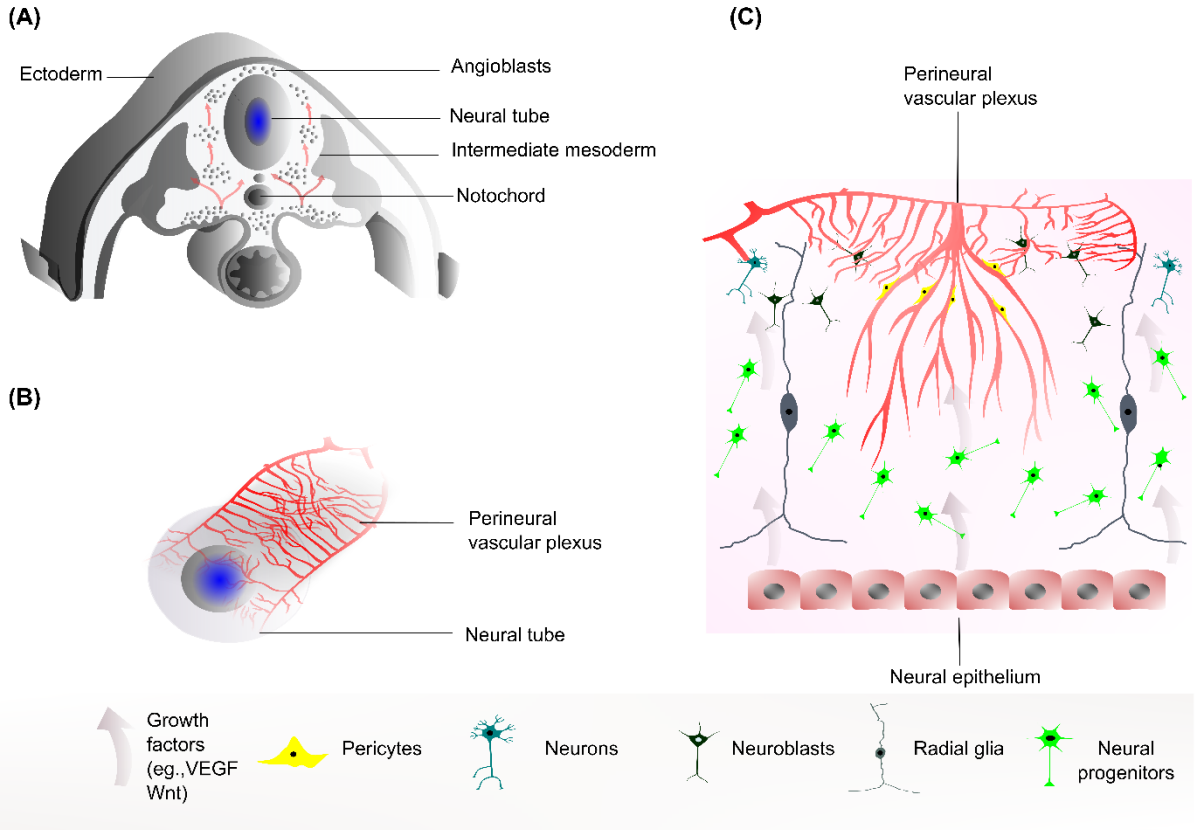

Figure 2: Schematic of BBB *in-vivo* development

Development of the BBB begins with the angiogenesis phase (A) where primary vascular tubes develop from differentiating angioblasts that are derived from the mesoderm. The angioblasts further differentiate into brain endothelial cells that form interconnected vascular tubes, thus enabling the formation of a primitive network of brain vessels in the differentiation phase (B). In the maturation phase (C), the endothelial cells sprout towards a concentration gradient of vascular endothelial growth factor (VEGF) and wingless/integrated (Wnt), produced by neuroepithelial cells located in the ventricular layer. Figure adapted and redrawn from (Tata, Ruhrberg et al. 2015, Saili, Zurlinden et al. 2017, Coelho-Santos and Shih 2020).

7.2.2 Molecular organization of junctional proteins at the blood-brain barrier

Central to the organization of barrier function at the BBB is the establishment of specific sealing junctional proteins. These proteins seal the brain endothelium and represent the core structure of the BBB (Bauer, Krizbai et al. 2014). Endothelial cells at the BBB show different properties

than those found in peripheral tissues. They are extremely thin, lack fenestration, demonstrate high polarization and possess elaborated and complex tight junctions (TJs) composed of intramembranous networks of protein strands. These proteins include occludin, claudins, junctional adhesion molecules (JAMs), adherence junctions (AJs) and membrane-associated guanylate kinase proteins (MAGUK)/scaffolding proteins (Daneman and Prat 2015) *(Figure 3, A).* The first component of the TJ strands was identified to be occludin, with a molecular mass of ~ 65 kilodalton (kDa), extracellular loops of occludin are required to regulate adhesion between cells (Furuse, Hirase et al. 1993). It was initially assumed that occludin formed the core transmembrane protein of TJs (Furuse, Itoh et al. 1994). Later studies identified that it is, however, not essential for the formation of TJ strands. Occludin deficient mouse embryos do not show morphological alterations of TJ generation (Saitou, Furuse et al. 2000). In humans, mutations of the occludin coding gene causes a rare neurological disorder called polymicrogyria, that results in malformations of cortical development (O'Driscoll, Daly et al. 2010). The next most important TJ belongs to the claudin family. In humans and mice a total of 27 different claudins have been identified (Mineta, Yamamoto et al. 2011). Although claudins show tissue specific expression patterns (Ohtsuki, Yamaguchi et al. 2008, Daneman, Zhou et al. 2010), in mice BCECs, mRNA levels of claudin-5 is ~ 600 times higher compared to claudin-1, -3 and -12 (Ohtsuki, Yamaguchi et al. 2008, Daneman, Zhou et al. 2010). Importantly, claudin-5 knockout mice do not survive within 10 hours (h) of birth (Nitta, Hata et al. 2003). Overexpression of claudin-5 increases paracellular tightness in exogenously cultured rat BCECs (Ohtsuki, Sato et al. 2007) and transfection of claudin-5 into epithelial cells increases barrier functions (Amasheh, Schmidt et al. 2005), thereby illustrating it´s key role in BBB physiology. In humans, claudins -1, -5, -11, -12, -25 and -27, are responsible in determining the degree of tightness and permeability of the BBB (Berndt, Winkler et al. 2019). Amongst these, claudin-5 (~ 23 kDa) has been recognized as the most dominant (Greene, Hanley et al. 2019). In humans decreased claudin-5 protein levels in the frontal cortex are kown to play a key role in the development of mental disorders such as schizophrenia and depression (Nishiura, Ichikawa-Tomikawa et al. 2017, Greene, Hanley et al. 2020).

Although non-essential to TJ formation, JAMS are involved in the assembly of TJ components and establishment of cellular polarity. They are transmembrane proteins belonging to the immunoglobulin (Ig) superfamily (Luissint, Artus et al. 2012). Major members include JAM-A (~ 32 kDa), mainly expressed in endothelial and epithelial cells, JAM-B (~ 33 kDa), JAM-C (~31 kDa) and endothelial cell selective adhesion molecule (ESAM, ~ 25 kDa). They behave as adhesion molecules via both hemophilic and heterophilic interactions (Jia, Martin et al. 2013). The expression of JAMs is usually proportional to the number of TJs and JAM-A is expressed earlier than other TJ markers (Martinez-Estrada, Villa et al. 2001). JAM-A interacts with several cytoplasmic scaffolding proteins, aiding in the establishment and regulation of the

barrier (Bauer, Krizbai et al. 2014). The formation of TJs requires the pre-existence of adherence junctions (AJs). AJs have a similar organization to TJs and are established between neighbouring cells by hemophilic interactions of transmembrane proteins such as vascular endothelial cadherin (VE-cadherin, ~ 87 kDa) and platelet endothelial cell adhesion molecule-1 (PECAM-1) (Tietz and Engelhardt 2015). VE-cadherin is linked to the actin cytoskeleton via cytoplasmic/scaffolding proteins and catenins (α, β, γ, p120), and plays a crucial role in upstream transcription of claudin-5 by β-catenin sequestration (Luissint, Artus et al. 2012). β- and γ-catenin link cadherin to α-catenin which, in turn, couples the complex to actin microfilaments of the cytoskeleton (Stamatovic, Keep et al. 2008). Unlike neural-cadherin (N-cadherin) expressed in several other cell types, such as neural cells and mesenchymal cells, VE-cadherin is exclusive to brain endothelial cells (Li, Chen et al. 2018) and is a highly dynamic adhesion molecule (Orsenigo, Giampietro et al. 2012). PECAM-1 is a type 1 transmembrane glycoprotein of the Ig superfamily of cell adhesion molecules (Newman and Newman 2003). Ultrastructure studies of developing mouse BBB demonstrate that PECAM-1 is initially expressed on the luminal and abluminal surfaces of brain endothelial cells in newborn mice, and expression patterns increase 7 - 10 days post-partum, with decrease to luminal cell surfaces at two weeks postpartum (Lossinsky, Wiśniewski et al. 1997). *In-vitro* based primary mouse studies show that lack of PECAM-1 leads to impaired BBB barrier integrity and increased permeability of small molecule tracers (Wimmer, Tietz et al. 2019). In healthy adult human brain, differences in expression patterns of PECAM-1 are observed in gray matter and white matter suggesting the existence of variation of structure and function in different brain regions (Mbagwu and Filgueira 2020). The most prominent subgroup of scaffolding proteins localizing to TJs belong to the MAGUK protein family. Here, scaffolding proteins such as zonula occludens (ZO), ZO-1 (~ 225 kDa), ZO-2 (~ 160 kDa) and ZO-3 (~ 130 kDa) form a large network of structural connections, by cross-linking to TJs and by tethering to the actin cytoskeleton (Bauer, Krizbai et al. 2014, Lochhead, Yang et al. 2020). Deficiency of ZO-1 results in mislocalization of endothelial junctional adhesion complexes and leads to defects in angiogenesis and early embryonic lethality (Katsuno, Umeda et al. 2008). Reduced expression of ZO-1 correlates to increased proliferation of brain endothelial cells as seen in human brain tumors. Apart from reduced expression, ZO proteins may also regulate cellular proliferation by nuclear translocation (Bauer, Krizbai et al. 2014). Techniques such as freeze-fracture electron microscopy (FFEM) provides detailed descriptions of the ultrastructure of TJs *(Figure 3, B)*. In FFEM micrographs, TJs appear as a complex network of continuous cylindrical strands on protoplasmic leaflet (P-face) of the plasma membrane with complementary grooves on the exoplasmic leaflet (E-face) (Chalcroft and Bullivant 1970, Staehelin 1974). The complexity of the TJ strand network additionally reflects on the integrity of the barrier and functionality of the cells, measured via electrical resistances and permeability assays (Liebner, Kniesel et al.

2000, Lippoldt, Kniesel et al. 2000). Other than sealing the para-cellular space, functional TJs have a pivotal role in establishing apical-basal polarity, where cells are oriented with the apical part of the plasma membrane towards the capillary lumen and the basolateral part towards the parenchyma (Bauer, Krizbai et al. 2014).

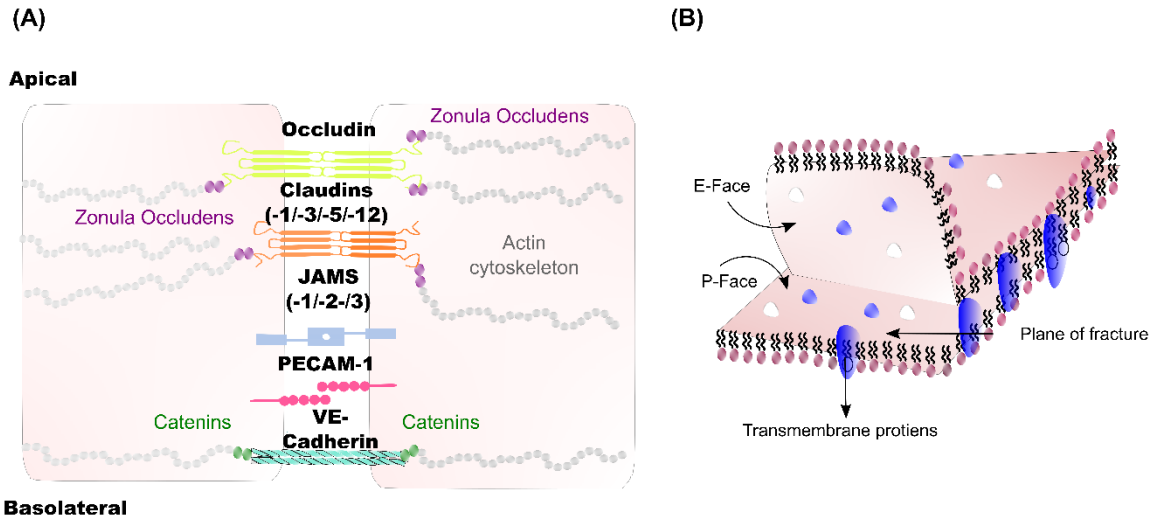

Figure 3: Schematic representation of BBB molecular junctional organization and FFEM technique

Apical-basolateral polarity in endothelial cells is established by correct molecular organization of junctional proteins. Claudins, occludins and junction adhesion molecules (JAMS) form key tight junctions while platelet endothelial cell adhesion molecule-1 (PECAM-1) and cadherins form adherence junctions. Transmembrane spanning regions of occludens and catenins bind and adhere junctional proteins to the actin cytoskeleton (A). Figure adapted and redrawn from (Greene, Hanley et al. 2019). Freeze fracture electron microscopy technique is used to visualize membrane structures and protein distributions in junction forming cells. Here, a cell is first rapidly frozen, and then cleaved along the fracture plane, thereby splitting the lipid bilayer. This separation exposes proteins embedded within the membrane, the seperated layers are then coated with a heavy metal followed by an acidic wash, which results in the formation of cellular replicas. The replicas are then visualzed via electron microscopy. Bumps on the surface of the sample represent organized transmembrane proteins at the E-face and P-face (B). Figure adapted and redrawn from (Fawcett 1994).

7.2.3 Molecular transport mechanisms at the blood-brain barrier

In the 1800´s English scientists Charles Roy (1854 - 1897) and Charles Sherrington (1857 - 1952) investigated the movement of a range of substances into the brain and reported that many lipid-soluble molecules such as morphine and caffeine can cross into the brain, while other lipid-insoluble molecules cannot (Liddelow 2011). It has been well documented that for a substance to gain entry into the CNS, biological features such as expression of transporters and enzymes as well as physiochemical properties such as low MW, lipophilicity and hydrogen bonding capacity play a crucial role (Abbott, Patabendige et al. 2010, Wong, Ye et al. 2013).

Several specialized transporter systems and mechanisms are present at the BBB that allows specific substance influx and efflux at the BBB *(Figure 4)*.

Transcellular transport, also known as passive diffusion, is the process where small lipids, non-polar molecules and gases pass the BBB. This process is highly depending on a concentration gradient and only molecules having a MW < 500 Da, with less than five hydrogen bonds can pass through transcellularly (Wong, Ye et al. 2013, Bellettato and Scarpa 2018). Small water solube molecules and immune cells use the paracellular transport mechanism, essentially passing through intercellular clefts to enter the brain parenchyma (Wong, Ye et al. 2013, Upadhyay 2014). The brain consumes around ~ 0.6 moles of glucose per day, almost all of which needs to pass the BBB. The uptaken glucose is then metabolized by active neurons which generate water at a rate of ~ 28 nl/gmin^{-1}. Water homeostasis is then maintained via ion channels. Transport of sodium (Na^+), pottasium (K^+) and chloride (Cl^-) is maintained by these ion channels. The BBB is however largely impermeable to most ions such as calcium (Ca^{2+}) and magnesium (Mg^{2+}). These ions act as a buffering system thereby stabilizing the potential of hydrogen (pH) of blood and surrounding fluids (Upadhyay 2014, Serlin, Shelef et al. 2015, Hladky and Barrand 2016, Bellettato and Scarpa 2018).

Carrier mediated transport/solute carriers (SLC) mediate the influx of polar molecules such as glucose, amino acids, nucleosides, organic cations and anions (Morris, Rodriguez-Cruz et al. 2017). This transport is driven by concentration or electrochemical gradients. They can be either facilitated or secondary active transporters enabling bi-directional transport and are divided into many categories as listed in *(Table 1)* (Smith 2000, Wong, Ye et al. 2013, Georgieva, Hoekstra et al. 2014, Upadhyay 2014, Serlin, Shelef et al. 2015, Barar, Rafi et al. 2016, Bellettato and Scarpa 2018).

Diapedesis is a mechanism where immune cells infiltrate the BBB during inflammatory conditions without disrupting the TJs. Mainly, mononuclear leukocytes can penetrate the barrier either paracellularly or transcellularly. Once they enter the parenchyma, they form microglia, becoming the immune component of the brain (Carman 2009, Bellettato and Scarpa 2018).

In polarized cell types, unidirectional transcytosis usually refers to transport of macromolecules from the apical to basolateral side. Importantly the steps include endocytosis, intracellular vesicular trafficking and exocytosis (Pulgar 2018). Transcytosis can be either specific receptor-mediated transcytosis (RMT) involving transferrin receptor (TfR), low-density lipoprotein (LDL) receptor and insulin receptor (INSR) or non-specific adsorptive mediated transcytosis (AMT) mainly involving cationic proteins. Transcytosis is mediated by various vesicular transport mechanisms (Georgieva, Hoekstra et al. 2014, Serlin, Shelef et al. 2015, Bellettato and Scarpa 2018, Pulgar 2018, Villasenor, Lampe et al. 2019). In brain endothelial cells three main types

of endocytic vesicles have been identified, namely clathrin coated pits involved in most of the RMT, caveolae that participates in AMT of extracellular molecules and receptor trafficking as well as macropinocytotic vesicels (Mayor and Pagano 2007). These two mechanisms have been explored in drug delivery strategies using penetrative peptides (Hervé, Ghinea et al. 2008) and antibodies (Pulgar 2018).

Efflux pumps/ATP-binding cassette (ABC) transporters are multi domain integral membrane proteins that actively efflux lipid soluble and neurotoxic molecules. These transporters use energy derived from adenosine triphosphate (ATP) hydrolysis to pump/translocate molecules and solutes against a concentration gradient. Energy dependent ABC active transporters are mainly located on the luminal side of endothelial cells. The superfamily consists of 48 distinct transporters with seven families (ABC-A to G) (Löscher and Potschka 2005, Gomez-Zepeda, Taghi et al. 2019). From the ABC family, the most studied and BBB relevant transporter is P-glycoprotein (P-gp or MDR1) encoded by the gene *ABCB1*. Also relevant for efflux transports at the BBB are the multidrug resistance proteins (MRP), namely MRP1, MRP4 and MRP5, encoded by the genes *ABCC1*, *ABCC4*, *ABCC5* and breast cancer resistance protein (BCRP), encoded by *ABCG2* (Smith 2000, Georgieva, Hoekstra et al. 2014, Upadhyay 2014, Barar, Rafi et al. 2016, Bellettato and Scarpa 2018). Each transporter is responsive to specific substrates and inhibitors *(Table 2)*.

Table 1: List of SLC transporter family members, role, localization and species-specific expression

Transport system	Members and role	Localization	Species-specific expression at BBB
Hexose transport system	Glucose transport at the BBB is mediated by a family of facilitated glucose transporters (GLUTs).GLUTs belong to the major facilitator superfamily with GLUT1 and GLUT3 are the main glucose transporters in the brain, GLUT1 is localized in the endothelium and astrocytes while GLUT3 is found in neurons (Nguyen, Ha et al. 2021)	GLUT1 polypeptide is localized to the luminal membrane, the cytosol, and the abluminal membrane (Koepsell 2020)	Human and primate brain capillaries both high and low expression of GLUT1 were distinguished (Koepsell 2020)
Monocarboxylic acid transport (MCT)	Only two MCT isoforms namely MCT1 and MCT8 are expressed in human BCECs, they regulate the transport of lactate, pyruvate, ketone bodies and thyroid hormones (Morris, Rodriguez-Cruz et al. 2017)	MCT1 is localized at the luminal and abluminal membranes of the BBB in rats (Gerhart, Enerson et al. 1997, Roberts, Black et al. 2008),with no localization information available in other species (Morris, Rodriguez-Cruz et al. 2017)	MCT1 expression in brain capillaries of rats (12.6 fmol/µg protein) and mice (23.7 fmol/µg protein) are much higher in comparison to humans (1.46 and 2.27 fmol/µg protein) (Kamiie, Ohtsuki et al. 2008, Shawahna, Uchida et al. 2011, Uchida, Ohtsuki et al. 2011, Hoshi, Uchida et al. 2013)
Neutral amino acid transporter systems (NAAT)	L-alpha amino acid transporters (LATs) are divided into large (LAT1) and small (LAT2) systems, that transport neutral amino acids, including phenylalanine, leucine, tryptophan, and tyrosine .They are also involved in the transport of drugs with CNS activity including gabapentin, pregabalin and Levodopa, (del Amo, Urtti et al. 2008)	LAT1 is expressed on the luminal and abluminal membranes and functions as an antiporter(Morris, Rodriguez-Cruz et al. 2017)	LAT1 expression was upto ten times higher in mice and rats, as compared to humans (3.00 versus 0.43–0.8 fmol/µg protein)(Kamiie, Ohtsuki et al. 2008, Shawahna, Uchida et al. 2011, Hoshi, Uchida et al. 2013) suggesting the existence of species differences in brain penetration of LAT1 substrates.
Organic cation transporters (OCT)	OCT1, OCT2, and OCT3 are involved in the Na+ independent electrogenic transport of organic cations and weak bases, depending on the electrochemical gradient of the substrate (Koepsell and Endou 2004)	OCT1 and OCT2 are localized to the luminal membranes (Lin, Tai et al. 2010)	Similar expression patterns of OCT are observed in humans and rodents with functional activity observed in cultured rat BMCEs (Lin, Tai et al. 2010) and protein expression in humans (Geier, Chen et al. 2013) while OCT1 and OCT2 protein expression is below limit of quantification in hCMEC/D3 cells(Ohtsuki, Ikeda et al. 2013)
Organic anion transporters (OAT)	OAT family has broad substrate specificity for endogenous and exogenous compounds that bear a negative charge at physiological pH.(Morris, Rodriguez-Cruz et al. 2017)	OAT3 is localized to the luminal and abluminal membranes (Mori, Takanaga et al. 2003, Hoshi, Uchida et al. 2013)	In humans, cynomologus monkeys and marmosets, OAT1 was undetected while OAT3 expression was below the limit of quantification (Kamiie, Ohtsuki et al. 2008, Uchida, Ohtsuki et al. 2011, Hoshi, Uchida et al. 2013). Additionally, OAT3 expression was below the limit of quantification in hCMEC/D3 cells (Ohtsuki, Ikeda et al. 2013)

Organic anion transporting polypeptides (OATPs)	OATPs are uptake transporters that are ATP and Na+ independent and transport a diverse range of endogenous and exogenous compounds including bile salts, hormones, and polypeptides (Hagenbuch and Meier 2003)		Various OATP isoforms are expressed and they include distinct species differences at the BBB. In humans, OATP1A2, OATP1C1 and OATP2B1 are expressed in Brain endothelial cells (Hagenbuch and Meier 2003, Hagenbuch and Meier 2004, Geier, Chen et al. 2013)
Nucleoside transport system:	Nucleoside transporters can be classified into two families: concentrative nucleoside transporters (CNTs) and equiliBrate nucleoside transporters (ENTs) (Kong, Engel et al. 2004). CNT1 and CNT2 preferentially transport pyrimidine and purine nucleosides, respectively, while CNT3 transports both purines and pyrimidines(Kong, Engel et al. 2004). ENT1 and ENT2 function as facilitated carriers and mediate the uptake and efflux of nucleosides depending on the concentration gradient across the membrane (Kong, Engel et al. 2004). ENT1, ENT2, and ENT3 transport both purines and pyrimidines with broad and overlapping substrate specificities(Kong, Engel et al. 2004, Govindarajan, Bakken et al. 2007)	ENT2 is localized to the luminal membrane of brain capillaries in rats (Redzic, Biringer et al. 2005) while the localization of ENT1 has not been determined.	CNT2 is detected in rodent brain capillaries and their activity has been demonstrated in cultured rat BCECs (Redzic, Biringer et al. 2005). CNT1-3 expression was below the limit of quantification in proteomic analysis of human, rat, and marmoset brain microvessels (Hoshi, Uchida et al. 2013). Expression of ENT1 is quantified in brain microvessels isolated from humans, monkeys, and mice (Ito, Uchida et al. 2011, Shawahna, Uchida et al. 2011, Uchida, Ohtsuki et al. 2011). Humans and monkeys have similar expression of ENT1 with approximately 0.5–0.6 fmol/µg protein while mice demonstrated 2-fold greater expression (0.99 fmol/µg protein (Ito, Uchida et al. 2011, Uchida, Ohtsuki et al. 2011). Studies showing higher ENT1 expression in humans (0.86 fmol/µg protein) (Shawahna, Uchida et al. 2011) suggest there may be substantial interindividual variability in human expression levels. hCMEC/D3 cells on the other hand demonstrate higher expression of ENT1 (5.94 fmol/µg protein), ~11.7-fold higher than observed in human brain capillaries (Ohtsuki, Ikeda et al. 2013)

Table 2: List of efflux transporter family members, role, localization, species-specific expression, involved substrates and inhibitors.

Adapted and taken from (Löscher and Potschka 2005)

Transport systems	Members and role	Localization	Species-specific expression at BBB	Substrates	Inhibitors
P-gp	There are two types of human P-gp. Type 1 encoded by the *ABCB1* gene. Type II encoded by *ABCB2* gene (Löscher and Potschka 2005). P-gp is usually involved in the transport of amphipathic cations and organic molecules (Gomez-Zepeda, Taghi et al. 2019)	Luminal (Gomez-Zepeda, Taghi et al. 2019)	In rodents P-gp expression is measured to be ~ 1.6 - 24.9 fmol/µg protein (Hoshi, Uchida et al. 2013, Zhang, Tachikawa et al. 2018), while in humans it is ~ 3.98 fmol/µg protein (Shawahna, Uchida et al. 2011)	➢ Anticancer drugs (Doxorubicine, daunorubicine, vinblastine, vincristine, etoposide, teniposide, paclitaxel, methotrexate) ➢ Immunosuppressive agents (Cyclosporin A) ➢ Corticoids (Dexamethasone, hydrocortisone, corticosterone, cortisol, aldosterone) ➢ Antidiarrheal agents (Loperamide) ➢ Calcium channel blocker (Verapamil) ➢ Antiepileptic drugs (Phenytoin, carbamazepine, lamotrigine, phenobarbital, felbamate, gabapentin, topiramate) ➢ Antiemetics (Domperidone, ondansetron) ➢ Cardiac glycosides (Digoxin) ➢ Diagnostic dyes (Rhodamine-123)	➢ 1st Generation (Verapamil, cyclosporin A, quinidine, quinine, amiodarone, detergents) ➢ 2nd Generation (Valspodar, Elacridar, Biricodar, Dexverapamil) ➢ 3rd Generation (Zosuquidar, Tariquidar, Laniquidar)

				➢ Antidepressants (Amitryptiline, nortryptiline, doxepin, venlafaxine, paroxetine) ➢ Antibiotics (Erythromycin, valinomycin, tetracyclines, fluoroquinolines)	
MRP	The MRP subfamily comprise 12 protein-coding genes for humans, while nine are related to the MRP subclasses MRP1-6 and MRP7-9 (Löscher and Potschka 2005). MRPS are involved in the efflux of organic anions, glutathione conjugates (Gomez-Zepeda, Taghi et al. 2019)	Luminal (Gomez-Zepeda, Taghi et al. 2019)	In rodents MRP1 expression ~0.671 fmol/µg protein, MRP4 ~0.510 fmol/µg protein, MRP6 ~0.165 fmol/µg protein, and MRP-7 ~0.118 fmol/µg protein (Zhang, Tachikawa et al. 2018). In humans MRP4 expression was ~ 0.31 fmol/µg protein (Shawahna, Uchida et al. 2011)	➢ Anticancer drugs (Etoposide, teniposide, vincristine, doxorubicine, daunorubicine, methotrexate) ➢ Gutathione, glucuronide, and sulfate conjugates ➢ Unconjugated compounds (Fluorescein)	➢ MRP1, MRP2(Sulfinpyrazone, Probenecid, Cyclosporin A, Verapamil) ➢ MRP 3 (Organic anion transport inhibitors such as sulfinpyrazone, indomethacin, and probenecid) ➢ MRP5 (Probenecid, phosphodiesterase inhibitors such as trequensin or sildenafil)
BCRP	Tissue distribution of BCRP shows extensive overlap with that of P-gp, suggesting that they both have overlapping substrate specificities and thus may provide dual protection against toxicants(Gomez-Zepeda, Taghi et al. 2019)	Luminal (Gomez-Zepeda, Taghi et al. 2019)	BCRP expression in humans is nearer to rodents than to other primates, in rodents it is ~3.2-3.475 fmolhomodimer/µg protein (Hoshi, Uchida et al. 2013, Zhang, Tachikawa et al. 2018) while in humans ~6.15 fmolhomodimer/µg protein) (Shawahna, Uchida et al. 2011)	➢ Several anticancer drugs; considerable overlap with Pgp, MRP1, and MRP2. ➢ Anthracyclines, mitoxantrone, bisantrene, the camptothecins topotecan and SN-38, prazosin	➢ GF120918 (inhibits also P-gp), fumitremorgin C (FTC) and FTC analogues such as Ko132 and Ko134, CI1033

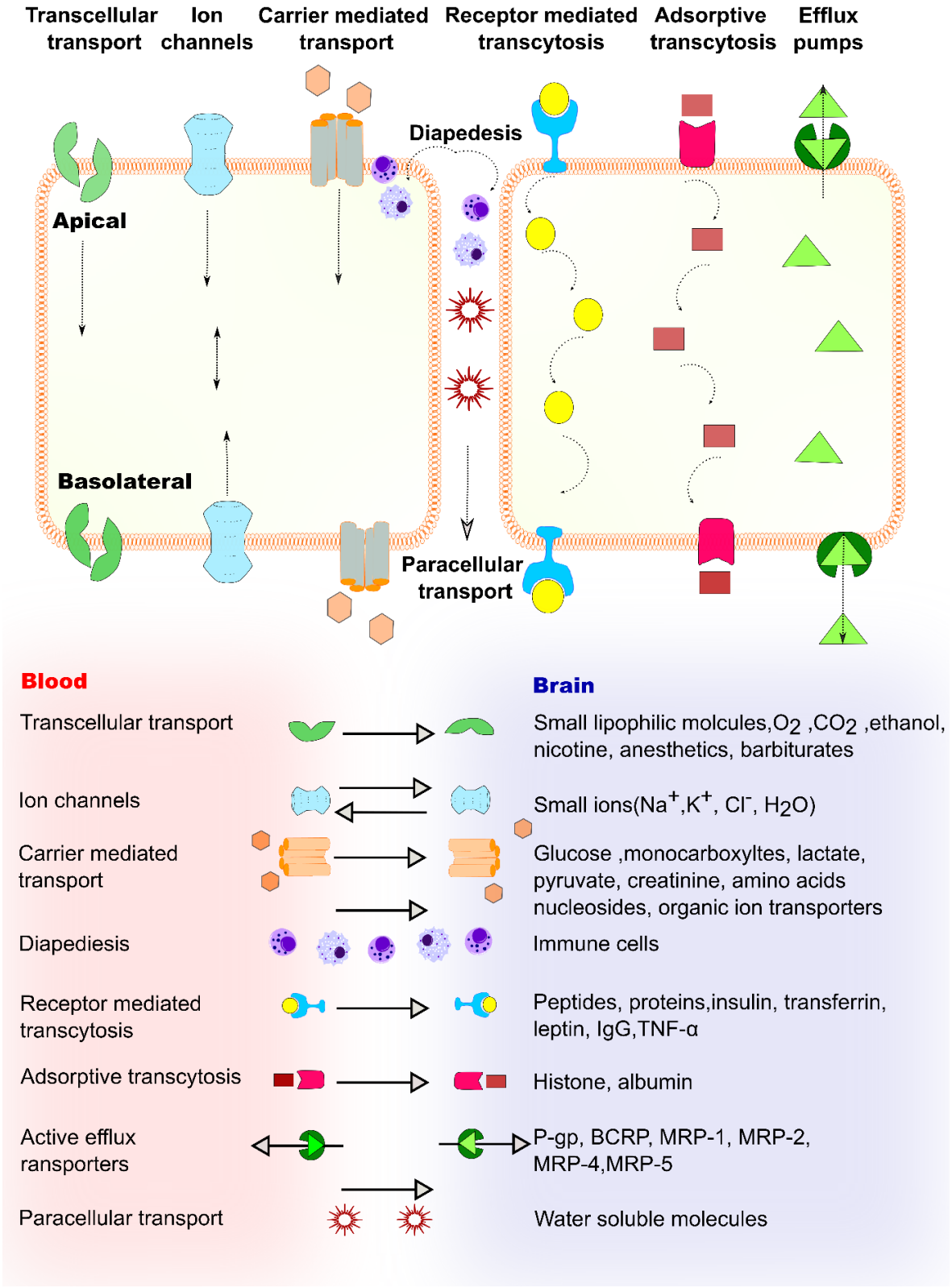

Figure 4: Schematic representation of molecular transport mechanisms at the BBB

Paracellular transport is severely restricted due to the presence of tight junctions. However, small ions and water molecules can cross into the brain via ion channels or paracellularly. Metabolites and other polar substaces are transporterd via efflux pumps, or carrier mediated transport systems such as receptor-mediated transcytosis or adsorptive transcytosis. Figure adapted and redrawn from (Wong, Ye et al. 2013).

7.3 Neurovascular unit, importance of pericytes and astrocytes

The neurovascular unit (NVU) broadly describes the structural and functional multicellular association between brain cells and brain blood vessels. Cellular components of the NUV includes neurons, BCECs, ACs, PCs and microglia (Bell, Miller et al. 2019). The word pericyte originates from Latin, where “peri” means “around” and “cyte” means “cell”, thereby illustrating its anatomical localization in covering the abluminal surface of capillaries (Santos, Magno et al. 2019). PCs at the CNS are involved in the regulation of angiogenesis, blood flow, capillary diameter control, vascular remodeling, wound healing, immune infiltration, regulation, deposition of ECM and maturation of the BBB (Daneman and Prat 2015, Ghersi-Egea, Strazielle et al. 2018, Bennett and Kim 2021). The origin of PCs is heterogeneous and dependent on the anatomical location of the cells. Peripheral PCs are said to be of mesodermal origin (Santos, Magno et al. 2019). Forebrain PCs are derived from neural crest cells while hindbrain PCs are derived from the mesoderm. Possibilities exist that there may be more than one type of PCs, with additional regional variations (Majesky 2007, Daneman and Prat 2015, Bennett and Kim 2021). Some studies even suggest that they could be multipotent stem cells (Dore-Duffy, Katychev et al. 2006) with similar characteristics as mesenchymal stem cells. PCs communicate with their microenvironment via several paracrine and autocrine signaling pathways *(Figure 5)*. Amongst these signaling pathways, platelet derived growth factor receptor beta (PDGFR-β), transforming growth factor-beta (TGF-β), angiopoietin-1 (Ang-1) and notch pathways play crucial roles in controlling PCs attachment at the abluminal side of BCECs, thereby contributing to the establishment, survival and maintenance of the NVU (Winkler, Bell et al. 2011, ElAli, Theriault et al. 2014). PCs at the CNS show varied properties than those in other tissues. In the CNS there is highest coverage of PCs with endothelial to PCs ratio varying from 1:1-3:1 as compared to muscle tissue, where the ratio is 100:1 (Shepro and Morel 1993). PCs extend long cellular processes lining the abluminal surface of the brain endothelium. Most of the cell body and processes do not directly touch the endothelium and are separated by a vascular BM. At the points where they touch the endothelium, they send finger like projections similar to peg and socket junctions, thereby binding to the endothelial cells. These connections are mediated via N-cadherin and connexin hemi channels (Dore-Duffy, Katychev et al. 2006, ElAli, Theriault et al. 2014) *(Figure 5)*. A major difficulty in studying PCs is the lack of specific markers, with the most validated current markers of CNS PCs being PDGFR-β, neuronal/glial 2 (NG2), alanyl aminopeptidase (CD13), α-smooth muscle actin (αSMA), regulator of G protein signaling 5 (RGS5) and desmin (Krueger and Bechmann 2010, Kamouchi, Ago et al. 2011, Bennett and Kim 2021). Pathological conditions of the NVU such as Alzheimer´s disease (AD), Parkinson´s disease, or ischemic stroke can lead to PCs loss by detachment and migrations (ElAli, Theriault et al. 2014, Bennett and Kim 2021) *(Figure 5).*

After oligodendrocytes, ACs are the major glial cell type found in the CNS, and are five-fold more numerous than neurons (Liu, Yang et al. 2018). They are stellar shaped cells with multiple cellular processes that reach neurons and blood vessels, thereby regulating both neuronal and endothelial functions (Abbott, Ronnback et al. 2006). In detail, they regulate brain endotheial angiogenesis, morphology, and are responsible for metabolic functions such as K^+ buffering, release of glutamate via calcium signaling, control of brain pH and secretion of growth factors such as TGF-β, glial derived neurotropic factor (GDNF), and basic fibroblast growth factor (bFGF) during development. ACs play a primary role in the expression of TJ proteins, including occludin, claudin-5 and ZO-1 in mature brain vasculature, which correlates with the induction and maintenance of BBB integrity (Cabezas, Avila et al. 2014, Daneman and Prat 2015, Liu, Yang et al. 2018). ACs are globally characterized by the expression of glial fibrillary acidic protein (GFAP) and vimentin. There exists a great heterogeneity amongst ACs, with two main types described in the CNS, namely the protoplasmic ACs associated with grey matter and fibrous ACs associated with white matter (Cabezas, Avila et al. 2014). They also show a number of different morphologies depending on where they are located and which cell types they are associated with (Abbott, Ronnback et al. 2006). The fibrous population type expresses GFAP while the protoplasmic types express elevated S100 calcium-binding protein beta (S100-β) levels (Abbott, Ronnback et al. 2006, Cabezas, Avila et al. 2014, Khakh and Deneen 2019). The endfeet of ACs almost completely envelop the vascular tube, and contain a discrete array of proteins including dystroclycan, dystrophin and aquaporin 4 (AQP-4) *(Figure 5)*. AQP-4 is arranged into orthogonal arrays of particles, which is critical for regulating water homeostasis at the CNS. Metabolization of glucose in the brain generates water that is elimintated by the brain, and astrocytic end feet have particular roles in this process (Noell, Wolburg-Buchholz et al. 2011, Wolburg, Wolburg-Buchholz et al. 2011). Under pathological conditions such as Alzheimer's disease (AD) and glioblastoma, agrin is lost from the abluminal surface of the endothelium, leading to BBB damage and redistribution of astrocytic AQP-4 (Abbott, Ronnback et al. 2006). This process involves both molecular and morphological changes in ACs including hypertrophy of cell bodies and glial processes, detachment of endfeet from the endothelium and increased expression of GFAP, vimentin and nestin (Cabezas, Avila et al. 2014) *(Figure 5)*.

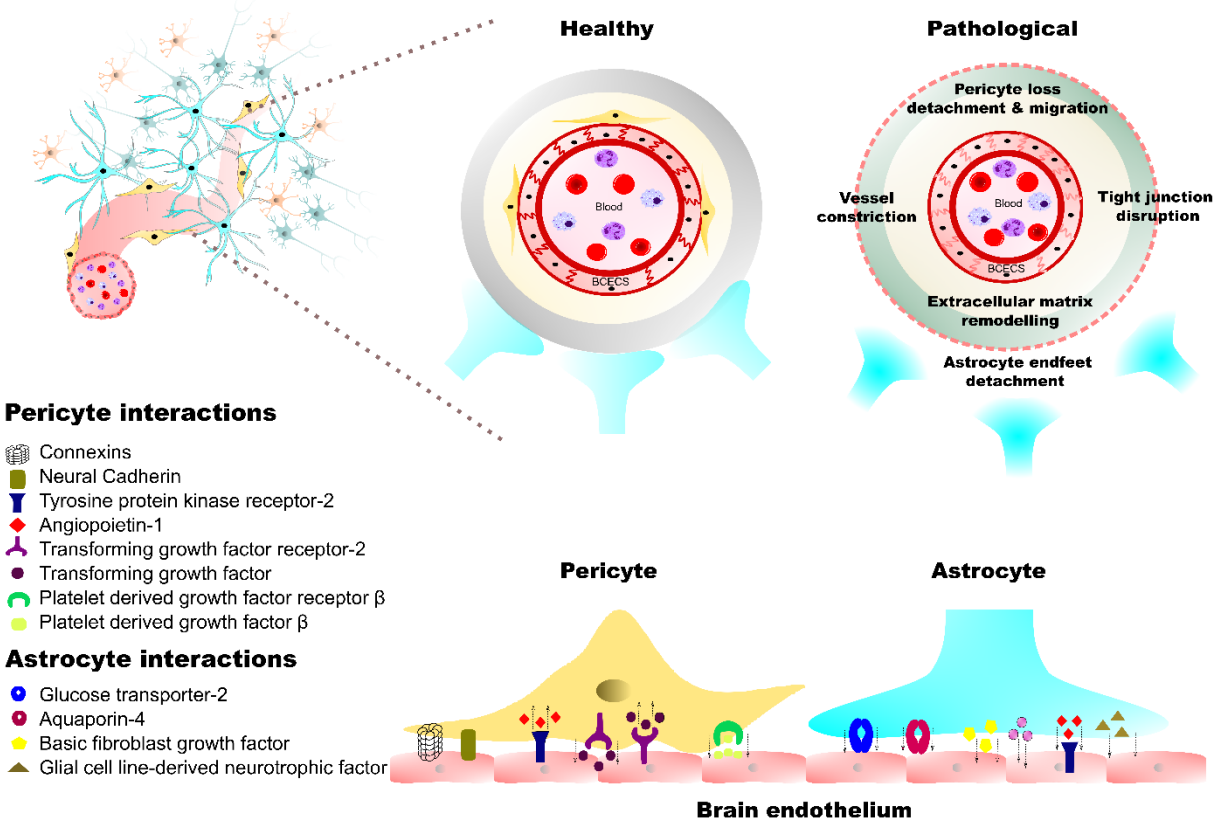

Figure 5: Schematic of cellular interactions at theNVU

The neurovascular unit (NVU) is a hetero-cellular complex formed by glia, neurons, smooth muscle cells, peicytes (PCs), astrocytes (ACs), microglia, and brain capillary endothelial cells (BCECs). In diseased conditions, multilevel changes are observed at the NVU including vessel constriction, tight junction disruption and extracellular matrix remodeling. PCs are connected to the endothelium via connexins and Neural-cadherins in so-called “peg and socket” junctions. ACs are involved in water and glucose homeostasis via gluocose transporters and aquaporins. Growth factor interactions further allows the development and maintenance of the blood-brain barrier. These multiple cellular interactions and cross talk help in maintaining NVU homeostasis.

7.4 Status quo of blood-brain barrier *in-vitro* models and analysis methods

The most broadly studied BBB *in-vitro* models are based on transwells that utilize rodent, procine or bovine cells as a primary source of BCECs (Thomsen, Humle et al. 2021). Although, some co-cultures of mouse BCECs and ACs present BBB characteristics such as expression of occludin, claudin-5, P-gp and barrier integrity representing a TEER ~ 800 Ω*cm^2 (Coisne, Dehouck et al. 2005), other *in-vitro* models of both mouse and rat origin represent low barrier integrity of only ~ 100 – 300 Ω*cm^2 (Helms, Abbott et al. 2016). Porcine BBB *in-vitro* models generally develop very high TEER in both mono-culture and co-culture setups, reaching a TEER of ~ 500 Ω*cm^2 - ~ 1300 Ω*cm^2 (Patabendige, Skinner et al. 2013). The same is true for primary cultures of bovine origin which display TEER upto 2500 Ω*cm^2 (Helms, Hersom et al.

2014, Helms, Abbott et al. 2016). Apart from being labor intensive in isolation of pure populations and having batch to batch variations (Reichel 2006), BCECs derived from animal sources show several species based differences (Aday, Cecchelli et al. 2016, Thomsen, Humle et al. 2021). In examples of comparative studies of rodent and human endothelial cells more than 2-fold differences in protein expression was detected for MRP4, MCT1, LAT1 and OAT3 while the expressions of BCRP, GLUT-1 and INSR were similar (Shawahna, Uchida et al. 2011, Aday, Cecchelli et al. 2016). Compared to humans, P-gp expression in rodents is 2-4-fold higher (Uchida, Ohtsuki et al. 2011) *(Table 2)***.** Interspecies differences thereby play an important role on reproducibility and translation of pharmaceutical studies besides ethical concerns and economic implications of small and large animal testing makes it critical to develop more humanized BBB models (Aday, Cecchelli et al. 2016, Bhalerao, Sivandzade et al. 2020). BBB models based on primary cells cultivated from human tissue could be an alternative in avoiding this. However, it is difficult to obtain healthy human brain tissue on a regular basis and typically, from 5 – 10 mm^3 of fresh brain tissue, only 1×10^6 BCECs can be harvested even after proliferation for 1 month (Bernas, Cardoso et al. 2010), which further limits the possibility of establishing *in-vitro* models using cells of human origin. To circumvent these issues, a human immortalized cell line, named hCMEC/D3 was derived from human temporal lobe microvessels isolated from tissue excised during surgery for control of epilepsy. In the first passage, isolated cells were sequentially immortalized by lentiviral vector transduction with the catalytic subunit of human telomerase (hTERT) and SV40 large T antigen, followed by limited dilution cloning (Weksler, Subileau et al. 2005). These cells express characteristic BBB associated proteins such as PECAM-1, JAM-1, VE-cadherin and occludin. However, the expression of claudin-5 was reported to be much lower than intact microvessels, additionally reflected by TEER values in the range of 30 - 50 $\Omega*cm^2$ (Weksler, Romero et al. 2013, Helms, Abbott et al. 2016). In hCMEC/D3 cells, tighter barrier properties can be achieved together with co-cultures of NVU cell types or hydrocortisone treatments achieving a final TEER of ~ 300 $\Omega*cm^2$ (Förster, Burek et al. 2008). Atlhough it`s an easily avalilable and throughly characterized cell source of human origin, relatively low junctional tightness and loss of BBB phenotypes under routine culture make it challenging for usage in modelling the BBB *in-vitro*.

Alternatively, using cells differentiatied from human induced pluripotent stem cells (hiPSCs) as a cell source to model the BBB offers many advantages. Unlike primary cells, they can be propagated extensively *in-vitro* thereby, offering the possibility of scalability and indefinite expansion. Addtionally, they originate from a clonal source and their progeny have homogenous genetic profiles, this enhances their use in developing personalized isogenic BBB models (Lippmann, Al-Ahmad et al. 2013, Canfield, Stebbins et al. 2017).

Due to the aforementioned properties, hiPSC-derived BCECs (iBCECs) are attractive candidates for modeling the BBB (Appelt-Menzel, Oerter et al. 2020). Current technological status in hiPSC-derived BBB modelling focuses mainly on tranwells based co-cultures, organ-on-a-chip models, spheroids and organoids. Transwell-based BBB models are traditionally considered as a gold standard *in-vitro* BBB model due to their versitality, high reproducibility and easy practicality in set up (Appelt-Menzel, Cubukova et al. 2018). These models allow access to both apical and basal compartments for therapeutic testing. Proof of concept studies show that efflux ratios (ER) of 1.55 ± 0.40 are obtained for Vinblastine, a substrate of P-gp, while in the presence of P-gp inhibitor cyclosporine A, ER was decreased by 50% indicating the presence of functional P-gp efflux in hiPSC based transwell models. The same authors also showed that mean apparent permeability (Papp) values for CNS compounds such as dextromethorphan, caffeine, fumazenil, raclopride, buprenorphine, befoxatone, and propranolol, was in the range of 21.7×10^{-6} to 38.4×10^{-6} cm/s, consistent with high permeability (Roux, Jarray et al. 2019). Although transwell based models allow the possibility of co-culture of NVU cell types (Goodwin-Trotman, Patel et al. 2022), they do not accurately mimic *in-vivo* cell-cell contacts and 3 dimentional (3D) cellular organizations. They also require large numbers of cells for model establishment and lack dynamic flow and shear stresses (Gastfriend, Palecek et al. 2018, Prashanth, Donaghy et al. 2021).

Recently, in the field of biomedical research, fabricating miniaturized microsystems and microfluidics that aim to mimic precise biological organs, appears to be promising. Microfluidic channels on a micron and submicron scale regulate medium flow, shear forces, supply of nutrients and biochemical agents in gradients (Sinha and Bit 2020). These systems are emerging as an alternative to transwells due to their automation capabilities and facilitation of shear stresses mimicking the effect of blood flow *in-vivo* (Gastfriend, Palecek et al. 2018, Bhalerao, Sivandzade et al. 2020). Studies related to the usage of hiPSCs in microfluidic BBB platforms have found that under suitable dynamic culture conditions, iBCECs developed into a more specific BBB phenotype. In a recent study, mRNA expression showed 3.8 fold higher expression of *SLC7A1* and 3.3 fold higher expression of *ABCG2* in comparison to static 2 dimentional (2D) transwell cultures (Kurosawa, Sako et al. 2022). Other investigations showed that PC of caffeine in fluidic models was $3.04 \times 10^{-5} \pm 1.04 \times 10^{-5}$ cm/s, similar to values measured *in-vivo* with 3.1×10^{-5} cm/s. Static models on the other hand resulted in a PC value of $0.90 \times 10^{-5} \pm 1.22 \times 10^{-7}$ cm/s (Di Marco, Vignone et al. 2020). iBCECs also show stable TEER of at least 1000 Ω*cm^2 and long term stability for upto 5 days under dynamic conditions (Vatine, Barrile et al. 2019). Fluidic sytems however have a major drawback in being complex to assemble, expensive, requiring specialized equipments and are often not suitable to use for high throughput analysis (Bhalerao, Sivandzade et al. 2020, Prashanth, Donaghy et al. 2021).

As a promising alternative to transwells and fluidic models, self-assembled spheroids (Urich, Patsch et al. 2013, Cho, Wolfe et al. 2017) and vascularized brain organoids (Bergmann, Lawler et al. 2018, Bhalerao, Sivandzade et al. 2020, Sun, Ju et al. 2022) have been developed. These models present a more accurate representation of 3D *in-vivo* environment due to direct cellular contacts between different NVU cell types. Spheroid models are especially scalable, cheaper and much simpler to fabricate, requiring few reagents and cell numbers per spheroid (Prashanth, Donaghy et al. 2021). Urich and colleagues were the first to demonstrate that under low-attachment culture conditions, primary or immortalized human BCECs, ACs and PCs self-assemble into organized spheroidal structures. These spheroids consist of an ACs core covered with PCs, surrounded by an outer layer of BCECs (Urich, Patsch et al. 2013). Cho and colleagues further characterized these self-assembled spheroids and identified that they possessed higher expression of TJs, VEGF dependent permeability, efflux pump activity and RMT of angiopep-2 in contrast to static transwell co-culture systems, suggesting that this robust *in-vitro* BBB model could serve as a valuable next-generation platform for BBB studies (Cho, Wolfe et al. 2017). Kitamura and colleagues recently reported that BBB spheroids exhiBit barrier function against penetration of dextrans (5 and 70 kDa) and rhodamine123, a P-gp substrate into the core of the spheroids, additionally treatment with tumor necrosis factor-alpha elicited inflammatory responses, suggesting that BBB inflammation can be recapitulated in BBB spheroids (Kitamura, Umehara et al. 2021). Validation of TfR-mediated RMT takes place in BBB spheroids in a temperature and time dependent manner, reaching a final plateau after ~ 2 hours (h). This establishes that BBB spheroids can be used in evaluating RMT-mediated BBB permeability and have strong potentials in being a valuable model in identification and screening of macromolecules that could be used in surpassing the BBB (Kitamura, Okamoto et al. 2022). Incorporation of hiPSC-derived cell types is predicted to be the next important step in realizing the complete utility of self-assembled BBB spheroid systems (Gastfriend, Palecek et al. 2018). Here it becomes important to note that none of the models behaves in exactly similar ways, making it challenging to obtain clear overviews on the benefits and drawbacks of various systems. Therefore, the right choice of an *in-vitro* model for study highly depends on the research question at hand (Helms, Abbott et al. 2016).

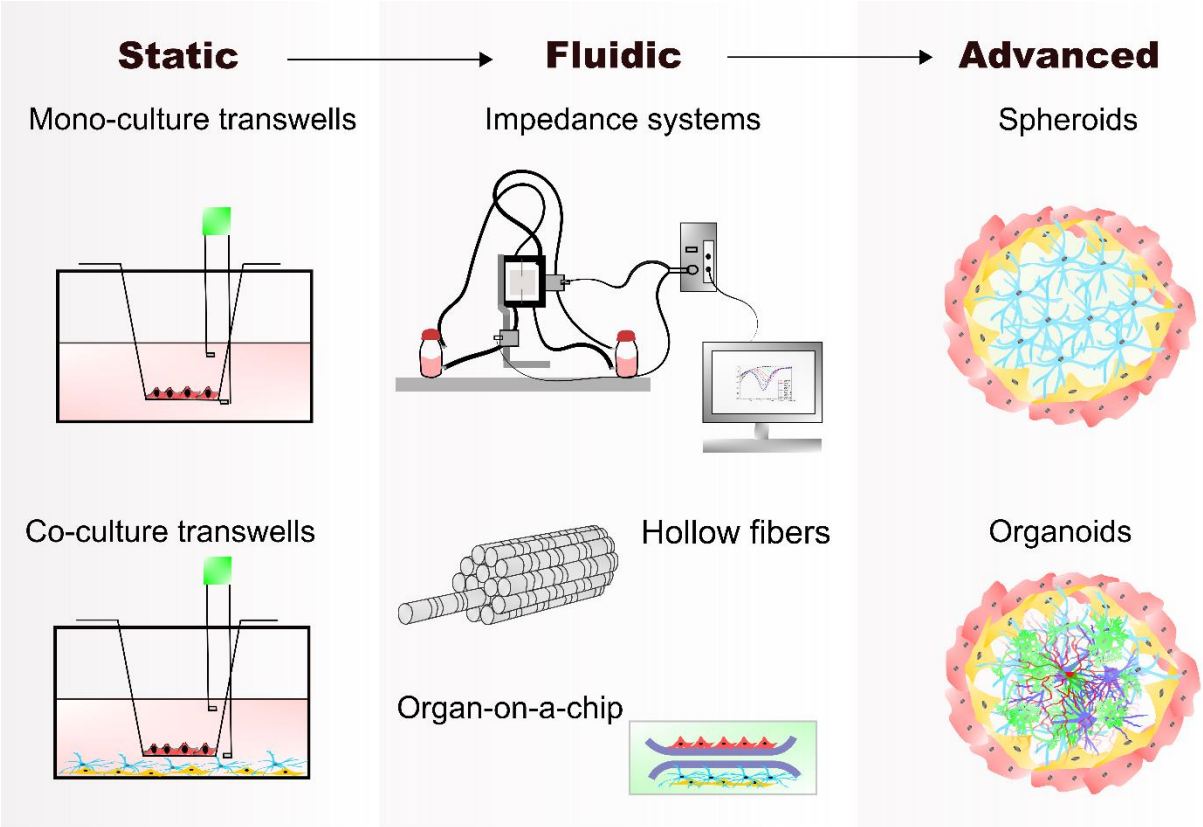

Figure 6: Overview of currently developed BBB *in-vitro* models

Static blood-brain barrier (BBB) models based on transwells in either mono-culture or co-culture formats are most commonly used as they are easy to generate and handle. In an attempt to mimic *in-vivo* flow and shear stress, fluidic models such as hollow fibers, flow bioreactor systems that measure barrier integrity non-invasively and organ-on-a chip are established. Advanced BBB *in-vitro* models such as spheroids and organoids attempt to closely resemble direct cellular contacts and architecture of NVU cell types.

7.4.1 Modelling the BBB using induced pluripotent stem cells

Stem cells refer to undifferentiated cells that have the potential to self-renew in addition to the multipotent ability to differentiate into various specialized lineages (Balistreri, De Falco et al. 2020). Stem cells are classified as per their degree of differentiation or lineage specification, namely as totipotent, pluripotent and multipotent. Totipotent stem cells can differentiate into both embryonic and extra-embryonic structures while pluripotent stem cells, such as embryonic stem cells (ESCs) and induced pluripotent stem cells (iPSCs), differentiate into all germ layers, but not extra embryonic structures. Multipotent stem cells develop into multiple specialized cells representing a specific tissue or organ *(Figure 7)* (Zakrzewski, Dobrzynski et al. 2019, Balistreri, De Falco et al. 2020). A significant breakthrough in science and medicine was delivered in 2006 when Yamanaka and colleagues reported the generation of iPSCs from somatic cells by using a cocktail of transcription factors. These factors were, octamer-binding transcription factor 4 (Oct-4), sex determining region Y-box 2 (Sox-2), kruppel-like factor 4 (Klf4), and cellular myelocytomatosis oncogene (c-Myc), termed together as OSKM or the

Yamanaka cocktail. iPSCs have similar charcteristics as ESCs and the potential to differentiate into any cell type of the body by the addition of developmental specific cues (Takahashi, Tanabe et al. 2007). HiPSCs provide an abundant source of patient derived cells in screening and testing experimental drugs (Scudellari 2016). Although the number of scientific publications using hiPSCs has exploded over the years, until now, no therapy based on hiPSCs has found it´s way into routine clinical use (Kim, Nam et al. 2022). Out of 131 worldwide studies including pluripotent stem cells the number of clinical trials using iPSCs were 74.8% the ones involving ESCs were 25.2% (Deinsberger, Reisinger et al. 2020). Eminent clinical trials conducted by the Kobe City Eye Hospital in Japan involved the transplantation of allogeninc hiPSC derived retinal pigment epithelium to treat age related macular degeneration. Here the degeneration process was stopped and photoreceptor recovery at the site of transplant was observed (Mandai, Watanabe et al. 2017). Another current study focusses on using hiPSC-derived dopaminergic neurons to target Parkinson's disease, the study is still running and progress for two years post transplantation is being determined (Takahashi 2020).

With regard to the BBB, to date there have been limited success in coaxing human primary BCECs to maintain their *in-vivo* characteristics *in-vitro* mainly due to their low yield, hetrogentiy between isolations and de-differentiaions under *in-vitro* cuture. Derivation of hiPSC-based brain capillary endothelial (iBCECs) cells offers the potential in offering scalability (Navone, Marfia et al. 2013). Unlike primary cells, hiPSCs can be propagated extensively *in-vitro* and as they can be derived from a clonal source and their progeny have a homogeneous genetic profile, they provide to be useful in personalized medicine applications (Lippmann, Al-Ahmad et al. 2013). A list of currently employed differentiation strategies in derivation of iBCECs is provided in *Table 3.* The most extensively used strategy is the co-differentiation (CD) protocol developed by Lippmann and colleagues in 2012. The outline of the differentiation lies in three main steps, firstly co-differentiation of hiPSCs into iNPCs and iBCECs, followed by selective maturation and proliferation of iBCECs and elimination of iNPCs by sub-culture onto specific ECM (Lippmann, Azarin et al. 2012, Lippmann, Al-Ahmad et al. 2014). Several updates have been made to the original method, where the use of defined or serum free media accelerates the differentiation process and results in consistent differentiations (Hollmann, Bailey et al. 2017, Neal, Marinelli et al. 2019). To tackle the problem of undefined nature of CD, Qian and colleagues focused on generating iBCECs using a directed differentiation (DD) strategy. Here hiPSCs are first treated with CHIR99021, a glycogen synthase kinase 3 (GSK-3) inhibitor to induce the primitive streak, followed by an intermediate mesoderm, endothelial progenitor stage and finally pure populations of cells (Qian, Maguire et al. 2017).

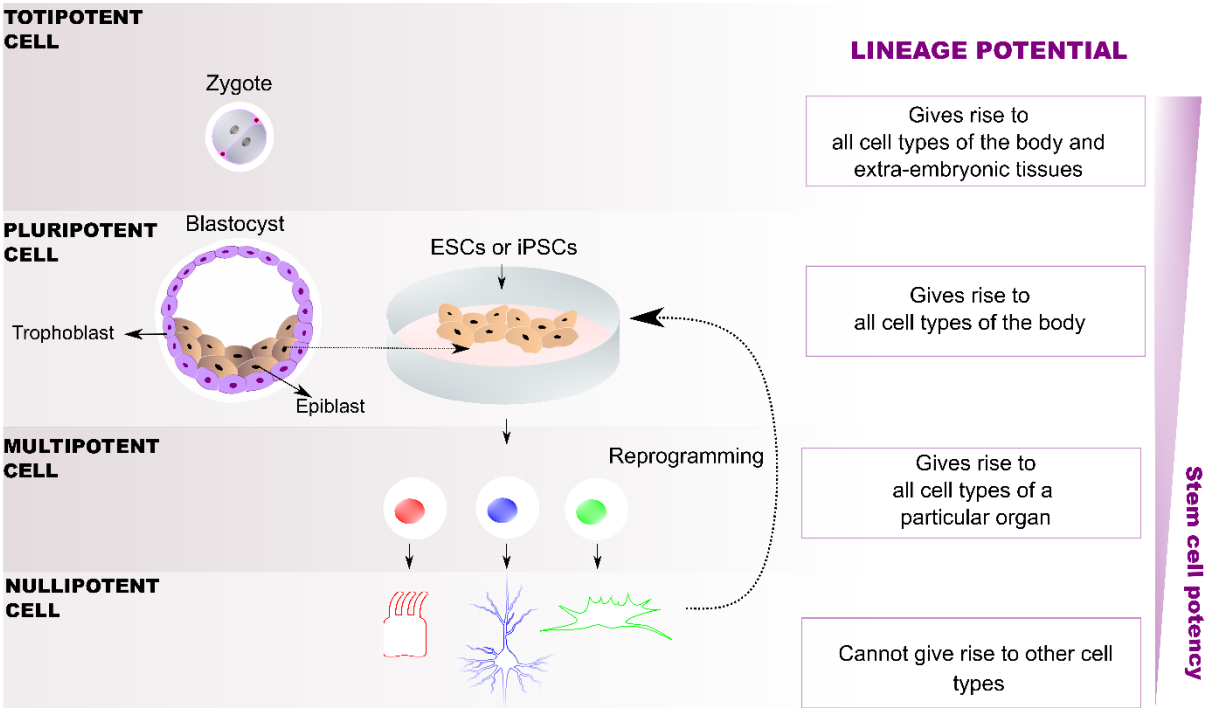

Figure 7: Schematic of stem cell hierarchy

Totipotent stem cells arising from the union of a sperm and egg sit at the top of the stem cell hierarchy. The resultant fertilized egg or zygote has the ability to give rise to all cell types of the body, including extra-embryonic tissues such as the umbilical cord and placenta. Totipotent stem cells further divide in order to give rise to the blastocyst containing an outer layer of cells called the trophoblast and an inner cell mass, which specifies to give rise to the epiblast and primitive endoderm. Cells of the epiblast are pluripotent and following developmental progresses, pluripotent cells further undergo lineage commitments resulting in limited potency and further specification into multipotent stem cells. Multipotent stem cells have restricted ability to give rise to specialized cell types within a tissue. Once differentiated, the specialized cells are nullipotnet, essentially meaning that they do not have the ability to give rise to other cell types. Figure and legend adapted and redrawn from (Balistreri, De Falco et al. 2020)

Table 3: Literature of hiPSC differentiation protocols

Comparison of methods used to derive iBCECs in terms of days required in differentiation, requirement for purification steps, barrier integrity, effects of co-culture, functionality and protein marker expression, table taken from (Appelt-Menzel, Oerter et al. 2020)

Strategy	**Co-differentiation**						**Directed differentiation**	
Original reference	(Lippmann, Azarin et al. 2012)	(Lippmann, Al-Ahmad et al. 2014)	(Hollmann, Bailey et al. 2017)	(Ribecco-Lutkiewicz, Sodja et al. 2018)	(Neal, Marinelli et al. 2019)	(Yamashita, Aoki et al. 2020)	(Qian, Maguire et al. 2017)	(Praca, Rosa et al. 2019)
Days required	~ 13	~ 13	~ 8	~ 21	~ 8	~ 13	~ 10	~ 15 - 20
Purification step	+	+	+	-	+	+	N/A	+
TEER [Ωcm^2] monoculture	~ 200	~ 3,000	~ 1,000 - 4,500	~ 300 - 800	~ 2,000 - 8,000	~ 1,500 - 4,000	~ 3,000	~ 50 - 60
TEER [Ωcm^2] co-culture (cells/conditioned medium)	~ 1,500	~ 5,000	~ 6,500	~ 1,000 - 1,500	~ 9,000 - 10,500	N/A	~ 30% increase	~ 50 - 60
Tube formation *in-vitro*	+	N/A	N/A	N/A	N/A	+	+	N/A
Marker expression (immunofluorescence)	claudin-5, GLUT-1, occludin, PECAM-1, P-gp, VE-cadherin, von Willebrand Factor (vWF), ZO-1	BCRP, claudin-5, GLUT-1, MRP-1, occludin, PECAM-1, P-gp, VE-cadherin	claudin-5, GLUT-1, occludin, PECAM-1, VE-cadherin	claudin-5, GLUT-1, IGFR, LRP-1, occludin, P-gp, PECAM-1, TfR, vWF, ZO-1	claudin-5, GLUT-1, occludin, PECAM-1, VE-cadherin	BCRP, claudin-5, GLUT-1, occludin, P-gp, VE-cadherin, ZO-1	BCRP, claudin-5, GLUT-1, occludin, MRP-1, PECAM-1, P-gp, VE-caderin, vWF, ZO-1	claudin-5, GLUT-1, occludin, PECAM-1, P-gp (moderate), Tie-2, VE-cadherin, vWF, ZO-1

7.4.1 Methods to assess barrier integrity *in-vitro*

The outcome of specialized molecular organization of junctional proteins at the BBB results in high trans-endothelial electrical resistances (TEER) of BCECs in comparison to peripheral endothelial cells (Vigh, Kincses et al. 2021). Principally, TEER describes barrier integrity as the electric ohmic resistance of cells cultivated *in-vitro*. It is determined by using a defined voltage (U) that is applied to two electrodes placed on each side of a cellular layer. The resulting current is then measured, leading to derivation of ohmic resistance R, calculated according to Ohm´s law (Benson, Cramer et al. 2013). The first measurements on the electrical resistance of brain surface micro-vessels were made in the early 1980´s, where average TEER in frog brain micro-vessels were estimated to be ~1870 $\Omega*cm^2$ (Crone and Olesen 1982). The most used system in measuring TEER is the Epithelial Voltohmmeter (EVOM) in combination with a chopstick electrode, which consists of two electrode arms, one positioned in the apical chamber and the other in the basolateral chamber of a cellular layer that is cultivated on a transwell. Here, an alternating current with a defined frequency of 12.5 Hertz (Hz) is applied to measure the resistance (Benson, Cramer et al. 2013). Electrical impedance spectroscopy (EIS) on the other hand allows to analyze the cellular system in a range of applied frequencies, thereby measuring total impedance of the cellular layer. It also provides information on the electrical resistance of cells, resistance of medium, paracellular/transcellular resistances, capacitance of electrodes and cell layer as readout parameters (Benson, Cramer et al. 2013, Choi, Mathew et al. 2022). To retrieve the readout parameters necessary in characterizing cellular systems, an equivalent electrical circuit diagram and corresponding mathematical models are usually applied. An example circuit diagram to derive total impedance Z of a cellular monolayer is show in *(Figure 8)*. In detail, the current through a cellular layer can take either the paracellular or transcellular pathways across the cells. The TJs represent an ohmic resistance, while at the transcellular level each lipid bilayer can be described as a parallel circuit of an ohmic resistance ($R_{membrane}$) and electrical capacitance (C_{cell}). Furthermore, the resistance of the medium (R_{medium}) and capacitance of electrodes ($C_{electrode}$) are also considered. Based on the equivalent circuit, corresponding modelling software can be used to determine the best fit parameters automatically and to extract desired readout parameters (Benson, Cramer et al. 2013).

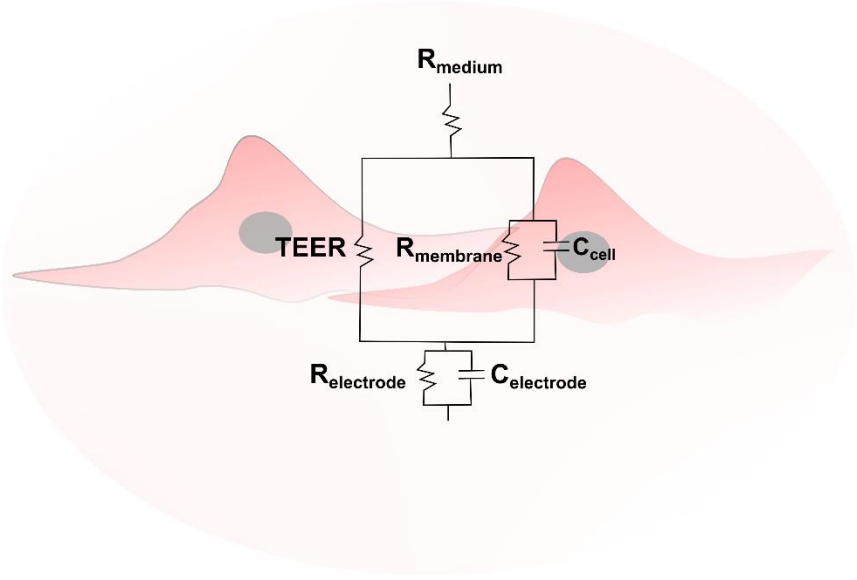

Figure 8: Schematic representation of cellular electrical circuit equivalent

A typical equivalent circuit diagram can be applied to analyze the impedance spectrum of cellular systems. Here, the current can follow either through the paracellular pathway or the transcellular pathway across cells. Within the paracellular pathway, the tight junctions represent an ohmic resistance (TEER) in the circuit diagram while each lipid bilayer represents current flow in the transcellular pathway, described as a parallel circuit of an ohmic resistance and electric capacitance. Electrical impedance spectroscopy gives additional information on ohmic resistance ($R_{membrane}$), electrical capacitance (C_{cell}), resistance of the medium (R_{medium}) and capacitance of electrodes ($C_{electrode}$). Figure adapted and redrawn from (Benson, Cramer et al. 2013).

7.4.2 Methods to investigate BBB transport mechanisms

Several experimental techniques are outlined in examining solute transport across the BBB *in-vitro* each having their own particular strengths and limitations (Santa-Maria, Heymans et al. 2020). In BBB literature, flux from plasma to brain or brain extracellular fluid is termed as “influx” and flux from brain or brain extracellular fluid to plasma is referred to as “efflux” (Smith 2003). There are two main transport modes available for a molecule to pass through a cellular membrane. (1) active transport, involving the use of ATP hydrolysis to shuttle molecules across a membrane and (2) passive transport, which involves diffusion with no energy consumption, this mode is the most common mode of drug passage through membranes and factors such as molecular weight, measures of molecular polarity and lipophilicity affects diffusion rates (Carpenter, Kirshner et al. 2014). Specific permeability values relly on the type of molecule and the size of the tracer itself, some examples of markers include lucifer yellow (442 Da), sodium fluorescein (376 Da), fluorescein isothiocyanate (FITC)-labeled dextrans (1 – 150 kDa) and radiolabeled markers including sucrose (342 Da), albumin (67 kDa), mannitol (182 Da), and inulin (5 kDa). Markers with lower MWs are preferred to study tighter cell layers, whereas bigger markers are used for cell layers with moderate to weak tightness (Santa-Maria, Heymans et al. 2020). Additionally, to validate the permeability status or quality of an *in-vitro*

model, an integrity marker with low permeability is usually used. These markers are commonly characterized by high hydrophilicity, high polarity and absence of active transport (Deli, Abrahám et al. 2005, Neuhaus, Bogner et al. 2006, Wegener, Seebach et al. 2014).

Permeability of compounds is usually assessed across a confluent cellular monolayer seeded on a cell culture insert with a permeable membrane. The insert is usually placed into a cell culture plate, thereby forming a compartmentalized setup; where one compartment mimics the "brain" side and the other "blood" side. The test compound is added to the donor compartment (either blood side for influx studies, or brain side for efflux studies). Finally, the compound is allowed to be transported across the cellular monolayer for defined time periods. The samples from both compartments are further collected as a requirement for calculating BBB permeability. Analysis is performed via scintillation counting for radiolabeled compounds or fluorescence spectrophotometry for fluorescent tracers (Dehouck, Vandenhaute et al. 2011, Kuhnline Sloan, Nandi et al. 2012). Permeability is described as a rate parameter or the flux through unit area under a unit concentration gradient, having the units of cm/s or µm/s. It is essentially the speed at which a test compound crosses the brain endothelial barrier and is often used as a parameter to quantify barrier tightness, functionality and brain permeation (Deli, Abrahám et al. 2005, Neuhaus, Bogner et al. 2006, Wong, Ye et al. 2013, Abbott, Dolman et al. 2014, Wegener, Seebach et al. 2014). BCEC permeability is commonly calculated by two different types of methods namely, endothelial permeability coefficient (PC) and the apparent permeability coefficient (Papp) (Santa-Maria, Heymans et al. 2020). Papp is determined by rate of flux of a test compound in the receiver compartment, normalized to the membrane surface area and initial donor concentration at time 0. (Eq.1). Importantly Papp values does not eliminate the influence of the plastic transwell membrane and coating, thereby adding extrinsic factors to the barrier formed by cells. Indoing so, comparing Papp values between different systems becomes difficult (Santa-Maria, Heymans et al. 2022).

$$\boldsymbol{P_{app} = \frac{dQ}{dt}\,\frac{1}{AC_0}} \quad (\mathbf{1})$$

P_{app} = Apparent permeability coefficient
A = Surface area of a cellular monolayer
Co = Donor concentration
dQ/dt = Permeability rate

P_{app} could additionally be used to assess active efflux, using a bidirectional permeability assay where the transport of a compound can be quantified in both directions (apical to basolateral (A-B) and basolateral to apical (B-A)). This enables the calculation of efflux ratios, indicating if an active efflux is occurring for a compound under study. An efflux ratio greater than 2 indicates drug efflux (Hellinger, Veszelka et al. 2012),while an efflux ratio lower than 0.5 is a hint for an active influx transport (Santa-Maria, Heymans et al. 2020) (Eq.2).

$$\boldsymbol{ER = \frac{P_{app}\,(B-A)}{P_{app}\,(A-B)}}\ \boldsymbol{(2)}$$

ER = Efflux ratio.
P_{app} (B-A) = Apparent permeability in basolateral to apical direction.
P_{app} (A-B) = Apparent permeability in apical to basolateral direction.

PC on the other hand is calculated based on the clearance principle in order to obtain a concentration-independent transport parameter (Siflinger-Birnboim, del Vecchio et al. 1987). The cleared volume (C_L) is calculated by dividing the diffused amount of compound in the receiver compartment (C_r) with the concentration of compound in the donor compartment (C_d) (Eq.3)

$$\boldsymbol{C_L = \frac{C_r}{C_d}}\ \boldsymbol{(3)}$$

C_L = Cleared volume of test substance.
C_r = Diffused amount of test substance in receiver compartment.
C_d = Diffused amount of test substance in donor compartment.

The average cumulative C_L is then subsequently plotted over time and the slope is determined via linear regression analysis. The slope values essentially give the permeability surface area product (PS) for each sample (Eq.4). To correct for permeability across cell-free inserts, the P_S products are calculated for both cell-free inserts (PS blank) and inserts with cells (PS cells)

$$\boldsymbol{P_s cell\ layer = \frac{1}{\left(\frac{1}{P_s\ cells} - \frac{1}{P_s blank}\right)}}\ \boldsymbol{(4)}$$

Ps cell layer = corrected permeability surface area product of the cellular layer.
Ps cells = permeability surface area product of the cellular layer.
Ps blank = permeability surface area product of the blank membrane.

PC values are then computed out of PS cell layer normalized by the surface area of cellular monolayers (Eq.5) (Garberg, Ball et al. 2005, Dehouck, Vandenhaute et al. 2011, Santa-Maria, Heymans et al. 2020)

$$\boldsymbol{Pc = \frac{P_s\ cell\ layer}{A}}\ \boldsymbol{(5)}$$

Pc cell layer = permeability co-efficient.
Ps cell layer = corrected permeability surface area product of the cellular layer.
A = Surface area of a cellular monolayer.

In-vivo, the permeation of a drug through the BBB and it´s intra-brain distribution is controlled by several physico-chemical properties. In the blood, drugs are present either bound to plasma proteins and erythrocytes or in an unbound form (Loryan, Reichel et al. 2022). Relevant

estimations of drug delivery to the brain can be narrated using predicted algorithms, quantitative structure activity relationships and molecular modeling studies. Commonly employed experimental parameters in order to predict molecular brain penetrance includes estimation of $K_{p,\ brain}$/logBB (ratio of total concentration of drug in brain versus blood) and logPS (product of *in-vivo* BBB permeability and surface area). $K_{p,\ brain}$ however does not provide information about the free concentration of drug available for transport and logPS neglects transporter mediated efflux (Dolgikh, Watson et al. 2016, Gupta, Bogdanowicz et al. 2020). Transport of any drug into, within and out of the brain is mainly governed by free unbound drug concentrations firstly in the plasma and by transport across both the BBB and the BCSFB (de Lange and Hammarlund-Udenaes 2015). The most appropriate parameter to predict free concentration of compounds avaiBle to act at the brain is $K_{p,uu\ brain}$ (steady state unbound brain to plasma drug ratio) (Hammarlund-Udenaes, Fridén et al. 2008, de Lange and Hammarlund-Udenaes 2015, Gupta, Bogdanowicz et al. 2020). $K_{p,uu\ brain}$ exclusively describes the unbound drug concentration in the brain ($C_{u,b}$) relative to blood ($C_{u,p}$) at equilibrium and is determined only by the net influx (CL_{in}) and efflux clearances (CL_{out}), *Figure 9*. $K_{p,uu\ brain}$ directly represents the quantitative description on how the BBB handles drugs regarding passive transport and active influx/efflux. $K_{p,uu\ brain}$ = ~1 indicates passive diffusion of the drug, $K_{p,uu\ brain}$ < 1 indicates active efflux and $K_{p,uu\ brain}$ > 1 indicates active influx (Hammarlund-Udenaes, Fridén et al. 2008, de Lange and Hammarlund-Udenaes 2015, Luptáková, Vallianatou et al. 2021, Loryan, Reichel et al. 2022). Combinatory mapping approaches are essential tollboxes in assessing intra and extracellular exposures of drugs in the entire brain in addition to specific brain regions. This technique is made possiBle by the development of high-throughput brain slice methods based on the unbound volume of drug distribution in the brain (Luptáková, Vallianatou et al. 2021). Investigation of drug binding in brain tissue homogenates and slices using equilibrium dialysis is often used to estimate the fraction of unbound drug in the brain ($f_{u,brain}$) and the unbound volume of drug distribution in the brain ($V_{u,brain}$). This method offers the advantage of a highly regulated *in-vitro* environment including the preservation of complex NVU cellular integrity and functionality (Loryan, Fridén et al. 2013). Comparison of $f_{u,\ brain}$ and $V_{u,brain}$ shows that brain slice assays represents overall tissue drug uptake and the brain homogenate method represents intracellular binding of drug compounds (Loryan, Reichel et al. 2022). $V_{u,brain}$ describes the relationship between the total drug concentration, in the brain and the concentration of unbound drug in the brain interstitial fluid (ISF), regardless of BBB function. The key assumption of this technique is that, at equilibrium, unbound-drug concentration in the ISF is equal to the drug concentration in the buffer in the beaker (Loryan, Fridén et al. 2013). These parameters and methodologies provide valuable estimates of brain penetration early in the drug discovery process, and have potential in correlating drug distribution in *in-vitro* test

systems (Hammarlund-Udenaes, Fridén et al. 2008, Sánchez-Dengra, González-Álvarez et al. 2021)

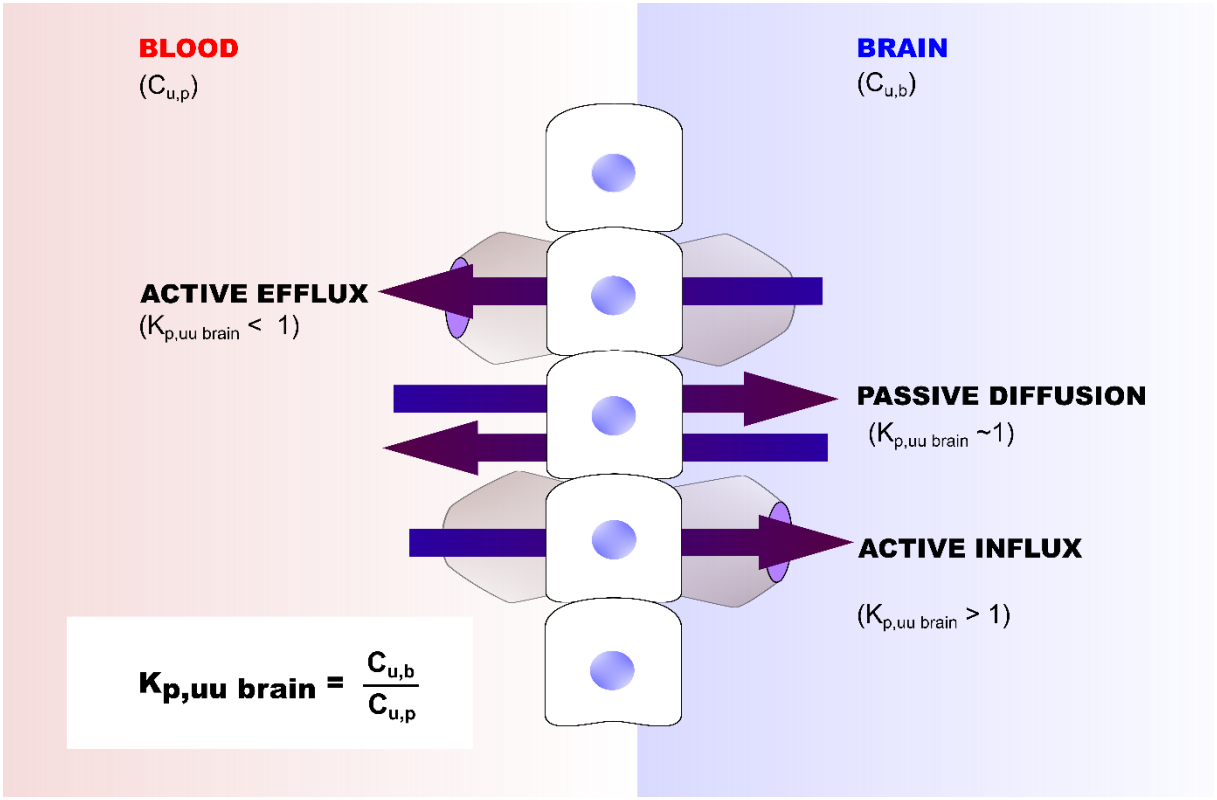

Figure 9: Schematic of bound and unbound drug distribution in brain and plasma.

$K_{p,uu\ brain}$ represents the ratio of unbound drug concentration in the brain ($C_{u,b}$) and unbound drug concentration in the plasma ($C_{u,p}$). $K_{p,uu\ brain}$ = ~1 indicates passive diffusion of the drug, $K_{p,uu\ brain}$ < 1 indicates active efflux and $K_{p,uu\ brain}$ > 1 indicates active influx. Figure adapted and redrawn from (Gupta, Bogdanowicz et al. 2020).

8. RESEARCH OBJECTIVES

8.1 Requirement for identification of optimal iBCEC differentiation and lineage commitment

In order to develop a robust humanized *in-vitro* model of the BBB, which holds a likelihood in pre-clinical testing it was critical to identify an optimal BCEC cell source. Since 2012, a plethora of hiPSC differentiation strategies has been reported in order to generate iBCECs (Appelt-Menzel, Oerter et al. 2020). These strategies differ in methods employed for BCEC induction, specification and purification. Each strategy also varies in finally obtained cellular barrier integrity and BCEC specific marker expressions. The first ever published evidence of hiPSC differentiation into iBCECs was reported in 2012 (Lippmann, Azarin et al. 2012) following the co-differentiation (CD) strategy. The CD strategy followed an undefined nature, resulting in hiPSC line-to-line variability, batch-to-batch variability in BCEC yield and phenotypes, therefore to circumvent this, a second strategy in BCEC derivation was developed following a chemically defined directed-differentiation (DD) approach (Qian, Maguire et al. 2017). However, similar to most hiPSC-derived cells, iBCECs are reported to not fully recapitulate all components of their *in-vivo* equivalents suggesting that they may not have pure endothelial cellular identities and final lineage commitment. In recent years, transcriptomic analyses have revealed an unanticipated feature of reported hiPSC derived iBCECs showing that they express a fundamental number of epithelial-associated transcripts, demonstrating disparity in their cellular identity (Delsing, Dönnes et al. 2018, Lu, Redmond et al. 2019, Vatine, Barrile et al. 2019). This particular issue is of considerable interest in the BBB community, and new recommendations to BBB practitioners include exercising care in choosing and commissioning iBCECs in novel model development and applications (Lippmann, Azarin et al. 2020). As the work of this thesis employs the use of iBCECs in establishing advanced BBB *in-vitro* models, the first aim focused on comparing and characterizing two mostly commonly used differentiation strategies in deriving iBCECs. The main aim focused on identifying which strategy would provide the most common attributes of BBB characteristics, in terms of endothelial specific cobble stone morphology, protein and gene expression, barrier integrity and tube formation capabilities.

8.2 Requirement for iBCEC maturation *in-vitro* via direct cellular contacts

Even under standard 2D transwell culture conditions, when iBCECs are in close contact with other NVU cell types, significant increase of barrier properties and BBB phenotypes are

observed (Appelt-Menzel, Cubukova et al. 2018), indicative of BCEC maturation. Maturation is defined as the process in which nascent BBB characteristics are fortified via NVU intercellular contacts and communications (Saili, Zurlinden et al. 2017). Importantly, intricate transport mechanisms, which are hallmarks of the BBB are not attributable to only BCECs, but are rather resulting due to dynamic interactions of NVU cell types (Barar, Rafi et al. 2016). Direct *in-vivo* cellular architecture is missing in standard 2D transwell models, mainly due to the existence of a thin plastic membrane, which prevents direct cellular contacts.

Previous reports have shown that BBB spheroids demonstrating *in-vivo* cellular architecture can be generated spontaneously using primary and immortalized NVU cell types. This cellular organization takes place independent of additional scaffolding materials, indicative of intrinsic cues within each specific cell type (Urich, Patsch et al. 2013, Cho, Wolfe et al. 2017, Kitamura, Umehara et al. 2021, Kitamura, Okamoto et al. 2022). In order to advace this state-of-the-art technology, the second aim of this thesis attempted at replicating NVU architecture and increasing maturation of iBCECs. For this purpose, 3D BBB spheroids were generated using iBCECs, primay ACs and primary PCs followed by further hallmark characterizations. Investigations of the spheroids included fulfillment of essential criteria required for a reproducible *in-vitro* based BBB model system via transcriptional profiling, ultrastructure analysis, barrier integrity, barrier function and expression of relevant BCEC proteins.

8.3 Requirement for iBCEC maturation via application of shear stress and dynamic flow

Apart from direct contact to other NVU cell types, the BBB is additionally subjected to shear stress and flow rates *in-vivo*. This shear stress is known to significantly upregulate maturation in primary BCECs by increasing TJ and AJ expressions (Cucullo, Hossain et al. 2011). With regard to iBCECs previous reports show that stress and dynamic flow is reported to increase the contact area between cells, which does not necessarily cause upregulaton of protein and gene expression of BBB markers (DeStefano, Xu et al. 2017). Additionally, a core problem in the development of BBB-on-chip models is the current lack of standardization and non-invasive barrier integrity quantification methods. Therefore, in order to firstly increase the maturation of iBCECs, provide a physiological controlled microenvironment and to enable real time, non-invasive and label-free barrier integrity readouts, iBCECs were cultivated under dynamic flow and shear stress in a bioreactor setup. The third aim of this thesis therefore focused on the usage of the bioreactor system in quantifying flow-based changes in iBCECs. In order to assess the response of iBCECs to flow they were cultivated in the system for upto seven days with static transwell cultures as a control. Investigations of iBCECs post dynamic flow included

monitoring of barrier integrity, cellular morphological changes and changes in both gene and protein expression of relevant BCEC markers

9. MATERIALS

9.1 hiPSC lines

Table 4: List of used hiPSCs

Cell line	Manufacturer	Identifier	Sex	Origin	Viral transduction	Used passages
IMR90-4	WiCell (USA)	Lot: iPSC (IMR90)-4-DL-01	Female	Fetal lung fibroblasts	Lentiviral	14 - 32
SBAD-02-01	StemBanc repository (University of Oxford, IM2PACT consortium)		Male	Male dermal fibroblasts	Sendai virus	33 - 44

9.2 Immortalized and primary cells

Table 5: List of used immortalized and primary cells

Cell line	Manufacturer	Identifier	Origin	Type	Used passages
hCMEC/D3	Merck Millipore	2683101	Human temporal lobe	Immortalized by lentiviral transduction	4 -6
HUVEC	Cell Systems Biotechnologie Vertrieb GmbH	FC-0003	Human umbilical vein	Primary cells	4- 6
Human primary ACs	Pelobiotech GmbH (D	PB-TSC-1800-5	Human brain ACs	Primary cells	4-7
Human primary PCs	Pelobiotech GmbH (D),	PB-CH-010-2211	Human brain PCs	Primary cells	4-7

9.3 Primary antibodies used for immunohistochemistry

Table 6: List of used primary antibodies and dyes for immunohistochemistry

Name	Fixative	Species	Dilution and application	Manufacturer	Identifier
Claudin-5	ROTI ® Histofix, 4%	Rabbit	➢ 1:100 (2D) ➢ 1:100 (3D)	Abcam®	ab15106

Name	Fixative	Species	Dilution and application	Manufacturer	Identifier
E-cadherin	ROTI ® Histofix, 4%	Mouse	➢ 1:100 (2D)	BD Transduction Laboratories™	610181
GFAP	ROTI ® Histofix, 4%	Rabbit	➢ 1:100 (2D) ➢ 1:500 (Paraffin sections)	Dako Deutschland GmbH (D)	Z 0334
GLUT-1	ROTI ®Histofix, 4%	Mouse	➢ 1:200 (2D) ➢ 1:200 (3D)	Abcam®	ab40084
Nestin	ROTI ®Histofix, 4%	Mouse	➢ 1:100 (2D)	Merck Millipore (D)	MAB5326
Occludin	ROTI ®Histofix, 4%	Mouse	➢ 1:200 (2D)	Thermo Fisher	33-1500
PECAM-1	ROTI ®Histofix, 4%	Mouse	➢ 1:50 (2D) ➢ 1:100 (3D)	DAKO Cytomation	M0823
PDGFR-β	ROTI ®Histofix, 4%	Rabbit	➢ 1:100 (2D)	Abcam®	ab32570
P-gp	MetOH:Acetone (1:1)	Rabbit	➢ 1:100 (2D)	Lundbeck	aa585-690
Sox-1	ROTI ®Histofix, 4%	Rabbit	➢ 1:500 (Paraffin sections)	Abcam®	ab109290
TFR-1	MetOH:Acetone (1:1)	Rabbit	➢ 1:100 (3D)	Lundbeck	ECD(89-760)
VE-cadherin	ROTI ®Histofix, 4%	Rabbit	➢ 1:100 (2D)	Sigma-Aldrich®	V1514
VWF	ROTI ®Histofix, 4%	Rabbit	➢ 1:100 (2D)	Abcam®	ab9378
ZO-1	ROTI ®Histofix, 4%	Rabbit	➢ 1:100 (2D)	Proteintech®	21773-1-AP

9.4 Secondary antibodies and dyes used for immunohistochemistry

Table 7: List of used secondary antibodies and dyes for immunohistochemistry

Name	Species	Dilution	Manufacturer	Identifier
Alexa Fluor ™ 555 anti-mouse	Donkey	1:400	Invitrogen™	A31570

Name	Species	Dilution	Manufacturer	Identifier
Alexa Fluor ™ 488 anti-rabbit	Donkey	1:400	Invitrogen™	A21204
Alexa Fluor™ 647 anti-rabbit	Donkey	1:400	Invitrogen™	A31573
DAPI-Fluoromount G®	N/A	Ready to use	Invitrogen™	00-4959-5
F-Actin CytoPainter Phalloidin-iFluor 555 Reagent	N/A	1:2000	Abcam®	ab176756
Sytox™ red Deep Red Nucleic Acid Stain	N/A	1:2000	Invitrogen™	S11381

9.5 Chemicals

Table 8: List of chemicals

Chemicals	Manufacturer	Identifier
Accutase, 100ml	Sigma-Aldrich®	A6964
Acetone	Carl Roth®	5025.5
Antibody dilution solution	DCS Innovative Diagnostik-Systeme	ALI20R500
Anti-adherence rinsing solution	STEMCELL™ Technologies	07010
Astrocyte medium kit	ScienCell Research Laboratories	1801
B27-Supplement	ThermoFisher Scientific GmbH™	17504-044
Citrate solution	Sigma-Aldrich®	854
β-mercaptoethanol	Sigma-Aldrich®	M3148-25ML
CHIR99021	Biomol GmbH	Cay13122-5
DAPI-Fluoromount G®	Biozol Diagnostica	0100-20
Descosept AF	Nerbe plus GmbH	142984
Dimethyl sulfoxide (DMSO)	Sigma-Aldrich®	D2438-50ML
DMEM/F12 without L-glutamine	ThermoFisher Scientific GmbH™	11330-057
Donkey-serum	Biozol Diagnostica	A6283
D-glucose	Sigma-Aldrich®	50-99-7
Pericyte medium kit	PeloBiotech	PB MH-031-4000
Phosphate-Buffered Saline minus $MgCl^2$ and $CaCl^2$ (PBS^-), 500 ml	Sigma-Aldrich®	D8537
Phosphate-Buffered Saline plus $MgCl^2$ and $CaCl^2$ (PBS^+), 500 ml	Sigma-Aldrich®	14040117
EDTA (500 mM stock solution)	AppliChem GmbH	A4892,0100

Chemicals	Manufacturer	Identifier
Entellan™	Merck Millipore	107960
Eosin, 1%	Morphisto	1.017.700.500
Ethanol, 100%	Sigma-Aldrich®	32205-4X2.5L-GL
Fetal bovine serum (FBS)	ThermoFisher Scientific GmbH™	10270-106
Fluorescein sodium salt (NaF)	Sigma-Aldrich®	F6377-100G
Fetal calf serum (FCS)	Bio&Sell GmbH	FCS.AAD.0500
Fluorescein sodium salt (NaF)	Sigma-Aldrich®	F6377-100G
Gelatin	SERVA Electrophoresis	22151
Gentle Cell Dissociation Reagent	STEMCELL™ Technologies	100-0485
Gluteraldehyde	Sigma-Aldrich®	605390
hbFGF (human basic fibroblast growth factor)	PeproTech	100-18B
Hematoxylin	Morphisto	1023.101000
HistoGel™	ThermoFisher Scientific GmbH™	HG-4000-012
Human endothelial serum free medium (hESFM)	ThermoFisher Scientific GmbH™	11111-044
Human serum	Sigma-Aldrich®	H4522
Hydrocortisone	Sigma-Aldrich®	H0135-1MG
Incidin Plus	Ecolab Deutschland GmbH (D)	30 115 20
Isopropanol	Carl Roth®	6752.2
KnockOut™ Serum Replacement (KO serum)	ThermoFisher Scientific GmbH™	10828-028
L-Glutamine	Sigma-Aldrich®	G7513-100ML
Matrigel®	BD Bioscience	354230
MEM Non-essential amino acid solution (MEM-NEAA)	ThermoFisher Scientific GmbH™	11140-035
Methanol	Sigma-Aldrich®	32213-2,5L
mTeSR™1 medium + supplement, 400 ml	STEMCELL Technologies	85851
PC medium kit	Pelobiotech	PB MH-031-4000
Poly-L-lysine-Coating, 10 mg/ml	Pelobiotech GmbH (D)	PB-TSC-0413
Retinoic acid	Sigma-Aldrich®	R2625-500MG
ROCK inhibitor /Y27632	Sigma-Aldrich®	Y0503-1MG
ROTI ®Histofix, 4%	Carl Roth®	P087.2
Saponin	Carl Roth®	9622.1
Surgical Guide Resin (Chips BR)	Formlabs	RS-F2-5GAM-01
Sylgard 184, PDMS (Bioreactors)	DOW,	101697

Chemicals	Manufacturer	Identifier
Trinatrium citrate	Sigma-Aldrich®	1.11037
Triton X100	Carl Roth®	3051.2
Trypanblue (0.4%), 100 ml	Sigma-Aldrich®	T8154
Trypsin-EDTA 10x	ThermoFisher Scientific GmbH™	15400-054
Tween-20	VWR	8.221.840.500
VascuLife® VEGF Endothelial Medium Complete Kit	LIFELINE Cell technology	LS-1020
VEGF	Cell Signaling	48143S
Versene	GiBco™	15040033
Wnt-7a	Preprotech	120-31-15
Xylene	Carl Roth	9713.3

9.6 Kits

Table 9: List of analysis kits

Kit	Application	Manufacturer	Identifier
High-Capacity cDNA Reverse Transcription Kit with RNase Inhibitor	cDNA synthesis	Applied Biosystems	4374966
RNeasy® Micro Kit	mRNA isolation	Qiagen	74004
HotStarTaq *Plus* Master Mix Kit	qRT-PCR	Qiagen	203646

9.7 Media compositions

Table 10: List of media compositions

Medium	Components	Mixture	Additional notes
AC medium	AC basis medium	96%	Mix components and store at 4 °C up to 1 month.
	AC growth supplement	1%	
	FBS	2%	
	Pen/Strep	1%	
DeSR1	DMEM/F12 minus L-Glutamine	100%	Mix components and store at 4 °C up to 1 month.
	MEM-NEAA	1:100	
	GlutaMAX	1:200	
	β-mercaptoethanol	1:500	
DeSR2	DeSR1	100%	Mix components and store at 4 °C up to 1 month.
	B27	1:50	
EC+	hESFM	100%	Mix components freshly

Medium	Components	Mixture	Additional notes
	B27	1:200	
EC++	hESFM	100%	Mix components freshly
	B27	1:200	
	hbFGF, 100 µg/ml	20 ng/ml	
	Retinoic acid, 10 mM	10 µM	
Freezing medium (hiPSC)	KO serum	90%	Mix components freshly
	DMSO	10%	
Freezing medium (other cell types)	Cell specific medium	80%	Mix components freshly
	FBS	10%	
	DMSO	10%	
hECSR1	hESFM	100%	Mix components freshly
	B27	1:50	
	hbFGF, 100 µg/ml	20 ng/ml	
	Retinoic acid, 10 mM	10 µM	
hECSR2	hESFM	100%	Mix components freshly
	B27	1:50	
mTeSR™1 medium	mTeSR™1 basal medium	80%	Mix components and store at 4ºC for a maximum of one week. Aliquot and store supplements at−20 °C.
	mTeSR™1 supplement	20%	
PC medium	Ready to use	N/A	Store at 4 °C
Spheroid medium	hESFM	50%	Mix components freshly
	AC medium	25%	
	PC medium	25%	
	B27	1:200	
	hbFGF, 100 µg/ml	20 ng/ml	
	Human serum	2%	
	Retinoic acid, 10 mM	10 µM	
	Wnt 7a, 10 µg/ml	10 ng/ml	
Unconditioned medium (UM)	DMEM/F12 minus L-glutamine	78,5%	Mix components and store at 4 °C up to 1 month.
	KO serum	20%	

Medium	Components	Mixture	Additional notes
	MEM-NEAA	1%	
	L-glutamine (1mM)	1%	
	β-mercaptoethanol (0,1mM)	1:500	
VascuLife® complete	VascuLife® basal medium	475 ml	Mix components and store at 4 °C up to 1 month.
	Ascorbic acid (50 µg/ml)	0.5ml	
	Hydrocortisone (1 µg/ml)	0.5ml	
	L-Glutamine (10 mM)	25ml	
	rh IGF-1 (15ng/ml)	0.5ml	
	rh EGF (5 ng/ml)	0.5ml	
	rh FGF basic (5 ng/ml)	0.5ml	
	rh VEGF (5 ng/ml)	0.5ml	
	Heparinsulfate (0,75 U/ml)	0.5ml	
	FBS	0.5ml	
	Gentamycin + Amphotericin B	0.5ml	
VascuLife® modified d0-d6	VascuLife® basal medium	475 ml	Mix components and store at 4 °C up to 1 month.
	Ascorbic acid (50 µg/ml)	0.5ml	
	L-Glutamine (10 mM)	25ml	
	rh IGF-1 (15ng/ml)	0.5ml	
	rh EGF (5 ng/ml)	0.5ml	
	rh FGF basic (5 ng/ml)	0.5ml	
	rh VEGF (5 ng/ml)	0.5ml	
	Heparinsulfate (0,75 U/ml)	0.5ml	
	FBS	0.5ml	
	Gentamycin + Amphotericin B	0.5ml	
VascuLife® modified d7- d10	VascuLife® basal medium	475 ml	Mix components and store at 4 °C up to 1 month.
	Ascorbic acid (50 µg/ml)	0.5ml	
	Hydrocortisone (1 µg/ml)	0.5ml	
	L-Glutamine (10 mM)	25ml	
	rh IGF-1 (15ng/ml)	0.5ml	
	rh EGF (5 ng/ml)	0.5ml	
	rh VEGF (5 ng/ml)	0.5ml	
	Heparinsulfate (0,75 U/ml)	0.5ml	
	FBS	0.25ml	

Medium	Components	Mixture	Additional notes
	Gentamycin + Amphotericin B	0.5ml	

9.8 Buffers and solutions

Table 11: List of buffers and solutions

Buffer/Solution	Components	Mixture	Additional notes
Blocking buffer (2D)	PBS^-	94.88%	Prepare freshly
	Donkey serum	5%	
	Saponin	0.02%	
	Triton X100	0.1%	
Blocking buffer (3D)	PBS^-	89.5%	Prepare freshly
	Donkey serum	10%	
	Triton X100	0.5%	
Citrate buffer pH 6	Tri-Sodium-citrate	2.5% (w/v)	Mix components, adjust pH and Store at −4 °C up to 12 months
	Citrate	1.4% (w/v)	
	D (+) Glucose	2% (w/v)	
CHIR99021, 10 mM	CHIR99021	5 mg	Storage at −20 °C up to 12 months
	DMSO	1.075 ml	
EtOH, 70% (sterilisation of electrodes)	Ethanol, 96%	73%	
	Ultrapure water	27%	
EtOH, 70% (RNA isolation)	Ethanol, 100%	70%	
	Ultrapure water	30%	
EtOH, 80% (RNA isolation)	Ethanol, 100%	80%	
	Ultrapure water	20%	
Sodium Fluorescein 1mM	hESFM	1 ml	Dilute and use in a final concentration of 10 µM (1:100 in hESFM)
	NaF	0.377 mg	
Gelatin, 1%	Gelatin	1 g	Mix and autoclave for 20 min at 120 °C, storage at 4 °C.
	Ultrapure water	100 ml	
hbFGF, 100 µg/ml	hbFGF	25 µg	Dissolve and store aliquots at −20 ° C up to 12 months.
	PBS- + 0.1% BSA	250 µl	
Lysis-buffer (mRNA isolation)	RLT buffer	1 ml	Mix components and use freshly.
	β-mercaptoethanol	10 µl	

Buffer/Solution	Components	Mixture	Additional notes
Matrigel® coating for hiPSC culture	DMEM/F-12 without L-glutamine Matrigel®, growth factor (GF) reduced	12 ml 1 mg	Prepare with ice-cold media, incubate for 1 h at RT, post coating, top up with media and store at 4 °C up to 10 days.
200 µg/ml Matrigel® coating	DMEM/F-12 without L-glutamine Matrigel®, growth factor (GF) reduced	5 ml 1 mg	Prepare freshly with ice-cold media, incubate for 1 h at RT.
Methanol:Acetone (1:1)	Methanol Acetone	50% 50%	Mix components and store at -20 °C
Permeabilization buffer (2D)	PBS- Triton X100	99.8% 0.2%	Prepare freshly
Permeabilization buffer (3D)	PBS- Triton X100	99.8% 0.5%	Prepare freshly
Retinoic acid, 10 mM (RA)	DMSO Retinoic acid	1 ml 3 mg	Dissolve and store aliquots at −20 ° C up to 12 months.
VEGF, 50 µg/ml	PBS- +0.1%BSA VEGF	100 µl 5 µg	Dissolve and store aliquots at −20 ° C up to 12 months.
Wnt 7a,10 µg/ml	PBS- +0.1%BSA Wnt 7a	1.5ml 15 µg	Dissolve and store aliquots at −20 ° C up to 12 months.
Y27632, 10 mM	Ultrapure water Y27632	312.5 µl 1 mg	Dissolve and store aliquots at −20 ° C up to 6 months.

9.9 Consumables

Table 12: List of consumables

Consumables	Manufacturer
Air filter	Sartorius Stedim Biotech GmbH 16596
Adaptors for bioreactor connections MTLL230-J1A, FTLL230-J1A, MTLS230-J1A, FTLLP-J1A	Norson Medical/ Medlab
Aluminium foil	Carl Roth
Autoclave bags	Nerbe plus GmbH
AggreWell 800- 24 well plate	STEMCELL™ Technologies
Bransonic® Ultrasonic Cleaner	Branson Ultrasonic Corporation

Consumables	Manufacturer
Cell culture flasks (T25)	TPP Techno Plastic Products AG
Cell culture surface plastic	Oxyphen Membran Greiner, Unique Mem Track Etched 168 Membrane, 0,4 µm Oxyphen, 210401U4 Sabeu GmbH & CO. KG, M-215258
Cell culture Multiwell plate Nunclon Delta Surface (6-well)	ThermoFisher Scientific
Cell culture plates (6-, 24-, 96-well)	TPP Techno Plastic Products AG
Cell culture plates (24well) for impedance measurement	BRANDplates® Insert System KG, 782880
Centrifugation tubes (15 ml, 50 ml)	Greiner Bio-One
Chamber slide, 8-well, Permanox®, Nunc® Lab Tek®	ThermoFisher Scientific
Chamber slide, 8-well, glass, Nunc® Lab Tek®	ThermoFisher Scientific
Cooling rack, Iso Freeze ®	SARSTEDT AG & Co.
Coverslips	Menzel-Gläser
Confocal microscope TCSP8	Leica Microsystems CMS GmbH
Cryovials (1.5 ml)	ThermoFisher Scientific
Descosept	Dr. Schumacher GmbH
Disposable pipettes, Polystyrol (5 ml, 10 ml, 25 ml, 50 ml)	Greiner Bio-One
Forceps	OMNILAB-LABORZENTRUM GmbH&Co. KG
Freezing container (Mr. Frosty)	ThermoFisher Scientific
Gloves nitrile	Medline International Germany GmbH
Imaging plate 96 CG	Mobitec, 130-098-262
Laboratory glassware	Schott
Lint-free wipes	KIMTECH science
Microscope slides (Poly-L-Lysine)	R. Langenbrinck Labor- und Medizintechnik
Microtome Blades: Type A35	pfm Medical
Multi well plate (black, flat ground) for fluorescence	Greiner Bio-One

Consumables	Manufacturer
Nanodrop measuring plate	Tecan Deutschland GmbH
Neubauer counting chamber	Assistant
PAP hydrophobic pen	Merck Millipore Z377821
Parafilm	Sigma-Aldrich
Parrafin	Carl Roth
PolySine® Slides	Thermo Fisher Scientific, J2800AMNZ
Pasteur pipettes, glass	BRAND GmbH & Co. KG
PDMS, Sylgard 184 (to prepare silicone bioreactors)	DOW, 101697
Petri dishes, uncoated	Greiner Bio-One
Pipettes tips, sterile	Nerbe plus GmbH
Pumptubes, ID 2,79 mm, length 381 mm	IDEX Health & Science GmbH, 070539-X18
Silikontubes TYGON T3304-23, Inner diameter 3,2 mm	Saint-Gobain Performance Plastics, France
Punch cutter	Facom, 245.J1A
QIAshredder Mini Spin Column	Qiagen 79656
Rack for centrifugation tubes	neoLab Migge Laborbedarf-Vertriebs GmbH
Reaction tubes (1.5 ml, 2 ml)	Eppendorf AG
Scalpel	Bayha GmbH
Scalpel blades	Bayha GmbH
Sterile filter 0.2 µm	ThermoFisher Scientific
Syringe	BD Biosciences
Surgical Guide Resin (used for BR chip preparation)	Formlabs, RS-F2-5GAM-01
Transwell-(PET-membrane-) cell culture inserts, 24-well, 0.4 µm pore size, transparent	CellQART® 24-Well Cell Culture Insert, 0,4 µm, PET 932 04 02

9.10 Laboratory devices

Table 13: List of laboratory devices

Laboratory devices	**Manufacturer**
Analytical balance	Kern & Sohn GmbH, ABJ 220-4M
Aspirator Vacusafe	NTEGRA Biosciences Deutschland GmbH
Bead bath	Grant Instruments
Biological safety cabinet class II	ThermoFisher Scientific, SAFE2020
Centrifuges	Eppendorf AG 5417R, Heraeus PICO17 and Sorvall Legend X1R
Cold room (4ºC)	Genheimer Kälte-Klima-Technik GmbH & Co. KG
Electrode STX3	World precision instruments
Electrical impedance analyser (3D spheroids)	Sciospec ISX3,01-000B-0159-0B09
EVOS XL	Carl Zeiss AG
Freezer−20 °C	Liebherr-International Deutschland GmbH
Freezer -80 °C	ThermoFisher Scientific
Fume hood	Prutscher Laboratory Systems GmbH
Hemocytometer	Hartenstein
Heating plate (37°C)	Harry Gestigkeit GmbH
Ice flaker AF-80 (Scotsman)	HIBU Eismaschinen GmbH & Co. KG
Incubator for cell culture	Heraeus Holding GmbH
Incubator system for bioreactors and transwells	Dr. Tobias Schmitz from the Department of Tissue Engineering and Regenerative Medicine, University Hospital Würzburg, Germany
Impedance chips for spheroids	Dr. Heinz-Georg Jahnke from the Center for Biotechnology and Biomedicine (BBZ), Molecular biological-biochemical Processing Technology, Universtiy of Leipzig, Germany
Laser scanning microscope TCS-SP8 (Confocal microscope)	Leica Microsystems GmbH
Microplate reader TECAN Infinite M200	Tecan Deutschland GmbH
Microscope BZ-9000 BIOREVO System	KEYENCE Deutschland GmbH
Microm STP120 Tissue Processor	Thermo Fisher Scientific
Microtom SM 2010R	Leica Microsystems GmbH
Millicell ERS-2	Merck Millipore

Laboratory devices	Manufacturer
Multifuge X1R	ThermoFisher Scientific
N2-Tank: MV 815 P-190 (-180°C)	Jutta Ohst German-cryo GmbH
Orbital shaker	VWR
Paraffin embedding system	TES Valida, Medite®
Pipetting aid	BRAND GmbH & Co. KG
Potentiostat/Galvanostat PGSTAT204	Metrohm Autolab B V
Rocking platform (shaker)	VWR international
Glass microscopy slide printer	Vogel GmbH & CO. KG, VSP 5001
Steam Cooker “MultiGourmet”	Braun
Tissue Drying Oven (TDO 66)	Medite®
Ultrapure water system	Merck Millipore
Ultrasonic cleaner	Branson Ultrasonic Corporation
Vortexer	Carl Roth
Water bath	LAUDA DR. R. WOBSER GmbH & Co. KG

9.11 Primer list

Table 14: List of primers

Symbol	Target	NM accession numbers
18SrRNA	18S ribosomal RNA	NR_003286.2
ABCA1	ATP binding cassette subfamily A member 1	NM_005502.4
ABCA7	ATP binding cassette subfamily A member 7	NM_019112.4
ABCB1	ATP binding cassette subfamily B member 1	NM_000927.4
ABCC1	ATP binding cassette subfamily C member 1	NM_004996.3
ABCC2	ATP binding cassette subfamily C member 2	NM_000392.4
ABCC3	ATP binding cassette subfamily C member 3	NM_003786.3
ABCC4	ATP binding cassette subfamily C member 4	NM_005845.4
ABCC5	ATP binding cassette subfamily C member 5	NM_005688.3

ABCG2	ATP binding cassette subfamily G member 2,	NM_004827.2
ACTB	Actin beta	NM_001101.4
APOE	Apolipoprotein E	NM_000041.4, NM_001302688.2, NM_001302689.2, NM_001302690.2, NM_001302691.2
AQP10	Aquaporin 10	NM_080429.2
AQP11	Aquaporin 11	NM_173039.2
AQP2	Aquaporin 2	NM_000486.5
AQP3	Aquaporin 3	NM_004925.4
AQP4	Aquaporin 4	NM_001317387.2, NM_001650.6
AQP5	Aquaporin 5	NM_001651.3
B2M	Beta-2-microglobulin	NM_004048.2
CDH1	Cadherin 1	NM_001317186.1, NM_001317185.1, NM_001317184.1, NM_004360.4
CDH5	Cadherin 5	NM_001795.4
CLDN1	Claudin 1	NM_021101.5
CLDN10 tva	Claudin 10	NM_182848.3
CLDN10 tvb	Claudin 10	NM_006984.4
CLDN11	Claudin 11	NM_005602.5
CLDN12 tv1	Claudin 12	NM_001185072.2
CLDN12 tv2	Claudin 12	NM_001185073.2
CLDN12 tv3	Claudin 12	NM_012129.4
CLDN14	Claudin 14	NM_012130.3, NM_001146078.2, NM_001146079.1, NM_001146077.1, NM_144492.2
CLDN15	Claudin 15	NM_014343.2, NM_001185080.1
CLDN16	Claudin 16	NM_006580.3
CLDN17	Claudin 17	NM_012131.2
CLDN18 tv1b	Claudin 18	NM_016369.3
CLDN19	Claudin 19	NM_148960.2
CLDN2	Claudin 2	NM_001171095.1
CLDN20	Claudin 20	NM_001001346.3
CLDN22	Claudin 22	NM_001111319.1
CLDN23	Claudin 23	NM_194284.2
CLDN24	Claudin 24	NM_001185149.1
CLDN25 tv1-4	Claudin 25	NM_001101389.1
CLDN25 tv7	Claudin 25	NM_001040181.1; NM_001040199.1
CLDN26	Claudin 26	NM_001146336.1
CLDN27	Claudin 27	NM_001204210.1, NM_001204211.1, NM_001204212.1
CLDN3	Claudin 3	NM_001306.3
CLDN4	Claudin 4	NM_001305.4
CLDN5	Claudin 5	NM_001130861.1, NM_003277.3
CLDN6	Claudin 6	NM_021195.4
CLDN7	Claudin 7	NM_001307.5
CLDN8	Claudin 8	NM_199328.2

CLDN9	Claudin 9	NM_020982.3
CTNNB1	Catenin beta-1	NM_001098209.1, NM_001904.3, NM_001098210.1
FN1	FiBronectin	NM_212474.2, NM_212476.2, NM_212478.2, NM_002026.3, NM_212482.2, NM_001306132.1, NM_001306131
GAPDH	Glyceraldehyde-3-phosphate dehydrogenase	NM_002046
INSR	Insulin receptor	NM_001079817.2, NM_000208.3
JAM1	Junctional adhesion molecule 1	NM_016946.4
JAM2	Junctional adhesion molecule 2	NM_021219.3
JAM3	Junctional adhesion molecule 3	NM_032801.4
KRT-1	Keratin 1	NM_006121.3
KRT18	Keratin 18	NM_199187.1, NM_000224.2
KRT19	Keratin 19	NM_002276.4
KRT8	Keratin 8	NM_001256293.1, NM_001256282.1
LRP1	LDL receptor related protein 1	NM_002332.2
LRP8	LDL receptor related protein 8	NM_004631.4, NM_001018054.2, NM_033300.3, NM_017522.4
LSR	Lipolysis-stimulated lipoprotein receptor	NM_001260489.2, NM_001260490.2, NM_001385215.1, NM_015925.7, NM_205834.4, NM_205835.4
MARVELD2	MARVEL domain containing 2	NM_001244734.1, NM_001038603.2
MFSD2A	Major facilitator superfamily domain containing 2A	NM_001349821.1, NM_001349823.1, NM_001349822.1, NM_032793.4, NM_001136493.2, NM_001287809.1,
MKI67	Marker of proliferation Ki-67	NM_001145966.1, NM_002417.4
MUC1 tva	Mucin 1	NM_001204294.1, NM_001204293.1, NM_001204285.1, NM_001018017.2, NM_001044390.2
MUC1 tvb	Mucin 1	NM_001204296.1, NM_001204297.1, NM_001204295.1, NM_001204292.1, NM_001204291.1, NM_001204289.2
MUC18	Mucin 18	NM_006500.2
MUC20	Mucin 20	NM_152673.3, NM_001291833.1, NM_020790.1, NM_001282506.1
OCLN	Occludin	NM_001205255.1, NM_001205254.1, NM_002538.3
PECAM1	Platelet endothelial cell adhesion molecule 1	NM_000442.5
PPIA	Peptidylprolyl isomerase A	NM_021130.4

RAGE	Receptor for advanced glycation endproducts	NM_001136.5, NM_001206929.2, NM_001206932.2, NM_001206934.2, NM_001206936.2, NM_001206940.2, NM_001206954.2, NM_001206966.2, NM_172197.3
RARA	Retinoic acid receptor alpha	NM_000964.4, NM_001024809.4, NM_001145301.3, NM_001145302.3
RXRA	Retinoic acid receptor RXR-alpha	NM_001291920.2, NM_001291921.2, NM_002957.6
RXRB	Retinoic acid receptor RXR-beta	NM_001270401.2, NM_001291989.2, NM_021976.5
S100A4 tv1	S100 calcium binding protein A4	NM_002961.2
S100A4 tv2	S100 calcium binding protein A4	NM_019554.2
SLC1A1	Solute carrier family 1 member 1	NM_004170.5
SLC5A1	Solute carrier family 5 member 1	NM_000343.3
SLC16A1	Solute carrier family 16 member 1	NM_003051.3, NM_001166496.1
SLC16A2	Solute carrier family 16 member 2	NM_006517.4
SLC29A1	Solute carrier family 29 member 1	NM_001078175.2, NM_001078177.1, NM_001304462.1
SLC2A1	Solute carrier family 2 member 1	NM_006516.2
SLC7A1	Solute carrier family 7 member 1	NM_003045.4
SLC7A3	Solute carrier family 7 member 3	NM_032803.5
SLC7A5	Solute carrier family 7 member 5	NM_003486.6
TFRC	Transferrin receptor protein 1	NM_001313966.1, NM_001313965.1, NM_003234.3, NM_001128148.2
TJP1	Tight junction protein 1	NM_003257.4
TJP2	Tight junction protein 2	NM_001170414.2, NM_201629.3, NM_001170416.1, NM_001170415.1, NM_004817.3
TJP3	Tight junction protein 3	NM_001267561.1
VEGFA	Vascular endothelial growth factor A	NM_001204384.1, NM_001171622.1, NM_001033756.2, NM_001025370.2, NM_001025369.2, NM_001025368
VIM	Vimentin	NM_003380.4
VWF	von Willebrand factor	NM_000552.5

9.12 Software list

Table 15: List of software

Software	Version	Application	Manufacturer
GraphPad Prism 9	9.0.0	Statistics and graphs	GraphPad Software, Inc.
GIMP	2.10.24	Grid overlay for image quantification	GIMP-Team
ImageJ	V1.52a	Image editing and quantification	Wayne Rasband, NIH
Inkscape	1.0	Schematic drawing and figure compilation	Inkscape Community
Keyence BZ II Analyzer	2.1	Fluoresence microscopy	Keyence
Keyence BZ II Viewer	2.1	Fluoresence microscopy	Keyence
Leica Application Suite X LAS X	3.5.6	Fluoresence microscopy	Leica Microsystems GmbH
Nova	2.1	Impedance measurement	Metrohm Autolab
IDAT	3.6.5	Impedance measurement	Dr. Heinz-Georg Jahnke from the Center for Biotechnology and Biomedicine (BBZ), Molecular biological-biochemical Processing Technology, Universtiy of Leipzig, Germany
Tecan iControl 200	2.11	Luminescence measurement	Tecan Deutschland GmbH

10. METHODS

10.1 Cell cuture working conditions

In order to ensure sterile conditions, all cell culture was performed in a class II biological safety cabinet, and care was taken that only sterile materials, media and solutions were used. Prior to medium change, all cell culture media was pre-warmed to room temperature (RT). All cells were cultured in an incubator that provided 95% humidity, 5% carbon dioxide (CO_2) concentration, and a temperature of 37 °C. Unless otherwise stated, all cells were centrifuged with the Multifuge X3R for 5 minutes (min) at 270 x g.

10.2 Preperation of cell culture coatings

10.2.1 Poly-L-Lysine-coating for ACs and PCs

To ensure optimal adherence of primary human ACs and PCs, T-75 cell culture flasks were coated with 10 ml of 10 µg/ml poly-L-lysine (PLL). PLL stocks of 10mg/ml were diluted in the ratio 1:1000 in sterile ultrapure water followed by incubation for a minimum of 1 h at 37 °C. The flasks were either used directly or stored at 4ºC after enwrapping the cap of the flask with Parafilm®. Flasks were stored for a maximum of seven days.

10.2.2 Gelatin coating for hCMEC/D3 cells

T75 cell culture flasks were coated with 1% gelatin solution for a minumim of 30 min at 37 °C to ensure optimal adherence and maintenance of hCMEC/D3 cells. The flasks were either used directly or stored at 4ºC after enwrapping the cap of the flask with Parafilm®. Flasks were stored for a maximum of seven days.

10.2.3 Matrigel® coating for cultivation of hiPSCs

To ensure optimal adherence of hiPSCs, 6-well Nunclon™ delta surface plates were coated with 100µg/ml of Matrigel®. 0.5 mg Matrigel® was mixed with 12ml cold DMEM/F-12 minus L-Glutamine. The prepared coating solution was then dispensed as 1 ml per well of a 6 well plate and incubated for 1 h at RT. After incubation, the plates were used either immediately or topped with 1 ml/well DMEM/F-12 minus L-Glutamine, in order to prevent drying of the coating. The plates were either used directly or stored at 4ºC after enwrapping the sides with Parafilm® upto a total of seven days.

10.2.4 Matrigel® coating for cultivation of iBCECs

Cell culture surfaces were coated with 200 µg/ml of Matrigel®. 0.5 mg Matrigel® was mixed with 5 ml cold DMEM/F-12 minus L-Glutamine to ensure optimal adherence of iBCECs.

The prepared coating solution was then dispensed as 100 µl per 24 well transwell insert or as 300 µl per bioreactor membrane followed by incubation for 1 h at RT. After incubation, the cell culture surfaces were used directly for seeding.

10.3 Cell culture specifications

10.3.1 Freezing and thawing of primary ACs, PCs and hCMEC/D3 cells

When cells reached a confluency of 80-90%, they were detached by incubation at 37 °C for 10 mins with Accutase™ for ACs and PCs or by incubation for 5 mins with Trypsin/EDTA for hCMEC/D3 cells. Detached cells were collected and centrifuged followed by dissolution of the cell pellet in cell specific pre-cooled freezing medium (80% cell specific medium + 10% Fetal bovine serum (FBS) + 10% DMSO). $1x10^6$ cells in 1 ml were transferred into a cryovial and stored for 24h at -80 °C in a Mr. Frosty™ freezing aid to guarantee a temperature decrease of 1 K/min. The cells were then moved on dry ice into a liquid nitrogen storage tank. To thaw cells, the cryovial containing cells was taken from the liquid nitrogen storage, transported on dry ice and immediately placed in a water bath at 37°C until only a small ice crystal was left. After disinfection of the vial, the thawed cell suspension was then transferred into a 15 ml falcon tube, containing 9 ml cell specific medium and centrifuged. Afterwards, cells were resuspended in 10 ml of respective medium and plated onto T75 cell culture flasks.

10.3.2 Freezing and thawing of hiPSCs

When hiPSCs reached a confluency of 70-80%, they were detached as colonies using 0.5 ml of respective enzymes. Gentle Cell Dissociation Reagent (GCDR) was used for IMR90-4 hiPSCs and Versene™ Solution was used for for SBAD-02-01 hiPSCs. Both enzymes required an incubation time of 1-2 mins at 37 °C. hiPSC colonies were then collected and centrifuged followed by gentle dissolution of the pellet in pre-cooled freezing medium (90% KnockOut™ Serum replacement + 10% DMSO). Cell clumps were collected such that each cryovial contains ~1 $x10^3$ cells/cm^2 in 1 ml (ie. ~half a 6 well plate per vial). The cryovials were then stored for 24h at - 80 °C in a Mr. Frosty™ freezing aid to guarantee a temperature decrease of 1 K/min. The cells were moved on dry ice into a liquid nitrogen storage tank post 24 h. To thaw hiPSCs, the cryovial containing the cells was taken from the liquid nitrogen storage, transported on dry ice and immediately placed in a water bath at 37°C until only a small ice crystal remained. After disinfection of the vial, the thawed cell suspension was then transferred into a 15 ml centrifuge tube, containing 9 ml mTeSR^{TM1} + 10 µM Y27632 (ROCK inhibitor) and centrifuged. The pellet was then further resuspended in 4 ml mTeSR^{TM1} + 10 µM Y27632 and redistributed into two wells of a pre-coated 6 well plate.

10.3.3 Passaging and maintenance of hiPS line-IMR90-4

When hiPSC line IMR90-4 reached a confluency of 50% -80%, they were split for maintenance cultures. In detail, the cell culture medium was aspirated, followed by incubation with 1 ml GCDR at 37 °C for 2 min. As soon as the colony edges started to detach, the GCDR solution was carefully aspirated and the colonies were washed once with 1 ml PBS- per well. PBS- was then aspirated and 1 ml of mTeSR^{TM1} + 10 µM Y27632 was added per well. The colonies were then completely detached from the cell culture surface using a cell scraper. Per ml of medium a maximal of two resuspension steps were performed in order to detach the colonies into small fragments. The colonies were then seeded in a ratio of 1:10 to 1:20 on Matrigel® coated 6-well plates in a total of 2 ml/well mTeSR^{TM1} + 10 µM Y27632. For the first 24 h of culture 10 µM Y27632 was added as an apoptosis inhibitor. Daily medium change was then performed with 2ml per well of mTeSR^{TM1}.

10.3.4 Passaging and maintenance of hiPSC-SBAD-02-01

When hiPSC line SBAD-02-01 reached a confluency of 50% - 80%, they were split for maintenance cultures. In detail, the cell culture medium was aspirated, followed by incubation with 1 ml Versene at 37 °C for 1 min. As soon as the colony edges started to detach, Versene solution was carefully aspirated and the colonies were washed once with 1 ml PBS- per well. PBS- was then aspirated and 1 ml of mTeSR^{TM1} + 10 µM Y27632 was added per well. The colonies were then completely detached from the cell culture surface using a cell scraper. Per ml of medium, a maximal of 2 resuspension steps were performed in order to detach the colonies into small fragments. The colonies were then seeded in a ratio of 1:10 to 1:20 on Matrigel® coated 6-well plates in a total of 2 ml/well mTeSR^{TM1} + 10 µM Y27632. For the first 24 h of culture 10 µM Y27632 was added as an apoptosis inhibitor. Daily medium change was then performed with 2 ml per well of mTeSR^{TM1}.

10.3.5 Cell counting

To seed cells in required numbers, they were counted using the Neubauer heamocytometer. Depending on the size of the pellet, the cells were resuspended in 2 - 10 ml of respective medium. From this suspension, 20 µl was mixed with 20 µl 0.4% Trypan blue solution in order to have a final dilution factor of 2. Trypan blue stains dead cells blue and living cells with intact cellular membranes are not colored. 10 µl of the cell suspension and Tryphan blue mixture was pipetted into the heamocytometer and living cells were counted under the microscope in all four large squares. The total number of cells were then counted using the following equation (Eq.6).

$$\boldsymbol{total\ cell\ number} = \frac{\boldsymbol{x}}{\boldsymbol{4}} \cdot \boldsymbol{10^4} \cdot \boldsymbol{DF} \cdot \boldsymbol{V_{solution}} \quad (\boldsymbol{6})$$

x = counted cell number in all 4 squares

10^4 = coefficient determined by the volume of the counting chamber

DF = dilution factor

$V_{solution}$ = volume of the cell suspension

10.3.6 Passaging and maintenance of primary HUVECS

Primary HUVECS that were used as controls were cultivated on uncoated T25 cell culture flasks with 7 ml of VascuLife® medium. Medium was renewed every 2 - 3 days. At a confluence of 80% the cells were passaged using Accutase™ with incubation for 7 min at 37 °C and seeded at a density of 6 x 10^3 - 8 x 10^3 cells/cm^2 into new T25 cell culture flasks.

10.3.7 Passaging and maintenance of immortalized hCMEC/D3 cell line

Human BBB-specific immortalized cell line hCMEC/D3 that were used as controls were cultivated on 1% gelatine-coated cell culture flasks and supplied with modified VascuLife® medium. Medium was renewed every 3 days. At a confluence of 90%, they were passaged using Trypsin/EDTA solution with incubation for 5 min at 37 °C. Enzymatic reaction was stopped with 1% FBS before harvesting and seeding at a density of 2 x 10^3 cells/cm^2 into new T25 cell culture flasks. In order to increase the barrier properties of hCMEC/D3 cells, once the cells reached 80% confluency the medium was chemically supplemented with 100 nM hydrocortisone for an additional 3 days.

10.3.8 Passaging and maintenance of human ACs

Primary human ACs were cultured on PLL coated T75 flasks and were supplied with 10 ml astrocyte medium. Media was changed in a 3-day rhythm. Passaging of the cells was performed at a confluency of about 80 - 90%. For passaging, ACs were incubated with Accutase™ for 10 min at 37 °C and seeded at a density of 1 x 10^6- 2 x 10^6 cells/cm^2 into new T75 cell culture flasks.

10.3.9 Passaging and maintenance of primary human PCs

Primary human PCs were cultured on PLL coated T75 flasks and were supplied with 10 ml pericyte medium. Media was changed in a 3-day rhythm. Passaging of the cells was performed at a confluency of about 80 - 90%. For passaging, PCs were incubated with Accutase™ for 10 min at 37 °C and seeded at a density of 0.5 x 10^6- 1 x 10^6 cells/cm^2 into new T75 cell culture flasks.

10.4 hiPSC differentiation via co-differentiation

CD of hiPSCs into iBCECs and iNPCs was performed as previously reported (Lippmann, Al-Ahmad et al. 2014) and detailed steps are outlined in *(Figure 10)*. In detail, at d-3, hiPSCs were detached by incubation with 1 ml/ well Accutase™ for 7 min at 37 °C per well to obtain single

cells. Isolated single cells were centrifuged, counted and then seeded at a density of 7.5 x 10^3 cells/cm^2 onto Matrigel® coated 6-well plates. Seeding was performed in 2 ml/well mTeSR ™1 including 10 µM Y27632 for the first 24 h. From the following day, medium was changed daily and hiPSCs were proliferated in 2 ml/well mTeSR™1 minus Y27632. hiPSC confluency was further monitored by counting one representative well in order to determine the optimal starting point of differentiation. Cells from the respresentative well were detached using 0.5 ml Accutase™ with incubation for 7 min at 37 °C. If the hiPSCs reached an optimal cell density of 2.5 – 3.5 x 10^4 cells/cm^2, CD to iBCECs and iNPCs was started by switching the medium to unconditioned medium (UM) for 6 days with daily media changes. For BCEC specification the medium was changed to 4 ml/well EC++medium at d6. On d7 no medium change was performed. On d8 of differentiation, the cells were treated with 2 ml/well Accutase™ with incubation for 30 min at 37 °C. The cells were then collected and resuspended to yield single cells. Counted cells were then purified by sub-passaging at a density of 1 x 10^6 cells/cm^2 in EC++ medium onto 200 µg/ml Matrigel® coated cell culture surfaces. In 24 well transwell formats, cells on top of the insert membrane were seeded in a total volume of 200 µl cell suspension with an additional 850 µl EC++ medium in the basolateral compartment. Medium was changed to 200 µl EC+ medium in the apical compartment and 850 µl EC+ medium in the basolateral compartment on d9. On d10 purified iBCECs were used for downstream applications. Since two different hiPSc lines were used for differentiations, 2D cultures of iBCECs derived from the CDstrategy are further labelled as CD $1_{(2D)}$ for IMR90-4 derived cells and CD $2_{(2D)}$ for SBAD-02-01 derived cells.

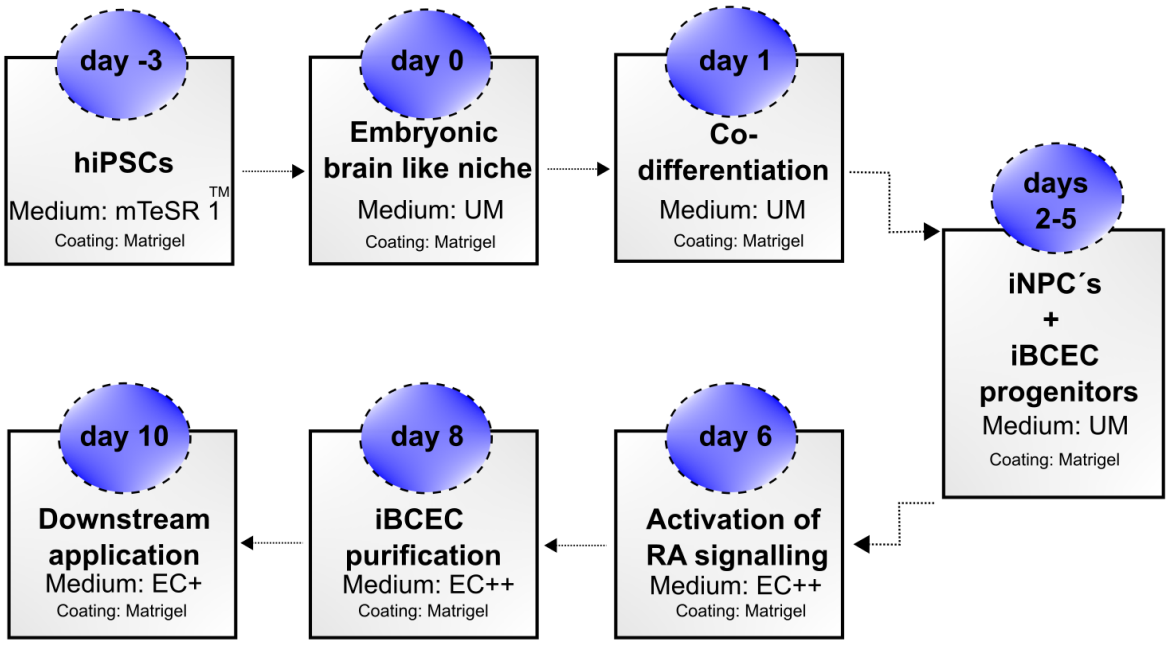

Figure 10: Schematic of co-differentiation

Human induced pluripotent stem cells (hiPSCs) were first seeded as single cells onto Matrigel® coated cell culture surfaces. Once optimal confluency of cells was achieved, differentiation was initiated by induction of an embryonic brain like niche. hiPSCs were then co-differentiated into brain capillary endothelial cells (iBCECs) and neural progenitors (iNPCs), followed by activation of retinoic acid (RA) for iBCEC specification and a final step including extracellular matrix (ECM) based purification before downstream 2D applications.

10.5 hiPSC differentiation via directed differentiation

DD of hiPSCs into iBCECs was performed as previously reported (Qian, Maguire et al. 2017) and detailed steps are outlined in *(Figure 11)*. In detail, at d-3, hiPSCs were detached by incubation with 1ml/ well Accutase™ per well for 7 min at 37°C to obtain single cells. Isolated single cells were centrifuged, counted and then seeded at a density of 35 x 10^3 cells/cm^2 onto Matrigel® coated 6-well plates. Seeding was performed in 2 ml/well mTeSR ™1 including 10 µM Y27632 for the first 24 h. From the following day, medium was changed daily and hiPSCs were proliferated in 2ml/well mTeSR™1 minus Y27632. Once the colonies reached a confluency of ~70-80%, differentiation process was initiated. At d0 the medium was changed to DeSR1 + 6 µM CHIR99021. CHIR99021 is an aminopyrimidine derivative that inhibits the enzyme GSK-3β and thus induces mesodermal differentiation. On d1, the medium was switched to DeSR2 for 5 days with daily medium changes. On d6 medium was changed to 4 ml/well hECSR1 to initiate BMEC specification. No medium change was performed on d7. On

d8 of differentiation, the cells were treated with 2 ml/well Accutase™ with incubation for 30 min at 37 °C. The cells were then collected and resuspended to yield single cells. Counted cells were then purified by sub passaging at a density of 1 x 10^6 cells/cm^2 in hECSR1 medium onto 200 µg/ml Matrigel® coated cell culture surfaces. In 24 well transwell formats, cells on top of the insert membrane were seeded in a total volume of 200 µl cell suspension with an additional 850 µl hECSR1 medium in the basolateral compartment. On d9 medium was changed to hECSR2 200 µl medium in the apical compartment and 850 µl medium in the basolateral compartment on d9. On d10 purified iBCECs were used for downstream applications. Since two different hiPSC lines were used for differentiations, 2D cultures of iBCECs derived from the DD protocol are further labelled as DD $1_{(2D)}$ for IMR90-4 derived cells and DD $2_{(2D)}$ for SBAD-02-01 derived cells.

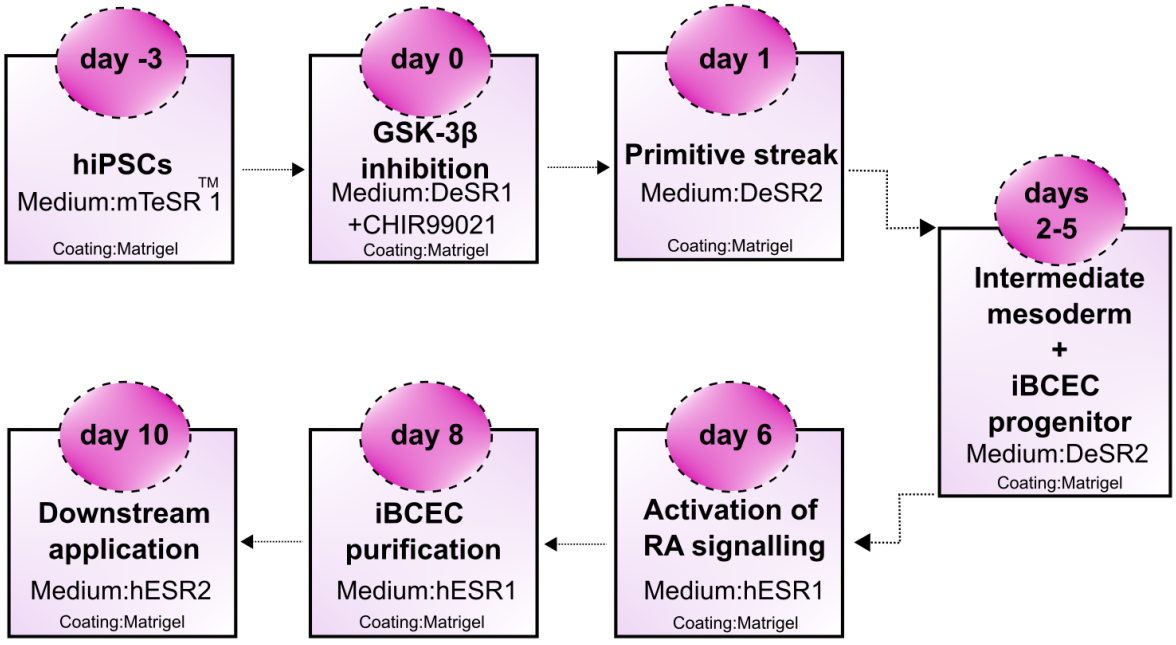

Figure 11: Schematic of directed differentiation

Human induced pluripotent stem cells (hiPSCs) were first seeded as single cells onto Matrigel® coated cell culture surfaces. Mesoderm specific differentiation was initiated by inhibition of Glycogen synthase kinase-3 beta (GSK-3β). hiPSCs were then co-differentiated into cells forming the primitive streak, followed by intermediate mesoderm and brain capillary endothelial cell (BCEC) progenitors. Activation of retinoic acid (RA) signaling was carried out for BCEC specification and a final step including extracellular matrix (ECM) based purification was performed before downstream applications.

10.6 Generation of BBB spheroids

AggreWell™ 800 Microwell culture plates were used in order to prepare spheroids. The plates were pre-prepared by coating with Anti-Adherence Solution in order to prevent cell attachment. Briefly, each well of the microwell plate was coated with 500 µl of Anti-Adherence Solution, and then centrifuged at 300 g for 5 minutes. Post centrifugation, the wells were visualized microscopically to ensure that all micro cavities were free from bubbles. In case of bubble formation, the centrifugation steps were repeated. Anti-Adherence Solution was then aspirated and the wells were rinsed once with 500 µl DMEM/F12 minus L-Glutamine. When pooled cell mixtures were ready for seeding, the media was aspirated out and respective pooled cell suspensions were added into each well in a total of 2 ml spheroid media. The plate was then centrifuged at 300 g for 5 minutes. Post centrifugation all wells were visualized microscopically to ensure that the cell suspensions filled the microcavities. The plate was then placed into the incubator at 37ºC and 5% CO_2 for 48h before usage of spheroids for further analysis. Total number of cells used for each spheroid condition is mentioned in *(Table 12)*. Since two different hiPSC lines were used for differentiations, 3D cultures of iBCECs derived from the CD strategy are further labelled as CD $1_{(3D)}$ for IMR90-4 derived cells and CD $2_{(3D)}$ for SBAD-02-01 derived cells. 3D cultures of iBCECs derived from the DD protocol are further labelled as DD $1_{(3D)}$ for IMR90-4 derived cells and DD $2_{(3D)}$ for SBAD-02-01 derived cells.

ACs and PCs were used upto passage 6 in all experiments. For the CD protocol, cell mixtures from d8 were used in order to incooperate both iBCECs and NPCs into the spheroids and in the DD protocol, iBCECs from d10 were used in preparing spheroids. For prolonged culture, medium was changed on the spheroids every alternate day, *(Figure 12)*.

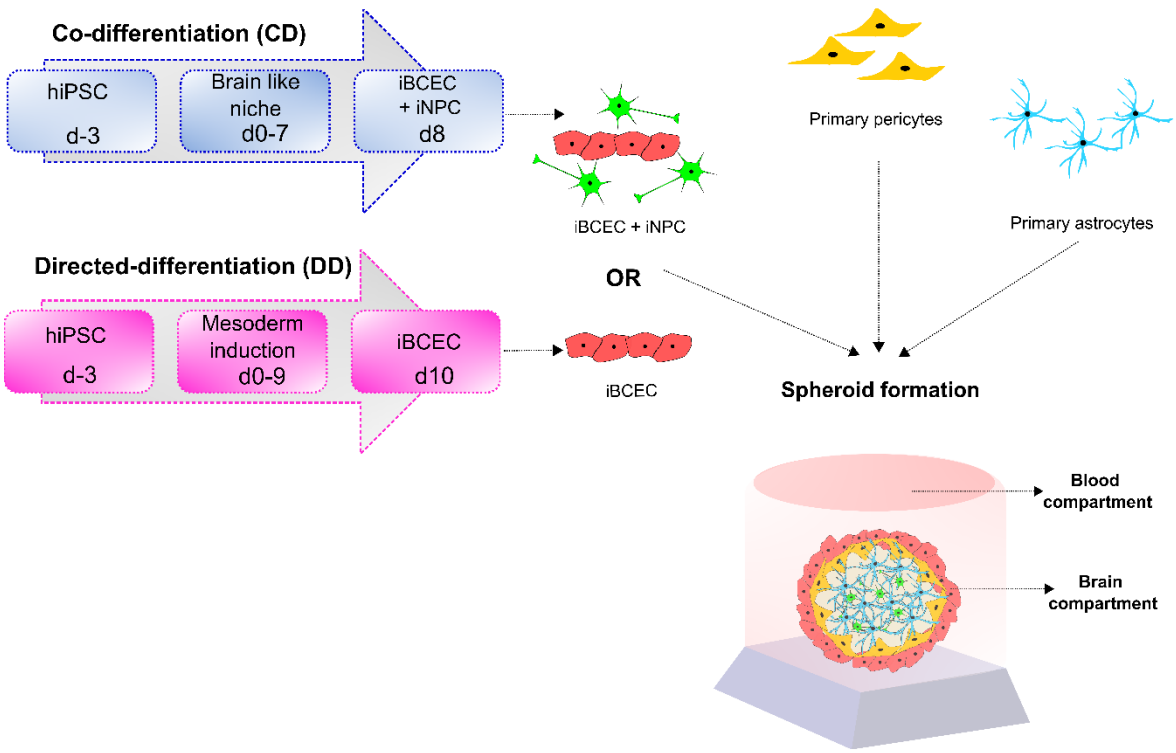

Figure 12: Schematic of spheroid formation

Human induced pluripotent stem cell (hiPSC) derived brain capillary endothelial cells (iBCECs) and neural progenitors (iNPC) on day 8 (d8) of differentiation from the co-differentiation strategy and iBCECs on d10 of differentiation from the directed differentiation strategy were pooled together with primary astrocytes and pericytes in order to form spheroids. Pooled cells in respective cellular ratios were cultivated on top of non-adhesive cell culture surfaces, the cells further self assembled to form spheroids which were used for downstream applications after 2 days of formation.

Table 16: Cell numbers used in spheroid generation

Spheroid type	AC	PC	d8 mixture of iBCEC+NPC	d10 iBCEC
AC	300,000	x	x	x
PC	300,000	x	x	x
AC+PC	300,000	300,000	x	x
AC+PC+CD 1 (CD $1_{(3D)}$)	300,000	300,000	600,000	x
AC+PC+CD 2 (CD $2_{(3D)}$)	300,000	300,000	600,000	x
AC+PC+DD 1 (DD $1_{(3D)}$)	300,000	300,000	x	300,000
AC+PC+DD 2 (DD $2_{(3D)}$)	300,000	300,000	x	300,000

10.7 Establishment of BBB microfluidic system

10.7.1 Coating and seeding of bioreactor chips

Gamma sterilized membrane chips were first carefully shifted into a 6-well plate such that each well contained one membrane chip. To ensure optimal adherence of iBCECs, 200 µg/ml of Matrigel® was used to coat each membrane chip. 0.5 mg Matrigel® was mixed with 5 ml cold DMEM/F-12 minus L-Glutamine and the prepared coating solution was dispensed in a volume of 300 µl onto each membrane chip followed by incubation at RT for a total of 1h before cell seeding. iBCECs derived from the IMR90-4 hiPSC line using the CD strategy (Lippmann, Al-Ahmad et al. 2014) were seeded on d8 at a density of $1.12x10^6$ cells and final volume of 300 µl per membrane chip. Post ~15 min adhesion time at RT, 2 ml/6well of EC++ medium was gently added around each membrane chip. On d9, medium was changed to EC+ for the rest of culture duration. The membrane chips were gently inverted (cell upside down) into one well of a 6 well plate containing 2 ml of EC+ medium on d9 such that the cells were in direct contact with medium. Additionally, 300 µl of medium was gently added on top of each membrane, thereby ensuring no drying. On d10 of differentiation, membrane chips were shifted to bioreactors.

10.7.2 Assembly of flow bioreactor system

Flow bioreactors, electrodes and chip membranes were sterilized, assembled and provided by Dr. Tobias Schmitz and Ms. Jihyoung Choi as previously described (Choi, Mathew et al. 2022). Briefly, the frames for holding and stabilizing the cell culture membranes were designed using SOLIDWORKS™ 3D design software and 3D printed using a biocompatible resin. The 3D-printed membrane frames were post-processed with cleaning (washing 3 x 5 min), hardening, and a final surface refinement. The membrane frames were then treated at least twice by ultra-sonification for 15 min in pure water and further incubated for ~15 min in 70% EtOH to remove any material residues. The parts were then autoclaved at 121 °C for 30 min. The membrane frame was composed of two fitting parts, allowing to sandwich the cell culture membrane without any creasing. To prepare a membrane chip for cell culture, the porous Polyethylene terephthalate (PET) membrane was positioned in between the membrane frames and glued using a thin layer of Polydimethylsiloxane (PDMS). During gluing, the sandwiched porous membrane was stretched evenly by gently pressing the membrane frames, thereby creating a cell culture area of 0.95 cm^2 *(Figure 13, A)*. The complete flow bioreactor system was composed of two medium bottles with a capacity 50 ml, silicone tubes cut to size (2x 33 cm, 4x 38 cm, 2x 3-5 cm), pump tubes, luer lock connectors (MTLS230-J1A, FTLL230-J1A), two Titanum nitride (TiN) coated tube electrodes, and the PDMS bioreactor. All the components were sterilized by autoclaving at 121 °C for 30 min prior to assembly. The frame with the

embedded cell culture membrane was sterilized by gamma sterilization prior to coating and seeding of the cells. The sterilized components were connected in a biological safety cabinet and assembling was performed as shown in *(Figure 13, B)*. The membrane chip pre-cultured with iBCECs was inserted in between the bioreactor chambers and tightened with 3D-printed reactor clamps on d10. Each chamber of the chip bioreactor was connected to individual flow regimes with a connected TiN-coated tube electrode. Each tube electrode was placed on the opposite side with the reactor in the middle. All silicone tubes were clamped tightly using screw clamps to prevent uncontrolled flow before starting the medium flow. Media bottles were filled with 25 ml of EC+ medium, each, and the whole system was moved to an in-house-adapted incubator system for dynamic culture and EIS measurements *(Figure 13, C)*. After installation, the screw clamps were removed and the peristaltic pump in the tailored incubator system was started with a flow rate of 0.3 ml/min. During the whole experiment, culture conditions in the incubator were kept constant at 37 °C and 5% CO_2. Due to a large supply, medium was not exchanged over the culture period in the bioreactor systems. Along with dynamic culture, the experiment on static culture in transwells was carried out over the same period. EC medium change was performed daily in transwells.

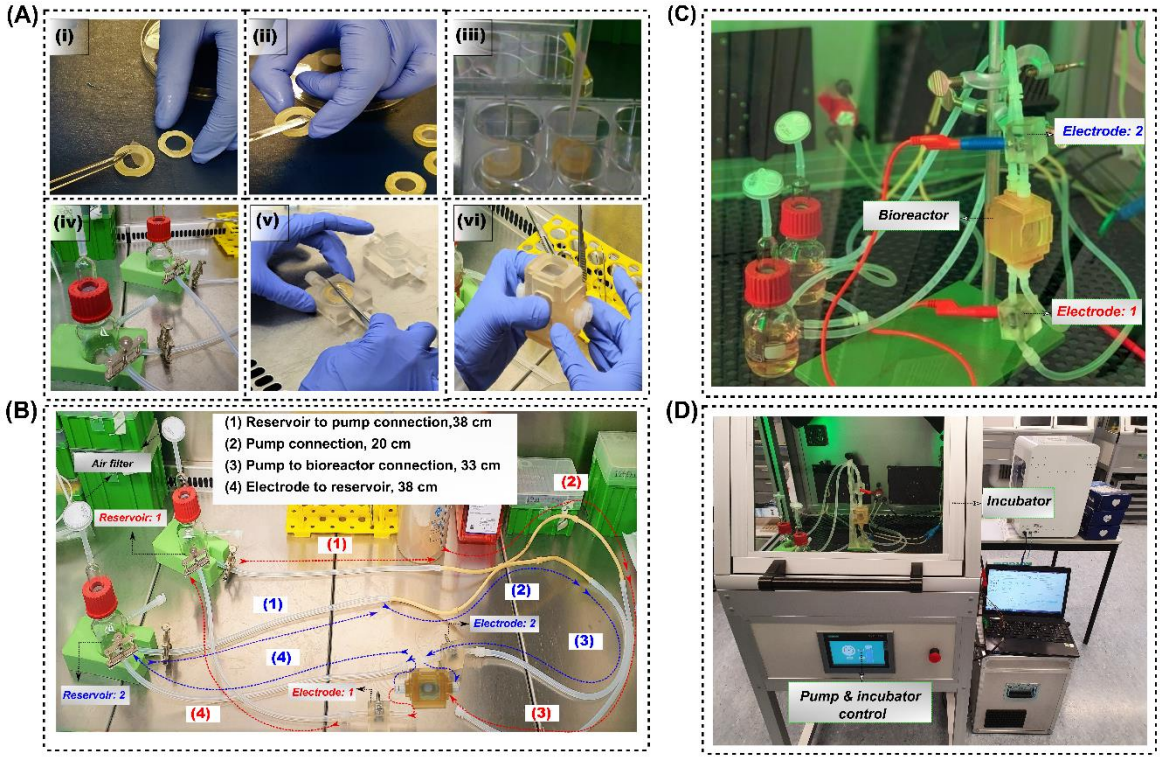

Figure 13: Schematic of chip and bioreactor assembly

Chip membranes were first prepared by coating a thin layer of polydimethylsiloxane on each side. Cell culture specific plastic was then carefully sandwitched between each side of the chip (A, i-ii). Human induced pluripotent stem cell (hiPSC) derived brain capillary endothelial cells (iBCECs) on d8 of differentiation was then seeded on

precoated chip membranes and allowed to settle down for 15 minutes before further cultivation for 24 hours (A, iii). Autoclaved bioreactors and medium reservoirs were prepared by first claming the medium exit points of the reservoir (A, iv). The chip containing a monolayer of iBCECs was then placed carefully inside the bioreactor, and the system was fastened (A, iv-vi). The entire system was connected to respective pumps (B) and shifted into an incubator system (C-D).

10.8 Tube formation assay

Tube formation assay was performed to test the functionality and vascularization capability of iBCECs. To start with, ~160 – 200 µl of pure Matrigel® was pipetted into one well of an 8-well chamber slide and allowed to solidify by incubation for 1 h at RT. Then iBCECs or control cell lines were seeded at a density of 5 x 10^4 cells/cm^2 in respective media that was additionally supplemented with 40 ng/ml VEGF. After 24 h, vascularization potential was visualized microscopically.

10.9 Barrier integrity measurements

10.9.1 2D-NaF permeability assay

On d10 of differentiation, NaF permeability assay was performed using a minimum of three iBCEC monoculture transwell models and one blank control (pre-coated transwell without cells). Post aspiration of cell culture medium, 850 µl of fresh medium (respective to d10 of differentiation) was added basolaterally. Apically, 200 µl of 10 µM NaF solution was added. The transwells were then placed onto an orbital shaker at 100 rpm for 1 h at 37ºC. Sampling was performed post incubation time, 200 µl of 10 µM NaF solution (donor sample, time = 0 min), 200 µl of transport medium/blank medium (respective to d10 of differentiation), 200 µl of basolateral medium and 150 µl of apical solution were pipetted as triplicates into a black 96-well plate for fluorescence measurements. The volumes of all samples taken from the apical side (150 µl) were adjusted to 200 µl by adding an additional 50 µl of transport medium. Measurements were performed with a fluorescence reader (TECAN Infinite® M200) with the following boundary conditions. 2 × 2 multiple measurements (circle) per well, frame 500 µm, excitation bandwidth 9 nm, emission bandwidth 20 nm, number of flashes 25, integration time 20 µs, deceleration and rest time 0 µs, excitation wavelength 490 nm, emission wavelength 525 nm, gain 57. In order to calculate PC, the measured values of the donor were first corrected by multiplying with 4/3. PC values were then calculated using (Eq.4)

10.9.2 3D-NaF permeability assay

NaF permeability assay was performed using one complete well ie., ~300 spheroids containing iBCECs and control spheroids containing only ACs and PCs. In this setup, the spheroids are considered as the basolateral compartment and the medium surrounding them is considered

the apical compartment. Cell culture medium was first gently removed from the Aggrewell containg spheroids and 1ml of 10 µM NaF solution was added very carefully, by pipetting onto the walls of the Aggrewell with minimum displacement of the spheroids. The plate was then placed into the incubator for 1 h at 37ºC. Sampling was performed post incubation time, 200 µl of 10 µM NaF solution (donor sample, time = 0 min), 200 µl of transport medium/blank medium, and 200 µl of NaF solution from the apical compartment were pipetted as triplicates into a black 96-well plate for fluorescence measurements. Measurements were then performed with a fluorescence reader (TECAN Infinite® M200) with the following boundary conditions. 2 × 2 multiple measurements (circle) per well, frame 500 µm, excitation bandwidth 9 nm, emission bandwidth 20 nm, number of flashes 25, integration time 20 µs, deceleration and rest time 0 µs, excitation wavelength 490 nm, emission wavelength 525 nm, gain 57. In order to calculate permeability, relative fluorescence unit (RFU) vaues of test conditions were first substracted from the blank values and then normalized to donor concentrations.

10.9.3 2D-TEER measurements

TEER measurements in 2D transwells was performed by using the Millicell® ERS-2 system and the measurement electrode STX01 at 12.5 Hz. Test electrode MERSSTX04 was first connected with the input connector and the system Millicell® ERS-2 was switched on with the operating switch function turned to Ω. The device is first checked for a display value of 1000 Ω, confirming correct calibration and functionality. The measurement electrode was then placed in a 50 ml falcon tube filled with 10 ml 70% EtOH for the purpose of disinfection, after 15 min the electrode was dipped in sterile water and then placed for another 15 min in 7 ml EC+ or hECSR2 medium to allow for equilibration. 40 min before TEER measurement was performed, the medium of the transwell models was changed (EC+ or hECSR2 medium respectively). The plug of the measurement electrode was then inserted into the input connector of the system. The longer end of the electrode was placed into the basolateral compartment and the shorter end into the apical compartment of each transwell insert. Each transwell was measured on three different positions of the transwell insert membrane. After the measurements were finished, the plug of the electrode was removed from the input connector and the device was shut off. Next, the electrode was dipped into sterile water and disinfected for 15 min by placing in a 50 ml falcon that was filled with with 10 ml 70% EtOH. The electrode was stored dry in a sterile 50 ml falcon enwrapped with Parafilm. The TEER value is then calculated from the resistance measured by electrode, including the cultivated area, using the following equation (Eq.7)

$$\boldsymbol{TEER}\left[\boldsymbol{\Omega} * \boldsymbol{cm^2}\right] = (\boldsymbol{Resistance_{cells}} - \boldsymbol{Resistance_{blank}}) * \boldsymbol{A} \quad (\mathbf{7})$$

Resistance cells [Ω] = measured resistance value of the endothelial cell layer,
Resistance blank [Ω] = measured resistance value of an empty insert (blank),
A [cm^2] = cell culture area

10.9.4 EIS analysis of iBCECs under static and dynamic conditions

In order to analyse barrier integrity via impedance spectroscopy, iBCECs cultivated on transwells were placed into BRAND 24 well plates® insert system, with special plate designs that allows the lid of the impedance electrodes to fit inside the transwell system. The impedance plate was designed and provided by Dr. Tobias Schmitz (*patent number: 10 2017 219 425.1*) (Schmitz, Schweinlin et al. 2018, Choi, Mathew et al. 2022). The surface of the lid electrodes is first sterilized thoroughly with 70% EtOh and air-dried under a cell culture hood. 40 minutes prior to measurement media in transwells was changed to 400 µl of EC+ in the apical compartment and 850 µl of EC+ in the basolateral compartment. EIS was performed with a potentiostat from Metrohm Autolab impedance analyzer and mathematical analysis was performed via NOVA 2.1 software as previously reported (Schmitz, Schweinlin et al. 2018). Measurements were carried out from 1Hz - 100kHz, and a sinusoidal alrternating current with amplitude of 0.05 V_{RMS} was applied. During measurement, care was taken that resting potential measurements did not exceed 0.8V. Post measurements the adapter plate with electrodes was again disinfected with 70% EtOH and air dried. The same set of parameters was applied for the EIS measurement of the dynamic system. TEER/Impedance values are further calculated using the following equation (Eq.8)

$$\boldsymbol{Z_{TEER} = (Z_{10Hz} - Z_{100kHZ}) * A} \ (\mathbf{8})$$

Z_{TEER} [Ωcm^2] = measured resistance value of the endothelial cell layer,*
Z_{10Hz} [Ω] = Impedance value specific to paracellular barrier of the models,
Z_{100kHz} [Ω] = Impedance value specific to media resistance of the model system,
A [cm^2] = cell culture area

10.9.5 EIS measurements and analysis on BBB spheroids

EIS on 3D BBB spheroids were measured using a microcavity array chip that was provided and previously reported by Dr.Heinz-Georg Jahnke from the University of Leipzig (Jahnke, Mewes et al. 2019). The microcavity array chip consisted of pyramidal cavities with an edge length of 300-400 µm and depth 100 µm thereby, allowing the spheroids to sit well within the cavity. Firstly, the array was washed with 1ml, 70% EtOH and followed by rinsing with 1ml PBS-. The arrays were then filled with 1ml pre-warmed EC+ medium and verified microscopically for the presence of bubbles. EIS was then measured and monitored using a previously developed multiplexer system and high precision impedance analyzer ISX-3 from

Sciospec Scientific Instruments, Germany (Jahnke, Braesigk et al. 2012, Poenick, Jahnke et al. 2014). Impedance spectra were recorded from 5 kHz to 5 MHz (51 points, 100 mV amplitude). EIS was first recorded for a blank cavity which did not contain any spheroid, followed by measurements of a minimum of 15 spheroids per sample condition. Raw data was then analyzed and processed with previously developed IDAT v3.6 software (Jahnke, Mewes et al. 2019). Relative impedance or extracted cell signals was calculated automatically by the software using the following equation (Eq.9).

$$\boldsymbol{Relative\ impedance}\% = \frac{|\boldsymbol{Z}|\ \boldsymbol{spheroid} - |\boldsymbol{Z}|\ \boldsymbol{blank}}{|\boldsymbol{Z}|\ \boldsymbol{blank}}\ \boldsymbol{x}\ \mathbf{100}\% \ (\mathbf{9})$$

Relative impedance% = measured final relative impedance values of 3D spheroids
$|Z|_{blank}$ [Ω] = Impedance value specific to blank cavity,
$|Z|_{spheroid}$ [Ω] = Impedance value specific to cavity with spheroids

10.10 Molecular biology techniques

10.10.1 Ribonucleic acid (RNA) sampling

Samples were collected from a minimum of 3 transwells per iBCEC monoculture, from one complete AggreWell ™ consisting of ~300 spheroids per biological replicate, and from one 90% confluent 6 well of hCMEC/D3 cells line for RNA extraction. The transwell samples were gently cut using a forcep and placed into a 1.5 ml Eppendorf tube 350 µl of lysis buffer was added into the tube and the samples were immediately frozen at -80ºC until extraction. For the spheroids, samples were collected from one complete AggreWell™ into a 15 ml falcon tube. Remaining media was removed gently using a 1000 µl pipette, 350 µl of lysis buffer was then added and the samples were passed through a 2 mm gauge needle several times in order to homogenize the spheroids, post homogenization, they were stored in 1.5ml eppis at -80ºC until extraction. For 2-D hCMEC/D3 cells, 350 µl of lysis buffer was added directly onto the cells and incubated for 5 mins before collection with 1000 µl pipette.

10.10.2 RNA extraction

RNA extraction was performed using the RNeasy® Micro Kit as per kit instructions. Briefly, 350 µl of the lysed samples were first homogenized using a QIAshredder homogenizer mini spin column. The spin column was then centrifuged for 2 min at 20,238 rcf. The column was discarded and 350 µl of 70% EtOH was added to the lysate. After resuspension, the complete lysate volume was then transferred into a RNeasy® MinElute spin column placed in a fresh 2 ml collection tube. The spin column was then centrifuged. Unless otherwise stated, all samples were centrifuged for 15 s at at 20,238 rcf. The flow-through was discarded and 350 µl of wash buffer, RW1 was added to the column. The columns were then centrifuged and the flow-through was discarded. A mixture of 10 µl Deoxyribonuclease I stock solution and 70 µl

of digestion buffer, RDD was added to each RNeasy® MinElute spin column membrane. After 15 min incubation at RT, 350 µl of wash buffer, RW1 was added in order to wash the membrane. After centrifugation, the collection tube with the flow-through was discarded and the spin column was placed into a fresh 2 ml collection tube, followed by the addition of 500 µl of mild washing buffer, RPE. The columns were centrifuged again and the flow-through was discarded. Next, 500 µl of 80% EtOH was added into each column and centrifuged. The collection tube was discarded, and flow through was placed into a fresh 2 ml collection tube, the samples were then centrifuged for 5 min with an open lid in order to dry the membrane. The RNeasy® MinElute spin column was then placed in a 1.5 ml eppendorf tube and after adding 20 µl of RNase-free water and 1 min of centrifugation at full speed. Yielded RNA was immediately placed on ice. The quantity and purity of the RNA in each sample was measured with a fluorescence reader (TECAN Infinite® M200). For measurements, 1 µl of the sample was used after blanking with the same volume of RNase-free water. Only RNA which fulfilled the puritiy ratio (A260/A280), within the range of 1.8 and 2 was used for downstream applications.

10.10.3 Complementary Deoxyribonueclic acid (cDNA) synthesis

cDNA synthesis was carried out using the High-Capacity cDNA Reverse Transcription Kit from Applied Biosystems™.To carry out chip-based quantitative real-time polymerase chain reaction (qPCR) analysis, a minimum amount of 250 ng/ µl RNAwas used. It was assumed that 1µg of cDNA was obtained from 1 µg of RNA, therefore, the corresponding sample amount was calculated from isolated RNA concentrations and transferred to a 0.5 ml Eppendorf. As per the kit instructions, a total volume of 20 µl of cDNA was synthesized. Component mixtures are specified in *(Table 17)* and details of thermal cycler run is specified in *(Table 18)*. Generated cDNA was then stored at -15 to - 25°C until analysis.

Table 17: Mixture components for cDNA synthesis

Component	Volume (µl)
10x reverse transription buffer	2,0
25x DeoxyriboNucleotide TriPhosphate mix (100mM)	0,8
10x reverse transription random primers	2,0
MultiScribe ™ Reverse Transcriptase	1,0
RNase Inhibitor	1,0
Nuclease free water	x
250ng/ul RNA sample	x
Total volume per reaction	20

Table 18: Run settings for cDNA synthesis

Step	Temperature(ºC)	Time(min)	Cycle

Priming	25	10	1x
Reverse transcription	37	120	1x
Inactivation	85	5	1x
Hold	4	∞	1x

10.10.4 High-throughput multiplex qPCR of relevant BBB transcripts

For high-throughput multiplex qPCR of relevant BBB transcripts, 250 ng RNA per sample was transcriBed into a final volume of 20 µl cDNA. For pre-amplification of the samples Qiagen Mastermix and HotStar PlusTaq Polymerase combined with the tenfold concentration of gene targeting primers was used (Mineta, Yamamoto et al. 2011). High-throughput qPCR was performed by Dr. Winfried Neuhaus from the Austrian Institute of Technology GmbH, Center Health and Bioresources, Competence Unit Molecular Diagnostics, Vienna, Austria. The Biomark™System (Fluidigm™) including an IFC Controller HX and 96.96 Dynamic Arrays™IFC with the run settings described in *(Table 19)* was used for multiplexing.

Table 19: Run settings used for high-throughput qPCR

Step	Temperature(ºC)	Time	Cycle
Initial activation	95	15(min)	1
Denaturation	95	40(s)	18
Annealing	60	40(s)	18
Annealing	80	40(s)	18
Annealing	72	40(s)	18
Final extention	72	7 (min)	1

10.11 Tissue staining techniques

10.11.1 Fixation, paraffin embedding and staining

For standard tissue slice stainings, a minimum of 20 - 30 spheroids were first collected in a 15 ml falcon tube and washed 3 times with PBS-. They were then fixed with 1ml of 4% Roti®-Histofix at RT for 15 mins. Fixed spheroids were washed once with PBS- and embedded directly. To begin with, spheroids were carefully placed down onto a clean microscopy glass slide, excess mount of PBS- was removed gently using a 10 µl pipette. 50 µl of molten Richard-Allan Scientific HistoGel™ was then pipetted on top of the spheroids very gently, such that they all elevated and located at the same horizonzal plane. Once the gel solidified an additional 100 µl of molten Richard-Allan Scientific HistoGel™ Histogel was added on top. Post gel solidification, the whole construct was fixed again with 1 ml of 4% Roti®-Histofix at RT for 15 mins. The gel plus spheroid construct was placed directly into an embedding cassette that included a filter paper. The closed cassette was placed into the embedding machine, and the paraffin embedding protocol as described in *(Table 20)* was performed. After embedding the samples were removed from the plastic cassette and placed onto a metal sample holder. The

holder was filled with fresh molten paraffin in order to prepare a block that can be cut by aid of a microtome. 5 µm thick sections of the samples were prepared and collected onto a PLL coated microscopy slide and left in an oven at 37 °C overnight for drying. For analysis of different tissue structures, Hematoxylin and Eosin staining (H&E) *(Table 21)* or paraffin immunohistochemistry *(Table 22)* was performed.

Table 20: Steps followed in tissue paraffin embedding

Step	Solution	Duration (h)
Washing	Deionized H_2O	1
Dehydration	Ethanol 50%	1
(ascending alcohol series)	Ethanol 70%	1
	Ethanol 80%	1
	Ethanol 96%	1
	Isopropanol 1	1
	Isopropanol 2	1
	1:2 Isopropanol-Xylene mixture	1
Removal of alcohol	Xylene 1	1
	Xylene 2	1
Paraffin embedding	Paraffin 1	1.5
	Paraffin 2	1.5

Table 21: Steps followed in H&E staining

Step	Solution	Incubation time
Deparaffinization and Rehydration	Xylene 1	30s
	Xylene 2	30s
	Ethanol 96%	1 dip
	Ethanol 96%	1 dip
	Ethanol 70%	1dip
	Ethanol 50%	1 dip
	Deionized H_2O	1dip
Staining of cell nuclie	Heamatoxylin	6 min
Washing	Deionized H_2O	4 dips (till color runs out)
Staining of cytoplasm and ECM	Eosin	6 min
Washing	Deionized H_2O	4 dips (till color runs out)
Draining	Ethanol 70%	1 dip
	Ethanol 96%	1 dip
	Isopropanol 1	30s
	Isopropanol 2	30s
	Xylene 1	30s
	Xylene 2	30s
Embedding	Rapid mounting medium Entellan™	Overnight, RT

Table 22: Steps followed in paraffin immunohistochemistry

Step	Solution	Incubation time
Deparaffinization and Rehydration	Xylene 1	30s
	Xylene 2	30s
	Ethanol 96%	1 dip
	Ethanol 96%	1 dip
	Ethanol 70%	1dip
	Ethanol 50%	1 dip
	Deionized H_2O	1dip
Heat-mediated antigen retrieval	Boiling in 10x Citrate buffer (pH 6)	8 min
Marking with hydrophobic PAP pen	-	-
Washing	PBS- + 0.5% Tween-20	1 dip
Blocking	Blocking buffer (2D)	20 min
1º Antibody	1º Antibody in anitbody dilution solution	Overnight,4ºC
Washing	PBS- + 0.5% Tween-20	3x, 5 mins each
2º Antibody	2º Antibody in anitbody dilution solution	2 h,RT
Washing	PBS- + 0.5% Tween-20	3x, 5 mins each
Embedding	Mounting medium Fluoremount-G™+ DAPI	Overnight, RT

10.11.2 2D immunofluoresence staining

Immunofluoresence stainings were used to analyse the expression of relevant proteins in 2D using fluorochrome-labelled antibodies. Firstly, iBCECs cultivated on transwells were rinsed with 300 µl PBS- and then fixed with 300 µl 4% Roti®-Histofix at RT for 15 mins. Post fixation, the cells were washed once with 500 µl PBS- and stored in PBS- at 4 °C for a maximum of 2 days until staining was performed as detailed in *(Table 23)*. Stained cells were visualized within 3 days using a Keyence fluorescence microscope or Confocal SP8 microscope.

Table 23: Steps followed in 2D immunofluoresence staining

Step	Solution	Incubation time
Permeabilization	Permeabilization buffer (2D)	5 min
Washing	PBS- + 0.5% Tween-20	3x, 5 mins each
Blocking	Blocking buffer (2D)	20min
1º Antibody	1º Antibody in Antibody dilution solution	Overnight, 4ºC
Washing	PBS- + 0.5% Tween-20	3x, 5 mins each
2º Antibody	2º Antibody in Antibody dilution solution	2 h, RT
Washing	PBS- + 0.5% Tween-20	3x, 5 mins each
Embedding	Mounting medium Fluoremount-G™+ DAPI	Overnight

10.11.3 3D whole mount immunofluoresence staining

Immunofluoresence stainings were used to analyse the expression of relevant proteins in 3D using fluorochrome-labelled antibodies. A mimum of ~20-30 spheroids per sample were first collected into a 15 ml falcon and rinsed once with PBS-. The spheroids were then fixed with 500 µl ice cold Methanol: Acetone (1:1) for 5 min at RT or 500 µl 4% Roti®-Histofix at RT for 15 mins 30 mins depending on the Antibody used. Post fixation, the cells were washed once with 500 µl PBS- and stored in PBS- at 4 °C for a maximum of 2 days until staining was performed *(Table 24)*. Stained spheroids were embedded into 96 well glass bottom plates and visualized using a Confocal SP8 microscope.

Table 24: Steps followed in 3D whole mount immunofluoresence staining

Step	Solution	Incubation time
Permeabilization	Permeabilization buffer (3D)	30 min
Washing (3x)	PBS-	3x, 5 mins each
Blocking	Blocking buffer (3D)	30 min
1º AB	1º Antibody in Antibody dilution solution	Overnight, 4ºC
Washing (3x)	PBS-	3x, 5 mins each
2º AB + Nuclear staining	2º Antibody+ SYTOX™ red nuclear stain in Antibody dilution solution	Overnight, 4ºC
Washing (3x)	PBS-	3x, 5 mins each
Embedding	Mounting medium Fluoremount-G™	Overnight

10.12 Microscopy

Histological samples stained with H&E or with furochromes were visualized using the inverse fluorescence microscope BZ-9000 (Keyence) or the confocal microscope TCS SP8 (Leica Microsystems).

10.13 ImageJ quantifications

10.13.1 Quantifications of immunohistological images using ImageJ

With regard to quantifications regarding effects of shear stress on iBCECs, a minimum of 3 captured 40x IF images were quantified per sample using the ImageJ software. All images were first overlayed with grid on GIMP with the following dimentions 150 μm^2 x 150 μm^2. Within this grid area, the following parameters were measured (1) total number of cells, measured by nuclie count (2) total number of cells with intact cell border staining (3) area of cellular nuclie

and (4) area of cell (specific to ZO-1) staining pattern. Firstly, the set scale dialog was used to define the spatial scale of an active image, such that the measurement results can be presented in calibrated units of µm, depending on the original scale of the captured image. The straight-line selection tool was then used to draw a line across the scale bar; this was done in order to make a line selection that corresponds to a known distance. Then the option *Analyze* > *Set Scale* was selected. Once the Set Scale window opens, the distance measured in pixels is automatically displayed and the known distance for example, 50 µm is entered as a unit of length. The *freehand selections tool* was then used to trace respective nuclie and cellular borders. With the aid of the *ROI (Region of Interest) Manager* each selection from different locations on an image are combined into a repository and stored as*.csv* files. Values from the repository were then copied into Excel for further analysis.

10.13.2 Quantifications of spheroid size using ImageJ

A minimum of 3 phase contrast images were captured with the 10x objective and dimensions per sample were determined using the ImageJ software. Firstly, the set scale dialog was used to define the spatial scale of an active image, such that the measurement results can be presented in calibrated units of µm, depending on the original scale of the captured image. The straight-line selection tool was then used to draw a line across the scale bar; this was done in order to make a line selection that corresponds to a known distance. Then the option *Analyze* > *Set Scale* was selected. Once the Set Scale window opens, the distance measured in pixels is automatically displayed and the known distance for example, 100 µm is entered as a unit of length. The *line selection tool* was then used to trace the width and height of each spheroid. The average of the width and height was taken to be the diameter of each spheroid.

10.13.3 Quantification of freeze fracture micrographs

A minimum of 100 Spheroids or 3 transwells per condition were first washed with 1 ml PBS+. Following this 1 ml of 2.5% glutaraldehyde solution was added to the samples as a fixative for 2h at RT. The samples were washed once again with PBS+ and stored in 0.025% glutaraldehyde at RT until sample processing. All further steps of processing and preparation of ultrathin sections and imaging and were performed by Dr. Jörg Piontek from the Charité Universitätsmedizin Berlin, Clinical Physiology & Nutritional Medicine, Department of Gastroenterology, Rheumatology & Infectious Diseases, Berlin, Germany. For analysis, FFEM images captured at 50000x were quantified for TJ complexity. FFEM images were overlaid with full image grids of size 1.9 μm^2 x 1.9 μm^2 with horizontal and vertical lines of 100 nm. TJs were redrawn using a red pencil tool for easier identification. Quantifications were carried out using the multipoint tool in ImajeJ for a minimum of 3 images per sample set, and the following parameters were accounted for. TJ stand abundance was calculated as the sum of horizonal (HSI) and vertical intersections (VSI) of strands and lines. Strand density in a mesh of strands

was calculated by dividing the stand abundance by the mesh area. Strand abundance was calculated as the product of the number of strand-containing grid boxes and the box area of 0,01 µm². Mesh elongation was calculated as HIS/VSI.

10.14 Statistical analysis

Unless otherwise stated all data are presented as mean ± standard deviations (SD). Statistical analysis and determination of significances were done by one-way or two-way ANOVA with appropriate multiple comparisons using the GraphPad Prism 9 software. For transcroptomic analysis, statistics was performed using standard Excel functions and student's t-tests using normalized Ct values. Significant values are represented with * with the following implications $p \leq 0.0001$ =****, $p \leq 0.001$=***, $p \leq 0.01$=**, $p \leq 0.05$=* and $p > 0.05$=not significant (ns).

11. SUMMARY OF FINDINGS

11.1 Comparison of iBCECs differentiated via co- and directed differentiation

Over the past decade, hiPSC technology has enabled the generation of iBCECs via various differentiation strategies. These iBCECs display several key BBB characteristics such as proper organizations of TJ, expression of BBB transporters and effective barrier integrity with drug permeabilities co-relating *in-vivo* measurements. (Lippmann, Al-Ahmad et al. 2014, Appelt-Menzel, Cubukova et al. 2017, Qian, Maguire et al. 2017). In order to benchmark and validate iBCECs, identification of optimal differentiation strategy for further use in the development of new BBB models was carried out. Characterization critera included identification of morphological changes and tissue specific protein expression, specifically for endothelial markers such as PECAM-1, epithelial marker E-Cadherin and junctional proteins (claudin-5 and occludin). BBB specific gene expression profiling was conducted using a microarray. Barrier integrity of iBCECs was further monitored with TEER measurements and determination of permeability co-efficient of NaF. Additionaly, endothelial tube formation capability of iBCECs in the presence of angiogenic stimuli was investigated in order to determine functionality. All characterizations were performed on two different hiPSC lines in order to account for line specific differentiation capabilities.

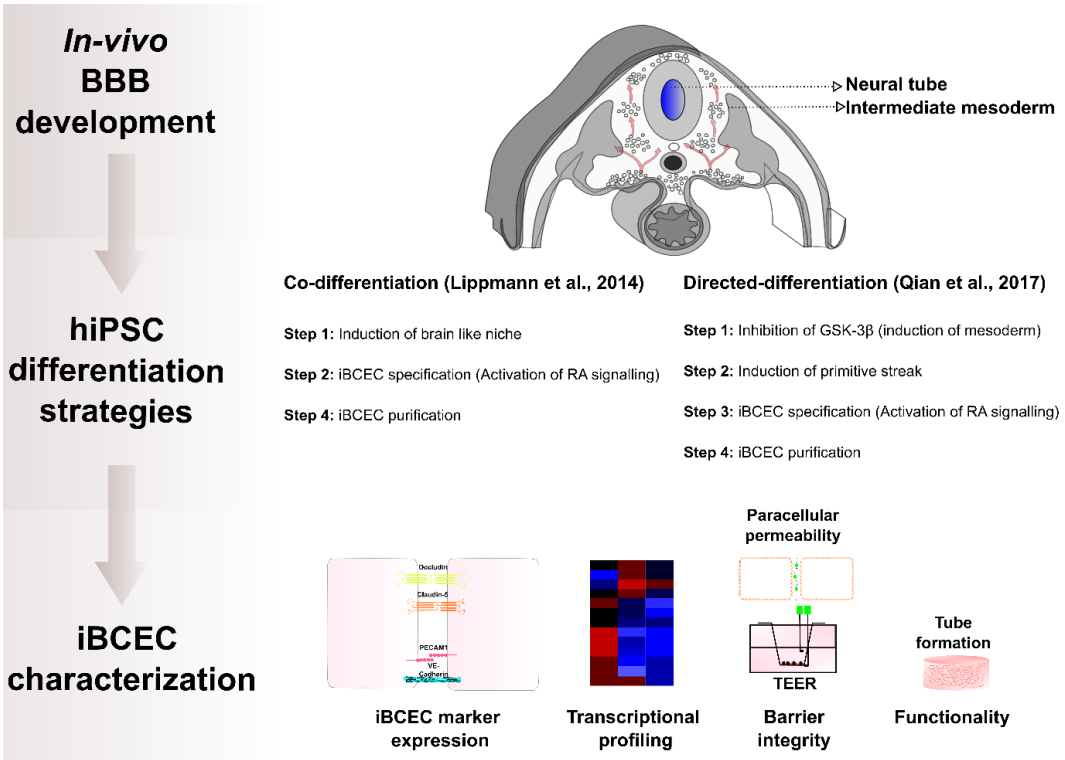

Figure 14: Schematic of differentiation strategies employed and characterization criteria

In order to benchmark and validate current hiPSC differentiation protocols, two different strategies were employed on two hiPSC lines. Co-differentiation exercises the induction of a brain like niche, followed by activation of retinoic acid (RA) signaling leading to brain capillary endothelial cell (BCEC) specification and finally an extracellular matrix (ECM) based purification step to obtain hiPSC derived BCECs (iBCECs). The directed-differentiation strategy is based on the canonical Wingless-related integration site (Wnt) pathway, where the inhibition of glycogen synthase kinase -3 beta (GSK-3β) enables the induction of mesoderm, followed by the primitive streak. iBCECs are further specified via activation of RA signaling. As a last step, purification of iBCECs are performed by subcultivation onto defined ECM. For characterization, the presence of hallmark BCEC markers were investigated via immunofluorescence and transcriptional profiling. Additionally, barrier integrity was verified via TEER and paracellular permeability measurements. Endothelial functionality was further investigated via tube formation assays.

11.1.1 Morphological changes and tissue-specific protein expression in hiPSC derived IBCECs

Two different hiPSC lines namely IMR90-4 and SBAD-02-01 were differentiated via two previously established strategies, namely co-differentiation (CD) (Lippmann, Al-Ahmad et al. 2014) and directed differentiation (DD) (Qian, Maguire et al. 2017). Observations from phase contrast images showed different morphological changes of hiPSCs throughout the differentiation period, thus indicating different cellular stages. Upto d6 of differentiation, hiPSC colonies became significantly large and completely covered the well plate with no major changes observed morphologically for both strategies *(Figure 15 A, B, i and iv)*. Within CD at d8, the formation of compact clusters exposing iBCECs were observed. The exposed cells demonstrated endothelial cobblestone like morphology *(Figure 15 A, ii and v)*. However, in DD at d8, no such compact structures were visible *(Figure 15 B, ii and v)*. On the final day of differentiation d10, CD resulted in iBCECs with highly dense populations of cells showing compacted hexagonal morphology (*Figure 15 A, iii and vi).* Furthermore, iBCECs obtained from DD showed rather elongated cellular morphologies in comparison to CD *(Figure 15 B, iii and vi)*. The expression of key BCEC proteins were further investigated and compared between the two strategies via immunofluorescence staining. Endothelial specific expression of PECAM-1 was negative in iBCECs derived from both strategies for both hiPSC lines *(Figure 16 A, i-ii and B, i-ii)*. Sparce populations of iBCECs derived via DD showed positive expression of epithelial marker E-Cadherin in both hiPSC lines *(Figure 16 B, iii-iv)*, while iBCECs derived via CD showed profound expression of E-Cadherin in cells derived from the SBAD-02-01 hiPSC line in comparison to those derived from the IMR90-4 hiPSC line *(Figure 16 A, iii-iv)*. The expression of the TJ proteins, claudin-5 *(Figure 16 A, v -vi)* and occludin *(Figure 16 A, vii-viii)* was verified at cellular borders in iBCECs derived via CD similar to previous reports (Lippmann, Al-Ahmad et al. 2014) *(Figure 16 A, v-vii)*. DD only demonstrated unspecic claudin-5 expression *(Figure 16 B, v-vi)* in iBCECs derived from the IMR90-4 hiPSC line while no cell

border specific expressions were observed in iBCECs derived with the SBAD-02-01 hiPSC line *(Figure 16 B, v-vi)*. Apart from that TJ occludin was hardly expressed in iBCECs derived via DD in both hiPSC lines *(Figure 16 B, vii-viii)*.

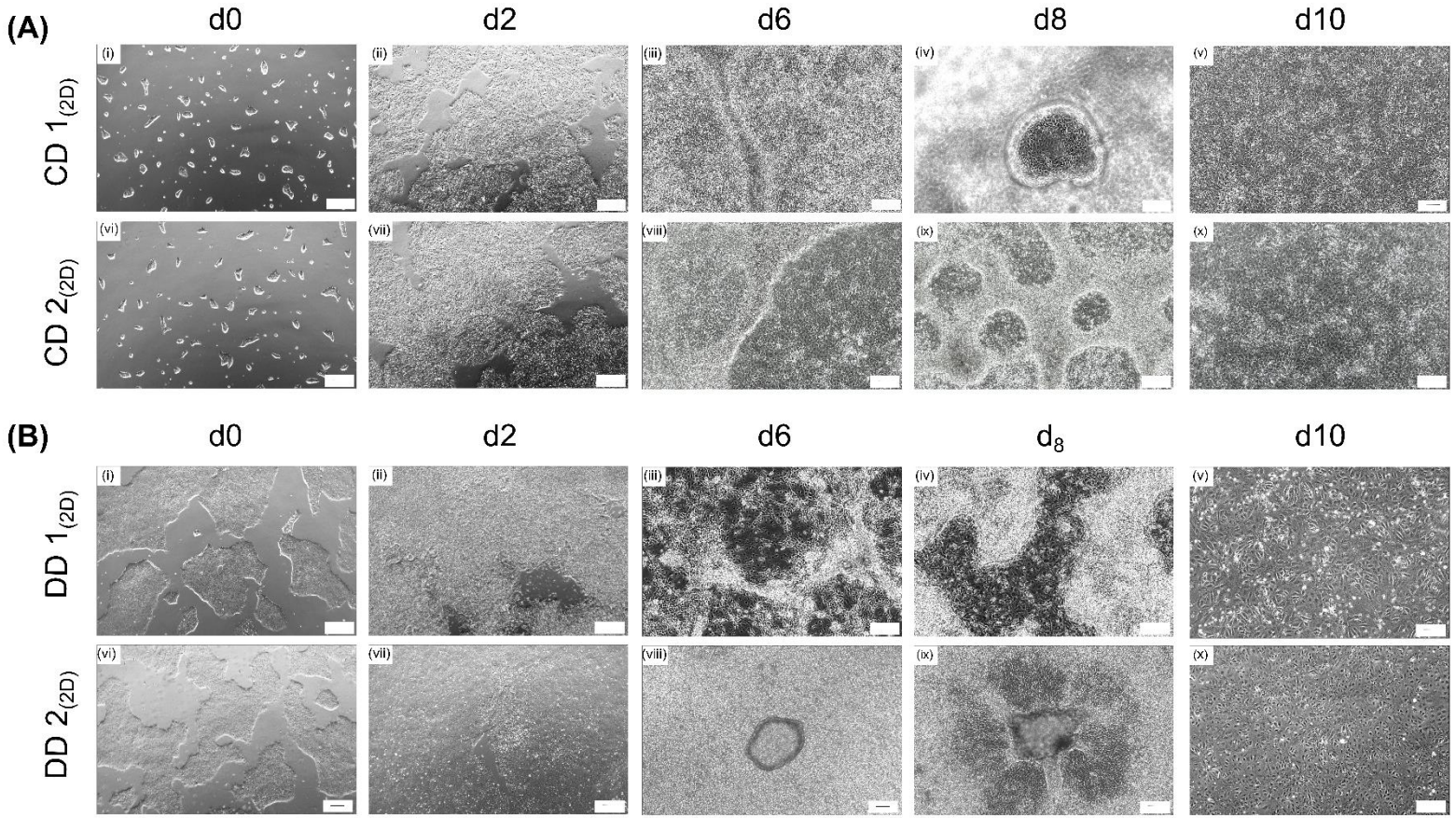

Figure 15: Morphological changes associated with the differentiation of hiPSCs into iBCECs

Phase contrast images demonstrate morphological changes of human induced pluripotent stem cell (hiPSCs) during ten days of differentiation into brain capillary endothelial cells (BCECs). During co-differentiation (CD) (A, i, vi) hiPSCs became significantly larger from d0 to d6, demonstrating complete merging of colonies resulting in confluent cultures. On d8 iBCECs were visible as clusters of cells with endothelial cobble stone like morphology (A, ii, v). They are then purified by ECM based selection at d8 resulting in highly compacted and dense cellular layers and are used for further 2D experiments on d10. Regarding directed differentiation (DD), from d0 to d6 similar to CD, hiPSCs complete merge resulting in

confluent and dense cultures. On d8 iBCECs do not demonstrate clusters of cells with endothelial cobblestone morphology, but rather show a very densed and packed layer of cells. iBCECs are then plated onto Matrigel™ at d8, further resulting in cells with more elongated cellular morphologies. These differentiatied cells were then used for further 2D and 3D experiments on d10. Images were captured using the EVOS microscope at 10x magnification. Scale bars=100 µm.

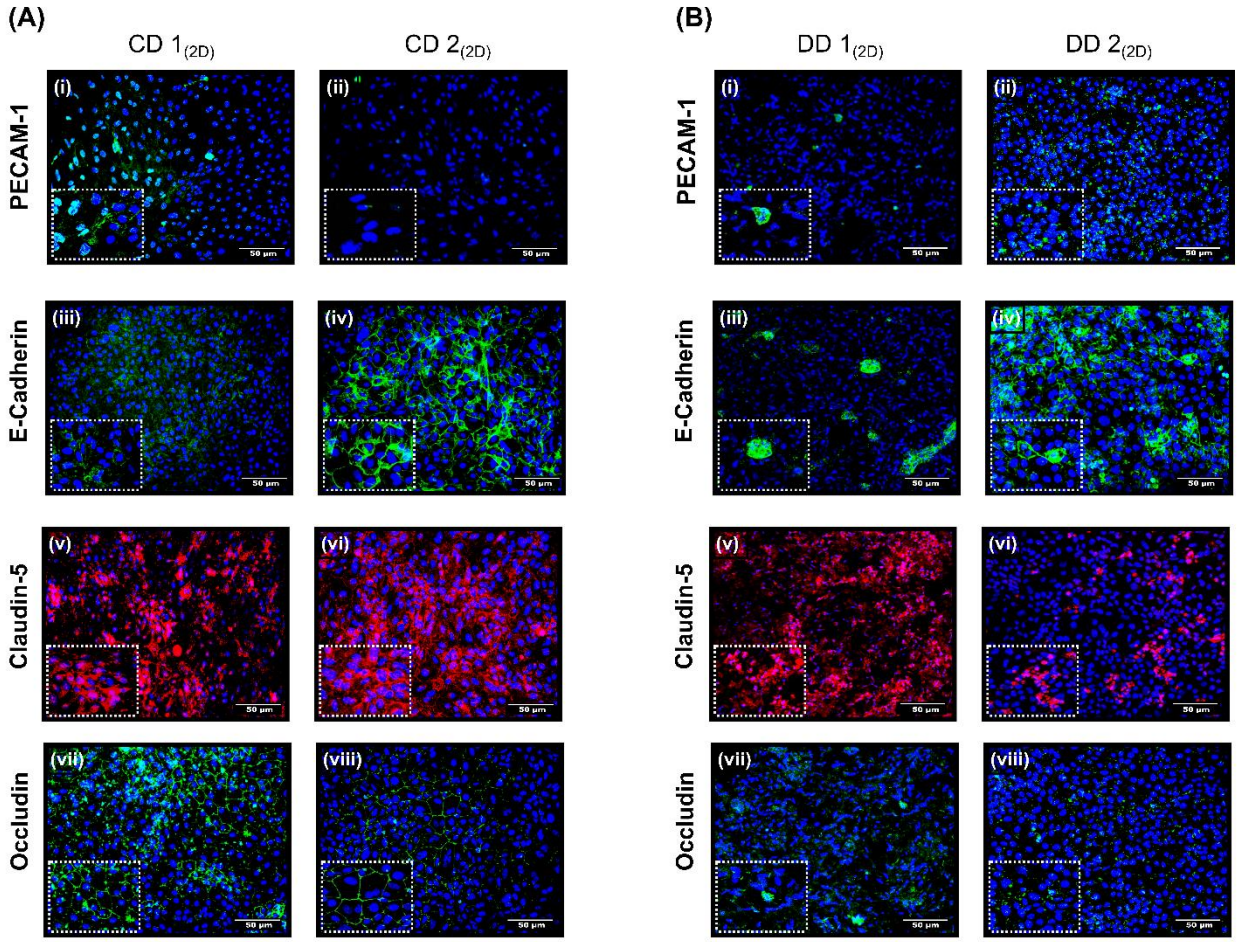

Figure 16: Protein expression patterns of hallmark endothelial, epithelial and TJ markers in iBCECs

Human induced pluripotent stem cell (hiPSC) derived brain capillary endothelial cells (iBCECs) were investigated for the expresson of key endothelial, epithelial and tight junction markers on d10 of differentiation. No positive expression of endothelial specific marker platelet endothelial cell adhesion molecule-1 (PECAM-1) was observed in iBCECs derived from both differentiation strategies (A, i-ii and B i-ii). iBCECs derived via diected differentiation (DD) showed positive expression of Epithelial-Cadherin (E-Cadherin) in sparce cell populations in both hiPSC lines (B, iii-iv) while iBCECs derived via CD showed profound expression of E-Cadherin in CD $2_{(2D)}$ in comparison to CD $1_{(2D)}$ (A, iii-iv). The expression of the tight junction (TJ) proteins, claudin-5 and occludin was verified at cellular borders in iBCECs derived via CD (A, v-vii*)*. DD demonstrated unspecific claudin-5 expression (B, v-vi) in DD $1_{(2D)}$ with no specifc expression in DD $2_{(2D)}$ (B, v-vi). Additionally, occludin was hardly expressed in iBCECs derived via DD using both hiPSC lines (B, vii-viii). Images were captured using the Keyence microscope at 20x magnification. Nuclei are labelled with DAPI. Scale Bar = 50 µm

.

11.1.2 Gene expression profile of iBCECs

A high-throughput multiplex qRT-PCR chip was used to analyse possible differences in gene expression of iBCECs from both differentiation strategies. iBCECs derived via CD and DD using both hiPSC lines, were compared against human immortalized line hCMEC/D3. Values of relative mean Log_2 fold changes of the analyzed BBB targets including transporters, claudin subtypes, TJ, and other BBB targets are presented as a heat map *(Figure 17, A)*. Significantly regulated transcripts with p values ≤ 0.05 are represented in *(Figure 17 D-G)*. CD $1_{(2D)}$ resulted in 39 downregulations out of which 12 were significant and 29 upregulations out of which four were significant. CD $2_{(2D)}$ resulted in 30 downregulations out of which 15 were significant and 30 upregulations, out of which none were significant. DD $1_{(2D)}$ resulted in 34 downregulations out of which 20 were significant and 37 upregulations, out of which 8 were significant. DD $2_{(2D)}$ resulted in a total of 38 downregulations out of which 21 were significant and with 22 upregulations out of which one was significant. iBCECs generated from CD showed common downregulations in 28 transcripts, while 25 transcripts were commonly upregulated in iBCECs derived from both hiPSC lines, while with the DD protocol 27 genes were commonly downregulated and 22 were commonly upregulated *(Figure 17, B-C)*. Amongst these common transcript regulations, iBCECs derived via CD resulted in 78% of transporters and 72% of claudins being downregulated. While DD resulted in 35% of transporters and 50% of claudins being downregulated. Regarding upregulations, CD resulted in 21% of transporters and 27% of claudins being upregulated, while DD resulted in 14% of transporters and 16% of claudins being upregulated. Importantly, compared to the human BBB cell line hCMEC/D3 iBCECs derived via CD showed significant downregulations in transporter *ABCB1* (CD $1_{(2D}$ (Log_2 (FC) = -4.52 ± 2.79, p = 0.002), CD $2_{(2D)}$ (Log_2 (FC) = -5.15 ± 1.903, p ≤ 0.0001)). Junctional genes such as *CLDN5* was downregulated in CD $2_{(2D)}$ (Log_2 (FC) = -2.75 ± 2.23, p = 0.0133). *CDH5* was downregulated in iBCECs derived from both cell lines (CD $1_{(2D)}$ (Log_2 (FC) = -4.03 ± 2.63, p = 0.0002), CD $2_{(2D)}$ (Log_2 (FC) = -6.05 ± 2.87, p ≤ 0.0001)). *PECAM1* was similarly downregulated (CD $1_{(2D)}$ (Log_2 (FC) = -7.67 ± 1.5, p ≤ 0.0001), CD $2_{(2D)}$ (Log_2 (FC) = -6.05 ± 2.87, p ≤ 0.0001)), *(Figure 17, D-E)*.

Several transporters were significantly downregulated in iBCECs derived via DD in comparison to CD. *ABCB1* (DD $1_{(2D)}$ (Log_2 (FC) = -4.97 ± 1.98, p ≤ 0.0001), DD $2_{(2D)}$ (Log_2 (FC) = -6.56 ± 3.41, p ≤ 0.0001)), *ABCC3* (DD $1_{(2D)}$ (Log_2(FC) = -4.50 ± 0.26, p ≤ 0.0001) and *SLC7A1* (DD $1_{(2D)}$ (Log_2 (FC) = -2.05 ± 1.87, p = 0.040), DD $2_{(2D)}$ (Log_2(FC) = -3.833 ± 3.303, p = 0.002)) were downregulated. Additionally, *CLDN5* was significantly downregulated in iBCECs derived from both hiPSC lines (DD $1_{(2D)}$ (Log_2 (FC) = -2.58 ± 0.73, p = 0.00037), DD $2_{(2D)}$ (Log_2 (FC) = -2.62 ± 1.03, p = 0.00073). *CDH5* was downregulated in DD $1_{(2D)}$ (Log_2 (FC) = -2.17 ± 1.20, p

= 0.005). *PECAM1* was downregulated in DD $1_{(2D)}$ (Log_2 (FC) = -3.91 ± 2.48, p = 0.001) and in DD $2_{(2D)}$ (Log_2 (FC) = -3.26 ± 2.46, p = 0.001), *(Figure 17, F-G)*. With regard to upregulations CD $1_{(2D)}$ demonstrated significant upregulations in genes encoding for *SLC16A2* (Log_2 (FC) = 2.45 ± 0.67, p = 0.027), *APOE* (Log_2 (FC) = 2.17 ± 0.31, p = 0.0027), *RARTVA* (Log_2 (FC) = 6.97 ± 1.01, p = 0.0498) and *CDH1* (Log_2 (FC) = 13.01 ± 0.25, p ≤ 0.0001). *(Figure 17 D).* DD $1_{(2D)}$ demonstrated significant upregulations in genes encoding for transporters such as *ABCG2* (Log_2 (FC) = 1.92 ± 0.15, p = 0.00098), *SLC16A2* ((Log_2 (FC) = 4.94 ± 0.031, p ≤ 0.0001). *JAM1* ((Log_2 (FC) = 1.30 ± 0.67, p = 0.029), *FN1* ((Log_2 (FC) = 2.73 ± 0.36, p = 0.007), *APOE* ((Log_2 (FC) = 4.53 ± 0.68, p = 0.02845)*, LRP1* ((Log_2 (FC) = 1.34 ± 0.40, p =0.0245), *RARVTVA* ((Log_2 (FC) = 7.79 ± 0.49, p = 0.01131) and *CDH1* ((Log_2 (FC) = 12.77 ± 0.08, p ≤ 0.0001) were also upregulated. DD $2_{(2D)}$ only demonstrated significant upregulations in *CLDN10* ((Log_2 (FC) = 7.80 ± 0.76, p = 0.01887), *(Figure 17, F-G)*.

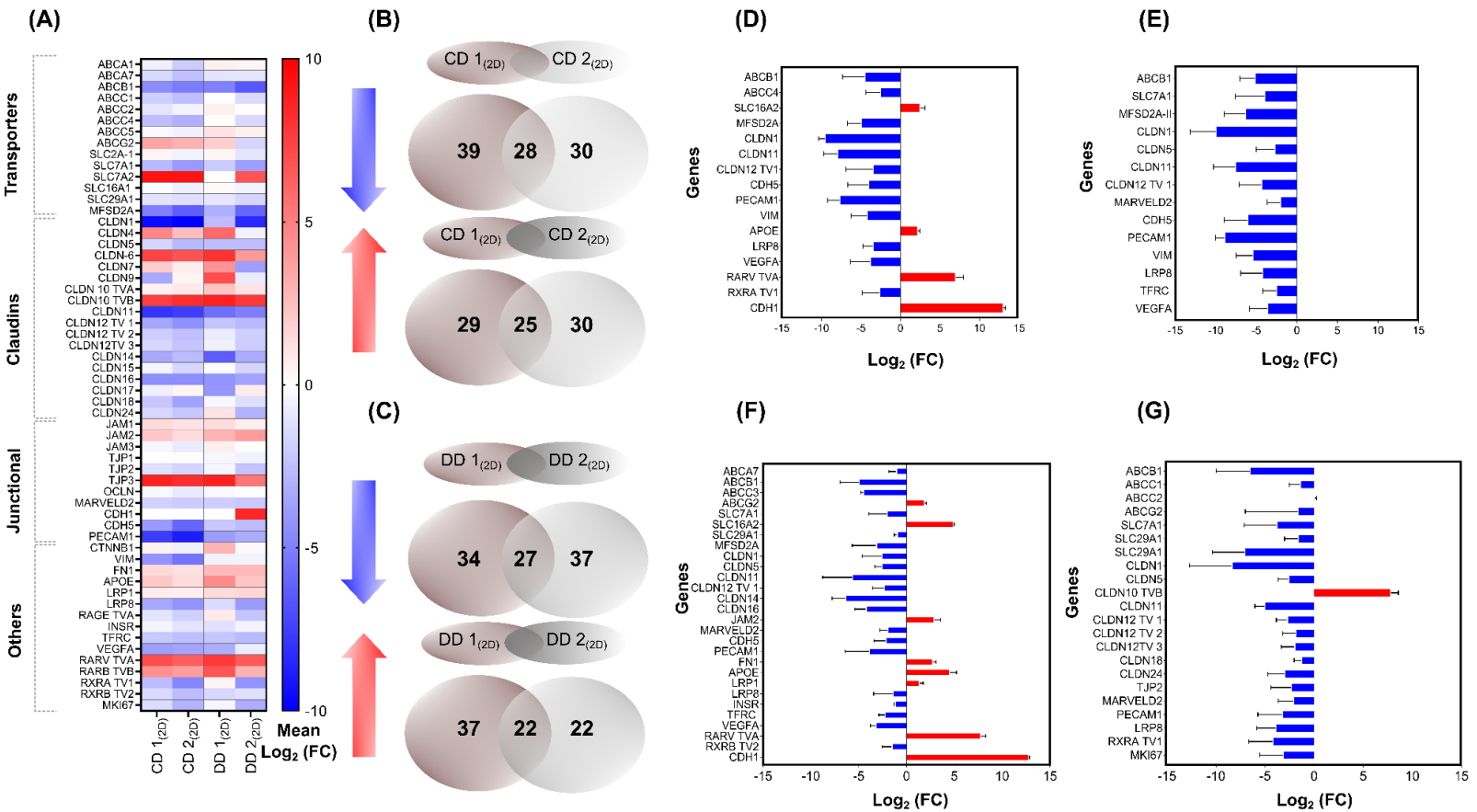

Figure 17: Transcriptomic comparison of iBCECs

Relative gene expression of characteristic blood-brain barrier transcripts obtained via high-throughput multiplex qRT-PCR was analyzed using the $2^{-\Delta\Delta Ct}$ method with hCMEC/D3 cells as a reference. Mean Log_2 (fold change (FC)) values indicating differentiation specific effects on iBCECs for the corresponding hiPSC lines is presented as a heat map (A). Venn diagrams represent the total number of regulations and overlapping transcripts for each differentiation (B-C). Significantly regulated transcripts in CD $1_{(2D)}$ (D), CD $2_{(2D)}$ (E), DD $1_{(2D)}$ (F) and DD $2_{(2D)}$ (G) in comparison to hCMEC/D3 are presented as Mean Log_2 (FC) ± SD in terms of bar graphs. Statistical significances were determined by paired two tailed t-Test and p values ≤ 0.05 were considered as significant. Analysis was performed for n=3 independent differentiations (exception n=2 for DD $1_{(2D)}$).

11.1.3 Barrier integrity and functionality of iBCECs

To determine the barrier integrity and functionality of iBCECs derived from both differentiation strategies, parameters such as TEER, small molecule tracer permeability and tube formation capabilities were investigated. iBCECs derived via CD presented with the highest TEER in comparison to those derived via DD. CD $1_{(2D)}$ presented a mean TEER of 2677 ± 85.44 Ω*cm^2 while CD $2_{(2D)}$ presented a mean TEER of 2106 ± 440.131 Ω*cm², showing significant differences between iBCECs derived from the different hiPSC lines. DD $1_{(2D)}$ presented a mean TEER of 284 ± 263.206 Ω*cm², while DD $2_{(2D)}$ presented a mean TEER of 429 ± 257.36 Ω*cm^2 *(Figure 18 A)*. With both hiPSC lines, the lowest TEER values were obtained at d10 of DD. To correspond with obtained TEER values, small molecule permeability of iBCECs were verified via PC calculations to small molecule tracer Sodium Fluorescein (NaF). In correlation with measured TEER values, iBCECs derived from DD yielded the highest PC values, demonstrating the lowest barrier integrity. PC values ranged from 5.2 ± 0.22 µm/min for DD $1_{(2D)}$ and from 6.1 ± 1.29 µm/min for DD $2_{(2D)}$ in comparison to CD where values ranged from 0.44 ± 0.21 µm/min for CD $1_{(2D)}$ to 0.35 ± 0.21 for CD $2_{(2D)}$ *(Figure 18 B)*. The higher the TEER values recorded the lower were the obtained PC values, thereby implicating the presence of a tighter barrier in iBCECs derived via CD. Analysis of BCEC functionality was carried out via tube formation assays. Correlating to control lines HUVEC and hCMEC/D3 *(Figure 18 E, i-ii)*, only iBCECs generated by aid of the DD formed tube-like structures with both hiPSC lines *(Figure 18 C)*, while iBCECs derived from the CD protocol did not *(Figure 18 D)*.

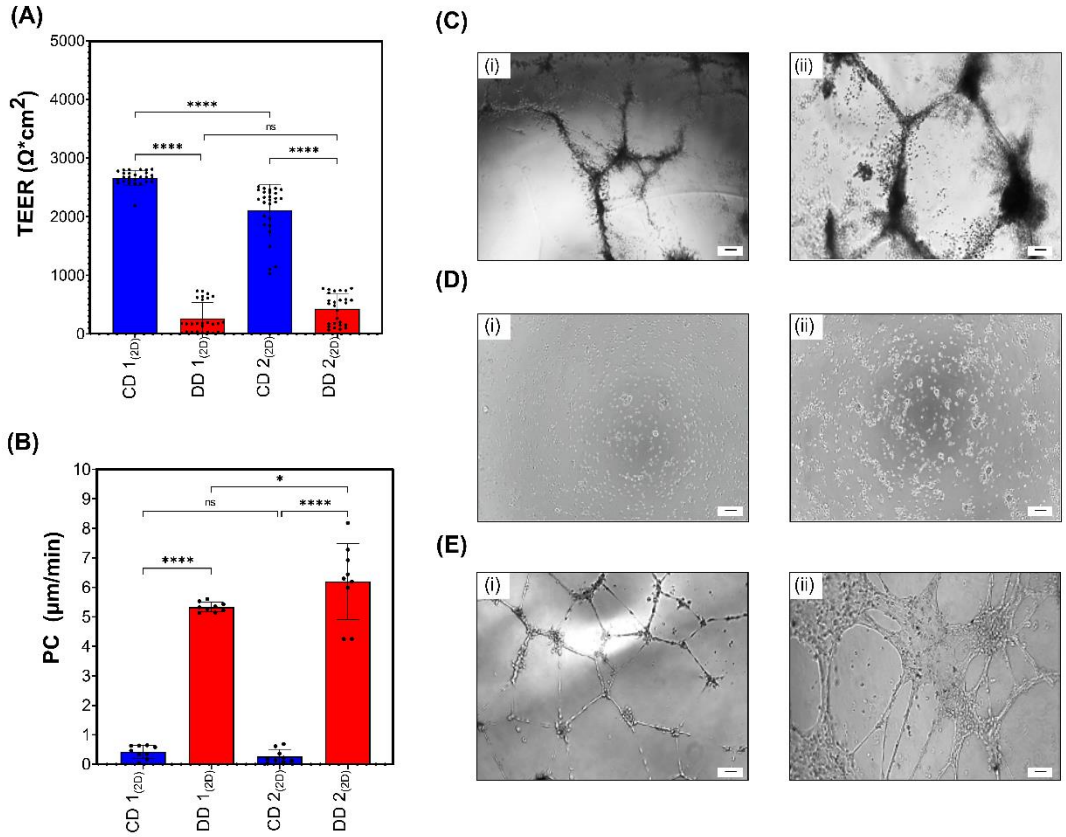

Figure 18: Comparison of barrier integrity and functionality in iBCECs

Barrier integrity of iBCECs was measured quantitatively via TEER and small molecule permeability of Sodium Fluorescein (NaF). Calculated TEER and PC values are represented as mean ± SD (A-B). Tube formation capacity of iBCECs were compared with positive controls HUVECS (E, i) and hCMEC/D3 (E, ii). iBCECs from DD $1_{(2D)}$ (C, i) and DD $2_{(2D)}$ (C, ii) formed tube like structures post 24 hours incubation with 40 ng/ml VEGF, while CD $1_{(2D)}$ (D, i) and CD $2_{(2D)}$ (D, ii) did not. Statistical significances were determined by one-way ANOVA, and multiple comparisons of mean values were assessed by Tukey´s multiple comparison test, **** indicates $p \leq 0.0001$ and * indicates $p \leq 0.05$. Representive phase contrast images were captured using the EVOS microscope at 10x magnification. Scale bar = 100µm.

11.2. Characterization of BBB spheroids

Modelling the BBB in 3D setups such as organoids and spheroids have gained noteworthy attention as a promising approach in developing better *in-vitro* BBB functionalities. Developing these setups are nonetheless still in early formative stages. In order to identify the benefits of cultivating iBCECs in spheroidal formats over traditional monoculture 2D setups, both settings were compared for transcriptomic and ultrastructural similarities. Spheroids which possessed higher BBB specific characteristics were further verified for the presence of barrier integrity via EIS and small molecule permeability, for longevity in *in-vitro* culture and for positive expression of BCEC specific markers such as claudin-5, VE-Cadherin, PECAM-1, GLUT-1. All initial characterizations were performed on two different hiPSC lines using two differentiation strategies.

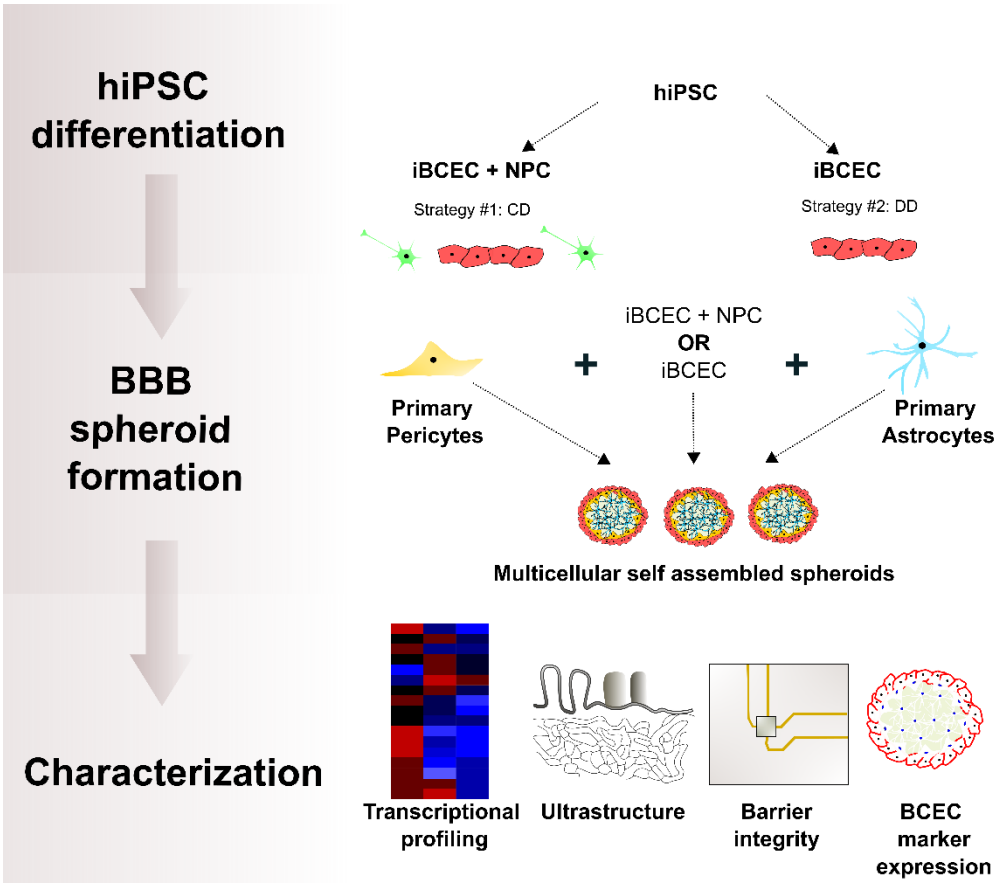

Figure 19: Schematic of BBB spheroid characterization

Human induced pluripotent stem cell (hiPSC) derived brain capillary endothelial cells (BCECs) derived via from two different strategies, along with primary astrocytes and pericytes were pooled together to generate spheroids. Self-assembled blood-brain barrier (BBB) spheroids were then characterized for BBB specific transcriptomic profile, ultrastructure, barrier integrity and protein expression.

11.2.1 Verification of characteristic BCEC transcriptomic profile in BBB spheroids

In order to improve BBB relevant marker expression and differentiation, hiPSC-derived iBCECs were cultured in spheroid formats to allow direct contact to ACs, PCs and iNPCs. The first goal in characterization of BBB spheroids was to identify via a high-throughput multiplex qPCR approach of ~96 key BCEC markers if the generated 3D spheroids have characteristic transcript expressions. Therefore, transcript expression levels were compared to respective iBCECs that were cultivated in 2D mono-culture formats *(Figure 20)*. Genes associated with junction formation, transport and other BBB relevant targets were evaluated and displayed as heat maps representing mean Log_2 fold change (FC) values *(Figure 20, A-C)*. BBB spheroids generated via CD showed noticeably higher number of differentially expressed genes (DEG) with more numbers of commonly upregulated genes between the two different hiPSC lines used to generate BBB spheroids. 43 genes were upregulated in CD $1_{(3D)}$ samples and 29 genes were upregulated in CD $2_{(3D)}$ samples. 23 genes were downregulated in CD $1_{(3D)}$ samples and 19 genes were upregulated in CD $2_{(3D)}$ samples. Amongst the two samples, 29 genes were commonly upregulated and 34 genes were commonly downregulated *(Figure 20, D)*. 19 genes were upregulated in DD $1_{(3D)}$ samples and 11 genes were upregulated in DD $2_{(3D)}$ samples. 50 genes were downregulated in DD $1_{(3D)}$ samples and 24 genes were upregulated in DD $2_{(3D)}$ samples. Amongst the two samples, 30 genes were commonly upregulated and 29 genes were commonly downregulated *(Figure 20, E)*.

Comparing the expression of transport-associated genes between spheroids generated using iBCECs derived via both strategies showed that CD $1_{(3D)}$ and CD $2_{(3D)}$ showed similar expression patterns to the DD $1_{(3D)}$ and DD $2_{(3D)}$. However, members of the ABC family such as *ABCG2* showed significant downregulations (CD $1_{(3D)}$, Log_2 (FC) = -5.22 ± 0.93, p = 0.0001. CD $2_{(3D)}$, Log_2 (FC) = -6.06 ± 2.39, p <0, 0001) while *ABCC2* (Log_2 (FC) 1.62 ± 0.04, p = 0.0009) and *ABCC5* (Log_2 (FC) 1.62 ± 0.11, p = 0.0009) were upregulated in CD $1_{(3D)}$ populations and downregulated in CD $2_{(3D)}$ populations, *ABCC2* (Log_2 (FC) -1.22 ± 0.72, p = 0.02) and *ABCC5* (Log_2 (FC) -1.65 ± 0.15, p <0, 0001). Comparing the expression of junction associated genes between the stamples showed that CD $1_{(3D)}$ and CD $2_{(3D)}$ had high expression of *CLDN1* (CD $1_{(3D)}$, Log_2 (FC) = 6.76 ± 1.77, p = 0.293, CD $2_{(3D)}$, Log_2 (FC) = 6.00 ± 4.08, p= 2.26). *CLDN5* (CD $1_{(3D)}$, Log_2 (FC) = 0.92 ± 1.03, p = 0.37, CD $2_{(3D)}$, Log_2 (FC) = 1.39 ± 0.57, p = 0.06). *CLDN11* (CD $1_{(3D)}$, Log_2 (FC) = 4.31 ± 1.67, p = 0.29, CD $2_{(3D)}$, Log_2 (FC) = 3.83 ± 1.56, p = 0.95). *JAM2* (CD $1_{(3D)}$, Log_2 (FC) = 6.03 ± 0.7, p = 0.096, CD $2_{(3D)}$, Log_2 (FC) = 4.94 ± 1.11, p = 0.11). *JAM3* (CD $1_{(3D)}$, Log_2 (FC) = 1.64 ± 0.33, p = 0.05. CD $2_{(3D)}$, Log_2 (FC) = 1.68 ± 0.59, p = 0.04). *PECAM-1* (CD $1_{(3D)}$, Log_2 (FC) = 6.03 ± 1.31, p = 0.224, CD $2_{(3D)}$, Log_2 (FC) = 6.12 ± 1.74, p = 0.20), in comparison to spheroids generated using iBCECs derived via DD *(Figure 20 A and C)*.

Epithelial-associated TJ markers were significantly downregulated in spheroids generated using iBCECs derived via CD. *CDH1* (CD $1_{(3D)}$, Log_2 (FC) = -4.13 ± 2.18, p = 0.006, CD $2_{(3D)}$, Log_2 (FC) = -3.51 ± 1.65, p = 0.0006) and *CLDN6* (CD $1_{(3D)}$, Log_2 (FC) = -2.04 ±0.71, p = 0.013, CD $2_{(3D)}$, Log_2 (FC) = -3.55 ± 1.56, p = 0.0003). TJ markers *TJP2* (CD $1_{(3D)}$, Log_2 (FC) = -0.71 ± 0.45, p = 0.11, CD $2_{(3D)}$, Log_2 (FC) = -2.04 ± 1.10, p = 0.008) and *OCLN* (CD $1_{(3D)}$, Log_2 (FC) = -1.36 ± 0.37, p = 0.014. CD $2_{(3D)}$, Log_2 (FC) = -1.85 ± 0.77, p = 0.002) were significantly downregulated *(Figure 20 F, i-ii)*. Epithelial-associated TJ markers were also significantly downregulated in spheroids generated using iBCECs derived via DD. *CDH1* (DD $1_{(3D)}$, Log_2 (FC) = -2.19 ± 3.48, p = 0.58, DD $2_{(3D)}$, Log_2 (FC) = -2.77 ± 2.16, p = 0.003) and *CLDN6* (CD $1_{(3D)}$, Log_2 (FC) = -3.73 ± 3.43, p = 0.056, CD $2_{(3D)}$, Log_2 (FC) = -1.07 ± 1.79, p = 0.036) *(Figure 20 F, iii-iv)*. These transcript expressions collectively show that iBCECs obtain reduced epitheial transcript profiles upon direct contact to NVU cell types, further illustrating iBCEC maturation.

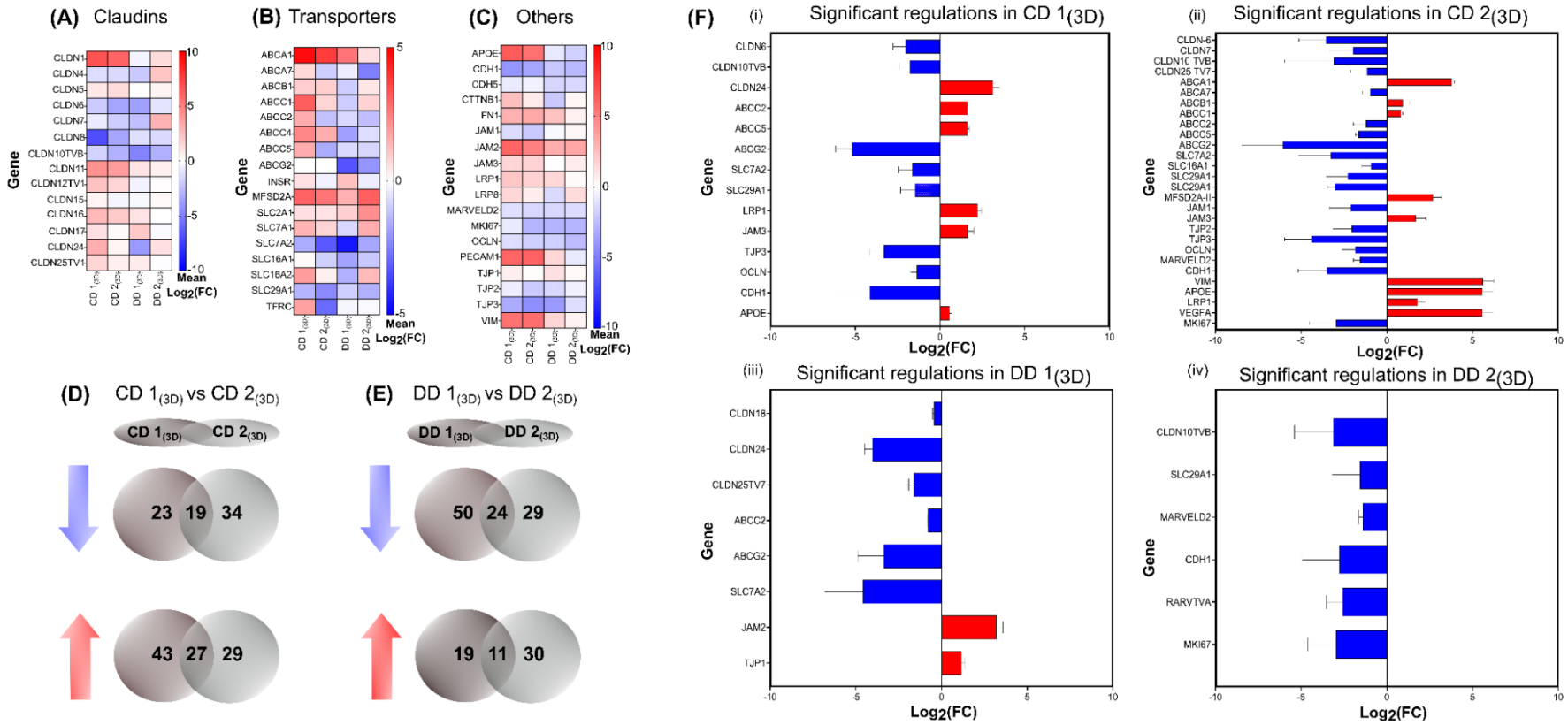

Figure 20: Transcriptomic comparison of BBB spheroids

Relative gene expression of characteristic BBB transcripts obtained via high-throughput multiplex qRT-PCR was analyzed using the $2^{-\Delta\Delta Ct}$ method with respective mono-culture iBCECs cultivated on transwells as a reference. Mean Log_2 (fold change (FC)) values indicating differentiation specific effects of co-cutlture on Claudins (A), transporters (B) and others (C) are represented as heat maps. Venn diagrams represent the total number of regulations and overlapping transcripts for each comparison (D-E). Significantly regulated transcripts in CD $1_{(3D)}$ (F,i), CD $2_{(3D)}$ (F,ii), DD $1_{(3D)}$ (F,iii) and DD $2_{(3D)}$ (F,iv) in comparison to their repective mono-cultures are presented as mean Log_2 (FC) ± SD in terms of bar graphs . Statistical significances were determined by paired two tailed t-Test and p values ≤ 0.05 were considered as significant. Analysis was performed for n=3 biological replicates (exception n=2 for DD $1_{(2D)}$ and CD $1_{(2D)}$).

11.2.2 Verification of characteristic ultrastructural BCEC tight junction meshwork

Freeze fracture analyses of the BBB spheroid samples in comparison to 2D samples of the same differentiations were verified for the presence of TJ structures and complexity at ultra structural level. TJ particles were found on the protoplasmic face (P-Face) and exoplasmic face (E-Face) of the plasma membrane in both 2D as well as 3D samples of iBCECs derived via CD. TJ strands were detected as particles and particle-free grooves on the E face (yellow arrow heads), while on the P face, partly beaded particles and partly continuous strands (blue arrows) were detected in both 2D as well as 3D samples *(Figure 21 A (i-ii) and B (i-ii))*. Blue arrows indicate TJ particles/fibrils on the P-Face (PF). Yellow arrowheads indicate grooves on the E-face (EF) that are complementary to TJ fibrils/strands on the P-face demonstrating an additional indication of TJ strands. 2D and 3D samples CD showed similar and complex networks of meshes with branched strands and mixed P/E face associations. Interestingly in iBCECs derived from the DD protocol, only very few TJ particles associated with only the P-face were idetifyable (*Figure 21 A (iii-iv) and B (iii-iv))*. This observation along with gene expression led to the exclusion of spheroids derived from the DD protocol from further quantitative investigations. In order to verify if there were any differences in TJ patterns/meshwork within 2D and 3D samples, and to identify if cellline-based differences are existing, the complexity of the network was quantified using different morphometric parameters such as number of strand intersections/strand abudance (n) *(Figure 22 A)*.

CD $1_{(2D)}$ showed strand abundance values of 83.6 ± 41.5, CD $1_{(3D)}$ showed strand abundance values of 90.0 ± 37 while CD $2_{(2D)}$ showed strand abundance values of 93.17 ± 42.9, CD $2_{(3D)}$ showed strand abundance values of 97.50 ± 31.4. Strand density, indicative of stand abundances per mesh area (n/µm^2) are presented in *(Figure 22, B).* CD $1_{(2D)}$ showed strand density values of 94.2 ± 6.2 n/µm^2 while CD $1_{(3D)}$ showed strand density values of 89.5 ± 23.2 n/µm^2, CD $2_{(2D)}$ showed strand density values of 93.66 ± 15.3 n/µm^2 and CD $2_{(3D)}$ showed strand density values of 92.76 ± 11.2 n/µm^2. Strand abundance and strand density are morphometric parameters that indicate the sum of intersections between each TJ strand and overlayed grid lines, ie. indicative of the number/length of strands detected. The higher the number of these paramertes, the larger would be the number of TJs detected. Mesh elongation, indicative of TJ stand elongation and spread uniformity are presented in *(Figure 22, C).* CD $1_{(2D)}$ showed mesh elongation values of 1.12 ± 0.16 µm^2 while CD $1_{(3D)}$ showed mesh elongation values of 1.05 ± 0.34 µm^2, CD $2_{(2D)}$ showed mesh elongation values of 1.04 ± 0.27 µm^{2}and CD $2_{(3D)}$ showed mesh elongation values of 1.12 ± 0.27 µm^2. Quantifications of these morphometric parameters showed no significant changes between both 2D and 3D samples derived via thereby indicating similar types of TJs to be found in both samples and providing evidence of successful incorportation of iBCECs into spheroids. Mesh elongation is

indicative of the spread of the TJ network. 0 would indicate a uniform 2D spread while 1 would indicate 10x elongation in one direction. In conclusion, the results obtained here provides the first indication of extensive and complex TJ meshes in CD samples in comparison to DD. However, they are not representative of iBCECs forming a tight outer layer that covers the spheroids, hence measurement of 3D EIS was carried out in the next steps in order to confirm these identified ultrastructural characteristics.

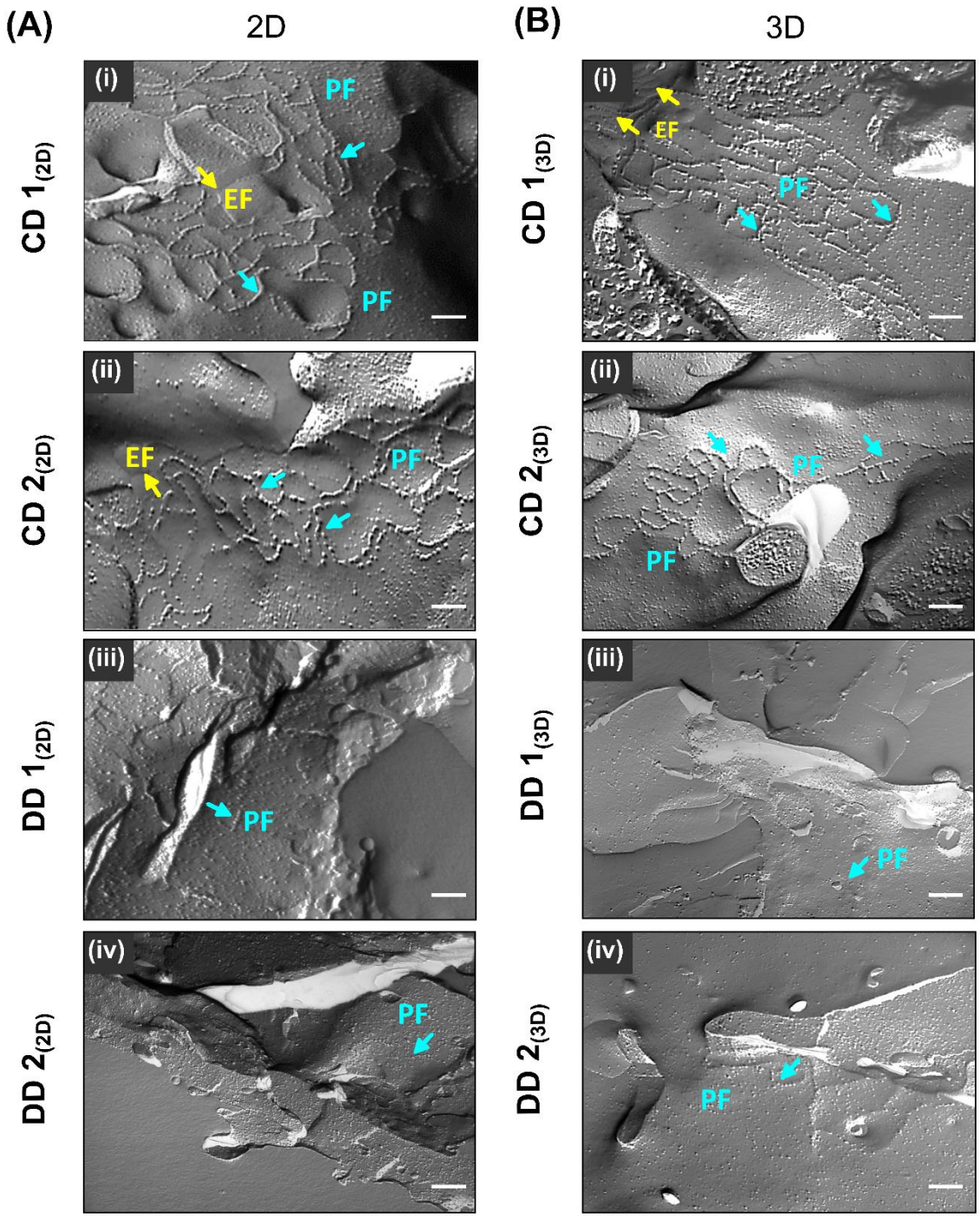

Figure 21: Verification of characteristic ultrastructural BCEC tight junction meshwork

Freeze fracture electron microscopy (FFEM) images captured at 50000x were verified and compared for the presence of characteristic brain capillary endothelial (BCEC) specific tight junctions between monoculture human

induced pluripotent stem cell derived BCECs (iBCECs) cultivated on transwells (2D) (A, i-iv) and BBB spheroids (3D) generated from two different differentiation strategies (B, i-iv). PF = protoplasmic leaflet, EF = ectoplasmic face. Scale bar = 200nm.

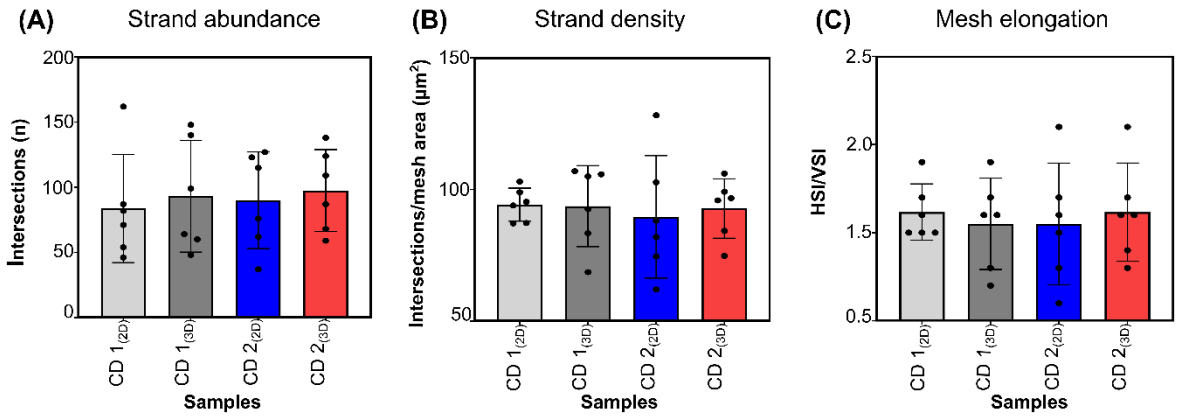

Figure 22: Quantification of tight junction strand complexity

For quantification of tight junction (TJ) strand complexity, freeze fracture electron microgrpahs were overlaid with full image grids (1.9 × 1.9 µm²) consisting of horizontal and vertical lines, each of size 100 nm. Quantifications were carried out for a minimum of three images per sample set. Strand abundance (n) and strand density (µm^2) indicates the sum of intersections between each TJ strand and overlayed grid lines, both are indicative of the number/length of strands detected. Mesh elongation (horizontal intersecting strands (HSI)/ vertical intersecting strand (VSI)) is indicative of the spread of the TJ network. 0 indicates a uniform 2D spread, 1 indicates 10x elongation in one direction. Measured values are represented as bar graphs with mean ± SD. Statistical significances were measured using one way ANOVA and multiple comparisons of mean values were assessed by Tukey´s multiple comparison test.

11.2.3 Verification of paracellular permeability and barrier integrity in BBB spheroids

To identify and monitor barrier integrity *in-vitro*, the measurement of TEER or impedance can be performed easily and non-invasively using commercially available electrodes in 2D setups. While this may seem difficult in a 3D setup, the development of micro cavity arrays in combination with impedance spectroscopy allows the possibility for bioelectronic analysis of barrier integrity in 3D models (Jahnke et al., 2019; Zitzmann et al., 2022). The chip array used to verify barrier integrity of BBB spheroids consists of several micro cavities with different diameters ranging from 150 µm – 450 µm size *(Figure 23 A)*. For measurement purposes, micro cavity size of 300 µm *(Figure 23 A, zoomed inlet image)* was used. Each measured spheroid was gently placed inside the micro cavity that is surrounded by four measuring electrodes *(Figure 23 B, C).* Relative impedance percentages (%) were compared between spheroids containg iBCECs and spheroids without BCEC layer (AC + PC spheroids). The complete spectra of relative impedance percentages (%) between frequency ranges of 5 x 10^2 and 5 x 10^6 are depicted in *(Figure 22 D)* while the maximum relative impedance percentages

obtained in a frequency range of 5 x 10^4 and 5 x 10^6 is depicted in *(Figure 23 E).* Within this range, statistically significant changes within the samples were identifyable, additionally cell line-based differences were observed. CD $2_{(3D)}$ samples showed lower relative impedance of 41.24 ± 11% in comparison to CD $1_{(3D)}$ 58.28 ± 17%. AC + PC spheroids which did not include iBCECs also showed lower relative impedance of 41.72 ± 13% indicative of low barrier integrity. Although the existence of a cellular barrier in spheroids was verified, this does not substantiate to a continuous barrier which prevents paracellular permeation. As a first proof of concept, a simple permeation study using a small molecule tracer NaF was carried out. Here relative fluorescence (RFU%) were calculated. RFU% values additionally corroborated relative impedance. Spheroids containing iBCECs showed lower permeability to NaF indicated by measurement of higher donor concentrations (verified by measuring medium surrounding spheroids) in comparison to AC + PC spheroids. CD $1_{(3D)}$ samples showed RFU% of 91 ± 6% and CD $2_{(3D)}$ showed RFU% of 83 ± 12 similar to AC + PC spheroids which presented with RFU% of 83 ± 8% *(Figure 23 F)*. These results indicate that BBB spheroids show a hiPSC line-based difference in barrier integrity.

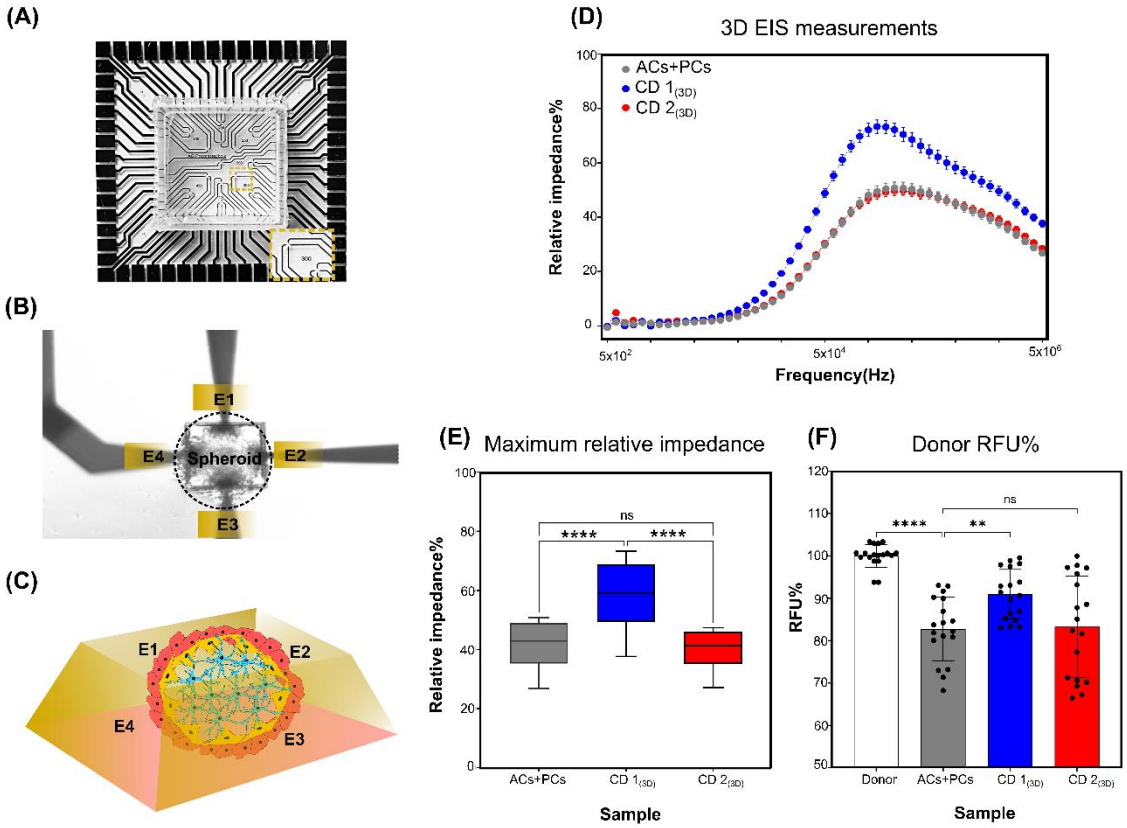

Figure 23: Verification of barrier integrity in BBB spheroids

Barrier integrity and small molecule permeability of human induced pluripotent stem cell derived brain capillary endothelial cells (iBCECs) incorporated into spheroids was verified with barrier integrity measurements via electrical impedance spectroscopy (EIS) and small molecule peremeabitiy for n = 3 biological replicates per condition (A-F). An impedance chip array with a cavity size of 300 µm (A) was used to determine EIS in spheroids. Each spheroid

was placed into the cavity, such that four measuring electrodes surrounded it (B, C). A minimium of ~15 spheroids were measured for each biological replicate and calculated relative impedance values are represented in percentage as mean ± SD for each condition. Relative impedance (%) as mean ± SEM spectra for a frequency range of of $5 \times 10^2 - 5 \times 10^6$ is represented in (D) and relative impedance (%) as mean ± SD corresponding to frequency of $5 \times 10^4 - 5 \times 10^6$ is represented in (E). Small molecule permeability of Sodium fluorescein is represented in terms of donor RFU% as mean ± SD, normalized to RFU of donor samples (100%). Statistical significances were determined by one-way ANOVA, and multiple comparisons of mean values are assessed by the Tukey´s multiple comparison test, **** indicates $p < 0.0001$, *** indicates $p \leq 0.001$, ns indicates no significances.

11.2.4 Verification of longevity in BBB spheroids

In order to identify if the BBB spheroids formed compact spheroids, could be cultivated for extended durations and to verify if their structural integrity was maintained, morphological examination was carried out via Heamatoxylin and Eosin (H&E) stainings. Wihin 24 hours in cultue, the cells self- assembled in order to form spheroids on d2 of spheroid formation, both CD $1_{(3D)}$ and CD $2_{(3D)}$ spheroids formed compact circular structures *(Figure 24, A, i and B, i)*. Starting from d4 of culture, the spheroids shrunk and lost their structural integrity *(Figure 24, A, ii and B, ii)*. From d6- d8, the spheroids completely lost their structure and form and they did not maintain sphericity or compactness *(Figure 24, A, iii-iv and B, iii-iv)*. In order to identify if this spheroid shrinkage phenomenon was attriButable to nutrition deficiency from a single cell type, spheroids were formed using difference cellular combinations namely, ACs alone, PCs alone, or ACs + PCs in 1:2 combination as well as BBB spheroids (combining hiPSC-derived iBCECs and NSCs with primary ACs and PCs). On d2 of formation AC spheroids had a mean diameter of 171.09 ± 18 µm, followed by a decrease to 149.44 ± 14 µm, 133.20 ± 13 µm and 115.524 ± 10 µm on d4, d6 and d8 respectively. On d2 of formation PC spheroids had a mean diameter of 169.24 ± 24 µm, followed by a decrease to 139.64 ± 18 µm, 125.54 ± 12 µm and 112.77 ± 12 µm on d4, d6 and d8 respectively. Additionally, in combination AC + PC spheroids showed similar decrease in size with increased culture duration. On d2 of formation AC + PC spheroids had a mean diameter of 225.02 ± 21 µm, followed by a decrease to 182.12 ± 22 µm, 174.76 ± 22 µm and 164.92 ± 19 µm on d4, d6 and d8 respectively. Similar decrease in size with increased culture duration was obseverd in both CD $1_{(3D)}$ and CD $2_{(3D)}$ samples. On d2 of formation CD $1_{(3D)}$ spheroids had a mean diameter of 232.75 ± 65 µm, followed by a decrease to 201.02 ± 11 µm, 176.28 ± 86 µm and 161.23 ± 49 µm on d4, d6 and d8 respectively. On d2 of formation CD $2_{(3D)}$ spheroids had a mean diameter of 218.23 ± 6 µm, followed by a decrease to 191.64 ± 5µm, 164.07 ± 1.5 µm and 149.70 ± 9 µm on d4, d6 and d8 respectively. Interestingly, the spheroids formed by the CD $2_{(3D)}$ were ~15 µm smaller in diameter than CD $1_{(3D)}$ *(Figure 24, C)*. Indicative of a cell line specific decrease in spheroid size. No statistical significances were found between AC+PC spheroids and CD $1_{(3D)}$ and CD $2_{(3D)}$

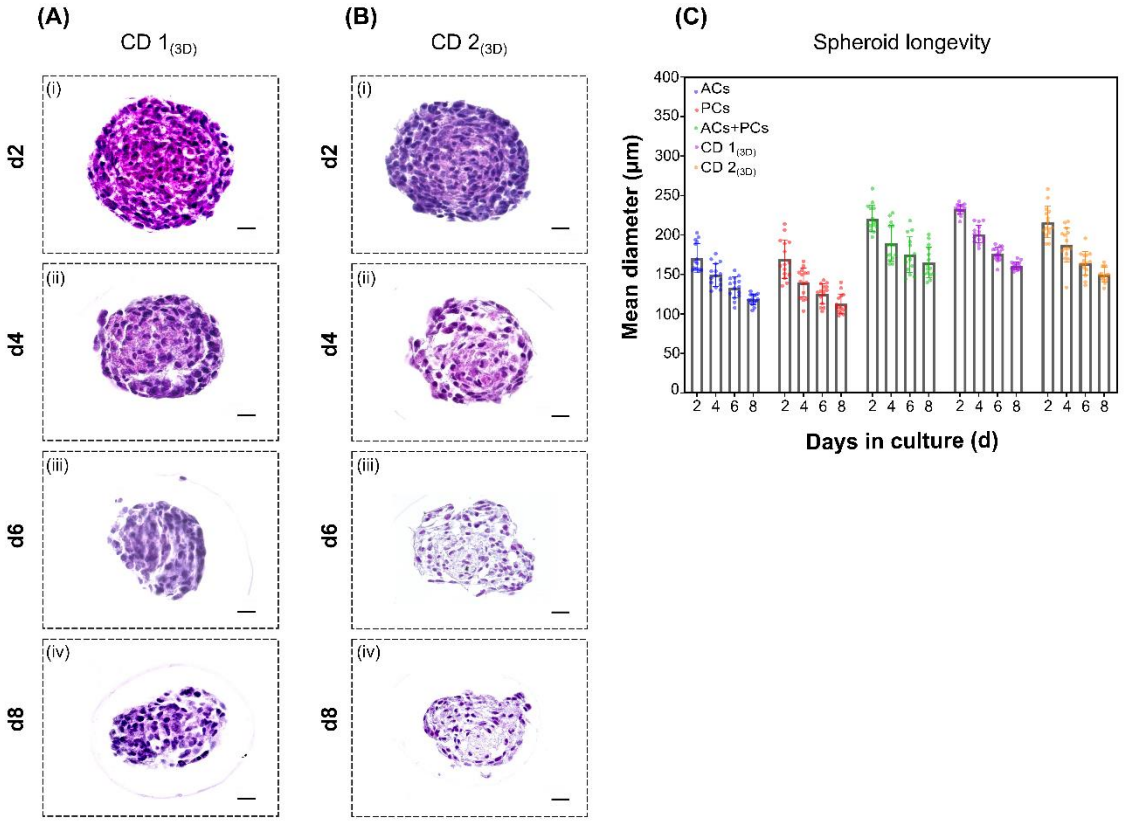

Figure 24: Verification of long-term stability of BBB spheroids

Generated blood-brain barrier (BBB) spheroids were investigated for their compactness as well as longevity in culture. H&E stainings of 5 µm slices of BBB spheroids, over a cultivation time of 8 days indicate that spheroid morphology is maintained only upto a maximum of 2 days (A). Mean diameter measurements represented in µm ± SD indicates that spheroids are decreasing in size with increased culture duration (B). Significances were determined via one way ANOVA and Dunnett´s multiple comparisons test. Images were captured using the Keynence microscope at 40x maginification. Scale bar = 50 µm

11.2.5 Verification of characteristic BCEC marker expression in 3D spheroids

Functionality of iBCECs and paracellular permeability is linked to the expression of junctional molecules and relevant transporters. Therefore, verification of key junctional molecules such as Claudin-5, VE-Cadherin, PECAM-1 and common transporters such as GLUT-1, and P-gp expression in BBB spheroids is critical. With the aid of confocal laser scanning microscopy (CLSM) key BCEC markers were identified within the spheroids and cell line-based differences were observed. Transporters such as GLUT-1, P-gp and receptors such as Tfr-1 were expressed similary in both CD $1_{(3D)}$ and CD $2_{(3D)}$ samples. GLUT-1 was homogenously expressed in the spheroids at cellular membranes extending as both a ring around the spheroid and towards the inside of each spheroid *(Figure 25 D and Figure 26 D)*. TfR-1 and P-gp were expressed only as a ring on the outer surface of each spheroid, mainly staining cellular borders *(Figure 25 E, F and Figure 26 E, F)*. VE-Cadherin was observed to be expressed the nucleus and the cytoplasm rather than defined staining to cellular borders *(Figure 24 B and Figure 25*

B). Strong expression of claudin-5 was observed on the edges of spheroids while zoomed in images show cell border specific expression patterns *(Figure 25 A and Figure 26 A)*. Surprisingly there were cell line-based differences in expression of PECAM-1. Hardly any PECAM-1 expression was identifiable in CD $2_{(3D)}$ samples *(Figure 25 C)* while CD $1_{(3D)}$ samples showed a few cells positive for PECAM-1 with distinctive elongated staining patterns *(Figure 26 C)*.

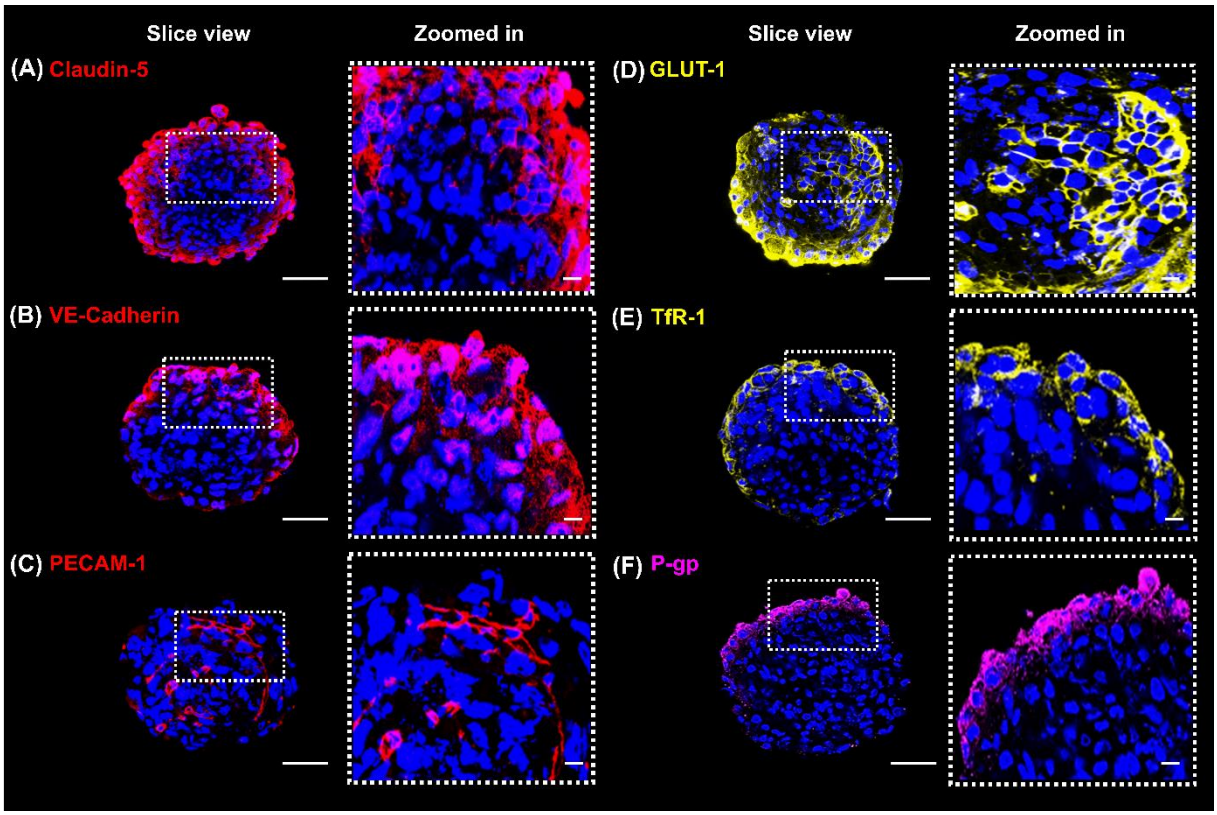

Figure 25: Verification of characteristic BCEC markers in CD $1_{(3D)}$

CD $1_{(3D)}$ samples were investigated for the expresson of key brain capillary endothelial cell markers. Nuclei were labelled with Sytox™ Red dead cell stain and indicated in blue. Expression and localization of junctional proteins claudin-5 (A), Vascular endothelial cadherin (VE-cadherin) (B) and platelet endothelial cell adhesion molecule-1 (PECAM-1) (C) was verified in blood-brain barrier spheroids. Claudin-5 staining patterns were visualized around cellular borders. VE-Cadherin was observed to be expressed in cellular nuclie and cytoplasm. Few PECAM-1 positive cells with elongated staining patterns were observed. Expression of markers such as glucose transporter (GLUT-1) (D), Transferrin receptor (TfR-1) (E) and P-glycoprotien (P-gp) (F) was additionally verified. Images were captured at 40x magnification through a maximum Z stack capacity of the Confocal SP-8 microscope and representative slice images of depth ranging from ~ 50 µm - 70 µm are presented via single Z stacks (Scale bar = 50 µm). Zoomed in areas are indicated on the right panel of each spheroid (Scale bar = 20 µm).

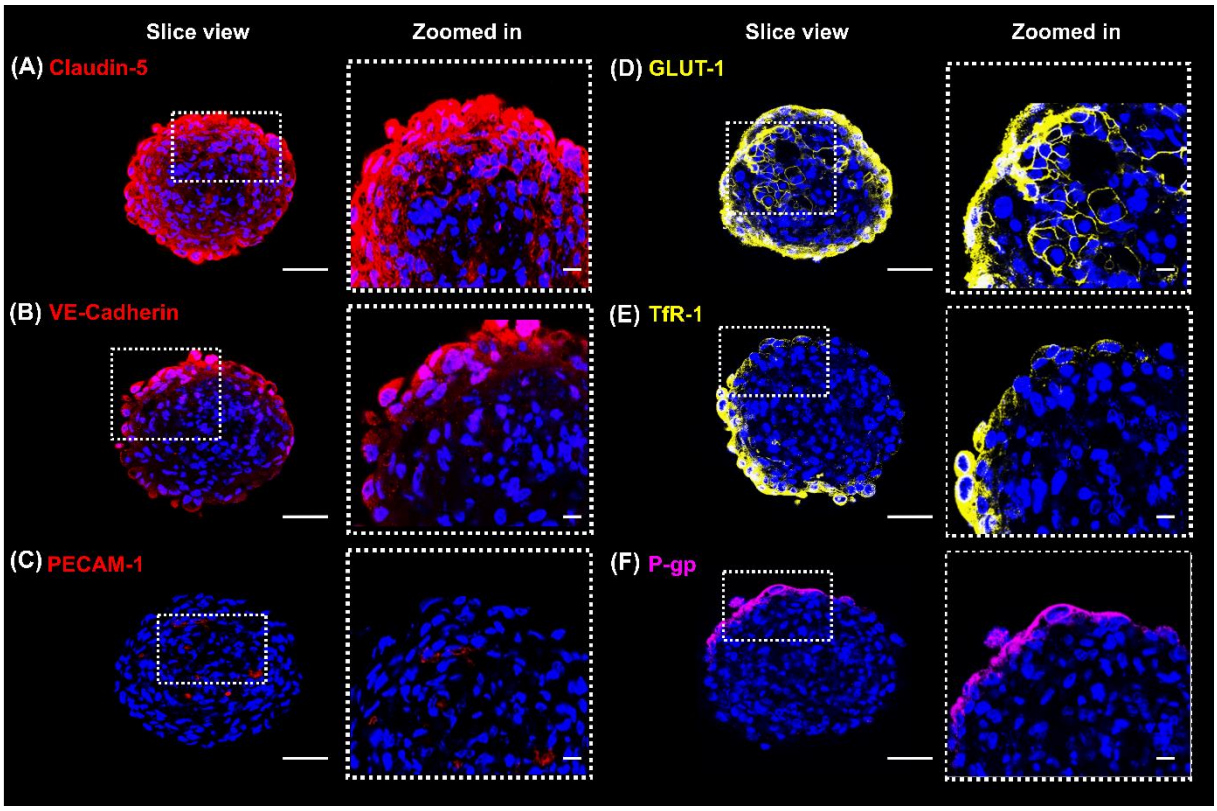

Figure 26: Verification of characteristic BCEC markers in CD $2_{(3D)}$

CD $2_{(3D)}$ samples were investigated for the expresson of key brain capillary endothelial cell markers. Nuclei were labelled with Sytox™ Red dead cell stain. Expression and localization of junctional proteins Claudin-5 (A), Vascular endothelial cadherin (VE-cadherin) (B) and platelet endothelial cell adhesion molecule-1 (PECAM-1) (C) was verified in BBB spheroids. Claudin-5 staining patterns were visualized around cellular borders. VE-Cadherin was observed to be expressed in cellular nuclie and cytoplasm. PECAM-1 positive cells were not identifyable. Expression of markers such as glucose transporter (GLUT-1) (D), Transferrin receptor (TfR-1) (E) and P-glycoprotien (P-gp) (F) was additionally verified. GLUT-1 was homogenously expressed in cellular borders, extending as both a ring around the spheroid and towards the inside of each spheroid. TfR-1 and P-gp on the other hand was observed to be found only as a ring on the outer surface of the spheroid, mainly with staining patterns around the cellular borders. mages were captured at 40x magnification through a maximum Z stack capacity of the Confocal SP-8 microscope and representative slice images of depth ranging from ~50µm-~70µm are presented via single Z stacks (Scale bar= 50µm). Zoomed in areas are indicated on the right panel of each spheroid (Scale bar= 20µm).

11.2.6 Verification of NVU cell types in BBB spheroids

In order to identify the incorporation of NVU cell types into the spheroids and to determine their localizations, immunohistochemistry on paraffin section slides were performed. In both CD $1_{(3D)}$ and CD $2_{(3D)}$ samples, the presence of ACs, PCs and NPCs was verified. ACs stained positively for GFAP and were expressed throughout the core of the spheroid *(Figure 27 A, i and B, i)*. GFAP known to be a principal AC marker was observed as short, thick and branching protrusions, indicative of protoplasmic subtypes. Similarly, NPCs expressed nestin *(Figure 27*

A, iii and B, iii) and SOX-1 *(Figure 27 A, iv and B, iv)*. The transcription factor SOX-1, known to be the earliest and most specific marker for mammalian NPCs was present in the cellular nuclei of BBB spheroids. Nestin which is an intermediate filament protein is also known to be an NPC marker was expressed as long filamentous protrusions. Both SOX-1 and nestin positive cells were found in the core of the spheroids indicating their localization. PCs showing positive expression for PDGFR-β staining cellular cytoplasms was observed to be localized as a ring around the spheroids and not at the core *(Figure 27 A, ii and B, ii)*.

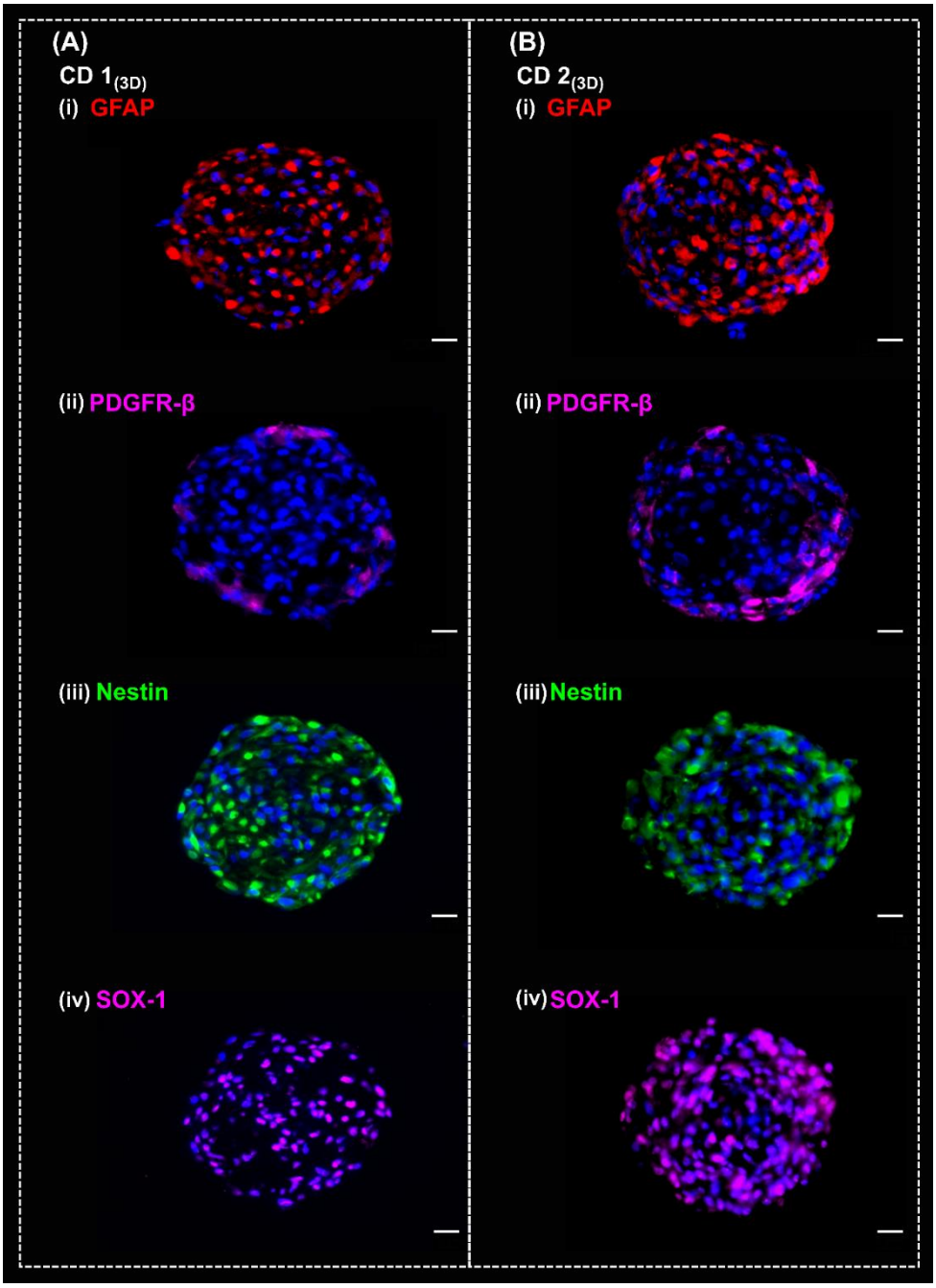

Figure 27: Verification of characteristic NVU cell types markers in BBB spheroids

Blood-brain barrier spheroids were investigated for the expresson of neurovascular unit cell types. Paraffin sections of 5 µm thickness were stained for astrocyte marker Glial fibrillary acidic protein (GFAP) (A, i and B, i), pericyte marker platelet-derived growth factor receptor beta (PDGFR-β) (A, ii and B, ii) and neural progenitor markers nestin

(A, iii and B, iii) and SRY-box transcription factor-1 (SOX-1) (A, iv and B, iv). Images were captured at 20x magnification using the Keyence microscope. Scale bar = 20µm. Nuclei were labelled with DAPI in blue. NPC and AC markers were localized throughout the middle/core of the spheroid, while PC marker showed a ring-like localization only on the borders of the spheroids.

11.3 Characterization of iBCECs under long-term and dynamic culture

The generation of microfluidic organ-chip based models has been one of the most notable recent advances in hiPSC derived models of the BBB with the main advantage being the applicability of fluid flow (Workman and Svendsen 2020). Several studies have been conducted in order to study iBCEC responses to fluid flow induced shear stress; however, one main challenge remains in maintenance of effective long-term barrier properties. In order to idetifiy the changes in barrier integrity and molecular expression patterns of iBCECs under long term fluidic flow conditions, iBCECs were cultivated in a novel bioreactor system developed at TERM. iBCECs were characterized for long-term stability via non-invasive barrier integrity measurements. Additionally changes in protein expression patterns for key endothelial markers such as VE-Cadherin and von Willebrand factor (vWF), TJ markers such as claudin- 5, occludin and transporter GLUT-1 was investigated. Identification of morphological changes due to long term and dynamic culture was performed with F-Actin staining and measurement of total number of nuclie, size of nuclie and the size of cells. Changes in BBB specific gene expressions were investigated using a microarray-based approach. All investiations were performed on iBCECs derived from the IMR90-4 hiPSCs via CD.

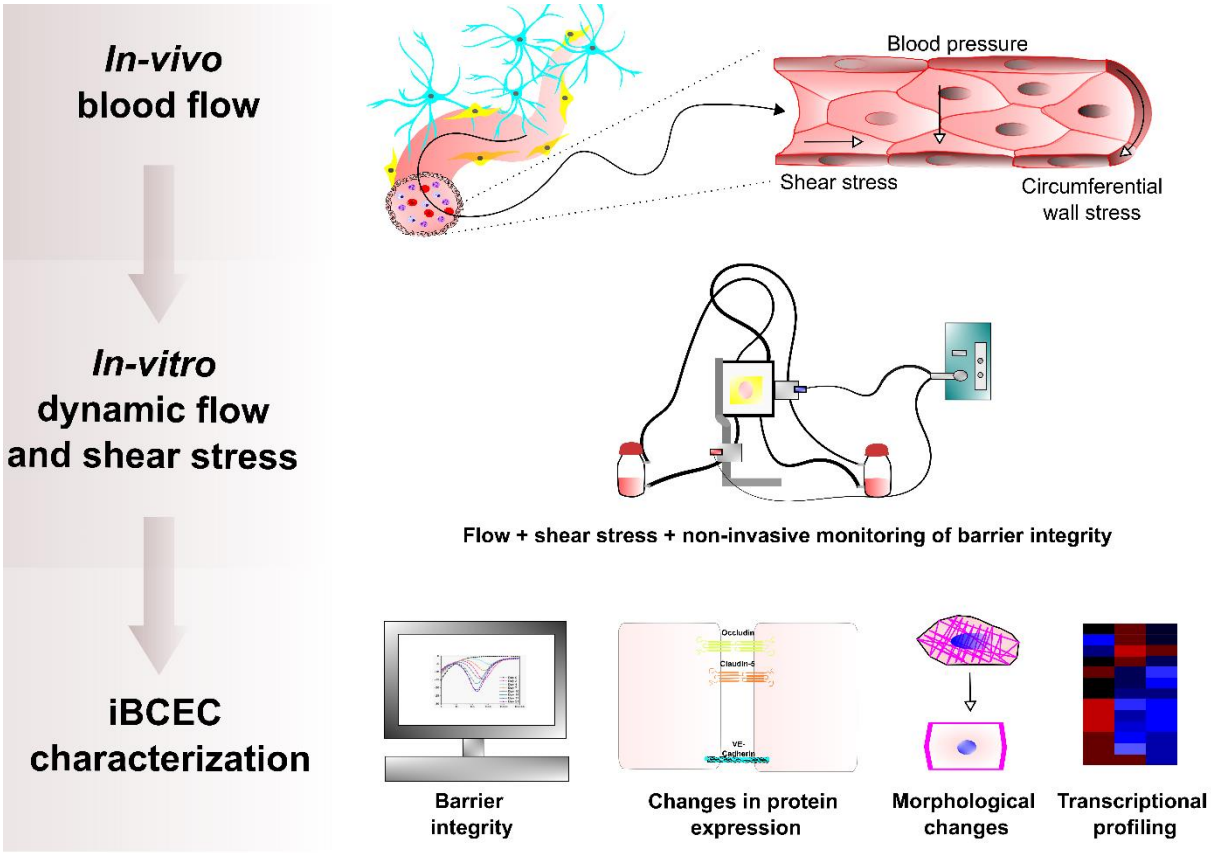

Figure 28: Schematic of characterization of iBCECs under long-term and dynamic culture

In order to identify flow-based changes in iBCECs, the cells were cultivated in a novel microfluidic system for upto seven days in total. Barrier integrity was monitored non-invasively via impedance measurements. Changes to BCEC specific protein were investigated along with characterization of morphological changes and transcriptional profiling.

11.3.1 iBCECs show prolonged culture capacities, with decreasing TEER

At d10 of CD, the chips containing a confluent monolayer of iBCECs were transferred from static culture conditions to microfluidic culture conditions in order to initiate dynamic flow and shear stress *(Figure 29, A)*. The cells were allowed to stabilize for a minimum of 6 hours before the first EIS measurement was carried out under 0.03 dynes/cm^2 dynamic conditions. Simultaneous measurements of static transwell based models using TiN lid electrodes were performed every 24 hours. TEER values of the TJ barrier as well as cell membrane capacitances were quantified by fitting equivalent electrical circuits. The equivalent electrical circuit corresponding to system design comprised of resistors representing cell culture medium (R_m), constant phase elements (C_{PE}) representing the electrodes, and a parallel connection of a resistor (R_T), and a capacitor (C_c) *(Figure 29, B)*. In dynamic culture, the capacitance increased slightly from 1.18 ± 0.41 µF/cm^2 to 1.47 ± 0.36 µF/cm^2 until d11, followed by stabilization during culture time, reaching a final value of 1.49 µF/cm^2 at d17 of dynamic culture. In static culture, a final capacitance value of 2.02 ± 0.22 µF/cm^2 was obtained. *(Figure 29, C)*. Measured TEER values on d10 post stabilization reached 2609 ± 1029 Ω*cm^2 under dynamic culture conditions. At d11 of static culture, the TEER values were 1865 ± 786 Ω*cm^2, while the dynamic culture achieved higher TEER values of 2513 ± 424 Ω*cm^2. During long-term culture, TEER values steadily dropped to 449 ± 149 Ω*cm^2 for static and 285 ± 76 Ω*cm^2 for dynamic culture, respectively for a total culture duration of d17 *(Figure 29, D)*. No statistical differences were observed between dynamic and static cultures.

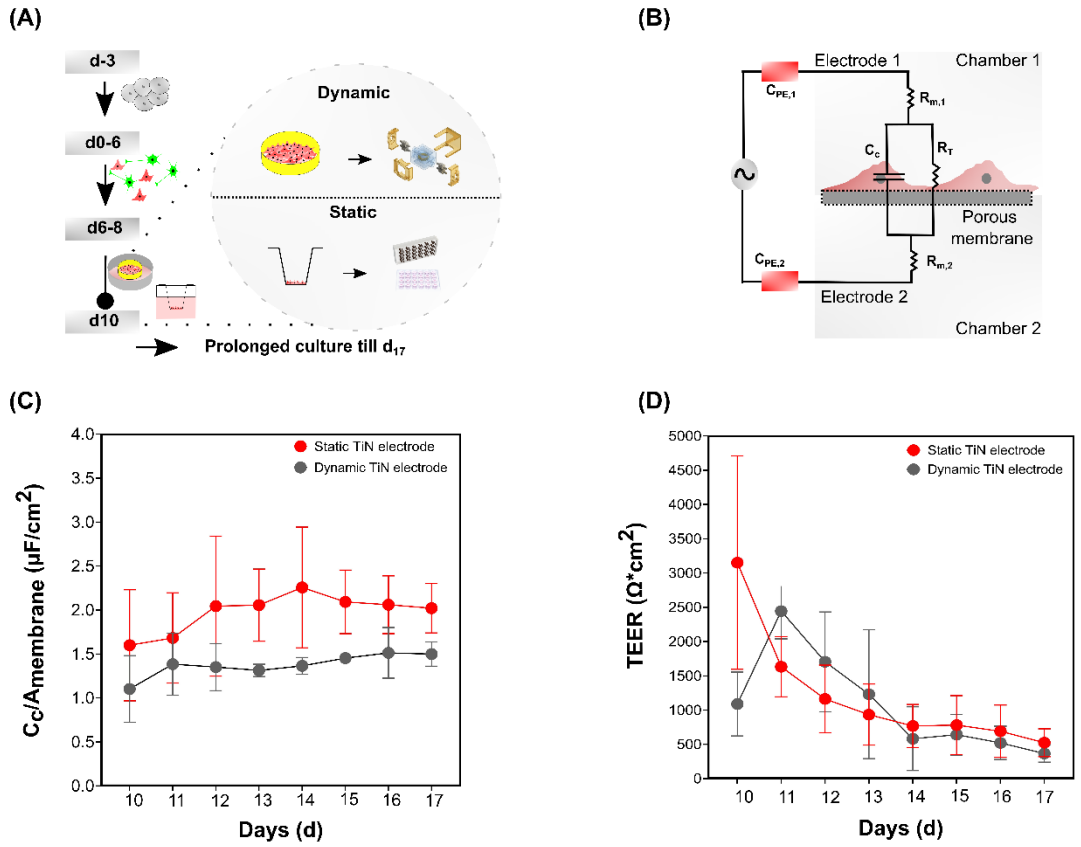

Figure 29: Comparison of barrier integrity between dynamic and static culture of iBCECs

Schematic illustration of time line of static and fludic cultured BBB models (A). iBCECs from d10 of differentiation were first shifted to either static or dynamic culture conditions for long term culture until d17. Equivalent circuit design based on the bioreactor culture system where C_{PE} indicates constant phase element of electrode, C_c indicates capacitance of cell membrane, R_T indicates resistance of tight junction barrier and R_m indicates resistance of culture medium (B). Barrier integrity and cellular capacitance was measured for upto seven days. Calculated TEER (D) and capacitance (C) values obtained by fitting and simulation of impedance data are represented in mean Ω*cm^2 ± SD and in mean µF/cm^2 ± SD respectively. Statistical significances were determined by two-way ANOVA, multiple comparisons of mean values were assessed by the Šidáks multiple comparisons test.

11.3.2 iBCECs cultivated under prolonged static and dynamic conditions posses cell junction specific protein expression and demonstrate changes in cellular morphology

In order to identify the influence of dynamic flow on iBCECs, and to analyze resulting changes in protein expression of characteristic BCEC markers such as GLUT-1**,** claudin-5, ZO-1, occludin, VE-cadherin, vWF and cytoskeletal marker F-actin, protein expression levels were investigated via immunofluorescence in direct comparison to static conditions *(Figures 30 and 31)*. Manual quantifications of BCEC markers, total number of nuclie, area of nuclie, circulatiy of nuclie and area of cells was conducted using IMAGE-J and comparisons were carried out between iBCECs cultivated for seven days under static or dynamic conditions. At d10 GLUT- 1 was observed to be expressed in the cytoplasm, with only 11 ± 0.13% of cells showing membranous staining patterns**,** while on d17, 62 ± 0.23% cells in static and 61 ± 0.14% cells

in dynamic showed continuous membranous expression *(Figure 30 A, i-iii).* Interestingly claudin-5 was expressed mostly in the cytoplasm region at d10 with only 5 ± 0.08% cells showing continuous membranous staining. With increase in culture duration, claudin-5 expression levels increased up to 18 ± 0.13% under static conditions at d17 and 31 ± 0.20% cell-cell border expression patterns were observed under d17 dynamic conditions, *(Figure 30 A, iv-vi).* Both Glut-1 and claudin-5 showed significant statistical differences in membranous expression between the investigated conditions *(Figure 30 B, i-ii)*. ZO-1 expression on the other hand showed no significant differences between the days with 66 ± 0.18% cells having cell-cell border expressions at d10, 58 ± 0.33% under d17 static conditions and 66 ± 0.18% cell-cell border expressions under d17 dynamic conditions *(Figure 30 A, vii-ix and B, iv)*. In contrast, occludin expressions showed significant statistical differences between the different conditions with 33 ± 0.29 cells showing cell-cell border expressions at d10, which increases with culture duration upto d17 with 53 ± 0.24% cells showing cell-cell border expressions in static conditions and 65 ± 0.16% cells showing cell-cell border expressions in dynamic conditions *(Figure 30 A, x-xii and B, iii).* Additionally interesting shifts in localization of proteins such as VE-cadherin and vWF was observed. VE-cadherin was expressed in the nuclei on d10 and translocation to cell-cell borders are visible in both prolonged d17 static and dynamic cultures *(Figure 31 A, i-iii)* while vWF was expressed in the cytoplasm of few cells at d10, followed by translocation into cellular borders in prolonged d17 cultures *(Figure 31 A, iv-v)*. Furthermore, it could be observed that vWF had an increased cell border expression pattern in dynamic d17 samples in comparison to static ones. Changes in cell morphology and remodeling was observed via F-actin cytoskeletal staining patterns. At d10, F-actin was localized rather non-homogenously as filamentous networks. With increase in culture duration, reconstitution of F-actin networks was observed in both static and dynamic conditions. F-actin was observed to be organized into contractile bundles, visible at cell-cell contacts, thereby indicating possible cellular polarization *(Figure 31 A, vii-ix).* Additionally, it was observed that the cells have much more spread-out morphology at d10 with an average area of 652.036 ± 94.011 μm^2, and more compacted morphology with prolonged culture duration with an average area of 236.703 ± 40.564 μm^2 under static conditions and 142.837 ± 25.673 μm^2 under dynamic *(Figure 31 B, i-ii)*. This was also true for area of nuclei being 214.32 ± 96 μm^2 at d10, 88.50 ± 40 μm^2 at d17 static, 79.91 ± 29.31 μm^2 at d17 dynamic conditions, thereby indicating cellular morphological changes and compaction *(Figure 30 B, iii).* Apart from this, the number of nuclei increased from 87.67 ± 45.28 at d10 to 209.33 ± 85.29 at d17 static and 235.00 ± 102.62 at d17 dynamic conditions *(Figure 31 B, i)*. Although the size and number of cellular nuclei decreased, no major differences were observed in nuclear circularity between the conditions with d10 static being 0.83 ± 0.08, d17 static being 0.87 ± 0.07 and d17 dynamic being 0.85 ± 0.08 *(Figure 31B, iii).*

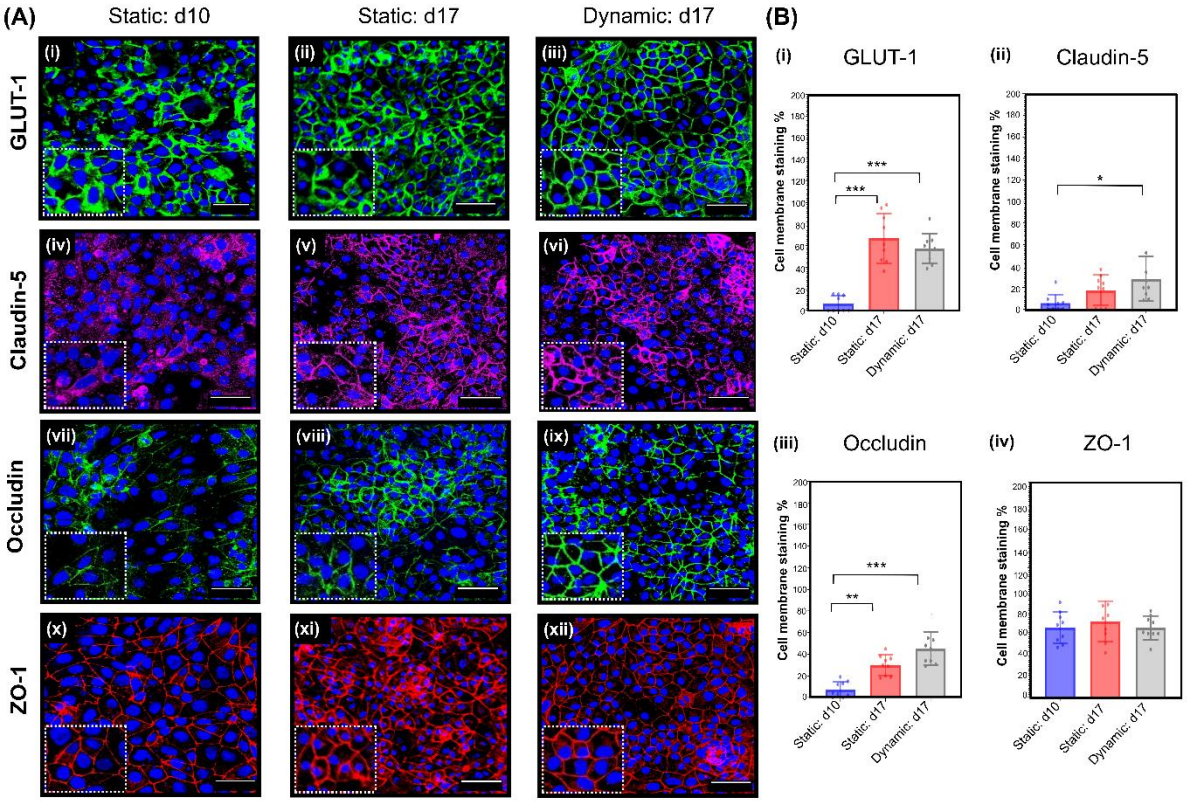

Figure 30: Comparison and quantification of iBCEC markers pre and post dynamic culture

A minimum of three images in an area of 150 µm x 150 µm were evaluated and quantified for cell membrane specificity of n = 3 biological replicates per condition. GLUT-1 was seen to be more localized in cellular borders upon long term culture and post flow as compared to static d10 samples (A, i-iii and B, i). Claudin-5 expression was profoundly increased with smooth cell border localizations that were visible post-dynamic conditions (A, iv-vi and B, ii). Occludin was observed to be profoundly inceased post flow (A, vii-ix and B, iii). No differences or changes were observed for ZO-1 (A, x and B, iv). Statistical significances were determined by two-way ANOVA, and multiple comparisons of mean values were assessed by the Tukey´s multiple comparison test (*** indicates p <0.001, * indicates p <0.005). Images were captured at 40x magnification using a Confocal SP8 microscope, with a minimum Z stack size of 5 µm. Scale bar indicates 50 µm.

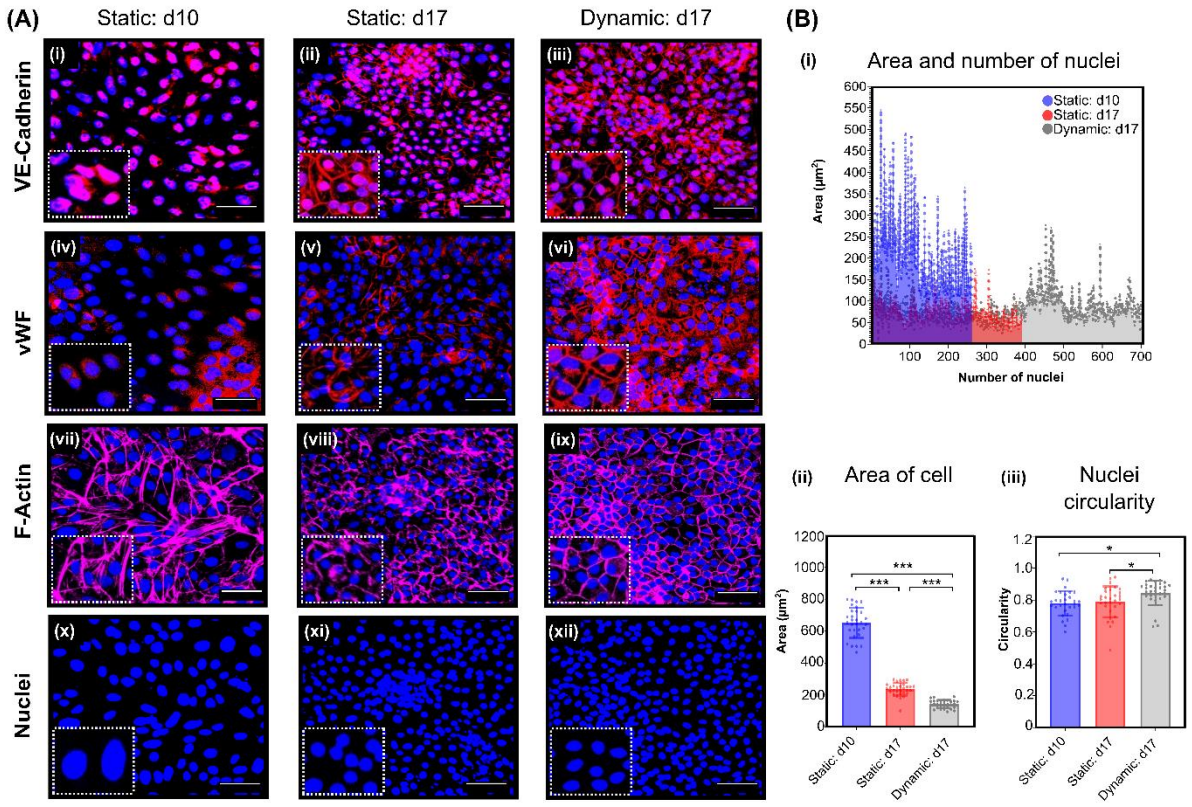

Figure 31: Comparison and quantification of morphometric parameters in iBCECs pre and post dynamic culture

A minimum of three images in an area of 150 µm x 150 µm were evaluated and quantified for morphological parameters of n = 3 biological replicates per condition. VE-cadherin was expressed in the cellular nuclie at d10 static conditions and protein translocation to cellular borders was seen in d17 static and d17 flow samples (A, i-iii). vWF expression in d10 static samples was in the cytoplasm, while d17 static samples showed junctional localization of vWF that was profoundly increased under d17 flow conditions (A, iv-vi). Cytoskeletal marker F-Actin was localized as disoriented stress fibers under d10 static sonditions, while in d17 static samples, more cortical patterning of F-Actin was observed. Under dynamic conditions on d17 a detailed cortical F-Actin meshwork was seen (A, vii-ix). Nuclie stained with DAPI were observed to be more oval, larger and fewer in d10 static samples while in d17 static and d17 flow samples they were much more in number and very compacted with a circular shape (A, x-xii). Quantified nuclie area, number of nuclie, area of cell and nuclear circularity between d10 static, d17 static and d17 flow samples show statistical significances (B, i-iii). Statistical significances were determined by one-way ANOVA, and multiple comparisons of mean values were assessed by the Tukey´s multiple comparison test (*** indicates p <0.001, * indicates p <0.005). Images were captured at 40x magnification using a Confocal SP8 microscope, with a minimum Z stack size of 5 µm. Scale bar indicates 50 µm.

11.3.3 iBCECs cultivated in prolonged static and dynamic conditions reveal significant transcriptomic downregulations

Comparison of transcript expression of iBCECs under prolonged static and dynamic d17 culture conditions and d10 static culture conditions were compared via high-throughput multiplex qRT-PCR analysis of relevant BBB markers *(Figure 32).* Heat map analysis indicates relative mean Log_2 (FC) values of analyzed targets in comparison to d10 static samples *(Figure 32, A)*. d17 static samples presented a total of 40 downregulations out of which 11 were significant and a total of 19 upregulations with 0 being significantly upregulated. d17 dynamic samples presented a total of 32 downregulations out of which 14 were significant and a total of 15 upregulations, out of which 3 were significant. Amongst both conditions 15 genes were commonly upregulated and 28 were commonly downregulated *(Figure 32, B)*. Significantly regulated genes with $p \leq 0.05$ are presented in *(Figure 32, C)*. Transporters *ABCC4* (static d17, Log_2 (FC) = -3.62 ± 1.85, p = 0.0013 and dynamic d17, Log_2 (FC) = -3.62 ± 1,31, p = 0.0001), *SLC7A3* (static d17, Log_2 (FC) = -4.03 ± 3.51 $p \leq 0.0001$ and dynamic d17, Log_2 (FC) = -5.07 ± 2.62 p = 0.001) and *SLC16A1* (static d17, Log_2 (FC)= -2.32 ± 1.56, p = 0.017 and dynamic d17, Log_2 (FC)= -2.15 ± 0.644 p = 0.0002) was significantly downregulated. *TJP1* (Log_2 (FC) = 1.58 ± 0.404, p = 0.023) and *TJP2* (Log_2 (FC) = 0.83 ± 0.51, p = 0.033) were significantly upregulated while *TJP3* was significantly downregulated (Log_2 (FC) = -2.03 ± 0.54, $p \leq 0.001$) in dynamic d17 samples. Obtained Log_2 (FC) values were further compared between d17 static and d17 dynamic samples *(Figure 33)*. Statistical significances were only observed in the expression of *ABCG2* (dynamic d17 Log_2 (FC) = -0.83 ± 1.3 (p = 0.502) and static d17 Log_2 (FC) = -3.86 ± 1.19 ($p \leq 0.001$) and *LRP8* (dynamic d17 Log_2 (FC) = -0.78 ± 1.61 (p = 0.83) and static d17 Log_2 (FC) = -2.70 ± 1.73 (p= 0.008), *(Figure 33, iv).*

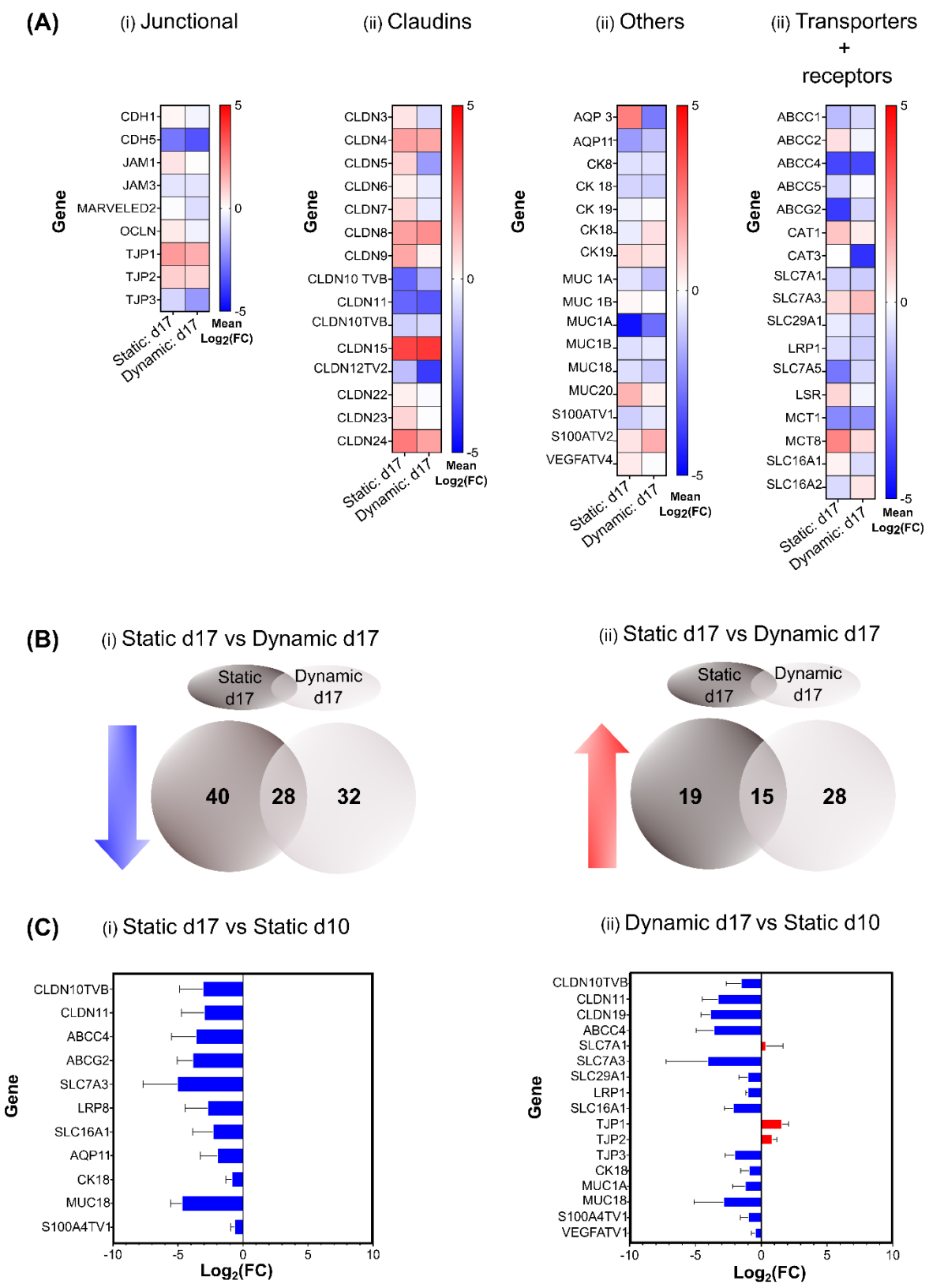

Figure 32: Transcriptomic comparison of iBCECs under dynamic and prolonged culture conditions

Relative gene expression of relevant BBB transcripts obtained via high-throughput multiplex qRT-PCR was analyzed using the $2^{-\Delta\Delta Ct}$ method with d10 static samples as reference. Mean Log_2 (Fold change, FC) are represented in the figure and p values ≤0.05 were considered significant. n = 3 independent biological replicates

were analyzed per condition. Heat maps represent relevant mean Log_2 (FC) values of junctional transcripts (A, i), claudins (A, ii), others (A, iii) and transporters (A, iv). Significantly regulated transcripts in d17 static samples in comparison to d10 static samples are presented in (B, i), while significantly regulated transcripts in d17 dynamic samples in comparison to d10 static samples are presented in (B, ii). Statistical significances were determined by paired two tailed t-Test (*** indicates p <0.001, * indicates p <0.005).

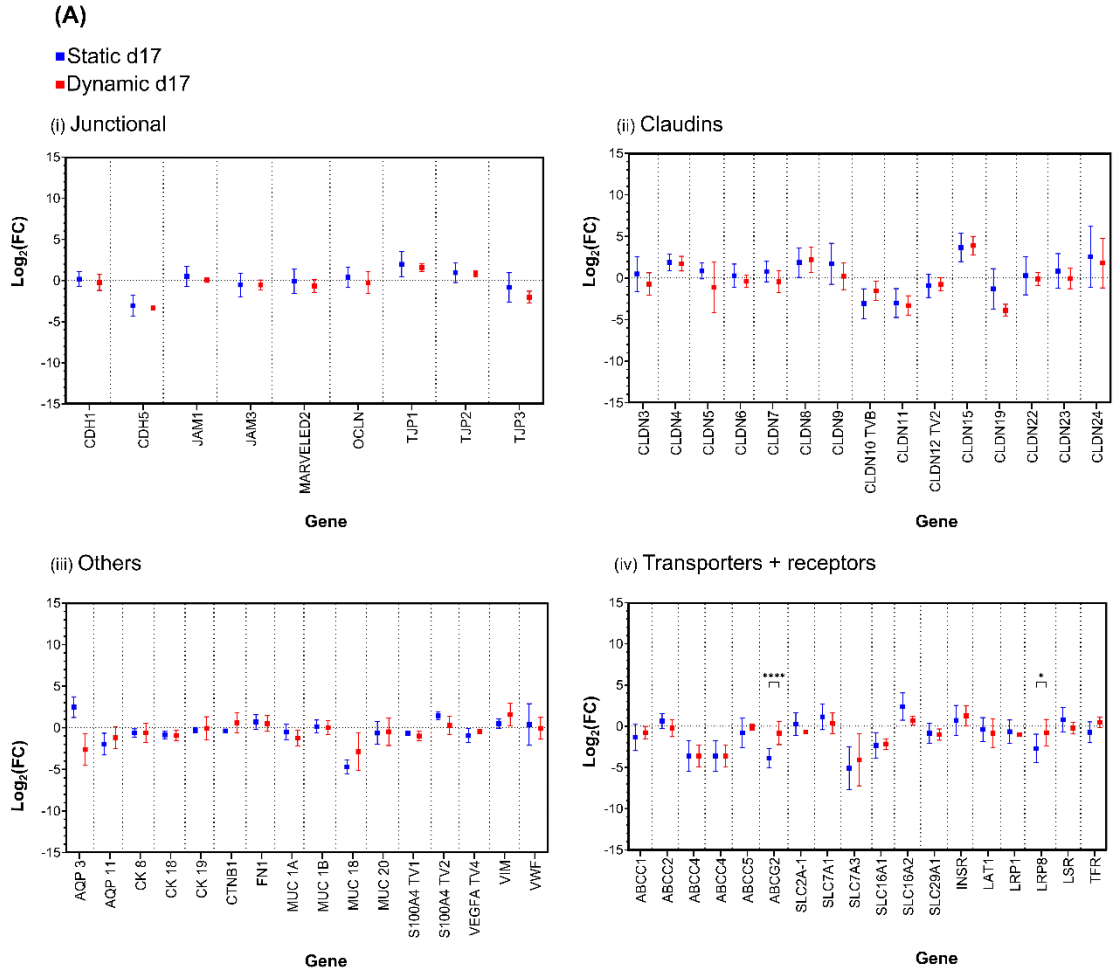

Figure 33: Comparison of Log_2 fold changes in iBCECs under dynamic and prolonged culture conditions

In order to identify changes in gene expression in junctional transcripts (A, i), claudins (A, ii), others (A,iii) and transporters + receptors (A, iv) of dynamic versus static conditions post seven days of culture, Log_2 (FC) values were compared via two- way ANOVA and Šidák multiple comparisons (**** indicates p <0.0001, * indicates p <0.005). Statistical differences were only obtained in the expression of *ABCG2* and *LRP8.*

12. DISCUSSION

12.1 Current hiPSC differentiations result in iBCECs with low generic endothelial equivalence.

HiPSCs have drastically boosted the development of predictive *in-vitro* BBB models, and differentiation strategies in delivering iBCECs play a vital role in BBB model development. While several hiPSC-based differentiation strategies demonstrate enhanced barrier properties and functions, recent reports indicate that iBCECs demonstrate an epithelial - like transcriptomic profile (Lu, Redmond et al. 2019, Lippmann, Azarin et al. 2020, Girard, Julien-Gau et al. 2022).

The search for a reliable human iBCEC source thus began with verifying classical endothelial characteristics in iBCECs using two well-established differentiation strategies. Generic endothelial cells of all vascular beds form a single cell layer *in-vivo* and retain important characteristics in *in-vitro* culture as they grow in typical “cobblestone” monolayer patterns. This distinct characteristic is therefore considered an essential criterion for identification of cultured vascular cells as representing the endothelium (Haudenschild 1984, Goncharov, Nadeev et al. 2017). During the differentiation process, distinguishable differences between the morphology of derived iBCECs were observed, especially at d10. Post differentiation, a more cobblestone and compacted morphology was observed in iBCECs derived via CD in comparison to those derived via DD. iBCECs derived via DD demonstrated cells with elongated and spindle shapes. Expression of PECAM-1 is an obligate critera of endothelial cell specificity as it is critical in endothelial barrier functionality (Privratsky, Paddock et al. 2011, Privratsky and Newman 2014, Goncharov, Nadeev et al. 2017). Additionally, it is reported that 100% of purified iBCECs should express PECAM-1 at d10 (Lippmann, Al-Ahmad et al. 2014, Stebbins, Wilson et al. 2016, Qian, Maguire et al. 2017). The findings presented in this thesis indicate that on d10, post purification, iBCECs derived from both differentiation strategies do not robustly express PECAM-1. Importantly, lack of endothelial PECAM-1 is known to impair BBB properties via reduced transendothelial electrical resistance (TEER) and increases in permeability of small molecular tracers (Wimmer, Tietz et al. 2019). iBCECs at d10 additionally show strong expression of E-cadherin, in line with recent studies, suggesting that they resemble a more epithelial or rather immature phenotype (Delsing, Dönnes et al. 2018, Lu, Redmond et al. 2019, Martins Gomes, Westermann et al. 2019, Vatine, Barrile et al. 2019, Girard, Julien-Gau et al. 2022). TJs claudin-5 and occludin were expressed specifically on protein levels in iBCECs derived via CD in line with previous reports (Lippmann, Al-Ahmad et al. 2014, Stebbins, Wilson et al. 2016). HiPSC line specific changes in claudin-5 were observed in iBCECs derived via

DD. Claudin-5 was faintly expressed in DD $1_{(2D)}$ but not in DD $2_{(2D)}$, while no occludin expression was observed in both DD $1_{(2D)}$ and DD $2_{(2D)}$. A critical clarification for this result could be that the hiPSC differentiation using the DD protocol highly depends on initial cell seeding density. As previously reported, only cells differentiated at the optimal seeding density of 3.5×10^4 cells/cm^2 would yield pure claudin-5 and occludin-expressing populations, while subpopulations of cells differentiated from non-optimal starting densities lack junctional expression or exhibit discontinuous TJP localization (Qian, Maguire et al. 2017).

As the BBB is principally a vascular structure, it is critical that iBCECs are phenotypically, transcriptionally and functionally similar to definitive BCECs (Lu, Redmond et al. 2019, Girard, Julien-Gau et al. 2022). Recent bulk RNA sequencing data show a statistically significant decrease in mRNA expression of *PECAM1, CDH5, CLDN5*, and *VWF*, in iBCECs relative to the other endothelial cell types. Additionally, iBCECs expressed *CLDN4, CLDN6*, and *CLDN7* indicating the presence of epithelial or pluripotent cellular junctions (Ben-David, Nudel et al. 2013, Delsing, Dönnes et al. 2018, Lu, Redmond et al. 2019, Girard, Julien-Gau et al. 2022). In order to probe into these arising discrepancies regarding iBCECs, gene expression of key BBB markers was verified in comparison to a standard immortalized BBB cell line namely the hCMEC/D3 line using a high-throughput multiplex qPCR approach. iBCECs derived from both differentiation strategies showed significant downregulations in junctional genes such as *CLDN5*, *CDH5* and *PECAM1* in comparison to hCMEC/D3 cells, consistent with recent findings (Delsing, Dönnes et al. 2018, Lu, Redmond et al. 2019, Girard, Julien-Gau et al. 2022). Additionally, significant downregulations in transporters such as *ABCB1*, *ABCC3*, *SLC7A1* were observed especially in DD derived iBCECs.

Generic endothelial cells are known to differentiate in the presence of angiogenic stimuli and form tube like structures containing a lumen when cultured on specific ECM (DeCicco-Skinner, Henry et al. 2014). Under the influence of VEGF, control cell lines hCMEC/D3 and human umbilical vein endothelial cells (HUVECS) readily form tubes. Purified iBCECs on d10 of DD formed tubes, while d10 iBCECs from CD did not, contrary to initial reports (Lippmann, Al-Ahmad et al. 2014). Lack of tube formation thereby implies a lack of cellular maturation and endothelial lineage specification. In summary, the findings here indicate that iBCECs are not entirely analogous to *in-vivo* BCECs and lack accepted generic endothelial profiles. The work in this thesis further hypothesizes that key marker expressions are missing due to the lack of complete maturation of iBCECs. Cell progeny specification is diverse and often determined by a blend of transcriptional, translational and functional phenotypes presented by a parent cell. This is predominantly true for hiPSC-derived cell types as *in-vitro* differentiations often leads to achievement of a target cell type that is not completely analogues to their *in-vivo* counterparts (Daley 2015). One of the most common issues pertaining to hiPSC-derived cell types is cellular immaturity as they are typically fetal-like based on transcriptional analyses.

Further cellular maturations often require addition of complex supplements to cell culture media or overexpression of relevant target genes. Until now, no single study has been able to demonstrate that any hiPSC-derived tissue is functionally and transcriptionally identical to it´s adult counterpart (Sharma, Sances et al. 2020). With regard to *in-vitro* BBB modeling, cautious interpretations related to *in-vivo* relevance must be taken, as *in-vitro* differentiations may not reiterate *in-vivo* development. Moreover, it is unlikely that iBCECs will ever fully imitate the proteome and transcriptome of *in-vivo* BCECs (Lippmann, Azarin et al. 2020). The accuracy of an *in-vitro* BBB model is additionally defined as observable characteristics that can recapitulate the human BBB in terms of barrier integrity, functionality and reponses to external stimuli (Linville and Searson 2021). Specific transcription of genes in BCECs are at least in some measures dictated by other cells within the NVU (Urich, Lazic et al. 2012). Further studies including single-cell RNA sequencing and protemomic analysis in direct comparisons to primary human BCECs could provide excellent options in identifying, evaluating and dissecting characteritics of hiPSC derived iBCECs (Sharma, Sances et al. 2020, Volpato and Webber 2020). Observable characteristics of an *in-vitro* BBB model are chiefly derived from local microenvironments and cellular components established in the model (Linville and Searson 2021). Apart from the effect of BCECs, the whole NVU provides links to successful hindrance of substance passage through the brain, therefore development of hiPSC co-culture models is in focus (Appelt-Menzel, Cubukova et al. 2017, Appelt-Menzel, Oerter et al. 2020).

12.2 iBCECs derived via co-differentiation show enhanced blood-brain barrier characteristics in terms of barrier integrity

Adult primary BCECs readily lose their *in-vivo* phenotype and demonstrate low TEER in the range of 100 Ω*cm^2 - 200 Ω*cm^2, with 100x higher paracellular permeability in comparison to their *in-vivo* counterparts (Rubin, Hall et al. 1991, Lippmann, Al-Ahmad et al. 2013). A vital hallmark of *in-vivo* BCECs is high TEER that authenticates TJ interactions between adjacent cells. To collate, the highest documented *in-vivo* TEER in rodents was measured to be above 1,000 Ω*cm^2 (Crone and Olesen 1982, Butt, Jones et al. 1990). TEER values > 1,000 Ω*cm^2 are difficult to achieve *in-vitro* using primary BCECs or immortalized cell lines (Weksler, Romero et al. 2013, Sun, Ou et al. 2022). Primary human BCECs isolated from fresh biopsies yields a TEER of ~ 350 Ω*cm^2 (Rubin, Hall et al. 1991), much lesser than documented *in-vivo* values. iBCECs on the other hand report robust and elevated TEER (Lippmann, Al-Ahmad et al. 2014, Qian, Maguire et al. 2017, Appelt-Menzel, Cubukova et al. 2018). Maximum reported TEER for mono-culture iBCEC transwell setup using cells derived via DD was ~ 3,000 Ω*cm^2 (Qian, Maguire et al. 2017), 4,118 ± 119 Ω cm^2 and 1,897 ± 76 Ω cm^2 (Grifno, Farrell et al. 2019). Contrary to these reports, in this work, lowest TEER values ranging from 284 ± 263.206 Ω*cm^2 – 429 ± 257.36 Ω*cm^2 were obtained in iBCECs derived via DD, while CD

produced a consistently high TEER of 2106 ± 0.131 Ω*cm^2 – 2677 ± 85.44 Ω*cm^2 with two different hiPSC lines. These consistent high TEER of iBCECs derived via CD is in line with previous reports namely 3980 ± 151 Ω*cm^2 (Hollmann, Bailey et al. 2017), 3,670 ± 370 (Lippmann, Al-Ahmad et al. 2014) or 1,198 ± 265 (Appelt-Menzel, Cubukova et al. 2018). *In-vivo*, the BBB is not only characterized by high TEER values, but also by its operational molecular exclusion and functional transport systems. Therefore, in order to determine the ability of iBCEC mololayers to restrict passage of small molecule tracers and to determine if tracer permeability paralleled TEER measurements, permeability of small molecule NaF was investigated. Similar to previous studies (3.3 ± 0.3 × 10^{-7} cm/s (Sun, Ou et al. 2022)**,** 1.33 ± 0.29 µ/s (Appelt-Menzel, Cubukova et al. 2017), 1.95 × 10^{-7} cm/s (Hollmann, Bailey et al. 2017), 1 × 10^{-6} cm s^{-1} (Danz, Höcherl et al. 2022)), iBCECs derived via CD yielded low PC values ranging from 0.44 ± 0.21 µ/s to 0.35 ± µ/s. On the other hand, iBCECs derived via DD demonstrated high PC of 5.2 ± 0.22 µ/s to 6.1 ± 1.29 µ/s, correlating with measured TEER. It is important to note that, above a threshold TEER value of 500 Ω*cm^2, permeability to NaF remains constantly low, further illustrating that permeability and TEER are inversely correlated (Mantle, Min et al. 2016). Apart from this, several studies support and highlight the applicability of iBCECs derived via CD as they can be used to study bacterial (Kim, Bee et al. 2017, Kim, McDonagh et al. 2019, Martins Gomes, Westermann et al. 2019), viral (Alimonti, Ribecco-Lutkiewicz et al. 2018, Krasemann, Haferkamp et al. 2022) and fungal (Patel, Hossain et al. 2018) infections. iBCECs derived via CD additionally find applications in modelling neurodegenerative disorders such as Alzheimer´s disease, Parkinson´s disease, Huntington´s disease (Lim, Quan et al. 2017, Katt, Mayo et al. 2019) and psychomotor retardation (Vatine, Al-Ahmad et al. 2017, Vatine, Barrile et al. 2019). Data presented in this work largely focusses on paracellular barrier properties of iBMECs as the expression and function of influx and efflux transporters have been extensively reported in iBCECs derived via CD (Mantle, Min et al. 2016, Appelt-Menzel, Cubukova et al. 2018, Roux, Jarray et al. 2019, Danz, Höcherl et al. 2022). In comparison to iBCECs derived via CD, only two other studies illustrate the applicability of iBCECs derived via DD (Qian, Maguire et al. 2017, Grifno, Farrell et al. 2019). Results obtained in this work supports previous literature in achieved TEER values and provide evidence of an operational paracellular barrier indicating that although iBCECs derived from the CD protocol may lack endothelial transcriptional profiles, they still provide as a useful tool in establishing novel *in-vitro* models for pre-screening. The work conducted in this thesis therefore concludes that although iBCECs derived via CD lacks transcriptional cellular identity in congruence to standard immortalized BCECs, they still present elevated TJ phenotypes with additionally relevant TEER demonstrating high passive barrier functions in comparison to iBCECs derived via the DD strategy. It was therefore, consequently anticipated and hypothesized that the CD would be more optimal in developing advanced *in-vitro* models of the BBB.

12.3 Blood-brain barrier spheroids demonstrate enhanced BCEC transcriptomes

Mammalian development specifies that induction of BBB specific characteristics is due to a conglomeration of events that occurs during CNS angiogenesis, beginning with angiogenic sprouting at the PNVP. Newly formed naïve capillaries timely sprout and invade the neuroepithelium thereby forming a functional vascular network (Tata, Ruhrberg et al. 2015). Importantly in the developing human brain, TJs such as occludin and claudin-5 are detectable at the interface of adjacent endothelium only at 14 weeks of gestation (Virgintino, Errede et al. 2004). Brain vessel development highly depends on several cellular signals derived from the surrounding NVU. During the invasion of the neuroepithelium, BCECs secrete factors such as PDGFβ thereby recruiting PCs, essentially forming enhaced TJs. Evidence demonstrates that PCs specifically are vital to control the relative permeability of CNS during embryogenesis (Daneman, Zhou et al. 2010, Bennett and Kim 2021). In early embryogenesis, NPCs connect with BCECs and PCs to actively encourage BBB maturation as they induce angiogenesis and BBB gene expression via the Wnt signaling pathway (Daneman, Agalliu et al. 2009, Daneman, Zhou et al. 2010, Tata, Ruhrberg et al. 2015, Tata and Ruhrberg 2018). Additionally ACs are essential for maintenance of the BBB as they do not appear to participate in this process at early embryonic stages (Daneman, Zhou et al. 2010). Mature ACs produce factors regulating BBB function and integrity. ACs secrete Ang-1 and angiotensin thereby restricting BBB permeability and supporting efficient organization of TJs (Bautch and James 2009, Blanchette and Daneman 2015, Haddad-Tóvolli, Dragano et al. 2017), importantly they are even know to induce barrier properties in non CNS endothelial cells *in-vivo* (Janzer and Raff 1987). Although signalling mechanisms and interactions remain to be fully elucidated, it is clear that many BBB properties are induced and well formed during early embryogenesis and cellular interactions plus molecular signals of the entire NVU is responsible for this. The presence of NVU cell types is therefore paramount to achieve the formation of a fully functional BBB (Tata, Ruhrberg et al. 2015). Culturing of iBCECs together with other NVU cell types indeed enhances BBB specific properties (Appelt-Menzel, Cubukova et al. 2018). However, to date only one sole *in-vitro* model can replicate direct cellular contacts of the NVU. This is the spheroid model, which is a 3D miniaturized *in-vitro* NVU. This model has been previously developed and investigated using immortalized or primary cells (Urich, Patsch et al. 2013, Cho, Wolfe et al. 2017, Kitamura, Umehara et al. 2021), but never with iBCECs.

In comparison to monocultured iBCECs, BBB spheroids derived from the CD strategy showed higher expression levels of junctional associated genes such as *CLDN1, CLDN5, CLDN11, JAM2, JAM3, PECAM1*, in comparison to spheroids generated using the DD strategy. In humans it is reported that *CLDN5* expression increases during postnatal development and

signaling molecules secreted from different NVU cell types are responsible for this (Greene, Hanley et al. 2019). While enhanced expression of *CLDN1* is known to reduce BBB leakiness for both blood borne tracers and endogenous plasma proteins (Pfeiffer, Schäfer et al. 2011). Profound upregulations of *PECAM1* is reported to regulate BBB integrity and stabilization (Wimmer, Tietz et al. 2019). Interestingly, BCECs derived from human fetal donors show higher expression levels of PECAM-1 than those derived from adult donors (Andrews, Lutton et al. 2018). Importantly epithelial TJ markers such as *CDH1* and *CLDN6* were significantly downregulated in BBB spheroids in comparison to mono-cultured iBCECs generated from the CD strategy for both hiPSC lines indicating enhanced maturation of iBCECs as a consequence of direct co-culture. These transcript regulations collectively indicate that direct cellular contacts with ACs, PCs and NPCs induces definitive matured BCEC phenotypes. However, in BBB spheroids, the expression of transport - associated genes between spheroids generated from both strategies showed that CD $1_{(3D)}$ and CD $2_{(3D)}$ have similar expression patterns to DD $1_{(3D)}$ and DD $2_{(3D)}$. However, members of the ABC family such as *ABCG2* showed significant downregulations, while *ABCC2* and *ABCC5* were upregulated in CD $1_{(3D)}$ populations and downregulated in CD $2_{(3D)}$ populations respectively. Not much information is available on the developmental expression of *ABCG2*, *ABCC2* and *ABCC5*. However, general agreement exists that *ABCG2* expression is noticed specifically by week 22 of human gestation with high expression levels at the BBB early during development (Daood, Tsai et al. 2008). In summation, the newly developed BBB spheroids represents characteristic BCEC-like TJ transcripts but varied transporter transcripts. It is therefore presumed that direct contact with NVU cell types could lead to maturation of iBCECs within the spheroids with respect to TJ formation. However, further indepth proteomic analysis and transporter specific permeability assays are required to confirm these results and verify the role of transporters.

12.4 Blood-brain barrier spheroids possess characteristic tight junctions and marker expressions

A prerequisite to the organization of barrier functionality at the BBB is the establishment of various sealing TJs at intercellular clefts (Bauer, Krizbai et al. 2014). In order to characterize TJs in BBB spheroids at the ultrastructural level, FFEM was performed in comparison to standard 2D iBCEC mono-cultures. The complexity of a given TJ network is defined by the integrity of TJ strands and the degree of TJ particle association to the protoplasmic and ectoplasmic leaflet of the membrane bilayer (Kniesel, Risau et al. 1996). Both 2D and 3D samples of the CD protocol showed similar and complex networks of meshes with branched strands and mixed P/E face associations while iBCECs derived from the DD protocol, showed only few TJ particles associated with the P-face. As TJ particles were hardly detectable in the iBCECs derived via DD, in addition to the presence of low BCEC hallmark characteristics in

2D samples of iBCECs derived via DD, a clear-cut decision to eliminate the use of iBCECs derived via DD in spheroid generation was taken. In order to verify if there were any differences in TJ patterns within 2D and 3D samples of iBCECs derived via CD, various morphometric parameters were quantified. Quantifications showed no significant changes between both 2D and 3D samples derived via CD thereby indicating similar types of TJs to be found in both samples, providing evidence of successful incorportation of iBCECs into spheroids, and formation of TJs in BBB spheroids. Previous reports show that iBCECs in combination with NVU cell types show a tendency for higher TJ complexity compared to mono-cultures respectively. For example, strand abundance values of co-cultured iBCECs were reported to be 33.0 ± 5.0 versus 26.1 ± 2.8 for co-cutlured iBCECs (Appelt-Menzel, Cubukova et al. 2017). In this work, a much higher number of strand abundances were found in mono-cultures of iBCECs 83.6 ± 41.5 (CD 1_{2D}), 93.17 ± 42.9 (CD 2_{2D}), while spheroidal co-culture samples showed a tendency for increase in strand abundances 90.0 ± 37(CD 1_{3D}), 97.50 ± 31.4 (CD 2_{3D}), corroborating the positive effects of NVU cell types on iBCECs. Mesh elongations, indicative of TJ strand elongations and spread uniformity was similar to previous reports with values of 1.1 ± 0.1 μm^2 in iBCEC mono-cultures versus 0.9 ± 0.1 μm^2 in co-cultures (Appelt-Menzel, Cubukova et al. 2018). In this work no major difference in mesh longation was found between 2D and 3D samples. Mesh elongation values of 1.12 ± 0.16 μm^2 (CD $1_{(2D)}$) to 1.05 ± 0.34, μm^2 (CD $2_{(2D)}$) were obtained in mono-cultured 2D iBCECs, while values of 1.04 ± 0.27 μm^2 (CD $1_{(3D)}$) to 1.12 ± 0.27 μm^2 (CD $2_{(3D)}$) were obtained in spheroids. Associations of TJ particles with either membrane leaflet is reported to be the result of expression and molecular organizations of various claudins (Furuse, Sasaki et al. 1999, Morita, Sasaki et al. 1999, Liebner, Kniesel et al. 2000, Piontek, Fritzsche et al. 2011). In general, TJ strands are mosaics of different claudin types, and their TJ function is dependent on the right claudin combination and content (Furuse 2010). For example, knockout of claudin-3 in mice resulted in fewer strand abundances (~ 20 meshes/μm^2) with slightly more E-face association in the majority of replicas (61%) and a lower density of particles on the strands (Winkler, Blasig et al. 2021). In rat and chicken brain claudin-1 forms TJs associated with the P-face while claudin-5 forms TJs associated with E-Face (Liebner, Kniesel et al. 2000), with particle distribution directly depending on the ratio between the expression of claudin1/5 (Liebner, Fischmann et al. 2000).

In order to identify if these ultrastructural TJs could be related to the expression of claudin-5, immunofluorescence stainings of BBB spheroids were carried out. In addition to claudin-5, the presence of other BCEC relevant markers such as VE-cadherin, PECAM-1, TfR, P-gp and GLUT-1 were investigated. Corroborating results obtained from ultrastuctural analysis, both CD $1_{(3D)}$ and CD $2_{(3D)}$ spheroids showed positive membranous immuostaining for claudin-5. Since VE-cadherin is known to regulate the expression of claudin-5 and since AJ assembly

and organization is known to precede the formation of TJs (Harris and Nelson 2010), the presence of AJs VE-cadherin and PECAM-1 were additionally verified in BBB spheroids. Interestingly VE-cadherin was visualized at cellular cytoplasms of both CD $1_{(3D)}$ and CD $2_{(3D)}$ samples. This could be due to the association of p120-catenin with VE-cadherin, which prevents clathrin-dependent endocytosis of VE-cadherin (Harris and Nelson 2010). Additionally, the association of VE-cadherin with β-arrestin could also regulate the amount of VE-cadherin at the plasma membrane. In contrast to p120-catenin binding, β-arrestin promotes internalization of VE-cadherin into clathrin-coated vesicles (Harris and Nelson 2010). However, these mechanisms and possible explanations need to be investigated further. Interestingly hiPSC line-specific difference was observed in PECAM-1 staining of BBB spheroids. While CD $1_{(3D)}$ samples showed few positive cells expressing PECAM-1, CD $2_{(3D)}$ samples showed hardly any positive staining. One likely explanation for this could be the epigenetic memory biases of hiPSCs in differentiation and maturation to BCECs. It is importat to also note that IMR90-4 hiPSCs are of fetal female lung fibroblast origin, while the SBAD-02-01 hiPSCs are of male dermal fibroblast origin. These biases originating from methylation signatures and histone modifications of hiPSC tissue origin are known to drive phenotypical differences and donor dependent variations that affect differentiation potentials and functional properties (Kim, Doi et al. 2010, Scesa, Adami et al. 2021). With regard to the BBB, histone modifications are reported to play a critical role in controlling the expression of TJ and AJ proteins (Ihezie, Mathew et al. 2021). However, further investigations are required to fully understand the mechanisms that contribute to such effects when using different hiPSC lines in BBB spheroid generation.

TfR is a representative RMT receptor and has gained significant attention as several approaches aim in exploiting TfR in enabling proteins to cross the BBB via RMT (Pardridge 2019). Bi-specific antibodies with one arm binding to TfR and one arm binding to the desired target at the CNS are used as novel BBB transport vehicles (Kariolis, Wells et al. 2020). Since one of the aims of generating BBB spheroids is to use them as *in-vitro* screening tools, it was necessary to identify the presence of TfR. Both CD $1_{(3D)}$ and CD $2_{(3D)}$ samples stained positive for TfR-1. Additionally, the expression of efflux transporter P-gp .and GLUT-1 could be verified in both CD $1_{(3D)}$ and CD $2_{(3D)}$. P-gp is an efflux transporter, which is known to restrict CNS drug delivery. It´s inhibition is known to show promising outcomes of drug delivery in animal models, but high clinical failures in humans (Aryal, Fischer et al. 2017). Efflux pump activity is additionally responsible for the active transport of a variety of drugs out of the brain capillary, thereby, the expression of P-gp on spheroids may strictly regulate access of molecules into the spheroid core. GLUT-1 is the main glucose transporter in BCECs. Glucose enters the brain via facilated diffusion through GLUT-1, making it´s expression crucial for both CNS development and homeostasis (Tang, Gao et al. 2017, Veys, Fan et al. 2020). Impaired

glucose transport across the BBB due to deficiency of GLUT-1 is characterized by infantile seizures, developmental delay, acquired microcephaly, spasticity, ataxia, and hypoglycorrhachia (Wang, Pascual et al. 2005). Assessment methods such as immunofluoresent staining and ultrastructural analysis are required to further complement TEER as well as permeability assays, however these are not sufficient enough to quantify barrier tightness on their own (Aazmi, Zhou et al. 2022). The validation parameters investigated on BBB spheroids have additionally all been shown to have functional importances at the BBB, which makes verification of their expression in the model important (Helms, Abbott et al. 2016, Osipova, Komleva et al. 2018). It is important to note here, that initial characterizations of BBB spheroids can only confirm the presence of iBCECs in the spheroids. However, due to microscopy limitations, the coverage of iBCECs throughout the BBB spheroids is not yet confirmed. Other studies have also confirmed that confocal laser scanning fluorescence microscopy (CLSFM) is not the most appropriate technique to image complete spheroids as it only allows the possibility to scan a Z-Stack depth of 100 µm (Cho, Wolfe et al. 2017, Kumarasamy and Sosnik 2021). Clearing of spheroids using standard techniques (Nurnberg, Vitacolonna et al. 2020) and usage of light sheet microscopy techniques can offer the possibility to solve this drawback (Albert-Smet, Marcos-Vidal et al. 2019, Lazzari, Vinciguerra et al. 2019).

12.5 Blood-brain barrier spheroids possess limited long-term stability

The size of a 3D spheroid is contigent on the different cell types from which they are formed and their culture conditions. Typically, spheroid sizes range from ~100 µm to > 500 µm (Achilli, Meyer et al. 2012, Singh, Abbas et al. 2020). Oxygen and nutrients such as sugars, peptides and ions permeate the inside of spheroids via diffusion, this gradient is prompted via increased spheroid size during spheroid culture. The larger the spheroid size, the more difficult it is for diffused oxygen and nutrients to reach the core of the spheroids (Ward and King 2003, Bertuzzi, Fasano et al. 2010, Edmondson, Broglie et al. 2014). This altered and undefined mass transport in differently sized spheroids further modulates distribution, retention and penetration of drugs, directly affecting drug response studies (Eilenberger, Rothbauer et al. 2021). Additionally, development of necrotic cores in spheroids is size dependent and therefore typically associated with speroids formed by proliferating cells (Barisam, Saidi et al. 2018). In order to identify if the BBB spheroids maintained their structural integrity and proliferated with increase in culture duration, H&E stainings and spheroid diameter measurements were carried out from d2 - d8. Results showed that the spheroids formed compact, rounded aggregates at d2 of formation in both CD $1_{(3D)}$ and CD $2_{(3D)}$ samples. However, with increase in culture duration the shape and compaction of spheroids

disintegrated in both samples. In order to verify if one particular cell type was deprived of nutrients, spheroids that were generated with different cellular combinations were measured in diameter from d2 - d8. In all conditions again, spheroid size decreased with increased culture duration. This result establishes that in defined 3D culture conditions, ACs, PCs as well as iBCECs did not proliferate. A possible explanation for this effect could be that 3D culture conditions or self-assemblies induce maturity/differentiation within each cell types reducing the rate of proliferation thereby pushing the cells to G0 stage of cell cycle. This decrease in spheroid size could not be attributed to lack of nutrition diffusion to the core of the spheroid as the first signs of necrosis were usually noted in spheroids that are > 500 µm in diameter (Barisam, Saidi et al. 2018). This was not the case in spheroids generated in this study, as the maximum spheroid size obtained was only ~ 230 µm. Other reports of BBB spheroids fomed using primary/immortalized NVU cells show viability of over seventeen days with homogenus diameter ~ 300 µm throughout the culture duration (Cho, Wolfe et al. 2017). Heterocellular NVU spheroids using primary/immortalized NVU cells, as BCECs, PCs, ACs, and primary neonate rat cortical neurons and microglia showed cellular viability at 5 days with possibility of culture upto 10 days (Kumarasamy and Sosnik 2021). Spheroidal models of the human cortex generated with ACs + PCs + BCECs + hiPSC derived microglia, oligodendrocytes and neurons show a viability of 21 days respectively (Nzou, Wicks et al. 2018). Due to the short-term cultivation possibility of BBB spheroids, this model possesses the drawback of not being useful in evaluating long-term effects of drug toxicity and permeability.

12.6 Blood-brain barrier spheroids include NVU cell types in defined localizations

Mimicking the BBB *in-vitro* is highly ambitions and often limited to the use of mono-culturing BCECs on standard plastic-based transwells or microfluidics. Accomplishing the inclusion of NVU cell types aims to advance and accurately model the BBB (Aazmi, Zhou et al. 2022). Regarding CD $1_{(3D)}$ and CD $2_{(3D)}$ spheroids, the inclusion and localization of ACs, PCs and NPCs was verified to be similar to *in-vivo* architecture. In order to distinguish these cell types and identify structural organization within the spheroids, formalin fixed and paraffin embedded sections were stained. Congruent with previous findings (Urich, Patsch et al. 2013, Cho, Wolfe et al. 2017) of BBB spheroids generated from immortalized/primary cells, ACs were observed to be settled in the spheroid core, while PCs formed a ring encasing the spheroids. As cells from d8 of CD were used in generating spheroids, the inclusion and localization of NPCs were further investigated. As ACs also NPCs were observed to settle at the spheroid core. These results were homogenous in both CD $1_{(3D)}$ as well as CD $2_{(3D)}$ spheroids demonstrating that *in-vivo* like NVU architecture is mimicked *in-vitro* in both conditions. Spontaneous self-assembly of these cell types and distinct localizations reproduce morphological NVU cellular

arrangements as previously reported (Urich, Patsch et al. 2013, Cho, Wolfe et al. 2017). Self-assembly of different cell types is a natural occurance happening *in-vivo* during embryogenesis, morphogenesis, and organogenesis. This phenomenon is complex and driven by chemical forces resulting from the binding of different proteins expressed on cellular surfaces (Youssef, Nurse et al. 2011). Formation of these complex BBB spheroids is much more sophisticated than putting together a solution with right composition of NVU cell types. Specific interactions between each cell type and organization into localized structures will determine how each cell type works together in the formed tissue. Since no scaffolds or extrinsic parameters are used, the localization of the different cell types is primarily driven by cell-cell interactions (Mueller, Rasoulinejad et al. 2020). This employs the intrinsic nature of NVU cell type interactions. PCs are known to extend cellular processes lining the abluminal surface of BCECs where their cell body and processes do not directly touch the endothelium since they are separated by a vascular BM. The points at which they touch the endothelium, they send finger like projections that bind to the endothelium, comparible with peg and socket junctions. These connections are mediated further via N-cadherin and connexin hemi channels (Dore-Duffy, Katychev et al. 2006, ElAli, Theriault et al. 2014). The endfeet of ACs completely envelop the vascular tube, and contain a discrete array of proteins including dystroclycan, dystrophin and aquaporin 4 (AQP-4) (Hubbard, Hsu et al. 2015). Additionally, NPCs are known to stimulate vessel branching, angiogenesis and maturation via VEGF-A and Wnt 7A/7B signalling (Tata and Ruhrberg 2018). The inclusion, localization and direct contact of these other NVU cell types was further hypothesized to increase barrier functionality and integrity of iBCECs within CD $1_{(3D)}$ and CD $2_{(3D)}$ spheroids.

12.7 Blood brain barrier spheroids possess barrier integrity and low paracellular permeability

Quantification of barrier integrity, paracellular permeability and transporter functionality of *in-vitro* BBB models is realized via various techniques and methods such as TEER measurement, EIS measurements and quantitative measurement of tracer fluxes. The measurement method of choice can significantly influence experimental outcomes and findings; therefore, much care should be taken in designing appropriate design paramerters (Santa-Maria, Heymans et al. 2020). Amongst the various available methods, TEER measurement and permeability assessment are most commonly used to non-invasively quantify the tightness of *in-vitro* BBB models (Aazmi, Zhou et al. 2022). TEER is widely used as a quantitative technique to measure cellular barrier integrity across BCEC monolayers cultivated on semipermeable membranes (Santa-Maria, Heymans et al. 2020). However, this conventional method is limited in application to 3D *in-vitro* models, including spheroids and complex 3D organoids (Curto, Ferro et al. 2018, Ahn, Jung et al. 2021). To overcome this limitation, impedance-based techniques

have been applied to evaluate barrier physiology of 3D tissue structures such as spheroids (Jahnke, Braesigk et al. 2012, Poenick, Jahnke et al. 2014, Jahnke, Mewes et al. 2019, Zitzmann, Schmidt et al. 2022). In order to assess the barrier integrity of BBB spheroids, relative impedance was measured in CD $1_{(3D)}$, CD $2_{(3D)}$ and AC+PC spheroids. Statistically significant changes were observed within the samples, along with cell line-based differences. CD $2_{(3D)}$ samples and AC+PC spheroids showed lower relative impedance of 41.24 ± 11% and 41.72 ± 13% resepectively in comparison to CD $1_{(3D)}$ 58.28 ± 17%. These results substantiated that spheroids which incuded iBCECs derived using the IMR90-4 hiPSC line had enhanced barrier integrity. Although the existence of a cellular barrier in spheroids was manifested, this result alone does not verify low paracellular permeations as several physical and technical parameters can greatly influence the measurement of TEER across BBB culture models (Vigh, Kincses et al. 2021). Therefore, in order to collate measured impedance values in spheroids, a permeation study using 10 µM NaF was performed. The results obtained supported barrier integrity measurements as quantified RFU% showed overall higher donor concentrations in the medium surrounding spheroids which contained iBCECs, indicative of low penetration into the spheroid core. These results show that BBB spheroids developed in this study posses both barrier integrity and low permeation to small molecule tracer NaF (RFU% = 91 ± 6% (CD $1_{(3D)}$, 83 ± 12% (CD $2_{(3D)}$ and 83 ± 8% (AC+PC)). In order to assess the full potential of the generated model, further studies to identify qualitative discriminatory ability of BBB spheroids must be carried out. Permeability levels of anti-TfR antibodies, cyclic peptides, IgG, active transport of substances, evaluation of efflux pump activities have already been reported in spheroids generated from immortalized/primary cells (Cho, Wolfe et al. 2017, Kitamura, Okamoto et al. 2022).These studies indicate that BBB spheroids can be expected to expand in application to investigate various RMT/AMT receptors. However, several challenges lay ahead in assessment and development of novel strategies and techniques to assess drug permeabilities in BBB spheroids. Some novel and necessary options would be to assess pharmacokinetic and pharmakodynamic parameters such as $K_{p,uu}$ via classically used brain slice methods (Loryan, Reichel et al. 2022). Another strategy would be to determine intraspheroidal concentrations of antibodies, peptides and drug substances via enzyme-linked immunosorbent assays or liquid chromatography mass spectrometry. Apart from these assay establishment challenges to overcome, the addition of *in-vitro–in-vivo* correlation analyses would help in identifying the potential of BBB spheroids. Observable characteristics of an *in-vitro* BBB model are chiefly derived from local microenvironments and cellular components established in the model (Linville and Searson 2021). Apart from the effect of BCECs the whole NVU provides links for successful hindrance of substance passage through the brain, therefore development of hiPSC co-culture models is in focus (Appelt-Menzel, Cubukova et al. 2017, Appelt-Menzel, Oerter et al. 2020). Traditional *in-vitro* BBB models however are based on transwells, where

iBCECs are cultivated on top of thin cell culture plastic surfaces. An irrefutable drawback of this model type is that NVU cell types lack direct cellular ECM contacts and BM interactions (Helms, Abbott et al. 2016, Gastfriend, Palecek et al. 2018). Novel 3D spheroids of the BBB have shown that when immortalized/primary NVU cell types are allowed to be cultivated under non-adhesive cell culture conditions, they self-assemble to from a spheroid with structural architecture resembling *in-vivo* BBB physiology (Urich, Patsch et al. 2013, Cho, Wolfe et al. 2017, Kitamura, Umehara et al. 2021, Kitamura, Okamoto et al. 2022). Thereby, eliminating the requirement for external plastic scaffolds.

One of the aims of this thesis focused on generating hiPSC-derived spheroids using iBCECs. In line with the hallmark characteristics required to be possessed by an *in-vitro* BBB model, the developed BBB spheroids was validated using two different hiPSC lines and differentiation protocols and evaluated for characteristic BCEC transcript and protein expression, ultrastructural and quantification of barrier integrity and functionality. Importantly hiPSC line-based differences was observed in generated spheroids. These results highlight the need for well-documented quality control measures and use of “gold standard” hiPSC lines in BBB spheroids generation in order to maintain reproducibility (Volpato and Webber 2020). Hetrogentiy in hiPSCs and their differentiation potentials can be attributed to various factors such as donor sex and genetic backgrounds, cell culture conditions and passage numbers as reported by the human iPSC initiative (Kilpinen, Goncalves et al. 2017). Procedural augmentations would improve hiPSC line-to-line consistency in BCEC production, but as stated previously, the IMR90-4 hiPSC line (Lippmann, Al-Ahmad et al. 2013) would also be the current recommended choice of iBCEC derivation and BBB spheroid production.

12.8 iBCECs are cultivated under long-term and monitoring of barrier integrity is achieved under microfluidic conditions

Mammalian endothelial cells undergo effective physiological changes *in-vitro* under different molecular, cellular and physical stimuli enabling them to obtain specialized functions. While chemical signaling plays pivotal roles in cellular physiology, physical stimuli and shear stresses are underestimated physiological stimuli that contribute to vascular endothelial differentiation and maturation (Kadry, Noorani et al. 2020). Human BCECs are reported to show significant maturation and differentiation under shear stress, with increased TEER from 100 $\Omega*cm^2$ – 700 $\Omega*cm^2$, upregulation of TJ and AJ proteins, 5.91- and 2.13-fold increase in *Claudin-5* and *Cadherin-5* gene expression, respectively (Cucullo, Hossain et al. 2011). With regard to iBCECs, maintaining long-term culture under perfusion helps in maintaining barrier function through a combinatory effect of shear-induced mechanical cues and continual medium

circulation (DeStefano, Xu et al. 2017, Faley, Neal et al. 2019, Linville, DeStefano et al. 2019, Vatine, Barrile et al. 2019). Threfore, in developing a realistic *in-vitro* BBB model, recapitulating physiological parameters such as blood flow and shear stresses of the BBB is of utmost importance. In *in-vitro* BBB models including fluidic flow it is critical that barrier integrity is monitored non-invasively, especially if the developed *in-vitro* system should be used in pharmaceutical testing. For this purpose, a two chambered bioreactor system with steady laminar shear stress in the range of 1.76 x 10^{-3} to 8.34 x 10^{-2} dyne/cm^2 with integrated measuring electrodes, enabling non-invasive online monitoring of barrier integrity under dynamic conditions was used to study shear stress induced changes in iBCECs (Choi, Mathew et al. 2022). Within the developed system, firstly it was possible to readily identify cellular monolayer peeling as online monitoring showed an instant drop in measured TEER values to 0 Ω*cm^2 or to the system's baseline value in the recorded impedance spectra, respectively. TEER was measured within the system for a total of seven days post differentiation and TEER values of iBCECs in dynamic culture was comparable to static conditions. These results are similar to reported findings that iBCECs show decreased TEER with increased culture durations (Hollmann, Bailey et al. 2017). Not only TEER, but also cell membrane capacitance is used as an indicator of cellular changes such as differentiation, morphology, mortality and motility (Hildebrandt, Büth et al. 2010, Bagnaninchi and Drummond 2011, Reitinger, Wissenwasser et al. 2012). Increase in capacitance during culture time in both dynamic and static culture could be associated with the increasing number of cells at d17 compared to d10 as was revealed by increased cellular nuclei. Hence, it was hypothesized that proliferating cell numbers could have an impact on decreasing TEER values since larger the number of cells, more would be the number of cellular borders and therefore the pathways for ions to pass the cellular barrier (Felix, Tobias et al. 2021). As capacitance is strongly connected to the cell membrane surface area (Wegener, Seebach et al. 2014, Linz, Djeljadini et al. 2020), the lower values in the dynamic system could be attributed to an overall smaller membrane surface area of the iBCECs compared to the static system. Although endothelial responses to flow are extensively investigated, sparce studies tackle the influence of cell density in response to dynamic flow and shear stress. It is reported that low strains of 5 - 10% inhibit endothelial apoptosis and increase proliferation (Dessalles, Leclech et al. 2021). Another explanation for this increased number of cell nuclie in iBCECs could be due to the enhanced expression of claudin-5, as it is known that overexpression of claudin-5 in hCMEC/D3 cells enables enhanced proliferation *in-vitro* (Ma, Li et al. 2017). Nevertheless, the effect of varied strains, shear stress rates and the relation between iBCEC maturation and decreasing TEER needs to be investigated further.

12.9 iBCECs respond morphologically to shear stress and prolonged culture conditions

Endothelial cell sensitivity to shear stress is often involved in several physiological processes (Roux, Bougaran et al. 2020). Shear stress induces endothelial mechano-transduction, which in turn influences parameters such as ECM remodeling, cell behavior and gene expression (Russo, Banuth et al. 2020). One of the hallmarks of generic endothelial cells is elongation and alignment in response to shear stress, where they undergo a transition from cobblestone morphology to elongated spindle shaped morphology, especially aligning in the direction of flow (Levesque and Nerem 1985). With prolonged culture duration and dynamic flow, although the total number and area of iBCEC nuclei increased, iBCECs maintained their cobblestone morphology and well-defined nuclear shape, measured in terms of nuclear circularity. Interestingly the cellular area of iBCECs also decreased with prolonged culture, and rather than becoming more spread out and spindle shaped they were more tightly packed indicating that they do not elongate in response to shear stresses, but rather are denser and more flattened. These results corroborate previous findings (DeStefano, Xu et al. 2017, Faley, Neal et al. 2019) confirming that this is a unique phenotype attributing to iBCECs under flow. In response to mechanical forces, different cellular types and tissues can change their morphology via contractile forces generated by the cytoskeleton (Kim, Uroz et al. 2021). The actin cytoskeleton is a dynamic structure that undergoes polymerization and depolymerization depending on cellular demand (Fujiwara, Takeda et al. 2018). Filamentous actin (F-Actin) organizes into three distinct cytoskeletal structures, namely cortical actin ring and membrane skeleton that are situated close to cell membranes and stress fibers that extend throughout the cytoplasm (Prasain and Stevens 2009). These distinct actin structures were identifiable as d10 static samples showed a large presence of stress fibers, extending through iBCEC cytoplasm. With increase in culture duration, the stress fibers changed into a cortical phenotype, with a very moderate amount of stress fibers observed in d17 static samples, while in d17 dynamic samples a clear and distinguishable cortical actin ring structure was established. Cortical actin ring structures provide centrifugal forces to the cells thereby supporting and stabilizing the cell membrane outward as the cells pull outward from each other (Belvitch, Htwe et al. 2018, Chugh and Paluch 2018), further supporting the observation that iBCECs do not elongate in response to flow. This membrane stabilization in turn allows for joining TJs and creating linear and continuous AJ structures thereby decreasing barrier permeability (Prasain and Stevens 2009, Bayir and Sendemir 2021). These results hint at further maturation and enfothelial specific lineage specification of iBCECs in response to shear stress and prolonged culture.

12.10 Shear stress and prolonged culture conditions results in enhanced BCEC marker expression suggesting iBCEC maturation

The anchorage of junctional proteins to the cytoskeleton has a crucial role in the control of endothelial cell shape, movement, and permeability (Giannotta, Trani et al. 2013). Under d10 static conditions expression of BCEC markers such as GLUT-1, claudin-5, ZO-1, occludin and vWF was similar to previous reports, specifically the junction associated proteins and GLUT-1 was expressed at intercellular clefts and vWF was expressed in the cytoplasm (Lippmann, Al-Ahmad et al. 2014, Appelt-Menzel, Cubukova et al. 2017). Generally, it is accepted that endothelial cells form a confluent, resting monolayer in mature vessels, where VE-cadherin is clustered at cell-to-cell contacts (Li, Chen et al. 2018). However, at d10 VE-cadherin was localized more in the cytoplasm and nuclei of iBCECs and with prolonged culture, it translocated to iBCEC membranes, while additionally remaining in the nucleus. Availability of VE-cadherin at cell membranes is crucial in regulating cell–cell adhesion and endothelial barrier function (Noria, Cowan et al. 1999) and it´s trafficking and internalization is dynamically modulated in endothelial cells (Gavard 2014). Loss of VE-cadherin is reported to cause disorganizations of the cortical actin cytoskeleton (Sauteur, Krudewig et al. 2014). However, as with prolonged culture and flow conditions, the actin cytoskeleton was remodeled and more pronounced in iBCECs, leading to speculate that iBCECs under shear stress and prolonged culture achieve an endothelial phenotype. Endothelial vWF is secreted constitutively and stored in Weibel–Palade bodies from where it is released by regulated secretion into the plasma and basement membrane in response to activation (Sporn, Marder et al. 1989). On d10, vWF was expressed in the cytoplasm of iBCECs. Upon stimulation, Weibel-Palade bodies are known to be translocated to the plasma membrane (Denis 2002). With prolonged culture, vWF in iBCECs was translocated into cellular membranes and this translocation was more pronounced under d17 dynamic conditions. Due to its large molecular size, vWF is known to be flexible in its confirmation and responsiveness to shear stress. Conformational unfolding of vWF is shown as an effect of shear stress (Tsai 2003, Gogia and Neelamegham 2015), thereby allowing vWF to form threads that self-associate, forming long strands and web like structures, while a globular conformation remains in low/no shear conditions (Schneider, Nuschele et al. 2007). Quantitative analysis of the intensity of claudin-5, occludin, ZO-1, and F-actin expression of iBCECs under flow reveal no significant differences between static and flow conditions in previous studies (DeStefano, Xu et al. 2017). Contrarily, quantifications in this thesis work show that ZO-1, occludin, claudin-5 and GLUT-1 are more pronounced at the cellular borders at d17 dynamic culture conditions with smoother and thinner staining patterns. Importantly, at d10 claudin- 5 was found more in the cellular cytoplasm with hardly any in cellular junctions. Although occludin was found in cellular borders at d10, the number of cells

expressing distinct, continuous bands of occludin increased significantly under prolonged and dynamic culture conditions. Formation of these TJs is critical in BBB differentiation and maturation and changes in barrier integrity was easily monitored via impedance. During fetal development, occludin and claudin-5 are first detected as diffused staining patterns of the endothelial cytoplasm, and post 14 weeks of gestation, the staining shifts from the cytoplasm to the membranes of adjacent endothelial cells (Virgintino, Errede et al. 2004). This transitional phase results in discrete expression of TJs at cellular borders, indicating emergence of mature TJ complex formation and a functional physical BBB (Nagy, Peters et al. 1984, Andrews, Lutton et al. 2018). Importantly it is known that BBB maturity is not synonymous with function, and is said that the human brain is not technically mature until 20 years of adult age and maturation continues throught life as the NVU adapts to indespensible needs (Saili, Zurlinden et al. 2017). Apart from the benefits of direct NVU cell type contacts, the work performed in this thesis also concludes that shear stress and prolonged culture conditions plays a crucial role in some aspects of modulating iBCECs physiology. These include iBCEC morphology and maturation. In response to low shear stress, iBCECs exhibit distinctive phenotypes such as maintenance of cobblestone morphology, no elongation or alignment in the direction of flow, increased compactness and reorganization of the cytoskeleton and low mRNA transcripts of BBB associated genes. Although iBCEC TEER values decrease with prolonged and dynamic culture, they respond uniquely under shear stress conditions indicating an increased maturation. These functional effects of these observed results will have to be further validated to accurately predicted blood-to-brain permeability of pharmacologics. Additionally, the inclusion of other NVU cell types could maybe increase TEER of iBCECs as in previously reported studies (Vatine, Barrile et al. 2019).

12.11 Gene expression changes in iBCECs as a response to shear stress

Shear stress levels ranging from 5 - 23 dynes/cm^2 is reported in *in-vivo* brain capillaries, however cerebral microcirculation is also known to be highly heterogeneous with mean shear stress levels in brain microvessels estimated in a range of ~ 0.01 - 10 dynes/cm^2 in capillaries and ~ 10 - 100 dynes/cm^2 in arterioles (Luissint, Artus et al. 2012). iBCECs are known to be affected by even very low shear stress conditions ranging from 0.01 - 2.4 dyne/cm^2 induced by laminar medium flow. These changes translate to promotion of expression pathways related to BCEC maturation (Vatine, Barrile et al. 2019). Importantly, only *TJP1* and *TJP2* were significantly upregulated in d17 dynamic iBCECs, thereby indicating that this novel shear stress-based model maybe more suitable in studying paracellular transport mechanisms in iBCECs. Additionally, upregulation in *CTTNB1* an intermediate filament component in d17 dynamic samples supports the finding that cell matrix interactions involving actin and

microtubule re-organizations are evident in iBCECs under shear stress. Other reports indicate that the induction of shear stress in the range of 4 -12 dyne/cm^2 on iBCECs resulted in no change in TJ expression at gene and protein level (DeStefano, Xu et al. 2017). A variety of claudin subtypes are expressed in a tissue and cell specific manner at different stages of development of the BBB. They can be functionally divided into barrier forming/sealing claudins such as claudin -1, -3 and -5 (Gonçalves, Ambrósio et al. 2013). In this work, *CLDN4, CLDN8, CLDN15* and *CLDN24* was upregulated in both d17 static and d17 dynamic cultures in comparsion to d10 static samples. However, these changes were not significant. Genes coding for ABC transporters such as *ABCC1*, *ABCC4*, *ABCG2* were downregulated in both d17 static and d17 dynamic samples. Additionally, the cationic amino acid transporter *SLC7A1*, was significantly downregulated in d17 dynamic samples. Between both the samples d17 static and d17 dynamic significant changes were only observed in the expression of *ABCG2* and *LRP8*. Although similar to other studies overall low mRNA transcript abundance for BBB associated genes are observed in this work. Nevertheless, low shear stress levels evidently have an effect in iBCECs morphology and protein marker expression. Currently, it is however, unclear if perceived and reported transcriptional changes mirrors *in-vitro* culture conditions or low-transcript abundances (Faley, Neal et al. 2019).

13. FUTURE DIRECTIONS

In essence, no single *in-vitro* model or differentiation can perfectly replicate the complexity of the human body, let alone the BBB (Sharma, Sances et al. 2020). From an engineering perspective, BBB *in-vitro* models only need to recapitulate the particular function of interest and therefore should be engineered to answer specifc research questions (Linville and Searson 2021). However, when developed thoughtfully and accompanied with well-structured validation studies, *in-vitro* based models provide tools to study human physiology as well as to reduce the number of animals used in research. Thereby, the establishment of hiPSC-based model systems presented in this work can play a major role in the future of precision medicine (Arora, Mehta et al. 2011, Sharma, Sances et al. 2020). With regard to iBCECs, they are known to be enriched in pathways associated with cell proliferation, patterning, and ECM interactions which are reflective of cells at an earlier developmental stage (Workman and Svendsen 2020). While generating iBCECs it is imperative to dissect molecular cues of *in-vivo* developmental competence in order to drive iBCECs to a mature and specific cellular lineage (Peng, Tam et al. 2017). Some approaches include inhibiting TGF-β pathway using small molecules such as RepSox, A-83-01 or SB-431542 (Roudnicky, Zhang et al. 2020, Yamashita, Aoki et al. 2020). The issue with using these inhibitors is that they may additionally inhibit several other unknown pathways in addition to TGF-β signaling (Roudnicky, Zhang et al. 2020). In mice, high expression of transcription factors (TFs) Forkhead Box F2 (Foxf2), Forkhead Box Q1 (Foxq1*)* or Zic Family Member 3 (Zic3) transcripts correlate with increased expression of genes encoding BCEC lineage specification (Hupe, Li et al. 2017). Overexpression of these candidate TFs already paves the way for derivation of robust differentiation strategies. Although Foxf2 overexpression induces expression of several important BCEC tight junctions, only a modest effect in increasing the barrier integrity in addition to lower expression of claudin-5 was reported in iBCECs. Zic3 on the other hand induces PECAM-1, but with no change or increase in barrier integrity of iBCECs (Roudnicky, Zhang et al. 2020). Members of the Wnt/β-catenin signaling pathway are driving force in CNS specific angiogenesis and regulating BBB formation, post natal maturation and maintenance (Daneman, Agalliu et al. 2009, Liebner and Plate 2010). Wnt7A and Wnt7B are proposed to directly act on the CNS endothelium via the canonical Wnt signaling pathway to promote BCEC angiogenesis and early BBB differentiation *in-vivo* (Laksitorini, Yathindranath et al. 2019, Guérit, Fidan et al. 2021). During canonical Wnt signaling, Wnt ligands bind to Frizzled/LRP receptor complexes, thereby stabilizing β-catenin, which would otherwise be degraded by Axin/GSK-3/anaphase-promoting complexes. This stabilized β-catenin then translocates into the nucleus and via interactions with the T-cell factor/lymphoid enhancer factor complexes, regulating the expression of BBB specific genes

(Logan and Nusse 2004). One key to specification of iBCECs into a mature phenotype would be to achieve continuous stabilization of β-catenin. Studies show that simple supplementation of culture medium with Wnt lignads such as Wnt7A and Wnt7B is largely ineffective in activating Wnt/β-catenin signaling in iBCECs as Wnt ligands are known to have low solubility (Gastfriend, Nishihara et al. 2021). However, using direct co-cultures of endogenously Wnt-producing cells such as NPCs and ACs would be key in achieving iBCEC maturity *in-vitro* (Gastfriend, Nishihara et al. 2021, Guérit, Fidan et al. 2021). Furthermore, it is critical to remember that *in-vivo*, the BBB does not exist as a single entitiy, but as a complex with constant cross talk with the NVU and blood flow. Thereby increasing direct cellular contact in spheroid formats and induction of physiological flow would help in maturation of iBCECs. Apart from that, it should be noted that iBCECs are suggested to be more appropriately referred to as hiPSC derived BCEC-*like* cells (Lippmann, Azarin et al. 2020).

With regard to BBB spheroids, the work in this thesis reports for the first time generation of spheroids with an hiPSC origin, as all previous reports pertain to spheroids developed using cells of immortalized or primary origin (Urich, Patsch et al. 2013, Cho, Wolfe et al. 2017, Kitamura, Umehara et al. 2021). The work performed here has successfully identified the optimal hiPSC differentiation strategy, for derivation of iBCECs, useful in generating BBB spheroids. The spheroids were further validated for possession of hallmark BBB characteristics in terms of marker expression and barrier integrity via EIS measurements and evidence of low permeability to a small molecule tracer. The path to fully understand the application potential of this model is still in its infancy, but the possibilities are immense. The next steps would include addressing the standardized production of spheroids with high reproducibility in medium- to high-throughput formats, using robotic systems and introduction of fluidic shear stresses (Eilenberger, Rothbauer et al. 2021). It would further be important to assess how the spheroids can be used as an *in-vitro* screening platform for brain-penetrating molecules such as cell penetrating peptides, antibodies, nanotherapeutics including identification of efflux pump activities, as previously reported in spheroids of immortalized or primary cell origin (Cho, Wolfe et al. 2017, Kumarasamy and Sosnik 2021, Kitamura, Okamoto et al. 2022). Key strategies in future include the identification of spheroid penetrating capabilities of a broad spectrum of drug candidates namely, Pemetrexed (*Trade name: Alimta*), p-Chlorophenylalanine (*Trade name: Fenclonine*), Sulfasalazine (*Trade name: Azulfidine*), 6-NBGD (*Fluorescent d-glucose analog, for uptake studies*), Hydrocholothiazide *(Trade name: Apo-hydro)*, Loperamide *(Trade name: Imodium)*, 6-Caboxyfluorescein (*Fluorescent tracer)*, Thiamine *(Trade name: Thiamilate)* via Papp calculations. Here, calculation of absolute Papp values can aid correlation to other *in-vitro* BBB models. Assays will additionally be established to identify if calculation of drug pharmacokinetics via estimation of $K_{p,uu}$ will correlate with *in-vivo* rodent studies. Additionally, identification of penetration of macromolecules, specifically

of Tfr specific antibodies will be investigated via high throughput automation microscopic techniques and enzyme-linked immunosorbent assays. It is important to note that visualization of complete spheroids via traditional CLSM has been difficult. This can be overcome via application of tissue clearing techniques and light sheet microscopy. Two other unexplored applications of BBB spheroids will be the investigation of mechanisms involving pathogenic invasions of the BBB and identification of specific ECM components and interactions that allows for the self-assembly. Additional investigations can include identification of possibilities for spheroids to be cryopreserved such that they can be delivered in ready to use kit formats. Conjointly the culminating aim would be to generate a fully characteritzed and functional isogenic BBB spheroid, which would hold potential in personalized drug delivery strategies into the human brain. Isogenic spheroids would further enable understanding of patient specifc responses to drugs as well as disease specific changes to the NVU The work presented here only included characterizations and outlooks pertaining to iBCECs, however NPCs, ACs and PCs are in-corporated into the spheroids. Investigation of specific functions and interactions of these cell types remains highly unexplored. An additional novel prospect could be assembly of BBB spheroids via 3-D printing to generate tubes with defined dimensions, these assembled tubes could essentially provide to be capillary structures which could be further encorporated into brain organoids or tumoroids, essentially to mimic the often lacking vasculature in such systems. To conclude, spheroidal models of the BBB provide an exponential boost in not only modelling the BBB, but also the NVU.

The work conducted in this thesis further identifies that prolonged culture, dynamic flow and shear stresses, even at minimal rates induces maturation in iBCECs. The bioreactor system could provide an *in-vivo* like environment for further growth of iBCECs with long-term stability. In essence, this may even be the missing stimulis and link in correct lineage specification of iBCECs. It is important to note that this work has not investigated the effects of different flow rates, shear stresses and substrate rigidity. One future possibility could be the examination of iBCEC changes to these parameters.

With regard to tissue specific substrates, the possibility of iBCEC cultivation on soft hydrogels and synthetically modified substrates with tri-amino acid sequence, arginine-glycine-aspartate (RGD) and resulting changes due to variations in matrix stiffness could be investigated. The next steps would also include the addition of potential co-culture NVU cells on the chip membranes to assess their influence on iBCECs. Apart from that, mechanobiology of iBCECs remains relatively unexplored. It is still unknown how mechanical stimuli exterted on iBCECs are converted into intracellular biochemical responses. Here it could be a possibility to explore mechanosensitive ion channels, receptors and cell-ECM interactions (Janmey and McCulloch 2007). Abruptly stopping the flow in the bioreactors could also find a potential application in modelling BBB pathology *in-vitro*, similar to the i*n-vivo* situation in ischemic stroke. One

important parameter that is missing is the possibility to perform soulute permeability studies in organ-on- a-chip formats. Here it is important to forsee limitations such as attachement of hydrophilic compounds onto the pumps of the system and. To validate the physicological relevance of this shear stress based model, the passage of different passively or activtily transporterd substances will have to be tested and reported using suitable protocols (van der Helm, van der Meer et al. 2016).

14. AFFIDAVIT

I hereby confirm that my thesis entitiled ***"Development of blood-brain barrier spheroid models based on human induced pluripotent stem cells (hiPSCs) and investigation of shear stress on hiPSC-derived brain capillary endothelial-like cells"*** is the result of my own work. I did not receive any help or support from commercial consultants. All sources and or materials applied are listed and specified in the thesis.

Furthermore, I confirm that this thesis has not yet been submitted as part of another examination process neither in identical nor in similar form.

Place, Date Signature

Eidesstattliche Erklärung

Hiermit erkläre ich an Eides statt, die Dissertation eigenständig,***"Entwicklung von Sphäroid-Modellen der Blut-Hirn-Schranke basierend auf menschlichen induzierten pluripotenten Stammzellen (hiPSCs) und Untersuchung der Scherbeanspruchung von hiPSC-abgeleiteten Hirnkapillarendothel-ähnlichen Zellen"*** insbesondere selbständig und ohne Hilfe eines kommerziellen Promotionsberaters, angefertigt und keine anderen als die von mir angegebenen Quellen und Hilfsmittel verwendet zu haben.

Ich erkläre außerdem, dass die Dissertation weder in gleicher noch in ähnlicher Form bereits in einem anderen Prüfungsverfahren vorgelegen hat.

Place, Date Signature

15. LIST OF THESIS PUBLICATIONS

The work of this thesis will and have been included in the following publications

Accepted publications

- Choi, J., **S. Mathew**, S. Oerter, A. Appelt-Menzel, J. Hansmann and T. Schmitz (2022). "Online Measurement System for Dynamic Flow Bioreactors to Study Barrier Integrity of hiPSC-Based Blood-Brain Barrier In Vitro Models." Bioengineering (Basel) **9**(1).

- Appelt-Menzel, A., S. Oerter, **S. Mathew**, U. Haferkamp, C. Hartmann, M. Jung, W. Neuhaus and O. Pless (2020). "Human iPSC-Derived Blood-Brain Barrier Models: Valuable Tools for Preclinical Drug Discovery and Development?" Curr Protoc Stem Cell Biol **55**(1): e122.

Publications in preparation

- Advances in blood-brain barrier in-vitro modelling: Are multicellular spheroids the future?
  Authors: **Sanjana Mathew-Schmitt,** Sabrina Oerter, Sabine Gätzner, Evelin Reitenbach, Jörg Piontek, Heinz-Georg Jahnke, Paul Lutz, Winfried Neuhaus, Marco-Metzger, Antje Appelt-Menzel

- Shear stress related changes in hiPSC derived BCECs
  Authors: **Sanjana Mathew-Schmitt,** Markus Glaser, Sabrina Oerter, Katharina Müller, Antje Appelt-Menzel

16. LIST OF THESIS CONFERENCE PRESENTATIONS

- **2022:** Hengstberger symposium brain barriers in CNS diseases**,** novel therapeutic strategies and drug delivery approaches.
  Talk title: "*Shear induced changes in long-term culture of hiPSC-derived BCECs"*

- **2021**: 23rd International Symposium on Signal Transduction at the Blood-Brain Barriers, Virtual.
  Talk title: "*Novel hiPSC based spheroid model of the blood-brain barrier"*

- **2021:** 10th International Meeting-From Fundamental Biology to Translational Concepts, Virtual Conference Stem Cell Network North Rhine-Westphalia.
  Pitch title: "*Online impedance measurement system in a dynamic flow bioreactor to study barrier integrity of iPSC –based blood brain barrier in-vitro models"*

- **2019:** 22nd International Symposium on Signal Transduction at the Blood-Brain Barriers, Germany.
  Poster title: "*Novel hiPSC based spheroid model of the blood-brain barrier"*
  Poster title: "*Generation of a blood brain barrier spheroid model using hiPSC derived endothelial cells"*

- **2018:** 21st International symposium on Signal transduction at the blood brain barriers, Romania.
  Poster title: "*New insights into the human blood brain barrier, novel iPSC-based in-vitro models, culture systems and non-invasive characterization methods"*

17. ACKNOWLEDGEMENTS

I express my gratitude to my primary and secondary thesis supervisors PD Dr. Marco Metzger and Prof. Dr. Heike Walles for providing me the opportunity to complete my doctoral thesis at the Chair of Tissue Engineering and Regenerative Medicine (TERM), Würzburg, and additionally for their scientific guidance and time invested in my thesis. I extend my gratitude to my third supervisor Prof. Paul Dalton for suggestions and feedback during my annual reports. I would like to express my deepest gratitude to my fourth supervisor Dr. Antje Appelt-Menzel for giving me the chance to be a part of the blood-brain barrier group and especially for her dedicated support, guidance and review of my work. I am greatful that you took me under your wing. Your leadership and example has helped me grow. Your attention to detail is astounding and I am happy that I could learn this from you. I extend my gratitude to Dr. Sabrina Oerter for her patience, encouragement and review of my work. I am lucky to have both of you as my mentors since you invested your time in my work, taking special care, discussing critical experiments, desgining studies together and responding to my questions promptly. Not only have you fantastically mentored me, but you have also taught me how to mentor other students. I have learnt many remarkable qualities from both of you. I am greatful for your help and the success of this thesis is due to your constant support and guidance. Thank you for being great role models. I would like to additionally thank Alevtina Cubukova, Sabine Gätzner, Evelin Reitenbach, Markus Glaser and my students Simone Buchmann and Katharina Müller whose contributions are included in this work. Special thanks to Prof. Jan Hansmann, Dr. Tobias Schmitz and Ms. Jihyoung Choi for their cooperation resulting in a joint publication. I am extremely greatful to Dr. Heinz-Georg Jahnke and Dr. Jörg Piontek for offering their expertise, valuable discussions, prompt replies and insights. Thanks to Prof. Dr. Winfried Neuhaus for his collaborations. This work could not have been possible without the funding received by the graduate school of life sciences (GSLS) and SCIENTIA stipends offered by the University of Würzburg and the European Union's Horizon 2020 research and innovation program and EFPIA members within the IMI project IM^{2}PACT (Proposal number 807015-2).

I extend my gratitude to all members of the iPSC weekend duty. Thank you for your time and service. Apart from that I also thank all my colleagues at TERM who enabled

a positive and fun work environment. Special thanks to Anna Stefl and Özlem Elbert, for helping me with organizational matters. I would like to extend my gratitude to Dr. Christina Fey, Dr. Constantin Berger and Dr. Tobias Weigel and who are ever helpful in the laboratory and available for scientific discussions. Thank you to Dr. Joachim Nickel, Dr. Daniela Zdzieblo, Dr. Gudrun Dandekar, Heike Oberwinkler, Heidi Linß, Spyros Damigos and Silke Spudeit for interesting conversations. Lastly, I would like to thank you whole heartedly Matthias Peindl for supporting me with the internal seed grant. I have learnt a lot from you, thank you once again for sticking up for me (inside joke: did I stutter?).

Completing my dissertation required more than academic support, and I thank my friends and family for listening to and supporting me over the years. I express my gratitude and appreciation for their presence. Markus and Claudia thank you for your friendship and memorable evenings, especially when I was new to the city, and also for the wine. Even though I may not say it all the time, I appreciate all you do Kessie. Thank you Ezgi, Rita and Manli for your constant support and evening chats. Thank you Mimi for ever being my confidant and voice of motivation. Most importantly, none of this could have happened without my family. Dearest Appa and Amma, thank you always for your unconditional selflessness, countless sacrifices, values you instilled in me and support for my education which has opened several doors for me to grow and succeed, I hope I make you proud, you are the best parents in the world. Thank you Soppu for reminding me to take breaks and have fun when I was stressed out and Jive and Mary-Ann for taking care of me. I am indebted to my husband Tobi for his constant support and motivation. Whenever I was ready to quit you were always by my side motivating me, just like you never gave up on me as we climbed the Hoher Freschen. Thank you for believing in me and being by my side, with you beside me I can face every hurdle in life. Thank you for being my rock, it is a true blessing to have you as my life partner. Lastly, I am grateful to God for the good health, wellbeing and blessings I have received.

18. REFERENCES

Aazmi, A., H. Zhou, W. Lv, M. Yu, X. Xu, H. Yang, Y. S. Zhang and L. Ma (2022). "Vascularizing the brain in vitro." iScience **25**(4): 104110.

Abbott, N. J., D. E. Dolman, S. R. Yusof and A. J. D. D. t. t. b. Reichel (2014). "In vitro models of CNS barriers." 163-197.

Abbott, N. J. and A. Friedman (2012). "Overview and introduction: the blood-brain barrier in health and disease." Epilepsia **53 Suppl 6**: 1-6.

Abbott, N. J., A. A. Patabendige, D. E. Dolman, S. R. Yusof and D. J. J. N. o. d. Begley (2010). "Structure and function of the blood–brain barrier." **37**(1): 13-25.

Abbott, N. J., L. Ronnback and E. Hansson (2006). "Astrocyte-endothelial interactions at the blood-brain barrier." Nat Rev Neurosci **7**(1): 41-53.

Achilli, T. M., J. Meyer and J. R. Morgan (2012). "Advances in the formation, use and understanding of multi-cellular spheroids." Expert Opin Biol Ther **12**(10): 1347-1360.

Aday, S., R. Cecchelli, D. Hallier-Vanuxeem, M. P. Dehouck and L. Ferreira (2016). "Stem Cell-Based Human Blood-Brain Barrier Models for Drug Discovery and Delivery." Trends Biotechnol **34**(5): 382-393.

Ahn, J., K. B. Jung, O. Kwon, M.-S. Choi, J.-H. Ahn, H.-Y. Han, C.-R. Jung, S. Yoon, M.-Y. Son and J.-H. Oh (2021). "Impedance Measurement System for Assessing the Barrier Integrity of Three-Dimensional Human Intestinal Organoids." Analytical Chemistry **93**(25): 8826-8834.

Albert-Smet, I., A. Marcos-Vidal, J. J. Vaquero, M. Desco, A. Muñoz-Barrutia and J. J. F. i. n. Ripoll (2019). "Applications of light-sheet microscopy in microdevices." **13**: 1.

Alimonti, J. B., M. Ribecco-Lutkiewicz, C. Sodja, A. Jezierski, D. B. Stanimirovic, Q. Liu, A. S. Haqqani, W. Conlan and M. Bani-Yaghoub (2018). "Zika virus crosses an in vitro human blood brain barrier model." Fluids and Barriers of the CNS **15**(1): 15.

Amasheh, S., T. Schmidt, M. Mahn, P. Florian, J. Mankertz, S. Tavalali, A. H. Gitter, J.-D. Schulzke, M. J. C. Fromm and t. research (2005). "Contribution of claudin-5 to barrier properties in tight junctions of epithelial cells." **321**(1): 89-96.

Andrews, A. M., E. M. Lutton, L. A. Cannella, N. Reichenbach, R. Razmpour, M. J. Seasock, S. J. Kaspin, S. F. Merkel, D. Langford, Y. Persidsky and S. H. Ramirez (2018). "Characterization of human fetal brain endothelial cells reveals barrier properties suitable for in vitro modeling of the BBB with syngenic co-cultures." J Cereb Blood Flow Metab **38**(5): 888-903.

Appelt-Menzel, A., A. Cubukova, K. Günther, F. Edenhofer, J. Piontek, G. Krause, T. Stüber, H. Walles, W. Neuhaus and M. Metzger (2017). "Establishment of a Human Blood-Brain Barrier Co-culture Model Mimicking the Neurovascular Unit Using Induced Pluri- and Multipotent Stem Cells." Stem Cell Reports **8**(4): 894-906.

Appelt-Menzel, A., A. Cubukova and M. Metzger (2018). "Establishment of a Human Blood-Brain Barrier Co-Culture Model Mimicking the Neurovascular Unit Using Induced Pluripotent Stem Cells." Curr Protoc Stem Cell Biol **47**(1): e62.

Appelt-Menzel, A., S. Oerter, S. Mathew, U. Haferkamp, C. Hartmann, M. Jung, W. Neuhaus and O. Pless (2020). "Human iPSC-Derived Blood-Brain Barrier Models: Valuable Tools for Preclinical Drug Discovery and Development?" Curr Protoc Stem Cell Biol **55**(1): e122.

Arora, T., A. K. Mehta, V. Joshi, K. D. Mehta, N. Rathor, P. K. Mediratta and K. K. Sharma (2011). "Substitute of Animals in Drug Research: An Approach Towards Fulfillment of 4R's." Indian J Pharm Sci **73**(1): 1-6.

Aryal, M., K. Fischer, C. Gentile, S. Gitto, Y. Z. Zhang and N. McDannold (2017). "Effects on P-Glycoprotein Expression after Blood-Brain Barrier Disruption Using Focused Ultrasound and Microbubbles." PLoS One **12**(1): e0166061.

Bagnaninchi, P. O. and N. Drummond (2011). "Real-time label-free monitoring of adipose-derived stem cell differentiation with electric cell-substrate impedance sensing." Proc Natl Acad Sci U S A **108**(16): 6462-6467.

Balistreri, C. R., E. De Falco, A. Bordin, O. Maslova, A. Koliada and A. Vaiserman (2020). "Stem cell therapy: old challenges and new solutions." Mol Biol Rep **47**(4): 3117-3131.

Barar, J., M. A. Rafi, M. M. Pourseif and Y. Omidi (2016). "Blood-brain barrier transport machineries and targeted therapy of brain diseases." Bioimpacts **6**(4): 225-248.

Barisam, M., M. S. Saidi, N. Kashaninejad and N. T. Nguyen (2018). "Prediction of Necrotic Core and Hypoxic Zone of Multicellular Spheroids in a Microbioreactor with a U-Shaped Barrier." Micromachines (Basel) **9**(3).

Bauer, H. C., I. A. Krizbai, H. Bauer and A. Traweger (2014). ""You Shall Not Pass"-tight junctions of the blood brain barrier." Front Neurosci **8**: 392.

Bautch, V. L. and J. M. James (2009). "Neurovascular development: The beginning of a beautiful friendship." Cell Adh Migr **3**(2): 199-204.

Bayir, E. and A. Sendemir (2021). "Role of Intermediate Filaments in Blood-Brain Barrier in Health and Disease." Cells **10**(6).

Begley, D. J., M. W. J. P. t. Brightman and d. i. t. c. n. system (2003). "Structural and functional aspects of the blood-brain barrier." 39-78.

Bell, A. H., S. L. Miller, M. Castillo-Melendez and A. Malhotra (2019). "The Neurovascular Unit: Effects of Brain Insults During the Perinatal Period." Front Neurosci **13**: 1452.

Bellettato, C. M. and M. Scarpa (2018). "Possible strategies to cross the blood-brain barrier." Ital J Pediatr **44**(Suppl 2): 131.

Belvitch, P., Y. M. Htwe, M. E. Brown and S. Dudek (2018). "Cortical Actin Dynamics in Endothelial Permeability." Curr Top Membr **82**: 141-195.

Ben-David, U., N. Nudel and N. Benvenisty (2013). "Immunologic and chemical targeting of the tight-junction protein Claudin-6 eliminates tumorigenic human pluripotent stem cells." Nature Communications **4**(1): 1992.

Bennett, H. C. and Y. Kim (2021). "Pericytes Across the Lifetime in the Central Nervous System." Front Cell Neurosci **15**: 627291.

Benson, K., S. Cramer and H. J. Galla (2013). "Impedance-based cell monitoring: barrier properties and beyond." Fluids Barriers CNS **10**(1): 5.

Bergmann, S., S. E. Lawler, Y. Qu, C. M. Fadzen, J. M. Wolfe, M. S. Regan, B. L. Pentelute, N. Y. R. Agar and C.-F. Cho (2018). "Blood–brain-barrier organoids for investigating the permeability of CNS therapeutics." Nature Protocols **13**(12): 2827-2843.

Bernas, M. J., F. L. Cardoso, S. K. Daley, M. E. Weinand, A. R. Campos, A. J. Ferreira, J. B. Hoying, M. H. Witte, D. Brites, Y. Persidsky, S. H. Ramirez and M. A. Brito (2010). "Establishment of primary cultures of human brain microvascular endothelial cells to provide an in vitro cellular model of the blood-brain barrier." Nat Protoc **5**(7): 1265-1272.

Berndt, P., L. Winkler, J. Cording, O. Breitkreuz-Korff, A. Rex, S. Dithmer, V. Rausch, R. Blasig, M. Richter, A. Sporbert, H. Wolburg, I. E. Blasig and R. F. Haseloff (2019). "Tight junction proteins at the blood-brain barrier: far more than claudin-5." Cell Mol Life Sci **76**(10): 1987-2002.

Bertuzzi, A., A. Fasano, A. Gandolfi and C. Sinisgalli (2010). "Necrotic core in EMT6/Ro tumour spheroids: Is it caused by an ATP deficit?" J Theor Biol **262**(1): 142-150.

Bhalerao, A., F. Sivandzade, S. R. Archie, E. A. Chowdhury, B. Noorani and L. Cucullo (2020). "In vitro modeling of the neurovascular unit: advances in the field." Fluids Barriers CNS **17**(1): 22.

Blanchette, M. and R. Daneman (2015). "Formation and maintenance of the BBB." Mech Dev **138 Pt 1**: 8-16.

Butt, A. M., H. C. Jones and N. J. Abbott (1990). "Electrical resistance across the blood-brain barrier in anaesthetized rats: a developmental study." J Physiol **429**: 47-62.

Cabezas, R., M. Avila, J. Gonzalez, R. S. El-Bachá, E. Báez, L. M. García-Segura, J. C. Jurado Coronel, F. Capani, G. P. Cardona-Gomez and G. E. Barreto (2014). "Astrocytic modulation of blood brain barrier: perspectives on Parkinson's disease." Front Cell Neurosci **8**: 211.

Canfield, S. G., M. J. Stebbins, B. S. Morales, S. W. Asai, G. D. Vatine, C. N. Svendsen, S. P. Palecek and E. V. Shusta (2017). "An isogenic blood-brain barrier model comprising brain endothelial cells, astrocytes, and neurons derived from human induced pluripotent stem cells." J Neurochem **140**(6): 874-888.

Carman, C. V. (2009). "Mechanisms for transcellular diapedesis: probing and pathfinding by 'invadosome-like protrusions'." J Cell Sci **122**(Pt 17): 3025-3035.

Carpenter, Timothy S., Daniel A. Kirshner, Edmond Y. Lau, Sergio E. Wong, Jerome P. Nilmeier and Felice C. Lightstone (2014). "A Method to Predict Blood-Brain Barrier Permeability of Drug-Like Compounds Using Molecular Dynamics Simulations." Biophysical Journal **107**(3): 630-641.

Chalcroft, J. and S. J. T. J. o. c. b. Bullivant (1970). "An interpretation of liver cell membrane and junction structure based on observation of freeze-fracture replicas of both sides of the fracture." **47**(1): 49-60.

Cho, C.-F., J. M. Wolfe, C. M. Fadzen, D. Calligaris, K. Hornburg, E. A. Chiocca, N. Y. R. Agar, B. L. Pentelute and S. E. Lawler (2017). "Blood-brain-barrier spheroids as an in vitro screening platform for brain-penetrating agents." Nature Communications **8**(1): 15623.

Choi, J., S. Mathew, S. Oerter, A. Appelt-Menzel, J. Hansmann and T. Schmitz (2022). "Online Measurement System for Dynamic Flow Bioreactors to Study Barrier Integrity of hiPSC-Based Blood-Brain Barrier In Vitro Models." Bioengineering (Basel) **9**(1).

Chugh, P. and E. K. Paluch (2018). "The actin cortex at a glance." J Cell Sci **131**(14).

Coelho-Santos, V. and A. Y. Shih (2020). "Postnatal development of cerebrovascular structure and the neurogliovascular unit." Wiley Interdiscip Rev Dev Biol **9**(2): e363.

Coisne, C., L. Dehouck, C. Faveeuw, Y. Delplace, F. Miller, C. Landry, C. Morissette, L. Fenart, R. Cecchelli, P. Tremblay and B. Dehouck (2005). "Mouse syngenic in vitro blood-brain barrier model: a new tool to examine inflammatory events in cerebral endothelium." Lab Invest **85**(6): 734-746.

Crone, C. and S. P. Olesen (1982). "Electrical resistance of brain microvascular endothelium." Brain Res **241**(1): 49-55.

Cucullo, L., M. Hossain, V. Puvenna, N. Marchi and D. Janigro (2011). "The role of shear stress in Blood-Brain Barrier endothelial physiology." BMC Neurosci **12**: 40.

Curto, V. F., M. P. Ferro, F. Mariani, E. Scavetta and R. M. Owens (2018). "A planar impedance sensor for 3D spheroids." Lab Chip **18**(6): 933-943.

Daley, G. Q. (2015). "Stem cells and the evolving notion of cellular identity." Philos Trans R Soc Lond B Biol Sci **370**(1680): 20140376.

Daneman, R. (2012). "The blood-brain barrier in health and disease." Ann Neurol **72**(5): 648-672.

Daneman, R., D. Agalliu, L. Zhou, F. Kuhnert, C. J. Kuo and B. A. J. P. o. t. N. A. o. S. Barres (2009). "Wnt/β-catenin signaling is required for CNS, but not non-CNS, angiogenesis." **106**(2): 641-646.

Daneman, R. and A. Prat (2015). "The blood-brain barrier." Cold Spring Harb Perspect Biol **7**(1): a020412.

Daneman, R., L. Zhou, D. Agalliu, J. D. Cahoy, A. Kaushal and B. A. J. P. o. Barres (2010). "The mouse blood-brain barrier transcriptome: a new resource for understanding the development and function of brain endothelial cells." **5**(10): e13741.

Daneman, R., L. Zhou, A. A. Kebede and B. A. Barres (2010). "Pericytes are required for blood-brain barrier integrity during embryogenesis." Nature **468**(7323): 562-566.

Danz, K., T. Höcherl, S. L. Wien, L. Wien, H. von Briesen and S. Wagner (2022). "Experimental Comparison of Primary and hiPS-Based In Vitro Blood-Brain Barrier Models for Pharmacological Research." Pharmaceutics **14**(4).

Daood, M., C. Tsai, M. Ahdab-Barmada and J. F. J. N. Watchko (2008). "Abc transporter (P-Gp/Abcb1, Mrp1/Abcc1, Bcrp/Abcg2) expression in the developing human Cns." **39**(04): 211-218.

de Lange, E. C. and M. Hammarlund-Udenaes (2015). "Translational aspects of blood-brain barrier transport and central nervous system effects of drugs: from discovery to patients." Clin Pharmacol Ther **97**(4): 380-394.

DeCicco-Skinner, K. L., G. H. Henry, C. Cataisson, T. Tabib, J. C. Gwilliam, N. J. Watson, E. M. Bullwinkle, L. Falkenburg, R. C. O'Neill, A. Morin and J. S. Wiest (2014). "Endothelial cell tube formation assay for the in vitro study of angiogenesis." J Vis Exp(91): e51312.

Dehouck, M.-P., E. Vandenhaute, L. Dehouck, E. Sevin, A.-M. Lenfant, Y. Delplace, D. Hallier-Vanuxeem, M. Culot and R. Cecchelli (2011). Modelling the blood–brain barrier. Cell Culture Techniques, Springer**:** 145-160.

Deinsberger, J., D. Reisinger and B. Weber (2020). "Global trends in clinical trials involving pluripotent stem cells: a systematic multi-database analysis." npj Regenerative Medicine **5**(1): 15.

del Amo, E. M., A. Urtti and M. J. E. J. o. P. S. Yliperttula (2008). "Pharmacokinetic role of L-type amino acid transporters LAT1 and LAT2." **35**(3): 161-174.

Deli, M. A., C. S. Abrahám, Y. Kataoka and M. Niwa (2005). "Permeability studies on in vitro blood-brain barrier models: physiology, pathology, and pharmacology." Cell Mol Neurobiol **25**(1): 59-127.

Delsing, L., P. Dönnes, J. Sánchez, M. Clausen, D. Voulgaris, A. Falk, A. Herland, G. Brolén, H. Zetterberg, R. Hicks and J. Synnergren (2018). "Barrier Properties and Transcriptome Expression in Human iPSC-Derived Models of the Blood-Brain Barrier." Stem Cells **36**(12): 1816-1827.

Denis, C. V. (2002). "Molecular and cellular biology of von Willebrand factor." Int J Hematol **75**(1): 3-8.

Dessalles, C. A., C. Leclech, A. Castagnino and A. I. Barakat (2021). "Integration of substrate- and flow-derived stresses in endothelial cell mechanobiology." Communications Biology **4**(1): 764.

DeStefano, J. G., Z. S. Xu, A. J. Williams, N. Yimam and P. C. Searson (2017). "Effect of shear stress on iPSC-derived human brain microvascular endothelial cells (dhBMECs)." Fluids Barriers CNS **14**(1): 20.

Di Marco, A., D. Vignone, O. Gonzalez Paz, I. Fini, M. R. Battista, A. Cellucci, E. Bracacel, G. Auciello, M. Veneziano, V. Khetarpal, M. Rose, A. Rosa, I. Gloaguen, E. Monteagudo, T. Herbst, C. Dominguez and I. Muñoz-Sanjuán (2020). "Establishment of an in Vitro Human Blood-Brain Barrier Model Derived from Induced Pluripotent Stem Cells and Comparison to a Porcine Cell-Based System." **9**(4): 994.

Dolgikh, E., I. A. Watson, P. V. Desai, G. A. Sawada, S. Morton, T. M. Jones and T. J. Raub (2016). "QSAR Model of Unbound Brain-to-Plasma Partition Coefficient, Kp,uu,brain: Incorporating P-glycoprotein Efflux as a Variable." Journal of Chemical Information and Modeling **56**(11): 2225-2233.

Dore-Duffy, P., A. Katychev, X. Wang and E. Van Buren (2006). "CNS microvascular pericytes exhibit multipotential stem cell activity." J Cereb Blood Flow Metab **26**(5): 613-624.
Edmondson, R., J. J. Broglie, A. F. Adcock and L. Yang (2014). "Three-dimensional cell culture systems and their applications in drug discovery and cell-based biosensors." Assay Drug Dev Technol **12**(4): 207-218.

Ehrlich, P. J. E. F. S. (1885). "Das sauerstoff-bedurfnis des organismus."

Eilenberger, C., M. Rothbauer, F. Selinger, A. Gerhartl, C. Jordan, M. Harasek, B. Schadl, J. Grillari, J. Weghuber, W. Neuhaus, S. Kupcu and P. Ertl (2021). "A Microfluidic Multisize Spheroid Array for Multiparametric Screening of Anticancer Drugs and Blood-Brain Barrier Transport Properties." Adv Sci (Weinh) **8**(11): e2004856.

ElAli, A., P. Theriault and S. Rivest (2014). "The role of pericytes in neurovascular unit remodeling in brain disorders." Int J Mol Sci **15**(4): 6453-6474.

Faley, S. L., E. H. Neal, J. X. Wang, A. M. Bosworth, C. M. Weber, K. M. Balotin, E. S. Lippmann and L. M. Bellan (2019). "iPSC-Derived Brain Endothelium Exhibits Stable, Long-Term Barrier Function in Perfused Hydrogel Scaffolds." Stem Cell Reports **12**(3): 474-487.

Fawcett, D. W., & Bloom, W. (1994). Bloom and Fawcett, a textbook of histology.

Felix, K., S. Tobias, H. Jan, S. Nicolas and M. Michael (2021). "Measurements of transepithelial electrical resistance (TEER) are affected by junctional length in immature epithelial monolayers." Histochemistry and Cell Biology **156**(6): 609-616.

Förster, C., M. Burek, I. A. Romero, B. Weksler, P. O. Couraud and D. Drenckhahn (2008). "Differential effects of hydrocortisone and TNFalpha on tight junction proteins in an in vitro model of the human blood-brain barrier." J Physiol **586**(7): 1937-1949.

Fujiwara, I., S. Takeda, T. Oda, H. Honda, A. Narita and Y. Maéda (2018). "Polymerization and depolymerization of actin with nucleotide states at filament ends." Biophys Rev **10**(6): 1513-1519.

Furuse, M. (2010). "Molecular basis of the core structure of tight junctions." Cold Spring Harb Perspect Biol **2**(1): a002907.

Furuse, M., T. Hirase, M. Itoh, A. Nagafuchi, S. Yonemura, S. Tsukita and S. J. T. J. o. c. b. Tsukita (1993). "Occludin: a novel integral membrane protein localizing at tight junctions." **123**(6): 1777-1788.

Furuse, M., M. Itoh, T. Hirase, A. Nagafuchi, S. Yonemura, S. Tsukita and S. J. T. J. o. c. b. Tsukita (1994). "Direct association of occludin with ZO-1 and its possible involvement in the localization of occludin at tight junctions." **127**(6): 1617-1626.

Furuse, M., H. Sasaki and S. Tsukita (1999). "Manner of interaction of heterogeneous claudin species within and between tight junction strands." J Cell Biol **147**(4): 891-903.
Garberg, P., M. Ball, N. Borg, R. Cecchelli, L. Fenart, R. Hurst, T. Lindmark, A. Mabondzo, J. Nilsson and T. J. T. i. v. Raub (2005). "In vitro models for the blood–brain barrier." **19**(3): 299-334.

Gastfriend, B. D., H. Nishihara, S. G. Canfield, K. L. Foreman, B. Engelhardt, S. P. Palecek and E. V. Shusta (2021). "Wnt signaling mediates acquisition of blood–brain barrier properties in naïve endothelium derived from human pluripotent stem cells." eLife **10**: e70992.

Gastfriend, B. D., S. P. Palecek and E. V. Shusta (2018). "Modeling the blood-brain barrier: Beyond the endothelial cells." Curr Opin Biomed Eng **5**: 6-12.

Gavard, J. (2014). "Endothelial permeability and VE-cadherin: a wacky comradeship." Cell Adh Migr **8**(2): 158-164.

Geier, E. G., E. C. Chen, A. Webb, A. C. Papp, S. W. Yee, W. Sadee and K. M. Giacomini (2013). "Profiling solute carrier transporters in the human blood-brain barrier." Clin Pharmacol Ther **94**(6): 636-639.

Georgieva, J. V., D. Hoekstra and I. S. Zuhorn (2014). "Smuggling Drugs into the Brain: An Overview of Ligands Targeting Transcytosis for Drug Delivery across the Blood-Brain Barrier." Pharmaceutics **6**(4): 557-583.

Gerhart, D. Z., B. E. Enerson, O. Y. Zhdankina, R. L. Leino and L. R. Drewes (1997). "Expression of monocarboxylate transporter MCT1 by brain endothelium and glia in adult and suckling rats." Am J Physiol **273**(1 Pt 1): E207-213.

Ghersi-Egea, J. F., N. Strazielle, M. Catala, V. Silva-Vargas, F. Doetsch and B. Engelhardt (2018). "Molecular anatomy and functions of the choroidal blood-cerebrospinal fluid barrier in health and disease." Acta Neuropathol **135**(3): 337-361.

Giannotta, M., M. Trani and E. Dejana (2013). "VE-Cadherin and Endothelial Adherens Junctions: Active Guardians of Vascular Integrity." Developmental Cell **26**(5): 441-454.

Girard, S., I. Julien-Gau, Y. Molino, B. Combes, L. Greetham, M. Khrestchatisky and E. Nivet (2022). High and low permeability of human pluripotent stem cell-derived Blood Brain barrier models depend on epithelial or endothelial features, bioRxiv.

Gogia, S. and S. Neelamegham (2015). "Role of fluid shear stress in regulating VWF structure, function and related blood disorders." Biorheology **52**(5-6): 319-335.

Goldmann, E. E. (1913). Vitalfärbung am Zentralnervensystem: Beitrag zur Physio-Pathologie des Plexus chorioideus und der Hirnhäute, Königl. Akademie der Wissenschaften.
Gomez-Zepeda, D., M. Taghi, J. M. Scherrmann, X. Decleves and M. C. Menet (2019). "ABC Transporters at the Blood-Brain Interfaces, Their Study Models, and Drug Delivery Implications in Gliomas." Pharmaceutics **12**(1).

Gonçalves, A., A. F. Ambrósio and R. Fernandes (2013). "Regulation of claudins in blood-tissue barriers under physiological and pathological states." Tissue Barriers **1**(3): e24782.
Goncharov, N. V., A. D. Nadeev, R. O. Jenkins and P. V. Avdonin (2017). "Markers and Biomarkers of Endothelium: When Something Is Rotten in the State." Oxid Med Cell Longev **2017**: 9759735.

Goodwin-Trotman, M., K. Patel and A. Granata (2022). "An hiPSC-Derived In Vitro Model of the Blood-Brain Barrier." Methods Mol Biol **2492**: 103-116.

Govindarajan, R., A. H. Bakken, K. L. Hudkins, Y. Lai, F. J. Casado, M. Pastor-Anglada, C. M. Tse, J. Hayashi and J. D. Unadkat (2007). "In situ hybridization and immunolocalization of concentrative and equilibrative nucleoside transporters in the human intestine, liver, kidneys, and placenta." Am J Physiol Regul Integr Comp Physiol **293**(5): R1809-1822.

Greene, C., N. Hanley and M. Campbell (2019). Claudin-5: Gatekeeper of neurological function. Fluids and Barriers of the CNS, BioMed Central Ltd.

Greene, C., N. Hanley and M. Campbell (2020). "Blood-brain barrier associated tight junction disruption is a hallmark feature of major psychiatric disorders." Translational Psychiatry **10**(1): 373.

Grifno, G. N., A. M. Farrell, R. M. Linville, D. Arevalo, J. H. Kim, L. Gu and P. C. Searson (2019). "Tissue-engineered blood-brain barrier models via directed differentiation of human induced pluripotent stem cells." Sci Rep **9**(1): 13957.

Guérit, S., E. Fidan, J. Macas, C. J. Czupalla, R. Figueiredo, A. Vijikumar, B. H. Yalcin, S. Thom, P. Winter, H. Gerhardt, K. Devraj and S. Liebner (2021). "Astrocyte-derived Wnt growth factors are required for endothelial blood-brain barrier maintenance." Progress in Neurobiology **199**: 101937.

Gupta, M., T. Bogdanowicz, M. A. Reed, C. J. Barden and D. F. Weaver (2020). "The Brain Exposure Efficiency (BEE) Score." ACS Chemical Neuroscience **11**(2): 205-224.

Haddad-Tóvolli, R., N. R. V. Dragano, A. F. S. Ramalho and L. A. Velloso (2017). "Development and Function of the Blood-Brain Barrier in the Context of Metabolic Control." **11**.

Hagenbuch, B. and P. J. Meier (2003). "The superfamily of organic anion transporting polypeptides." Biochim Biophys Acta **1609**(1): 1-18.

Hagenbuch, B. and P. J. Meier (2004). "Organic anion transporting polypeptides of the OATP/ SLC21 family: phylogenetic classification as OATP/ SLCO superfamily, new nomenclature and molecular/functional properties." Pflugers Arch **447**(5): 653-665.

Hammarlund-Udenaes, M., M. Fridén, S. Syvänen and A. Gupta (2008). "On the rate and extent of drug delivery to the brain." Pharm Res **25**(8): 1737-1750.

Harris, E. S. and W. J. Nelson (2010). "VE-cadherin: at the front, center, and sides of endothelial cell organization and function." Curr Opin Cell Biol **22**(5): 651-658.

Hartmann, P., A. Ramseier, F. Gudat, M. J. Mihatsch and W. Polasek (1994). "[Normal weight of the brain in adults in relation to age, sex, body height and weight]." Pathologe **15**(3): 165-170.

Haudenschild, C. C. (1984). Morphology of vascular endothelial cells in culture. Biology of Endothelial Cells. E. A. Jaffe. Boston, MA, Springer US**:** 129-140.

Hawkins, B. T. and T. P. Davis (2005). "The blood-brain barrier/neurovascular unit in health and disease." Pharmacol Rev **57**(2): 173-185.

Hellinger, É., S. Veszelka, A. E. Tóth, F. Walter, Á. Kittel, M. L. Bakk, K. Tihanyi, V. Háda, S. Nakagawa, T. D. H. J. E. j. o. p. Duy and biopharmaceutics (2012). "Comparison of brain capillary endothelial cell-based and epithelial (MDCK-MDR1, Caco-2, and VB-Caco-2) cell-based surrogate blood–brain barrier penetration models." **82**(2): 340-351.

Helms, H. C., N. J. Abbott, M. Burek, R. Cecchelli, P.-O. Couraud, M. A. Deli, C. Förster, H. J. Galla, I. A. Romero, E. V. Shusta, M. J. Stebbins, E. Vandenhaute, B. Weksler and B. Brodin (2016). "In vitro models of the blood–brain barrier: An overview of commonly used brain endothelial cell culture models and guidelines for their use." Journal of Cerebral Blood Flow & Metabolism **36**(5): 862-890.

Helms, H. C., M. Hersom, L. B. Kuhlmann, L. Badolo, C. U. Nielsen and B. Brodin (2014). "An electrically tight in vitro blood-brain barrier model displays net brain-to-blood efflux of substrates for the ABC transporters, P-gp, Bcrp and Mrp-1." Aaps j **16**(5): 1046-1055.
Hervé, F., N. Ghinea and J. M. Scherrmann (2008). "CNS delivery via adsorptive transcytosis." Aaps j **10**(3): 455-472.

Hildebrandt, C., H. Büth, S. Cho, Impidjati and H. Thielecke (2010). "Detection of the osteogenic differentiation of mesenchymal stem cells in 2D and 3D cultures by electrochemical impedance spectroscopy." J Biotechnol **148**(1): 83-90.

Hladky, S. B. and M. A. Barrand (2016). "Fluid and ion transfer across the blood-brain and blood-cerebrospinal fluid barriers; a comparative account of mechanisms and roles." Fluids Barriers CNS **13**(1): 19.

Hogan, K. A., C. A. Ambler, D. L. Chapman and V. L. Bautch (2004). "The neural tube patterns vessels developmentally using the VEGF signaling pathway."

Hollmann, E. K., A. K. Bailey, A. V. Potharazu, M. D. Neely, A. B. Bowman and E. S. Lippmann (2017). "Accelerated differentiation of human induced pluripotent stem cells to blood–brain barrier endothelial cells." Fluids and Barriers of the CNS **14**(1): 9.

Hoshi, Y., Y. Uchida, M. Tachikawa, T. Inoue, S. Ohtsuki and T. Terasaki (2013). "Quantitative atlas of blood-brain barrier transporters, receptors, and tight junction proteins in rats and common marmoset." J Pharm Sci **102**(9): 3343-3355.

Hoshi, Y., Y. Uchida, M. Tachikawa, T. Inoue, S. Ohtsuki and T. J. J. o. p. s. Terasaki (2013). "Quantitative atlas of blood–brain barrier transporters, receptors, and tight junction proteins in rats and common marmoset." **102**(9): 3343-3355.

Hubbard, J. A., M. S. Hsu, M. M. Seldin and D. K. Binder (2015). "Expression of the Astrocyte Water Channel Aquaporin-4 in the Mouse Brain." ASN Neuro **7**(5).

Hupe, M., M. X. Li, S. Kneitz, D. Davydova, C. Yokota, J. Kele, B. Hot, J. M. Stenman and M. Gessler (2017). "Gene expression profiles of brain endothelial cells during embryonic development at bulk and single-cell levels." Sci Signal **10**(487).

Ihezie, S. A., I. E. Mathew, D. W. McBride, A. Dienel, S. L. Blackburn and P. K. Thankamani Pandit (2021). "Epigenetics in blood–brain barrier disruption." Fluids and Barriers of the CNS **18**(1): 17.

Ito, K., Y. Uchida, S. Ohtsuki, S. Aizawa, H. Kawakami, Y. Katsukura, J. Kamiie and T. Terasaki (2011). "Quantitative membrane protein expression at the blood-brain barrier of adult and younger cynomolgus monkeys." J Pharm Sci **100**(9): 3939-3950.

Jahnke, H.-G., A. Braesigk, T. G. A. Mack, S. Pönick, F. Striggow and A. A. Robitzki (2012). "Impedance spectroscopy based measurement system for quantitative and label-free real-time monitoring of tauopathy in hippocampal slice cultures." Biosensors and Bioelectronics **32**(1): 250-258.

Jahnke, H.-G., A. Mewes, F. D. Zitzmann, S. Schmidt, R. Azendorf and A. A. Robitzki (2019). "Electrochemical live monitoring of tumor cell migration out of micro-tumors on an innovative multiwell high-dense microelectrode array." Scientific Reports **9**(1): 13875.

Janmey, P. A. and C. A. McCulloch (2007). "Cell Mechanics: Integrating Cell Responses to Mechanical Stimuli." **9**(1): 1-34.

Janzer, R. C. and M. C. J. N. Raff (1987). "Astrocytes induce blood–brain barrier properties in endothelial cells." **325**(6101): 253-257.

Jia, W., T. A. Martin, G. Zhang and W. G. Jiang (2013). "Junctional adhesion molecules in cerebral endothelial tight junction and brain metastasis." Anticancer Res **33**(6): 2353-2359.

Kadry, H., B. Noorani and L. Cucullo (2020). "A blood–brain barrier overview on structure, function, impairment, and biomarkers of integrity." Fluids and Barriers of the CNS **17**(1): 69.

Kamiie, J., S. Ohtsuki, R. Iwase, K. Ohmine, Y. Katsukura, K. Yanai, Y. Sekine, Y. Uchida, S. Ito and T. Terasaki (2008). "Quantitative atlas of membrane transporter proteins: development and application of a highly sensitive simultaneous LC/MS/MS method combined with novel in-silico peptide selection criteria." Pharm Res **25**(6): 1469-1483.

Kamouchi, M., T. Ago, T. J. C. Kitazono and m. neurobiology (2011). "Brain pericytes: emerging concepts and functional roles in brain homeostasis." **31**(2): 175-193.

Kariolis, M. S., R. C. Wells, J. A. Getz, W. Kwan, C. S. Mahon, R. Tong, D. J. Kim, A. Srivastava, C. Bedard, K. R. Henne, T. Giese, V. A. Assimon, X. Chen, Y. Zhang, H. Solanoy, K. Jenkins, P. E. Sanchez, L. Kane, T. Miyamoto, K. S. Chew, M. E. Pizzo, N. Liang, M. E. K. Calvert, S. L. DeVos, S. Baskaran, S. Hall, Z. K. Sweeney, R. G. Thorne, R. J. Watts, M. S. Dennis, A. P. Silverman and Y. J. Y. Zuchero (2020). "Brain delivery of therapeutic proteins using an Fc fragment blood-brain barrier transport vehicle in mice and monkeys." Sci Transl Med **12**(545).

Katsuno, T., K. Umeda, T. Matsui, M. Hata, A. Tamura, M. Itoh, K. Takeuchi, T. Fujimori, Y. Nabeshima, T. Noda, S. Tsukita and S. Tsukita (2008). "Deficiency of zonula occludens-1 causes embryonic lethal phenotype associated with defected yolk sac angiogenesis and apoptosis of embryonic cells." Mol Biol Cell **19**(6): 2465-2475.

Katt, M. E., L. N. Mayo, S. E. Ellis, V. Mahairaki, J. D. Rothstein, L. Cheng, P. C. J. F. Searson and B. o. t. CNS (2019). "The role of mutations associated with familial neurodegenerative disorders on blood–brain barrier function in an iPSC model." **16**(1): 1-13.
Keller, A. (2013). "Breaking and building the wall: the biology of the blood-brain barrier in health and disease." Swiss Med Wkly **143**: w13892.

Khakh, B. S. and B. Deneen (2019). "The Emerging Nature of Astrocyte Diversity." Annu Rev Neurosci **42**: 187-207.

Kilpinen, H., A. Goncalves, A. Leha, V. Afzal, K. Alasoo, S. Ashford, S. Bala, D. Bensaddek, F. P. Casale, O. J. Culley, P. Danecek, A. Faulconbridge, P. W. Harrison, A. Kathuria, D. McCarthy, S. A. McCarthy, R. Meleckyte, Y. Memari, N. Moens, F. Soares, A. Mann, I. Streeter, C. A. Agu, A. Alderton, R. Nelson, S. Harper, M. Patel, A. White, S. R. Patel, L. Clarke, R. Halai, C. M. Kirton, A. Kolb-Kokocinski, P. Beales, E. Birney, D. Danovi, A. I. Lamond, W. H. Ouwehand, L. Vallier, F. M. Watt, R. Durbin, O. Stegle and D. J. Gaffney (2017). "Common genetic variation drives molecular heterogeneity in human iPSCs." Nature **546**(7658): 370-375.

Kim, B., O. Bee, M. McDonagh, M. Stebbins, S. Palecek, K. Doran and E. Shusta (2017). Modeling group B streptococcus and blood-brain barrier interaction by using induced pluripotent stem cell-derived brain endothelial cells. mSphere 2 (6): e00398-17.
Kim, B. J., M. A. McDonagh, L. Deng, B. D. Gastfriend, A. Schubert-Unkmeir, K. S. Doran and E. V. Shusta (2019). "Streptococcus agalactiae disrupts P-glycoprotein function in brain endothelial cells." Fluids and Barriers of the CNS **16**(1): 26.

Kim, J. Y., Y. Nam, Y. A. Rim and J. H. Ju (2022). "Review of the Current Trends in Clinical Trials Involving Induced Pluripotent Stem Cells." Stem Cell Reviews and Reports **18**(1): 142-154.

Kim, K., A. Doi, B. Wen, K. Ng, R. Zhao, P. Cahan, J. Kim, M. J. Aryee, H. Ji, L. I. Ehrlich, A. Yabuuchi, A. Takeuchi, K. C. Cunniff, H. Hongguang, S. McKinney-Freeman, O. Naveiras, T. J. Yoon, R. A. Irizarry, N. Jung, J. Seita, J. Hanna, P. Murakami, R. Jaenisch, R. Weissleder,

S. H. Orkin, I. L. Weissman, A. P. Feinberg and G. Q. Daley (2010). "Epigenetic memory in induced pluripotent stem cells." Nature **467**(7313): 285-290.

Kim, S., M. Uroz, J. L. Bays and C. S. Chen (2021). "Harnessing Mechanobiology for Tissue Engineering." Dev Cell **56**(2): 180-191.

Kitamura, K., A. Okamoto, H. Morio, R. Isogai, R. Ito, Y. Yamaura, S. Izumi, T. Komori, S. Ito, S. Ohtsuki, H. Akita and T. Furihata (2022). "Human Immortalized Cell-Based Blood–Brain Barrier Spheroid Models Offer an Evaluation Tool for the Brain Penetration Properties of Macromolecules." Molecular Pharmaceutics.

Kitamura, K., K. Umehara, R. Ito, Y. Yamaura, T. Komori, H. Morio, H. Akita and T. Furihata (2021). "Development, Characterization and Potential Applications of a Multicellular Spheroidal Human Blood-Brain Barrier Model Integrating Three Conditionally Immortalized Cell Lines." Biol Pharm Bull **44**(7): 984-991.

Kniesel, U., W. Risau and H. Wolburg (1996). "Development of blood-brain barrier tight junctions in the rat cortex." Brain Res Dev Brain Res **96**(1-2): 229-240.

Koepsell, H. (2020). "Glucose transporters in brain in health and disease." Pflügers Archiv - European Journal of Physiology **472**(9): 1299-1343.

Koepsell, H. and H. Endou (2004). "The SLC22 drug transporter family." Pflugers Arch **447**(5): 666-676.

Kong, W., K. Engel and J. Wang (2004). "Mammalian nucleoside transporters." Curr Drug Metab **5**(1): 63-84.

Krasemann, S., U. Haferkamp, S. Pfefferle, M. S. Woo, F. Heinrich, M. Schweizer, A. Appelt-Menzel, A. Cubukova, J. Barenberg, J. Leu, K. Hartmann, E. Thies, J. L. Littau, D. Sepulveda-Falla, L. Zhang, K. Ton, Y. Liang, J. Matschke, F. Ricklefs, T. Sauvigny, J. Sperhake, A. Fitzek, A. Gerhartl, A. Brachner, N. Geiger, E. M. König, J. Bodem, S. Franzenburg, A. Franke, S. Moese, F. J. Müller, G. Geisslinger, C. Claussen, A. Kannt, A. Zaliani, P. Gribbon, B. Ondruschka, W. Neuhaus, M. A. Friese, M. Glatzel and O. Pless (2022). "The blood-brain barrier is dysregulated in COVID-19 and serves as a CNS entry route for SARS-CoV-2." Stem Cell Reports **17**(2): 307-320.

Krueger, M. and I. Bechmann (2010). "CNS pericytes: concepts, misconceptions, and a way out." Glia **58**(1): 1-10.

Kuhnline Sloan, C. D., P. Nandi, T. H. Linz, J. V. Aldrich, K. L. Audus and S. M. Lunte (2012). "Analytical and biological methods for probing the blood-brain barrier." Annu Rev Anal Chem (Palo Alto Calif) **5**: 505-531.

Kumarasamy, M. and A. Sosnik (2021). "Heterocellular spheroids of the neurovascular blood-brain barrier as a platform for personalized nanoneuromedicine." iScience **24**(3): 102183.

Kurosawa, T., D. Sako, Y. Tega, Y. Debori, Y. Tomihara, K. Aoyama, Y. Kubo, N. Amano and Y. Deguchi (2022). "Construction and Functional Evaluation of a Three-Dimensional Blood–Brain Barrier Model Equipped With Human Induced Pluripotent Stem Cell-Derived Brain Microvascular Endothelial Cells." Pharmaceutical Research **39**(7): 1535-1547.

Laksitorini, M. D., V. Yathindranath, W. Xiong, S. Hombach-Klonisch and D. W. Miller (2019). "Modulation of Wnt/β-catenin signaling promotes blood-brain barrier phenotype in cultured brain endothelial cells." Sci Rep **9**(1): 19718.

Lazzari, G., D. Vinciguerra, A. Balasso, V. Nicolas, N. Goudin, M. Garfa-Traore, A. Féher, A. Dinnyes, J. Nicolas, P. J. E. J. o. P. Couvreur and Biopharmaceutics (2019). "Light sheet fluorescence microscopy versus confocal microscopy: In quest of a suitable tool to assess drug and nanomedicine penetration into multicellular tumor spheroids." **142**: 195-203.

Levesque, M. J. and R. M. Nerem (1985). "The elongation and orientation of cultured endothelial cells in response to shear stress." J Biomech Eng **107**(4): 341-347.

Lewandowsky, M. J. Z. k. M. (1909). "Zur lehre der cerebrospinalflussigkeit." **40**: 480-494.

Li, W., Z. Chen, I. Chin, Z. Chen and H. Dai (2018). "The Role of VE-cadherin in Blood-brain Barrier Integrity Under Central Nervous System Pathological Conditions." Curr Neuropharmacol **16**(9): 1375-1384.

Liddelow, S. A. (2011). "Fluids and barriers of the CNS: a historical viewpoint." Fluids Barriers CNS **8**(1): 2.

Liddelow, S. A., K. M. Dziegielewska, K. Mollgard, S. C. Whish, N. M. Noor, B. J. Wheaton, R. Gehwolf, A. Wagner, A. Traweger, H. Bauer, H. C. Bauer and N. R. Saunders (2014). "Cellular specificity of the blood-CSF barrier for albumin transfer across the choroid plexus epithelium." PLoS One **9**(9): e106592.

Liebner, S., A. Fischmann, G. Rascher, F. Duffner, E. H. Grote, H. Kalbacher and H. Wolburg (2000). "Claudin-1 and claudin-5 expression and tight junction morphology are altered in blood vessels of human glioblastoma multiforme." Acta Neuropathol **100**(3): 323-331.

Liebner, S., U. Kniesel, H. Kalbacher and H. Wolburg (2000). "Correlation of tight junction morphology with the expression of tight junction proteins in blood-brain barrier endothelial cells." Eur J Cell Biol **79**(10): 707-717.

Liebner, S., U. Kniesel, H. Kalbacher and H. J. E. j. o. c. b. Wolburg (2000). "Correlation of tight junction morphology with the expression of tight junction proteins in blood-brain barrier endothelial cells." **79**(10): 707-717.

Liebner, S. and K. H. Plate (2010). "Differentiation of the brain vasculature: the answer came blowing by the Wnt." Journal of Angiogenesis Research **2**(1): 1.

Lim, R. G., C. Quan, A. M. Reyes-Ortiz, S. E. Lutz, A. J. Kedaigle, T. A. Gipson, J. Wu, G. D. Vatine, J. Stocksdale and M. S. J. C. r. Casale (2017). "Huntington's disease iPSC-derived brain microvascular endothelial cells reveal WNT-mediated angiogenic and blood-brain barrier deficits." **19**(7): 1365-1377.

Lin, C. J., Y. Tai, M. T. Huang, Y. F. Tsai, H. J. Hsu, K. Y. Tzen and H. H. Liou (2010). "Cellular localization of the organic cation transporters, OCT1 and OCT2, in brain microvessel endothelial cells and its implication for MPTP transport across the blood-brain barrier and MPTP-induced dopaminergic toxicity in rodents." J Neurochem **114**(3): 717-727.

Linville, R. M., J. G. DeStefano, M. B. Sklar, Z. Xu, A. M. Farrell, M. I. Bogorad, C. Chu, P. Walczak, L. Cheng, V. Mahairaki, K. A. Whartenby, P. A. Calabresi and P. C. Searson (2019). "Human iPSC-derived blood-brain barrier microvessels: validation of barrier function and endothelial cell behavior." Biomaterials **190-191**: 24-37.

Linville, R. M. and P. C. Searson (2021). "Next-generation in vitro blood–brain barrier models: benchmarking and improving model accuracy." Fluids and Barriers of the CNS **18**(1): 56.

Linz, G., S. Djeljadini, L. Steinbeck, G. Köse, F. Kiessling and M. Wessling (2020). "Cell barrier characterization in transwell inserts by electrical impedance spectroscopy." Biosensors and Bioelectronics **165**: 112345.

Lippmann, E. S., A. Al-Ahmad, S. M. Azarin, S. P. Palecek and E. V. Shusta (2014). "A retinoic acid-enhanced, multicellular human blood-brain barrier model derived from stem cell sources." Scientific Reports **4**(1): 4160.

Lippmann, E. S., A. Al-Ahmad, S. M. Azarin, S. P. Palecek and E. V. Shusta (2014). "A retinoic acid-enhanced, multicellular human blood-brain barrier model derived from stem cell sources." Sci Rep **4**: 4160.

Lippmann, E. S., A. Al-Ahmad, S. P. Palecek and E. V. Shusta (2013). "Modeling the blood–brain barrier using stem cell sources." Fluids and Barriers of the CNS **10**(1): 2.

Lippmann, E. S., S. M. Azarin, J. E. Kay, R. A. Nessler, H. K. Wilson, A. Al-Ahmad, S. P. Palecek and E. V. Shusta (2012). "Derivation of blood-brain barrier endothelial cells from human pluripotent stem cells." Nat Biotechnol **30**(8): 783-791.

Lippmann, E. S., S. M. Azarin, S. P. Palecek and E. V. Shusta (2020). "Commentary on human pluripotent stem cell-based blood-brain barrier models." Fluids Barriers CNS **17**(1): 64.

Lippoldt, A., U. Kniesel, S. Liebner, H. Kalbacher, T. Kirsch, H. Wolburg and H. J. B. r. Haller (2000). "Structural alterations of tight junctions are associated with loss of polarity in stroke-prone spontaneously hypertensive rat blood–brain barrier endothelial cells." **885**(2): 251-261.

Liu, C. Y., Y. Yang, W. N. Ju, X. Wang and H. L. Zhang (2018). "Emerging Roles of Astrocytes in Neuro-Vascular Unit and the Tripartite Synapse With Emphasis on Reactive Gliosis in the Context of Alzheimer's Disease." Front Cell Neurosci **12**: 193.

Lochhead, J. J., J. Yang, P. T. Ronaldson and T. P. Davis (2020). "Structure, Function, and Regulation of the Blood-Brain Barrier Tight Junction in Central Nervous System Disorders." Front Physiol **11**: 914.

Logan, C. Y. and R. J. A. R. C. D. B. Nusse (2004). "The Wnt signaling pathway in development and disease." **20**: 781-810.

Loryan, I., M. Fridén and M. Hammarlund-Udenaes (2013). "The brain slice method for studying drug distribution in the CNS." Fluids Barriers CNS **10**(1): 6.

Loryan, I., A. Reichel, B. Feng, C. Bundgaard, C. Shaffer, C. Kalvass, D. Bednarczyk, D. Morrison, D. Lesuisse, E. Hoppe, G. C. Terstappen, H. Fischer, L. Di, N. Colclough, S. Summerfield, S. T. Buckley, T. S. Maurer and M. Fridén (2022). "Unbound Brain-to-Plasma Partition Coefficient, Kp,uu,brain—a Game Changing Parameter for CNS Drug Discovery and Development." Pharmaceutical Research **39**(7): 1321-1341.

Löscher, W. and H. Potschka (2005). "Blood-brain barrier active efflux transporters: ATP-binding cassette gene family." NeuroRx **2**(1): 86-98.

Lossinsky, A. S., H. M. Wiśniewski, M. Dambska and M. J. Mossakowski (1997). "Ultrastructural studies of PECAM-1/CD31 expression in the developing mouse blood-brain barrier with the application of a pre-embedding technique." Folia Neuropathol **35**(3): 163-170.

Lu, T. M., D. Redmond, T. Magdeldin, D.-H. T. Nguyen, A. Snead, A. Sproul, J. Xiang, K. Shido, H. A. Fine and Z. J. b. Rosenwaks (2019). "Human induced pluripotent stem cell-derived

neuroectodermal epithelial cells mistaken for blood-brain barrier-forming endothelial cells." 699173.

Luissint, A. C., C. Artus, F. Glacial, K. Ganeshamoorthy and P. O. Couraud (2012). "Tight junctions at the blood brain barrier: physiological architecture and disease-associated dysregulation." Fluids Barriers CNS **9**(1): 23.

Luptáková, D., T. Vallianatou, A. Nilsson, R. Shariatgorji, M. Hammarlund-Udenaes, I. Loryan and P. E. Andrén (2021). "Neuropharmacokinetic visualization of regional and subregional unbound antipsychotic drug transport across the blood–brain barrier." Molecular Psychiatry **26**(12): 7732-7745.

Ma, S. C., Q. Li, J. Y. Peng, J. L. Zhouwen, J. F. Diao, J. X. Niu, X. Wang, X. D. Guan, W. Jia and W. G. Jiang (2017). "Claudin-5 regulates blood-brain barrier permeability by modifying brain microvascular endothelial cell proliferation, migration, and adhesion to prevent lung cancer metastasis." CNS Neurosci Ther **23**(12): 947-960.

Majesky, M. W. (2007). "Developmental basis of vascular smooth muscle diversity." Arterioscler Thromb Vasc Biol **27**(6): 1248-1258.

Mandai, M., A. Watanabe, Y. Kurimoto, Y. Hirami, C. Morinaga, T. Daimon, M. Fujihara, H. Akimaru, N. Sakai and Y. J. N. E. J. o. M. Shibata (2017). "Autologous induced stem-cell–derived retinal cells for macular degeneration." **376**(11): 1038-1046.

Mantle, J. L., L. Min and K. H. Lee (2016). "Minimum Transendothelial Electrical Resistance Thresholds for the Study of Small and Large Molecule Drug Transport in a Human in Vitro Blood-Brain Barrier Model." Mol Pharm **13**(12): 4191-4198.

Marín-Padilla, M. (2012). "The human brain intracerebral microvascular system: development and structure." Front Neuroanat **6**: 38.

Martinez-Estrada, O. M., A. Villa, F. Breviario, F. Orsenigo, E. Dejana and G. Bazzoni (2001). "Association of junctional adhesion molecule with calcium/calmodulin-dependent serine protein kinase (CASK/LIN-2) in human epithelial caco-2 cells." J Biol Chem **276**(12): 9291-9296.

Martins Gomes, S. F., A. J. Westermann, T. Sauerwein, T. Hertlein, K. U. Förstner, K. Ohlsen, M. Metzger, E. V. Shusta, B. J. Kim, A. Appelt-Menzel and A. Schubert-Unkmeir (2019). "Induced Pluripotent Stem Cell-Derived Brain Endothelial Cells as a Cellular Model to Study Neisseria meningitidis Infection." **10**.

Mayor, S. and R. E. J. N. r. M. c. b. Pagano (2007). "Pathways of clathrin-independent endocytosis." **8**(8): 603-612.

Mbagwu, S. I. and L. Filgueira (2020). "Differential Expression of CD31 and Von Willebrand Factor on Endothelial Cells in Different Regions of the Human Brain: Potential Implications for Cerebral Malaria Pathogenesis." Brain Sci **10**(1).

Mineta, K., Y. Yamamoto, Y. Yamazaki, H. Tanaka, Y. Tada, K. Saito, A. Tamura, M. Igarashi, T. Endo and K. J. F. l. Takeuchi (2011). "Predicted expansion of the claudin multigene family." **585**(4): 606-612.

Mori, S., H. Takanaga, S. Ohtsuki, T. Deguchi, Y. S. Kang, K. Hosoya and T. Terasaki (2003). "Rat organic anion transporter 3 (rOAT3) is responsible for brain-to-blood efflux of homovanillic

acid at the abluminal membrane of brain capillary endothelial cells." J Cereb Blood Flow Metab **23**(4): 432-440.

Morita, K., H. Sasaki, M. Furuse and S. Tsukita (1999). "Endothelial claudin: claudin-5/TMVCF constitutes tight junction strands in endothelial cells." J Cell Biol **147**(1): 185-194.

Morris, M. E., V. Rodriguez-Cruz and M. A. Felmlee (2017). "SLC and ABC Transporters: Expression, Localization, and Species Differences at the Blood-Brain and the Blood-Cerebrospinal Fluid Barriers." Aaps j **19**(5): 1317-1331.

Mueller, M., S. Rasoulinejad, S. Garg and S. V. Wegner (2020). "The Importance of Cell–Cell Interaction Dynamics in Bottom-Up Tissue Engineering: Concepts of Colloidal Self-Assembly in the Fabrication of Multicellular Architectures." Nano Letters **20**(4): 2257-2263.

Nagy, Z., H. Peters, I. J. L. i. Hüttner, a. j. o. t. methods and pathology (1984). "Fracture faces of cell junctions in cerebral endothelium during normal and hyperosmotic conditions." **50**(3): 313-322.

Navone, S. E., G. Marfia, S. Nava, G. Invernici, S. Cristini, S. Balbi, S. Sangiorgi, E. Ciusani, A. Bosutti, G. Alessandri, M. Slevin and E. A. Parati (2013). "Human and mouse brain-derived endothelial cells require high levels of growth factors medium for their isolation, in vitro maintenance and survival." Vasc Cell **5**(1): 10.

Neal, E. H., N. A. Marinelli, Y. Shi, P. M. McClatchey, K. M. Balotin, D. R. Gullett, K. A. Hagerla, A. B. Bowman, K. C. Ess, J. P. Wikswo and E. S. Lippmann (2019). "A Simplified, Fully Defined Differentiation Scheme for Producing Blood-Brain Barrier Endothelial Cells from Human iPSCs." Stem Cell Reports **12**(6): 1380-1388.

Neuhaus, W., E. Bogner, M. Wirth, J. Trzeciak, B. Lachmann, F. Gabor and C. R. J. P. r. Noe (2006). "A novel tool to characterize paracellular transport: the APTS–dextran ladder." **23**(7): 1491-1501.

Newman, P. J. and D. K. Newman (2003). "Signal transduction pathways mediated by PECAM-1: new roles for an old molecule in platelet and vascular cell biology." Arterioscler Thromb Vasc Biol **23**(6): 953-964.

Nguyen, Y. T. K., H. T. T. Ha, T. H. Nguyen and L. N. Nguyen (2021). "The role of SLC transporters for brain health and disease." Cellular and Molecular Life Sciences **79**(1): 20.

Nishiura, K., N. Ichikawa-Tomikawa, K. Sugimoto, Y. Kunii, K. Kashiwagi, M. Tanaka, Y. Yokoyama, M. Hino, T. Sugino, H. Yabe, H. Takahashi, A. Kakita, T. Imura and H. Chiba (2017). "PKA activation and endothelial claudin-5 breakdown in the schizophrenic prefrontal cortex." Oncotarget **8**(55): 93382-93391.

Nitta, T., M. Hata, S. Gotoh, Y. Seo, H. Sasaki, N. Hashimoto, M. Furuse and S. Tsukita (2003). "Size-selective loosening of the blood-brain barrier in claudin-5-deficient mice." J Cell Biol **161**(3): 653-660.

Noell, S., K. Wolburg-Buchholz, A. F. Mack, A. M. Beedle, J. S. Satz, K. P. Campbell, H. Wolburg and P. Fallier-Becker (2011). "Evidence for a role of dystroglycan regulating the membrane architecture of astroglial endfeet." Eur J Neurosci **33**(12): 2179-2186.

Noria, S., D. B. Cowan, A. I. Gotlieb and B. L. Langille (1999). "Transient and steady-state effects of shear stress on endothelial cell adherens junctions." Circ Res **85**(6): 504-514.

Nurnberg, E., M. Vitacolonna, J. Klicks, E. von Molitor, T. Cesetti, F. Keller, R. Bruch, T. Ertongur-Fauth, K. Riedel, P. Scholz, T. Lau, R. Schneider, J. Meier, M. Hafner and R. Rudolf (2020). "Routine Optical Clearing of 3D-Cell Cultures: Simplicity Forward." Front Mol Biosci **7**: 20.

Nzou, G., R. T. Wicks, E. E. Wicks, S. A. Seale, C. H. Sane, A. Chen, S. V. Murphy, J. D. Jackson and A. J. Atala (2018). "Human Cortex Spheroid with a Functional Blood Brain Barrier for High-Throughput Neurotoxicity Screening and Disease Modeling." Sci Rep **8**(1): 7413.

O'Driscoll, M. C., S. B. Daly, J. E. Urquhart, G. C. Black, D. T. Pilz, K. Brockmann, M. McEntagart, G. Abdel-Salam, M. Zaki and N. I. J. T. A. J. o. H. G. Wolf (2010). "Recessive mutations in the gene encoding the tight junction protein occludin cause band-like calcification with simplified gyration and polymicrogyria." **87**(3): 354-364.

Ohtsuki, S., C. Ikeda, Y. Uchida, Y. Sakamoto, F. Miller, F. Glacial, X. Decleves, J. M. Scherrmann, P. O. Couraud, Y. Kubo, M. Tachikawa and T. Terasaki (2013). "Quantitative targeted absolute proteomic analysis of transporters, receptors and junction proteins for validation of human cerebral microvascular endothelial cell line hCMEC/D3 as a human blood-brain barrier model." Mol Pharm **10**(1): 289-296.

Ohtsuki, S., S. Sato, H. Yamaguchi, M. Kamoi, T. Asashima and T. Terasaki (2007). "Exogenous expression of claudin-5 induces barrier properties in cultured rat brain capillary endothelial cells." J Cell Physiol **210**(1): 81-86.

Ohtsuki, S., H. Yamaguchi, Y. Katsukura, T. Asashima and T. J. J. o. n. Terasaki (2008). "mRNA expression levels of tight junction protein genes in mouse brain capillary endothelial cells highly purified by magnetic cell sorting." **104**(1): 147-154.

Orsenigo, F., C. Giampietro, A. Ferrari, M. Corada, A. Galaup, S. Sigismund, G. Ristagno, L. Maddaluno, G. Y. Koh, D. Franco, V. Kurtcuoglu, D. Poulikakos, P. Baluk, D. McDonald, M. Grazia Lampugnani and E. Dejana (2012). "Phosphorylation of VE-cadherin is modulated by haemodynamic forces and contributes to the regulation of vascular permeability in vivo." Nat Commun **3**: 1208.

Osipova, E. D., Y. K. Komleva, A. V. Morgun, O. L. Lopatina, Y. A. Panina, R. Y. Olovyannikova, E. F. Vais, V. V. Salmin and A. B. Salmina (2018). "Designing in vitro Blood-Brain Barrier Models Reproducing Alterations in Brain Aging." Front Aging Neurosci **10**: 234.
Pardridge, W. M. (2019). "Blood-Brain Barrier and Delivery of Protein and Gene Therapeutics to Brain." Front Aging Neurosci **11**: 373.

Paredes, I., P. Himmels and C. Ruiz de Almodóvar (2018). "Neurovascular Communication during CNS Development." Developmental Cell **45**(1): 10-32.

Patabendige, A., R. A. Skinner and N. J. Abbott (2013). "Establishment of a simplified in vitro porcine blood-brain barrier model with high transendothelial electrical resistance." Brain Res **1521**: 1-15.

Patel, R., M. A. Hossain, N. German and A. J. J. M. r. Al-Ahmad (2018). "Gliotoxin penetrates and impairs the integrity of the human blood-brain barrier in vitro." **34**(4): 257-268.
Peng, G., P. P. L. Tam and N. Jing (2017). "Lineage specification of early embryos and embryonic stem cells at the dawn of enabling technologies." National Science Review **4**(4): 533-542.

Pfeiffer, F., J. Schäfer, R. Lyck, V. Makrides, S. Brunner, N. Schaeren-Wiemers, U. Deutsch and B. Engelhardt (2011). "Claudin-1 induced sealing of blood–brain barrier tight junctions

ameliorates chronic experimental autoimmune encephalomyelitis." Acta Neuropathologica **122**(5): 601.

Piontek, J., S. Fritzsche, J. Cording, S. Richter, J. Hartwig, M. Walter, D. Yu, J. R. Turner, C. Gehring, H. P. Rahn, H. Wolburg and I. E. Blasig (2011). "Elucidating the principles of the molecular organization of heteropolymeric tight junction strands." Cell Mol Life Sci **68**(23): 3903-3918.

Poenick, S., H.-G. Jahnke, M. Eichler, S. Frost, H. Lilie and A. A. Robitzki (2014). "Comparative label-free monitoring of immunotoxin efficacy in 2D and 3D mamma carcinoma in vitro models by impedance spectroscopy." Biosensors and Bioelectronics **53**: 370-376.

Pound, P. (2020). "Are Animal Models Needed to Discover, Develop and Test Pharmaceutical Drugs for Humans in the 21st Century?" Animals (Basel) **10**(12).

Praca, C., S. C. Rosa, E. Sevin, R. Cecchelli, M. P. Dehouck and L. S. Ferreira (2019). "Derivation of Brain Capillary-like Endothelial Cells from Human Pluripotent Stem Cell-Derived Endothelial Progenitor Cells." Stem Cell Reports **13**(4): 599-611.

Prasain, N. and T. Stevens (2009). "The actin cytoskeleton in endothelial cell phenotypes." Microvascular research **77**(1): 53-63.

Prashanth, A., H. Donaghy, S. P. Stoner, A. L. Hudson, H. R. Wheeler, C. I. Diakos, V. M. Howell, G. E. Grau and K. J. McKelvey (2021). "Are In Vitro Human Blood-Brain-Tumor-Barriers Suitable Replacements for In Vivo Models of Brain Permeability for Novel Therapeutics?" Cancers (Basel) **13**(5).

Privratsky, J. R. and P. J. Newman (2014). "PECAM-1: regulator of endothelial junctional integrity." Cell Tissue Res **355**(3): 607-619.

Privratsky, J. R., C. M. Paddock, O. Florey, D. K. Newman, W. A. Muller and P. J. Newman (2011). "Relative contribution of PECAM-1 adhesion and signaling to the maintenance of vascular integrity." J Cell Sci **124**(Pt 9): 1477-1485.

Pulgar, V. M. (2018). "Transcytosis to Cross the Blood Brain Barrier, New Advancements and Challenges." Front Neurosci **12**: 1019.

Qian, T., S. E. Maguire, S. G. Canfield, X. Bao, W. R. Olson, E. V. Shusta and S. P. Palecek (2017). "Directed differentiation of human pluripotent stem cells to blood-brain barrier endothelial cells." Sci Adv **3**(11): e1701679.

Raab, S., H. Beck, A. Gaumann, A. Yüce, H.-P. Gerber, K. Plate, H.-P. Hammes, N. Ferrara, G. J. T. Breier and haemostasis (2004). "Impaired brain angiogenesis and neuronal apoptosis induced by conditional homozygous inactivation of vascular endothelial growth factor." **91**(03): 595-605.

Raichle, M. E. and D. A. J. P. o. t. N. A. o. S. Gusnard (2002). "Appraising the brain's energy budget." **99**(16): 10237-10239.

Redzic, Z. B., J. Biringer, K. Barnes, S. A. Baldwin, H. Al-Sarraf, P. A. Nicola, J. D. Young, C. E. Cass, M. A. Barrand and S. B. Hladky (2005). "Polarized distribution of nucleoside transporters in rat brain endothelial and choroid plexus epithelial cells." J Neurochem **94**(5): 1420-1426.

Reichel, A. (2006). "The role of blood-brain barrier studies in the pharmaceutical industry." Curr Drug Metab **7**(2): 183-203.

Reitinger, S., J. Wissenwasser, W. Kapferer, R. Heer and G. Lepperdinger (2012). "Electric impedance sensing in cell-substrates for rapid and selective multipotential differentiation capacity monitoring of human mesenchymal stem cells." Biosens Bioelectron **34**(1): 63-69.
Ribecco-Lutkiewicz, M., C. Sodja, J. Haukenfrers, A. S. Haqqani, D. Ly, P. Zachar, E. Baumann, M. Ball, J. Huang, M. Rukhlova, M. Martina, Q. Liu, D. Stanimirovic, A. Jezierski and M. Bani-Yaghoub (2018). "A novel human induced pluripotent stem cell blood-brain barrier model: Applicability to study antibody-triggered receptor-mediated transcytosis." Sci Rep **8**(1): 1873.

Risau, W., R. Hallmann and U. J. D. b. Albrecht (1986). "Differentiation-dependent expression of proteins in brain endothelium during development of the blood-brain barrier." **117**(2): 537-545.

Roberts, L. M., D. S. Black, C. Raman, K. Woodford, M. Zhou, J. E. Haggerty, A. T. Yan, S. E. Cwirla and K. K. Grindstaff (2008). "Subcellular localization of transporters along the rat blood-brain barrier and blood-cerebral-spinal fluid barrier by in vivo biotinylation." Neuroscience **155**(2): 423-438.

Roudnicky, F., J. D. Zhang, B. K. Kim, N. J. Pandya, Y. Lan, L. Sach-Peltason, H. Ragelle, P. Strassburger, S. Gruener, M. Lazendic, S. Uhles, F. Revelant, O. Eidam, G. Sturm, V. Kueppers, K. Christensen, L. D. Goldstein, M. Tzouros, B. Banfai, Z. Modrusan, M. Graf, C. Patsch, M. Burcin, C. A. Meyer, P. D. Westenskow and C. A. Cowan (2020). "Inducers of the endothelial cell barrier identified through chemogenomic screening in genome-edited hPSC-endothelial cells." Proc Natl Acad Sci U S A **117**(33): 19854-19865.

Roux, E., P. Bougaran, P. Dufourcq and T. Couffinhal (2020). "Fluid Shear Stress Sensing by the Endothelial Layer." Front Physiol **11**: 861.

Roux, G. L., R. Jarray, A. C. Guyot, S. Pavoni, N. Costa, F. Theodoro, F. Nassor, A. Pruvost, N. Tournier, Y. Kiyan, O. Langer, F. Yates, J. P. Deslys and A. Mabondzo (2019). "Proof-of-Concept Study of Drug Brain Permeability Between in Vivo Human Brain and an in Vitro iPSCs-Human Blood-Brain Barrier Model." Sci Rep **9**(1): 16310.

Rubin, L., D. Hall, S. Porter, K. Barbu, C. Cannon, H. Horner, M. Janatpour, C. Liaw, K. Manning and J. J. T. J. o. c. b. Morales (1991). "A cell culture model of the blood-brain barrier." **115**(6): 1725-1735.

Ruck, T., S. Bittner and S. G. Meuth (2015). "Blood-brain barrier modeling: challenges and perspectives." Neural regeneration research **10**(6): 889-891.

Russo, T. A., A. M. M. Banuth, H. B. Nader and J. L. Dreyfuss (2020). "Altered shear stress on endothelial cells leads to remodeling of extracellular matrix and induction of angiogenesis." PLoS One **15**(11): e0241040.

Saili, K. S., T. J. Zurlinden, A. J. Schwab, A. Silvin, N. C. Baker, E. S. Hunter, 3rd, F. Ginhoux and T. B. Knudsen (2017). "Blood-brain barrier development: Systems modeling and predictive toxicology." Birth Defects Res **109**(20): 1680-1710.

Saitou, M., M. Furuse, H. Sasaki, J.-D. Schulzke, M. Fromm, H. Takano, T. Noda and S. J. M. b. o. t. c. Tsukita (2000). "Complex phenotype of mice lacking occludin, a component of tight junction strands." **11**(12): 4131-4142.

Sánchez-Dengra, B., I. González-Álvarez, F. Sousa, M. Bermejo, M. González-Álvarez and B. Sarmento (2021). "In vitro model for predicting the access and distribution of drugs in the brain using hCMEC/D3 cells." Eur J Pharm Biopharm **163**: 120-126.

Santa-Maria, A. R., M. Heymans, F. R. Walter, M. Culot, F. Gosselet, M. A. Deli and W. Neuhaus (2022). "Transport Studies Using Blood-Brain Barrier In Vitro Models: A Critical Review and Guidelines." Handb Exp Pharmacol **273**: 187-204.

Santos, G. S. P., L. A. V. Magno, M. A. Romano-Silva, A. Mintz and A. Birbrair (2019). "Pericyte Plasticity in the Brain." Neurosci Bull **35**(3): 551-560.

Saunders, N. R., J. J. Dreifuss, K. M. Dziegielewska, P. A. Johansson, M. D. Habgood, K. Mollgard and H. C. Bauer (2014). "The rights and wrongs of blood-brain barrier permeability studies: a walk through 100 years of history." Front Neurosci **8**: 404.

Sauteur, L., A. Krudewig, L. Herwig, N. Ehrenfeuchter, A. Lenard, M. Affolter and H.-G. Belting (2014). "Cdh5/VE-cadherin Promotes Endothelial Cell Interface Elongation via Cortical Actin Polymerization during Angiogenic Sprouting." Cell Reports **9**(2): 504-513.

Scesa, G., R. Adami and D. Bottai (2021). "iPSC Preparation and Epigenetic Memory: Does the Tissue Origin Matter?" Cells **10**(6).

Schmitz, T., M. Schweinlin, R. T. Kollhoff, L. Engelhardt, C. Lotz, F. Groeber-Becker, H. Walles, M. Metzger and J. Hansmann (2018). "Nanostructured TiN-Coated Electrodes for High-Sensitivity Noninvasive Characterization of in Vitro Tissue Models." ACS Applied Nano Materials **1**(5): 2284-2293.

Schneider, S. W., S. Nuschele, A. Wixforth, C. Gorzelanny, A. Alexander-Katz, R. R. Netz and M. F. Schneider (2007). "Shear-induced unfolding triggers adhesion of von Willebrand factor fibers." Proc Natl Acad Sci U S A **104**(19): 7899-7903.

Scudellari, M. (2016). "How iPS cells changed the world." Nature **534**(7607): 310-312.
Serlin, Y., I. Shelef, B. Knyazer and A. Friedman (2015). "Anatomy and physiology of the blood-brain barrier." Semin Cell Dev Biol **38**: 2-6.

Sharma, A., S. Sances, M. J. Workman and C. N. Svendsen (2020). "Multi-lineage Human iPSC-Derived Platforms for Disease Modeling and Drug Discovery." Cell Stem Cell **26**(3): 309-329.

Shawahna, R., Y. Uchida, X. Decleves, S. Ohtsuki, S. Yousif, S. Dauchy, A. Jacob, F. Chassoux, C. Daumas-Duport, P. O. Couraud, T. Terasaki and J. M. Scherrmann (2011). "Transcriptomic and quantitative proteomic analysis of transporters and drug metabolizing enzymes in freshly isolated human brain microvessels." Mol Pharm **8**(4): 1332-1341.
Shepro, D. and N. M. Morel (1993). "Pericyte physiology." Faseb j **7**(11): 1031-1038.
Siflinger-Birnboim, A., P. J. del Vecchio, J. A. Cooper, F. A. Blumenstock, J. M. Shepard and A. B. J. J. o. c. p. Malik (1987). "Molecular sieving characteristics of the cultured endothelial monolayer." **132**(1): 111-117.

Singh, S. K., S. Abbas, A. K. Saxena, S. Tiwari, L. K. Sharma and M. Tiwari (2020). "Critical role of three-dimensional tumorsphere size on experimental outcome." Biotechniques **69**(5): 333-338.

Sinha, S. K. and A. Bit (2020). 23 - Microfluidics in tissue engineering. Biomaterials for Organ and Tissue Regeneration. N. E. Vrana, H. Knopf-Marques and J. Barthes, Woodhead Publishing**:** 567-598.

Smith, Q. R. (2000). "Transport of glutamate and other amino acids at the blood-brain barrier." J Nutr **130**(4S Suppl): 1016S-1022S.

Smith, Q. R. (2003). "A review of blood-brain barrier transport techniques." Methods Mol Med **89**: 193-208.

Sporn, L. A., V. J. Marder and D. D. Wagner (1989). "Differing polarity of the constitutive and regulated secretory pathways for von Willebrand factor in endothelial cells." J Cell Biol **108**(4): 1283-1289.

Staehelin, L. A. J. I. r. o. c. (1974). "Structure and function of intercellular junctions." **39**: 191-283.

Stamatovic, S. M., R. F. Keep and A. V. Andjelkovic (2008). "Brain endothelial cell-cell junctions: how to "open" the blood brain barrier." Curr Neuropharmacol **6**(3): 179-192.

Stebbins, M. J., H. K. Wilson, S. G. Canfield, T. Qian, S. P. Palecek and E. V. Shusta (2016). "Differentiation and characterization of human pluripotent stem cell-derived brain microvascular endothelial cells." Methods **101**: 93-102.

Stern, L. and E. J. S. A. N. P. Rothlin (1918). "Effets de l'action directe du curare sur les différentes parties du cervelet." **3**: 234-254.

Sun, J., W. Ou, D. Han, A. Paganini-Hill, M. J. Fisher and R. K. Sumbria (2022). "Comparative studies between the murine immortalized brain endothelial cell line (bEnd.3) and induced pluripotent stem cell-derived human brain endothelial cells for paracellular transport." PLoS One **17**(5): e0268860.

Sun, X.-Y., X.-C. Ju, Y. Li, P.-M. Zeng, J. Wu, Y.-Y. Zhou, L.-B. Shen, J. Dong, Y.-J. Chen and Z.-G. Luo (2022). "Generation of vascularized brain organoids to study neurovascular interactions." eLife **11**: e76707.

Tajes, M., E. Ramos-Fernández, X. Weng-Jiang, M. Bosch-Morató, B. Guivernau, A. Eraso-Pichot, B. Salvador, X. Fernàndez-Busquets, J. Roquer and F. J. Muñoz (2014). "The blood-brain barrier: Structure, function and therapeutic approaches to cross it." Molecular Membrane Biology **31**(5): 152-167.

Takahashi, J. (2020). "iPS cell-based therapy for Parkinson's disease: A Kyoto trial." Regen Ther **13**: 18-22.

Takahashi, K., K. Tanabe, M. Ohnuki, M. Narita, T. Ichisaka, K. Tomoda and S. J. c. Yamanaka (2007). "Induction of pluripotent stem cells from adult human fibroblasts by defined factors." **131**(5): 861-872.

Takahashi, K. and S. Yamanaka (2006). "Induction of pluripotent stem cells from mouse embryonic and adult fibroblast cultures by defined factors." Cell **126**(4): 663-676.

Tang, M., G. Gao, C. B. Rueda, H. Yu, D. N. Thibodeaux, T. Awano, K. M. Engelstad, M.-J. Sanchez-Quintero, H. Yang, F. Li, H. Li, Q. Su, K. E. Shetler, L. Jones, R. Seo, J. McConathy, E. M. Hillman, J. L. Noebels, D. C. De Vivo and U. R. Monani (2017). "Brain microvasculature defects and Glut1 deficiency syndrome averted by early repletion of the glucose transporter-1 protein." Nature Communications **8**(1): 14152.

Tata, M. and C. Ruhrberg (2018). "Cross-talk between blood vessels and neural progenitors in the developing brain." Neuronal Signal **2**(1): Ns20170139.

Tata, M., C. Ruhrberg and A. Fantin (2015). "Vascularisation of the central nervous system." Mech Dev **138 Pt 1**: 26-36.

Thakur, J. D., A. Sonig, P. Chittiboina, I. S. Khan, R. Wadhwa and A. Nanda (2012). "Humphrey Ridley (1653-1708): 17th century evolution in neuroanatomy and selective cerebrovascular injections for cadaver dissection." Neurosurg Focus **33**(2): E3.

Thomsen, M. S., N. Humle, E. Hede, T. Moos, A. Burkhart and L. B. Thomsen (2021). "The blood-brain barrier studied in vitro across species." PLoS One **16**(3): e0236770.

Tietz, S. and B. Engelhardt (2015). "Brain barriers: Crosstalk between complex tight junctions and adherens junctions." J Cell Biol **209**(4): 493-506.

Tsai, H. M. (2003). "Shear stress and von Willebrand factor in health and disease." Semin Thromb Hemost **29**(5): 479-488.

Uchida, Y., S. Ohtsuki, Y. Katsukura, C. Ikeda, T. Suzuki, J. Kamiie and T. Terasaki (2011). "Quantitative targeted absolute proteomics of human blood-brain barrier transporters and receptors." J Neurochem **117**(2): 333-345.

Upadhyay, R. K. (2014). "Transendothelial Transport and Its Role in Therapeutics." Int Sch Res Notices **2014**: 309404.

Urich, E., S. E. Lazic, J. Molnos, I. Wells and P. O. Freskgård (2012). "Transcriptional profiling of human brain endothelial cells reveals key properties crucial for predictive in vitro blood-brain barrier models." PLoS One **7**(5): e38149.

Urich, E., C. Patsch, S. Aigner, M. Graf, R. Iacone and P.-O. Freskgård (2013). "Multicellular Self-Assembled Spheroidal Model of the Blood Brain Barrier." Scientific Reports **3**(1): 1500.
van der Helm, M. W., A. D. van der Meer, J. C. Eijkel, A. van den Berg and L. I. Segerink (2016). "Microfluidic organ-on-chip technology for blood-brain barrier research." Tissue Barriers **4**(1): e1142493.

Van Norman, G. A. (2019). "Limitations of Animal Studies for Predicting Toxicity in Clinical Trials: Is it Time to Rethink Our Current Approach?" JACC: Basic to Translational Science **4**(7): 845-854.

Vatine, G. D., A. Al-Ahmad, B. K. Barriga, S. Svendsen, A. Salim, L. Garcia, V. J. Garcia, R. Ho, N. Yucer and T. J. C. s. c. Qian (2017). "Modeling psychomotor retardation using iPSCs from MCT8-deficient patients indicates a prominent role for the blood-brain barrier." **20**(6): 831-843. e835.

Vatine, G. D., R. Barrile, M. J. Workman, S. Sances, B. K. Barriga, M. Rahnama, S. Barthakur, M. Kasendra, C. Lucchesi, J. Kerns, N. Wen, W. R. Spivia, Z. Chen, J. Van Eyk and C. N. Svendsen (2019). "Human iPSC-Derived Blood-Brain Barrier Chips Enable Disease Modeling and Personalized Medicine Applications." Cell Stem Cell **24**(6): 995-1005.e1006.
Veith, P., K. Watanabe, M. M. Shoja, C. Blaak, M. Loukas and R. S. Tubbs (2015). "Humphrey Ridley (1653-1708): forgotten neuroanatomist and neurophysiologist." Clin Anat **28**(1): 12-15.
Veys, K., Z. Fan, M. Ghobrial, A. Bouche, M. Garcia-Caballero, K. Vriens, N. V. Conchinha, A. Seuwen, F. Schlegel, T. Gorski, M. Crabbe, P. Gilardoni, R. Ardicoglu, J. Schaffenrath, C. Casteels, G. De Smet, I. Smolders, K. Van Laere, E. D. Abel, S. M. Fendt, A. Schroeter, J. Kalucka, A. R. Cantelmo, T. Walchli, A. Keller, P. Carmeliet and K. De Bock (2020). "Role of the GLUT1 Glucose Transporter in Postnatal CNS Angiogenesis and Blood-Brain Barrier Integrity." Circ Res **127**(4): 466-482.

Vigh, J. P., A. Kincses, B. Ozgür, F. R. Walter, A. R. Santa-Maria, S. Valkai, M. Vastag, W. Neuhaus, B. Brodin, A. Dér and M. A. Deli (2021). "Transendothelial Electrical Resistance Measurement across the Blood-Brain Barrier: A Critical Review of Methods." Micromachines (Basel) **12**(6).

Villasenor, R., J. Lampe, M. Schwaninger and L. Collin (2019). "Intracellular transport and regulation of transcytosis across the blood-brain barrier." Cell Mol Life Sci **76**(6): 1081-1092.
Virgintino, D., M. Errede, D. Robertson, C. Capobianco, F. Girolamo, A. Vimercati, M. Bertossi and L. Roncali (2004). "Immunolocalization of tight junction proteins in the adult and developing human brain." Histochem Cell Biol **122**(1): 51-59.

Volpato, V. and C. Webber (2020). "Addressing variability in iPSC-derived models of human disease: guidelines to promote reproducibility." Dis Model Mech **13**(1).
Wang, D., J. M. Pascual, H. Yang, K. Engelstad, S. Jhung, R. P. Sun and D. C. De Vivo (2005). "Glut-1 deficiency syndrome: clinical, genetic, and therapeutic aspects." Ann Neurol **57**(1): 111-118.

Wang, Y., A. Rattner, Y. Zhou, J. Williams, P. M. Smallwood and J. J. C. Nathans (2012). "Norrin/Frizzled4 signaling in retinal vascular development and blood brain barrier plasticity." **151**(6): 1332-1344.

Ward, J. P. and J. R. King (2003). "Mathematical modelling of drug transport in tumour multicell spheroids and monolayer cultures." Math Biosci **181**(2): 177-207.

Wegener, J., J. J. C. Seebach and t. research (2014). "Experimental tools to monitor the dynamics of endothelial barrier function: a survey of in vitro approaches." **355**(3): 485-514.

Weksler, B., I. A. Romero and P.-O. Couraud (2013). "The hCMEC/D3 cell line as a model of the human blood brain barrier." Fluids and Barriers of the CNS **10**(1): 16.

Weksler, B. B., E. A. Subileau, N. Perrière, P. Charneau, K. Holloway, M. Leveque, H. Tricoire-Leignel, A. Nicotra, S. Bourdoulous, P. Turowski, D. K. Male, F. Roux, J. Greenwood, I. A. Romero and P. O. Couraud (2005). "Blood-brain barrier-specific properties of a human adult brain endothelial cell line." Faseb j **19**(13): 1872-1874.

Wevers, N. R. and H. E. de Vries (2016). "Morphogens and blood-brain barrier function in health and disease." Tissue Barriers **4**(1): e1090524.

Wimmer, I., S. Tietz, H. Nishihara, U. Deutsch, F. Sallusto, F. Gosselet, R. Lyck, W. A. Muller, H. Lassmann and B. Engelhardt (2019). "PECAM-1 Stabilizes Blood-Brain Barrier Integrity and Favors Paracellular T-Cell Diapedesis Across the Blood-Brain Barrier During Neuroinflammation." **10**.

Wimmer, I., S. Tietz, H. Nishihara, U. Deutsch, F. Sallusto, F. Gosselet, R. Lyck, W. A. Muller, H. Lassmann and B. Engelhardt (2019). "PECAM-1 Stabilizes Blood-Brain Barrier Integrity and Favors Paracellular T-Cell Diapedesis Across the Blood-Brain Barrier During Neuroinflammation." Front Immunol **10**: 711.

Winkler, E. A., R. D. Bell and B. V. Zlokovic (2011). "Central nervous system pericytes in health and disease." Nat Neurosci **14**(11): 1398-1405.

Winkler, L., R. Blasig, O. Breitkreuz-Korff, P. Berndt, S. Dithmer, H. C. Helms, D. Puchkov, K. Devraj, M. Kaya, Z. Qin, S. Liebner, H. Wolburg, A. V. Andjelkovic, A. Rex, I. E. Blasig and R. F. Haseloff (2021). "Tight junctions in the blood-brain barrier promote edema formation and

infarct size in stroke - Ambivalent effects of sealing proteins." J Cereb Blood Flow Metab **41**(1): 132-145.

Wolburg, H., K. Wolburg-Buchholz, P. Fallier-Becker, S. Noell and A. F. Mack (2011). "Structure and functions of aquaporin-4-based orthogonal arrays of particles." Int Rev Cell Mol Biol **287**: 1-41.

Wong, A. D., M. Ye, A. F. Levy, J. D. Rothstein, D. E. Bergles and P. C. Searson (2013). "The blood-brain barrier: an engineering perspective." Front Neuroeng **6**: 7.

Workman, M. J. and C. N. Svendsen (2020). "Recent advances in human iPSC-derived models of the blood–brain barrier." Fluids and Barriers of the CNS **17**(1): 30.

Yamashita, M., H. Aoki, T. Hashita, T. Iwao and T. Matsunaga (2020). "Inhibition of transforming growth factor beta signaling pathway promotes differentiation of human induced pluripotent stem cell-derived brain microvascular endothelial-like cells." Fluids Barriers CNS **17**(1): 36.

Youssef, J., A. K. Nurse, L. B. Freund and J. R. Morgan (2011). "Quantification of the forces driving self-assembly of three-dimensional microtissues." **108**(17): 6993-6998.

Zakrzewski, W., M. Dobrzynski, M. Szymonowicz and Z. Rybak (2019). "Stem cells: past, present, and future." Stem Cell Res Ther **10**(1): 68.

Zhang, Z., M. Tachikawa, Y. Uchida and T. Terasaki (2018). "Drug Clearance from Cerebrospinal Fluid Mediated by Organic Anion Transporters 1 (Slc22a6) and 3 (Slc22a8) at Arachnoid Membrane of Rats." Mol Pharm **15**(3): 911-922.

Zitzmann, F. D., S. Schmidt, M. Naumann, D. Belder, H.-G. Jahnke and A. A. Robitzki (2022). "Multielectrode biosensor chip for spatial resolution screening of 3D cell models based on microcavity arrays." Biosensors and Bioelectronics **202**: 114010.